

# Durham E-Theses

---

## *MEMS sensors for wall shear stress and flow vector measurement*

Allen, Naomi

### How to cite:

---

Allen, Naomi (2008) *MEMS sensors for wall shear stress and flow vector measurement*, Durham theses, Durham University. Available at Durham E-Theses Online: <http://etheses.dur.ac.uk/2182/>

### Use policy

---

The full-text may be used and/or reproduced, and given to third parties in any format or medium, without prior permission or charge, for personal research or study, educational, or not-for-profit purposes provided that:

- a full bibliographic reference is made to the original source
- a [link](#) is made to the metadata record in Durham E-Theses
- the full-text is not changed in any way

The full-text must not be sold in any format or medium without the formal permission of the copyright holders.

Please consult the [full Durham E-Theses policy](#) for further details.

# MEMS sensors for wall shear stress and flow vector measurement

The copyright of this thesis rests with the author or the university to which it was submitted. No quotation from it, or information derived from it may be published without the prior written consent of the author or university, and any information derived from it should be acknowledged.

Naomi Allen MEng (Hons)  
School of Engineering  
Durham University

A thesis submitted to Durham University for the Degree of  
Doctor of Philosophy

December 2008



- 6 MAY 2009

## Abstract

The accurate measurement of airflows is an important area of experimental aerodynamics. MEMS technology has been applied to the measurement of wall shear stress and freestream velocity vectors. Existing methods of measuring wall shear stress vary greatly and have different strengths and weaknesses, making them each applicable to specific situations. Probes designed for measuring 3D velocity components are relatively large in diameter, introducing significant disturbances into the airflow. The tip diameters of such probes are typically of the order of several millimetres and the minimum diameter is around 1 mm.

A sensor for measuring wall shear stress, consisting of a surface fence structure 5 mm long, 750  $\mu\text{m}$  high and 20  $\mu\text{m}$  thick was developed. The fence, and main body on which it was mounted, were fabricated from the photo-definable polymer SU8 with an integrated gold resistive strain gauge to measure the pressure-induced deflection. Wind tunnel testing gave a voltage output of 0.18 mV for a shear stress of approximately 0.35 Pa.

This concept was then adapted and an in-plane cantilever sensor was developed. The cantilever sensor was manufactured from SU-8 with an integrated resistive strain gauge of NiCr. The pressure-induced deflection of the cantilever, calibrated by the integrated strain gauge, could be related to the wall shear stress on the surface. The sensor gave a response of  $9.6 \times 10^{-4} \text{ (mV/V)/}\mu\text{m}$  under mechanical deflection. For a 2 mm long, 400  $\mu\text{m}$  wide cantilever when tested on a flat plate in a wind tunnel, a response of 1mV for a shear stress of 0.35 Pa was seen.

Four cantilever sensors were arranged orthogonally to create a new type of probe for measuring flow direction and velocity, which could also measure total pressure. The probe was shown to be able to measure these variables and with further development had the potential to allow the fabrication of a smaller probe tip than that possible by conventional methods.

## **Acknowledgements**

I would like to thank Professor David Wood and Dr David Sims-Williams for their invaluable help and advice throughout my research.

My thanks to Mark Rosamond, Andrew Gallant and Mike Cooke for their guidance on all things 'clean room' and particularly the former for the use of his mechanical testing rig, along with the skilled operator!

I am also grateful to everyone else who has helped me, either by being a sounding board for ideas, or just by putting up with my preoccupation with small things for the last three years!



# **Declaration**

I declare that no material in this thesis has previously been submitted for a degree at this or any other university.

The copyright of this thesis rests with the author. No quotation from it should be published without their prior written consent and information derived from it should be acknowledged.

# Table of Contents

- Chapter 1 Introduction..... 1
  - 1.1 Background..... 1
  - 1.2 Shear stress..... 4
  - 1.3 MEMS Technology ..... 6
  - 1.4 Thesis structure ..... 7
- Chapter 2 Literature Review ..... 9
  - 2.1 Review of existing shear stress sensors..... 9
    - 2.1.1 Oil film interferometry..... 9
    - 2.1.2 Liquid crystal coating ..... 10
    - 2.1.3 Floating element sensors..... 10
    - 2.1.4 Thermal sensors..... 12
    - 2.1.5 Indirect optical sensors ..... 13
    - 2.1.6 Fence sensors..... 14
    - 2.1.7 Artificial haircells and micro-pillars..... 15
    - 2.1.8 Preston tubes ..... 16
    - 2.1.9 Summary ..... 16
  - 2.2 Review of freestream velocity vector measurement ..... 18
    - 2.2.1 Particle image velocimetry..... 18
    - 2.2.2 Laser doppler velocimetry ..... 19
    - 2.2.3 Multi-hole probes ..... 20
    - 2.2.4 Hot-wire probes..... 22
    - 2.2.5 Summary ..... 23
- Chapter 3 Experimental Methods..... 25
  - 3.1 MEMS fabrication processes ..... 25
    - 3.1.1 Mask making..... 26
    - 3.1.2 Patterning ..... 27
    - 3.1.3 Thin film deposition ..... 30
    - 3.1.4 Wet etching of metals ..... 34
    - 3.1.5 Sacrificial layer..... 34
  - 3.2 Force-deflection test rig..... 37

3.3	Wind tunnel testing.....	39
3.3.1	Wind tunnel apparatus .....	39
3.3.2	Data acquisition software.....	43
3.3.3	Sampling frequency and averaging .....	44
3.4	CFD background and theory.....	45
3.4.1	Fluent .....	45
3.4.2	Governing equations of fluid flow .....	45
3.4.3	Turbulence models .....	49
3.4.4	Equation discretization .....	49
3.4.5	Spatial discretization.....	50
3.5	Structural analysis .....	51
3.5.1	Beam theory .....	51
3.5.2	FEA.....	52
3.6	Summary.....	55
Chapter 4	Fence-style sensor for wall shear stress measurement .....	56
4.1	Theory of operation .....	56
4.2	Device Fabrication and Design .....	58
4.2.1	Design .....	58
4.2.2	Fabrication .....	60
4.3	CFD .....	65
4.3.1	Mesh approach .....	65
4.3.2	Mesh validation .....	66
4.3.3	Iteration dependency.....	69
4.3.4	CFD results.....	71
4.4	FEM .....	76
4.4.1	Initial FEM modelling .....	76
4.4.2	FEM results .....	77
4.5	Wind tunnel testing.....	80
4.5.1	Wind tunnel apparatus .....	80
4.5.2	Noise reduction.....	81
4.5.3	Initial wind tunnel results.....	84
4.5.4	Comparison of theoretical and experimental results .....	86

4.6	Summary .....	89
Chapter 5	Cantilever-style sensor for wall shear stress measurement.....	91
5.1	Theory of operation .....	91
5.2	Device design and fabrication.....	94
5.2.1	Device design .....	94
5.2.2	Resistor length.....	97
5.2.3	Resonant frequency of the cantilever .....	105
5.2.4	Variation of stress gradient with exposure dose.....	107
5.2.5	Sidewall coverage.....	112
5.2.6	Calculation of TCR.....	115
5.2.7	Fabrication .....	117
5.3	Results.....	122
5.3.1	Mechanical testing .....	122
5.3.2	FEA results.....	128
5.3.3	CFD results.....	129
5.3.4	Combined CFD and FE results.....	140
5.3.5	Wind tunnel results.....	145
5.4	Summary .....	155
Chapter 6	3D flow vector measurement .....	157
6.1	Background .....	157
6.2	Theory of operation .....	159
6.3	Design and Fabrication.....	163
6.3.1	MEMS Fabrication .....	163
6.3.2	Probe assembly.....	165
6.4	Results.....	169
6.4.1	FEM results .....	169
6.4.2	CFD Results .....	171
6.4.3	Wind tunnel results.....	182
6.5	Revised probe design.....	190
6.5.1	Design .....	190
6.5.2	Wind tunnel results.....	192
6.6	Summary.....	204

Chapter 7   Conclusions ..... 207

7.1   Fence-style shear stress sensor..... 207

7.2   Cantilever-style shear stress sensor..... 208

7.3   Probe for freestream flow vector measurement ..... 210

7.4   Further work..... 211

7.4.1   Wall shear stress sensors..... 211

7.4.2   Probe for freestream flow vector measurement ..... 212

# Nomenclature

A	Area [m <sup>2</sup> ]	w	Velocity [m/s]
b	Width of beam [m]		Distributed load [N/m]
C <sub>p</sub>	Pressure coefficient	x	Distance [m]
d	Displacement vector	X	Body force [N]
e	Internal energy	y	Distance [m]
E	Young's modulus [Pa]	Y	Body force [N]
F	Force [N]	z	Distance [m]
g	Distance under cantilever [m]	Z	Body force [N]
h	Height [m]		
	Heat transfer coefficient		
I	2 <sup>nd</sup> moment of area [m <sup>4</sup> ]	α	Thermal coefficient of resistivity [K <sup>-1</sup> ]
k	Thermal conductivity [W/mK]	β	Resistance /unit length [Ω/m]
	Turbulent kinetic energy	δ	Deflection [m]
K	Gauge factor		Boundary layer thickness [m]
	Stiffness matrix	ε	Turbulent dissipation
l	Length [m]	λ	Bulk viscosity
M	Moment [Nm]	μ	Dynamic viscosity [kg/ms]
n	Number of parallel wires	ν	Poisson's ratio
N	Number of samples	ρ	Density [kg/m <sup>3</sup> ]
P	Pressure [Pa]	σ	Stress [Pa]
Q	Heat flux [W]		Standard deviation
R	Resistance [Ω]	τ <sub>w</sub>	Shear stress [Pa]
	Radius of curvature		
t	Time [s]		
	Thickness [m]		
T	Temperature [K]		
u	Velocity [m/s]		
v	Velocity [m/s]		
	Deflection [m]		
V	Voltage [V]		

Dimensionless groups

Re     Reynolds number

Nu     Nusselt number

Pr     Prandtl number

Acronyms

CFD     Computational Fluid Dynamics

CNT     Carbon nanotube

DAQ     Data acquisition

DI     Deionised

DNS     Direct Numerical Simulation

DQN     Diazoquinone ester

DVM     Digital Voltmeter

FEA     Finite element analysis

HF     Hydrofluoric acid

MEMS     Microelectromechanical systems

MST     Microsystems Technology

LDV     Laser Doppler velocimetry

LVDT     Linear variable differential transformer

PIV     Particle image velocimetry

RANS     Reynolds-averaged Navier-Stokes equations

TCR     Thermal coefficient of resistivity

TMAH     Tetramethylammonium hydroxide



# Chapter 1

## Introduction

The application of MEMS technology to airflow measurement allows a new and innovative approach to be taken to both shear stress measurement and the measurement of freestream velocity vectors.

### 1.1 Background

In aerodynamic research, the ability to measure wall shear stress is important in a range of applications. The frictional forces of fluids flowing over a surface can have a significant impact on the aerodynamic performance of aircraft, vehicles and ships. Internal flows such as in jet engines or artificial heart pumps can also have an effect on the aerodynamic, as well as the mechanical efficiency, as a result of friction forces where the flow passes a wall.

A variety of sensors exist for measuring shear stress, and different methods of measuring the shear stress have different applications, depending on the measurement



range and the method's ability to measure both the magnitude and direction of the wall shear stress, and its distribution over a surface.

There are a number of key features for shear stress sensors which dictate their suitability for different applications and also their overall effectiveness. Some of these include

- Appropriate range of operation
- Good sensitivity
- Minimal intrusiveness
- Directionality
- Ease of mounting
- Signal-to-noise ratio
- High frequency response

Some sensors, such as floating element sensors, while they directly measure the wall shear stress with a high degree of sensitivity and have advantages such as the ability to measure the directionality of the shear stress, are both complicated to manufacture and are mounted within the plane of the surface to be measured. This makes them very difficult to integrate into existing models, and requires the design of wind tunnel models to be modified for the use of such sensors. It is also impossible to use them except in a test situation, as they cannot be incorporated into the surfaces of structures in their standard environment. This is not true of sensors such as hot-films, which can simply be attached to an existing surface without requiring modifications, and can then potentially be moved as required.

This work aims to develop a sensor that would be surface mounted in order to facilitate incorporation into wind tunnel models. The influence of the sensor on the airflow would be as small as possible, ideally with the entire sensor being incorporated within the laminar sub-layer. The sensor would be designed to operate over the range of shear stresses commonly found in wind tunnel testing, typically  $<10$  Pa and with a high

degree of sensitivity in this range. The sensor would be independent of changes in ambient temperature. The sensor would be capable of high frequency measurements.

Another critical aspect of experimental aerodynamics is the ability to measure 3D velocity vectors in the freestream accurately. There are non-invasive methods of doing this (such as Particle Image Velocimetry (PIV) or Laser Doppler Anemometry (LDA)) which have some advantages, but are generally expensive and require optical access to the region of interest. Therefore the most common method uses an invasive probe, usually either a multi-hole or hotwire device.

Similar criteria to those applying to shear stress sensors also apply to probes, for example:

- Minimal intrusiveness
- Appropriate range of operation
- Good sensitivity
- High frequency response
- Signal-to-noise ratio

The most important of these criteria is that, since this probe is introduced into the airflow and creates a blockage, the probe head is as small as possible in order to minimise the disruption to the airflow. The small size is also important for improving the spatial resolution.

This work aims to develop a probe based on a multi-hole probe due to the ease of operation and cheapness of this method of measuring flow vectors. However the objective is to minimise the principal disadvantage of this type of probe – the intrusiveness into the airflow, by reducing the tip diameter of the probe as far as possible. The probe should be capable of measuring velocity vectors with a magnitude of up to approximately 30 m/s in a range of  $\pm 30^\circ$  yaw and pitch. Ideally the probe would be able to make high frequency measurements.

## 1.2 Shear stress

Where a viscous fluid moves over a solid surface, a resultant force is present on that surface. This force can be considered in two parts – the shear stress which acts in the direction of the flow tangential to the surface, and the pressure which acts normal to the surface. In order to satisfy the no-slip boundary condition, the velocity of the flow is zero at the surface. A non-uniform velocity profile is then present as distance from the wall increases until the freestream velocity is reached. This region is the boundary layer.

At low Reynolds numbers ( $Re < 3 \times 10^5$ ) the boundary layer is laminar. Reynolds number ( $Re$ ) is defined as

$$Re = \frac{\rho u x}{\mu} \quad 1-1$$

where  $\rho$  is the density of the fluid,  $\mu$  is the dynamic viscosity of the fluid,  $u$  is the velocity and  $x$  is the characteristic length. In this case the length used for the calculation of  $Re$  is the distance upstream to the leading edge where the boundary layer starts to form.

As  $Re$  increases, the boundary layer passes through a transition zone and then becomes turbulent. Turbulent flow causes the formation of unsteady vortices (eddies) at a range of length scales. A turbulent boundary layer has a sub-layer very close to the wall where the flow remains laminar, as the presence of the wall damps out the eddies. The boundary layer thickness ( $\delta$ ) is defined as the position where the flow velocity has reached 99% of the freestream velocity. More details of the boundary layer are shown in Figure 1-1.

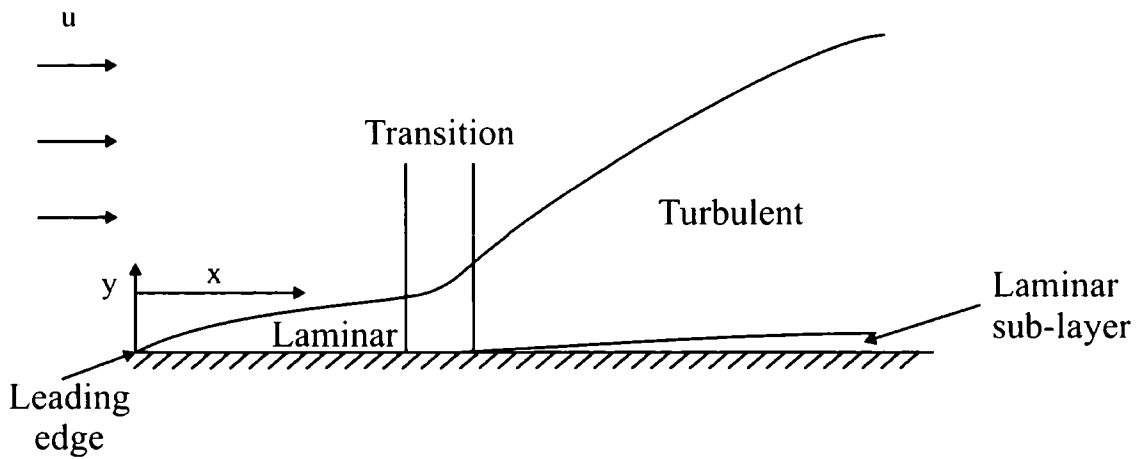


Figure 1-1 The sub-regions of a boundary layer

Laminar and turbulent boundary layers have different velocity profiles, with a turbulent boundary layer typified by a fuller profile. More mixing in the turbulent boundary layer results in a more uniform velocity through the boundary layer, and thus a steeper velocity gradient close to the wall. The different profiles are illustrated in Figure 1-2.

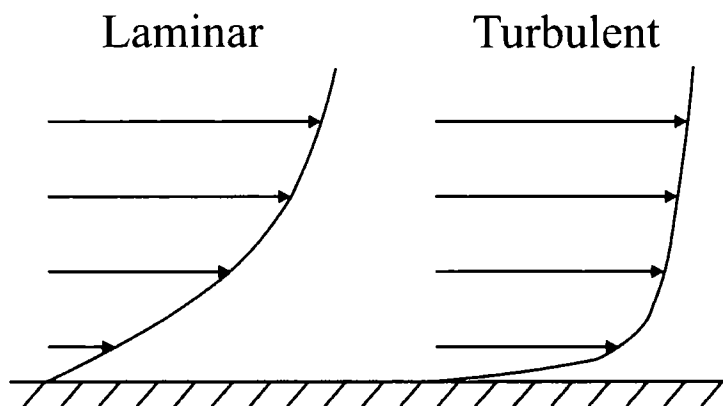


Figure 1-2 Laminar and turbulent boundary layer velocity profiles.

The shear stress,  $\tau_w$ , on a surface is proportional to the gradient of the velocity of the flow at the wall, and is defined as

$$\tau_w = \mu \left( \frac{du}{dy} \right)_w \quad 1-2$$

where  $\mu$  is the dynamic viscosity,  $u$  is the flow velocity parallel to the wall and  $y$  is the distance normal to the wall. This relationship only holds true for the laminar region, as

Reynolds stresses are also present in turbulent boundary layers. Because of the steeper velocity gradient close to the wall found in a turbulent boundary layer, the shear stress is usually greater than that found in a laminar boundary layer.

### **1.3 MEMS Technology**

Microelectromechanical Systems (MEMS) or Microsystems Technology (MST) uses the processes which have been developed by the semiconductor industry in order to fabricate devices which generally range from tens of microns in size up to a few millimetres. This technology first came to notice in the late 1960's and has since been developing rapidly. The principle characteristics of MEMS are miniaturisation, integration with microelectronics and reproducible mass production.

MEMS is the logical progression from the development of microelectronics – the incorporation of sensors and actuators onto the same substrate. A complete microsystem could consist of a control circuit with an actuator to implement the required alteration, and a sensor to determine when the variable has been adjusted to the required value so that feedback can be achieved.

Specific examples of applications of MEMS that are commonly seen, are the use of accelerometers (for such purposes as airbag deployment in vehicle collisions or game controllers such as the Nintendo Wii), inkjet printers, pressure sensors (such as those used in a car's inlet manifold) and for optical displays.

MEMS devices are commonly constructed from a combination of silicon, polymers and metals. Most MEMS devices are fabricated on silicon substrates, although other materials such as glass or flexible substrates like polyimide can also be used. Some new materials, particularly polymers, have been developed specifically for the MEMS industry.

MEMS structures are constructed in a series of patterned layers formed by a combination of depositing new material and selectively etching away existing material by the process of photolithography.

MEMS brings different design constraints compared with macro scale design constraints. For example, considering a cantilever, while the mass is so small as to allow the fabrication of cantilevers with aspect ratios impossible in the macroscopic world, stiction forces can become a problem. Stiction is a contraction of 'static friction' and in this context refers to surface adhesion forces being greater than the mechanical restoring force of the structure. The design of MEMS devices must take these considerations into account. In addition to this the layered nature of MEMS structures makes some mechanisms such as hinges hard to achieve, which should also be considered in the design process.

One of the advantages of MEMS is the cost savings in being able to manufacture batches of sensors and actuators on a single substrate. It is also possible to increase the reliability of such devices by these methods as well as reducing unit costs.

## **1.4 Thesis structure**

This thesis aims to utilise the advantages of MEMS technology in flow measurement. Both wall shear stress measurements and the measurement of freestream velocity components are addressed.

Chapter 2 reviews existing methods of measuring shear stress and freestream velocity vectors.

Chapter 3 gives an overview of the methods used for the work in this thesis. This includes the MEMS fabrication processes used for the construction of the sensors, the experimental setup used for testing the sensors (both mechanical and wind tunnel testing) and the modelling methods used for analysis (both CFD and FEA).

Chapter 4 covers the design, fabrication and testing of the first generation of shear stress sensors, based on a surface fence design. Modelling of the fence using both CFD and FEA is also presented here.

Chapter 5 concerns the development of the initial design and improvements leading to the cantilever design of the shear stress sensor, and also includes the fabrication and

testing of this second design. CFD modelling to calculate both the pressure difference across the cantilever and the thermal heating effects of the strain gauge is shown. FEA of the cantilever deflection is also carried out.

Chapter 6 covers the adaptation of the cantilever design into an airflow probe by using multiple cantilevers to give three-dimensional velocity measurements while also measuring the stagnation pressure. Modelling and testing of this probe as well as analysis of the data are shown here.

Chapter 7 provides conclusions on both types of wall shear stress sensor and also the probe, as well as suggestions for future work.



# Chapter 2

## Literature Review

Existing methods and designs of shear stress sensors are presented here, as well as existing methods of measuring freestream velocity components.

### 2.1 Review of existing shear stress sensors

There are two main methods (direct and indirect) of measuring wall shear stress. The former includes such methods as floating element sensors or oil film interferometry, and the latter methods which require calibration such as Preston tubes and surface fences.

Several reviews of shear stress measurement exist [1, 2, 3]. The following is a brief overview of the main methods of measuring shear stress.

#### 2.1.1 Oil film interferometry

Oil film interferometry measures shear stress based on the rate at which oil thins on a surface. This is controlled by the thin oil film equation, which is derived from the Navier-Stokes equations. The shear stress can be measured quantitatively by using

interferometry to measure the oil film height. The height of the oil film is related to the optical path length difference, and therefore the phase difference. The basis for this method of shear stress measurement was first developed by Squire [4], and then further developed by Tanner et al [5].

Oil film interferometry is commonly used only for average shear stress measurements, although work by Murphy et al [6] found that the oil film reacts very quickly to changes in the shear stress (for frequencies up to 10 kHz) and therefore it is possible to take unsteady measurements. The technique is most valuable in applications with high dynamic pressures (often supersonic flows), measuring shear stresses up to 700 Pa.

One of the most common problems with this method is dust, which can produce perturbations in the oil film. These subsequently convect downstream indicating the shear stress directions, but in larger quantities make the fringe pattern unusable.

### **2.1.2 Liquid crystal coating**

Shear stress measurements can also be made using liquid crystal coatings to obtain an instantaneous shear stress distribution over a surface. Liquid crystals produce a colour spectrum when illuminated by white light, and the colour varies with the shear stress magnitude. The colours can be calibrated provided the illumination and observation angles are taken into account, as they also have an impact on the colour observed. Recent work on this method has been done by Pradeep et al [7], Buttsworth et al [8] and Fujisawa et al [9].

The requirement for illuminating liquid crystals, and the importance of the quality of the illumination, makes the use of liquid crystals as a method of shear stress measurement possible, but only in specific applications. The sensitivity to both illumination and observation angles makes this technique limited in its applications, and so it is largely used for qualitative rather than quantitative shear stress measurements.

### **2.1.3 Floating element sensors**

Floating element sensors can be used to directly measure the wall shear stress, using an element suspended over an airgap and held in place by mechanical tethers. In-plane

displacement of the element is induced by the movement of a fluid over the surface and is then measured by a transducer. A number of different measurement methods have been used, including piezoresistive, optical and capacitive methods. A diagram of a generic floating element sensor is shown in Figure 2-1.

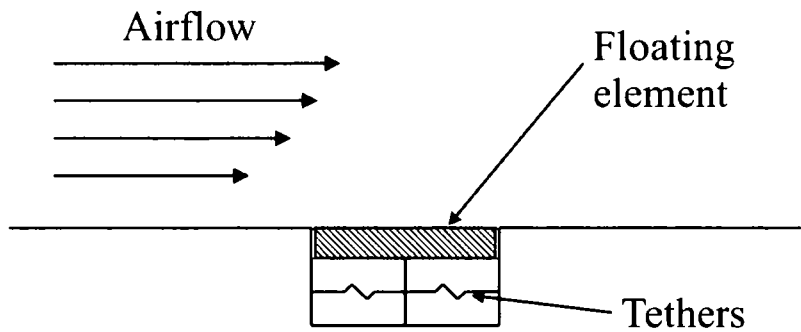


Figure 2-1 Diagram of floating element sensor

Macro-scale versions of these devices have in the past been limited due to the trade-off between sensor spatial resolution and the ability to measure small forces. Errors have been caused by sensor misalignment, the required gaps around the element, and pressure gradients. The devices have also been found to have cross-axis sensitivity to acceleration and vibration.

MEMS devices have been found to address these issues, partially due to their smaller scale. The way the devices are fabricated also helps to reduce misalignment errors. The gaps in the MEMS device are of the order of one micron, and can therefore be considered hydraulically smooth. Cross-axis sensitivity due to acceleration and vibration scales with element mass, and therefore reduces significantly for smaller scale devices. MEMS devices are also less prone to errors from thermal expansion of the element.

Padmanabhan et al [10] used photodiodes to measure the displacement of the element. The photodiodes are located symmetrically at the trailing and leading edges of the element. The movement of the element shutters the diodes, and the differential photocurrent is directly proportional to the shear stress, given uniform illumination from above.

An alternative method of detecting the movement optically is presented by Horowitz et al [11], which uses geometric Moiré interferometry.

Zhe et al [12] use a capacitive method for detecting the movement of the element. This design can measure shear stresses as low as  $0.05 \text{ Pa} \pm 0.005 \text{ Pa}$ . Another capacitive method is presented by Desai et al [13].

Piezoresistive floating element sensors have also been designed [14], and are generally used for measuring high shear-stress levels (1-100 kPa).

#### 2.1.4 Thermal sensors

The principle of using hot-film anemometry techniques for the measurement of shear stress has existed for many years [15]. This method of shear stress measurement uses the relationship between the thermal convection from a heated wire element, and the shear stress caused by the flow which is cooling the element.

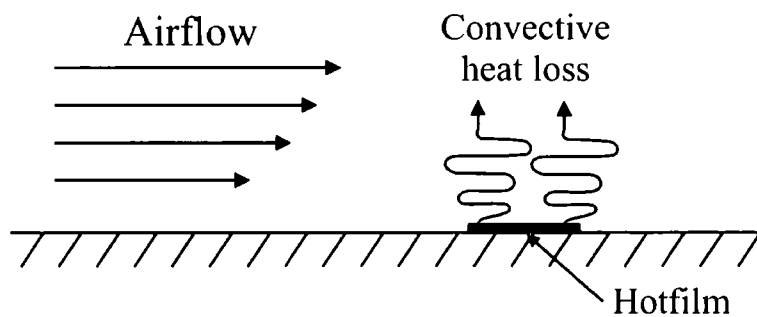


Figure 2-2 Operation of hot-film anemometer

Recent advances have been made in improving the performance of these devices. MEMS fabrication has allowed the conducting wire to be thermally isolated by means of creating a vacuum cavity beneath the sensor (Sheplak et al [16], Huang et al [17]). This has been found to increase the sensitivity by an order of magnitude.

Due to the measurement principle of hot-films, flow at an angle to the sensor gives a different response than if the flow is normal to the sensing wire [18]. However two flows normal to the sensor, but in opposite directions will give the same response. A

pulsed wire method of anemometry allows the detection of reversing flow using a thermal sensor, as by Dengel et al [19].

A method of raising the wire above the surface to increase the sensitivity is presented by Chen et al [20].

Thermal sensors are very sensitive to changes in the ambient temperature. However methods of electronically compensating for this temperature drift using a second sensor for temperature measurement have been developed by Huang et al [17].

An advantage of thermal sensors over some other sensors is that they can operate at a high frequency, in the order of several kHz, although this is not the case for pulsed wires. The advantage of pulsed wires is that they are able to detect regions with reversing flow, unlike most other hot-film sensors.

With recent advances in MEMS technology, a new method of using thermal sensors to measure shear stress has been developed. Liu et al [21] have developed a sensor very similar in principle to a traditional hot-film sensor, but using a polysilicon resistor. This is suspended above a vacuum cavity on a silicon-nitride diaphragm to reduce heat loss to the substrate. The sensor can be operated under constant current, constant voltage or constant temperature modes.

Tung et al [22] have used carbon nanotubes (CNT's) as a sensing element to indirectly measure the shear stress from the convective heat transfer from the heated CNT's. This sensor is operated in constant temperature mode. It is suitable for microfluidic applications due to its small size.

### **2.1.5 Indirect optical sensors**

Optical sensors use the Doppler shift of light scattered by particles passing through a diverging fringe pattern located in the viscous sub-layer of a boundary layer. This was originally done using conventional optics, but was adapted using optical MEMS fabrication technology by Fourgette et al [23].

A sensor embedded in the surface generates a diverging fringe pattern close to the wall, and as particles pass through it, they scatter light which is received by a detector. The frequency of the light signal is a function of the velocity and the fringe spacing, and thus the velocity gradient at the wall can be calculated since the fringe spacing depends on the geometry of the optics and the height above the wall. As the height above the wall is very small, the velocity gradient in this region is linear.

Problems with this type of sensor include difficulties in fabricating a device that contains a probe volume entirely within the laminar sub-layer of the turbulent boundary layer at high Reynolds numbers. Another limitation is the low data rate for unsteady measurements, due to the low seed density near the wall.

### 2.1.6 Fence sensors

A surface fence can be used to measure the static pressure drop between the upstream and downstream sides of the fence, which can be related to the shear stress using a calibration curve. Effectively, the velocity at a specific height is being measured and therefore the shear stress can be calculated using equation 1. This method is demonstrated by Vagt et al [24], and is illustrated in Figure 2-3.

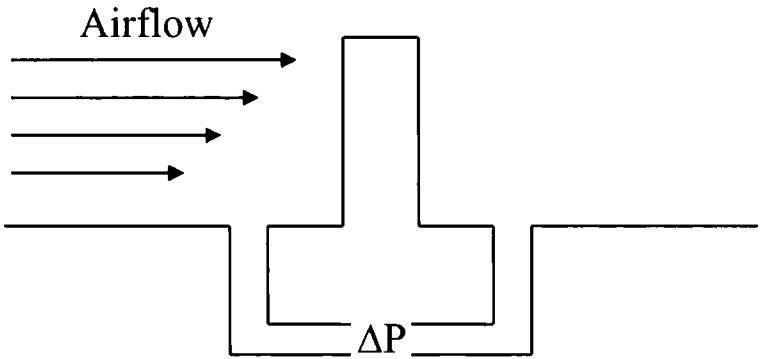


Figure 2-3 Surface fence for wall shear stress measurement

A design incorporating piezoresistors to directly measure the pressure-induced deflection of the fence has recently been developed by Papen et al [25]. The first generation of these fences allowed measurement of shear stresses below 1 Pa, with a resolution of 20 mPa, and at a frequency of 1 kHz. Subsequent improvements to the design (Papen et al [26]) have allowed an increase in resolution to 10 mPa, as well as

including a temperature monitor so that the temperature dependency of the device can be compensated for.

Schober et al [27] showed that this type of sensor is effective for skin friction measurements in separated flows with a temporal resolution of 1 kHz. Results from a wall-pulsed wire probe show good agreement with the micro-fence sensor for the mean skin-friction component. This design has good sensitivity, and temperature dependency can be compensated for. However, it is currently only appropriate for relatively low shear stress applications.

**2.1.7 Artificial haircells and micro-pillars**

Chen et al [28] have fabricated an artificial haircell, or cilia, based on the biological mechanoreceptor, which is effectively a cantilever with an integrated resistive strain gauge at the base. The sensitivity of the sensor depends on the dimensions of the cilia, however increasing the sensitivity by increasing the length of the cilia cause the device to extend further into the boundary layer. For the most sensitive cilia  $dR/R$  reaches 600 ppm at around 10 m/s. This sensor can be used to measure in regions of reversing flow, but because of the difficulty of achieving a 90° angle between the cilia and the substrate (due to the fabrication method), the response in both directions has not been found to be the same. While this sensor would be temperature sensitive, it should be possible to compensate for this electronically by means of a second resistor, amongst other methods. A diagram of a haircell is shown in Figure 2-4.

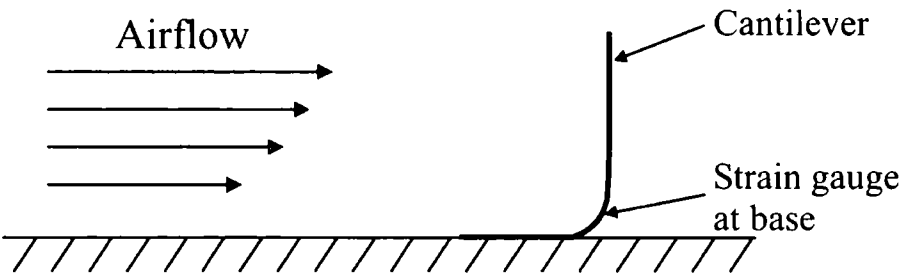


Figure 2-4 An artificial haircell for shear stress measurement

A similar technology to the hair-cell technology is using micro-pillars to measure shear stress [29, 30].

**2.1.8 Preston tubes**

The Preston tube was initially used by Patel [31] for measuring surface shear stress. A hypodermic tube is secured to the plate and used to measure the dynamic pressure within the boundary layer. This can then be converted into a shear stress by the same principle as for the surface fence (See equation 1-2). For the most accurate results, the smallest possible diameter of hypodermic tubing should be used, in order to obtain the measurement from as close to the plate as possible.

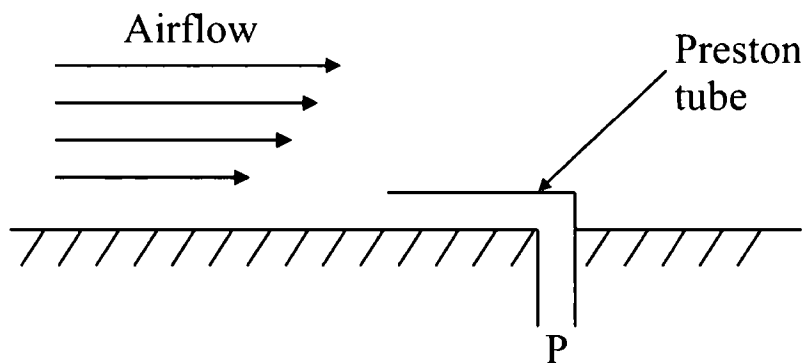


Figure 2-5 A Preston tube

**2.1.9 Summary**

The sensors or methods of measuring shear stress outlined above have a range of different uses and advantages as well as drawbacks. An overview of the principle advantages and disadvantages of the methods of shear stress measurement discussed here is shown in Table 2-1.



Method	Advantages	Disadvantages
Oil film interferometry	Large area of measurement Good for high shear stresses	Susceptible to dust disturbances
Liquid crystal coating	Large area of measurement	Requires optical access
Floating element sensors	Good for high shear stresses	Complicated to manufacture Require mounting within measurement surface
Thermal sensors	Easy to mount Low infringement into flow	Sensitive to changes in ambient temperature
Indirect optical sensors	Low infringement into flow	Requires mounting within measurement surface
Fence sensors	Good for low shear stresses	Requires mounting within measurement surface
Artificial haircells and micro-pillars	Can be mounted on surface	Cantilever length projects into airflow
Preston tubes	Simple and cheap measurement method	Accuracy limited by width of tube and thus increased at expense of frequency response

Table 2-1 Principal advantages and disadvantages of existing shear stress sensors

This work aims to design a shear stress sensor combining the best features of these existing shear stress sensors while attempting to minimise the disadvantages associated with them. This shear stress sensor would be surface mounted, but also interfere with the airflow as little as possible, ideally being contained within the laminar sub-layer. The sensor should be aimed at the range of shear stresses found in wind tunnel testing, for example in the automotive industry. These stresses are relatively low (typically  $<10$  Pa for most applications) and consequently a high degree of sensitivity is required. The sensor should be independent of variables, such as temperature, which are problematic with other sensors such as hot-films, which otherwise fulfil many of the necessary criteria. The use of MEMS technology will allow the manufacture of a sensor which is small, and thus allow good spatial resolution as well as broadening the range of sensing

methods which can be used. The sensor would ideally have the potential for high frequency measurements.

## **2.2 Review of freestream velocity vector measurement**

Both invasive and non-invasive methods can be used for the measurement of velocity vectors, each with different advantages and disadvantages.

Non-invasive methods such as Particle Image Velocimetry (PIV) and Laser Doppler Anemometry (LDA) are used to measure velocity vectors, but can be impossible to use in some circumstances since they require optical access to the flow being measured.

Invasive methods usually involve the use of a probe. In order to have the minimum blockage, and therefore to obstruct the airflow as little as possible, it is critical to minimise the probe head diameter. This also means that the spatial resolution is as high as possible. Macro-scale engineering has fundamental problems with reducing the probe head much below one millimetre in diameter regardless of the actual method of measuring the velocity components. The use of MEMS techniques allows the adaptation of sensors using different methods for measuring airflow, which can be manufactured at a size smaller than that achievable by conventional methods. Probes should have a high sensitivity to the measured variables, while having zero sensitivity to other variables such as, for example, temperature.

### **2.2.1 Particle image velocimetry**

Particle image velocimetry (PIV) allows the measurement of flow velocities by seeding the flow with tracer particles, which are then tracked to calculate the flow measurement. If the tracer particles are selected carefully for the application, they will not distort the flow, but will follow the streamlines and therefore provide a non-intrusive method of obtaining flow velocity data.

Adrian [32] provides an overview of the development of PIV since its conception in 1984 as a development of speckle velocimetry [33, 34].

Typically PIV uses a laser (such as a double-pulsed Nd:YAG laser) which is converted to a light sheet optically. The particles in the fluid scatter the light which is then captured by a camera. Measuring the velocity requires two images. Displacement vectors for the particles are calculated from the images, and the velocity is obtained from these using the time elapsed between the two images being recorded.

This method does not allow the measurement of the movement of particles in the z-axis i.e. towards or away from the camera. However two methods have been developed to allow 3D PIV – stereoscopic PIV [35, 36] and holographic PIV [37, 38].

Drawbacks to PIV include the expense of the system and the potential safety implications of using lasers, as well as the requirement for good optical access for the laser and camera.

In 1998 a  $\mu$ -PIV system was developed by Santiago et al [39] for flow measurements in micro-fluidic systems. This system varies from the standard method as, instead of defining the measurement domain in the out-of-plane direction by the thickness of the light sheet, it is defined by the small depth-of-field of the microscope through which the particle measurement is recorded.

### **2.2.2 Laser doppler velocimetry**

Laser Doppler Velocimetry (LDV) or Laser Doppler Anemometry (LDA) was first developed in the early 1970's and uses lasers to measure local velocity components by the determination of frequency shifts between incident and scattered radiation [40, 41]. LDV uses a laser which is split into two beams which are then made to intersect and generate straight fringes through the probe volume which are normal to the flow direction. A receiver is aligned so that light reflected from the probe volume is focussed onto a photodiode. Particles passing through the probe volume reflect light when passing through a region of constructive interference. The frequency of the sinusoid seen by the receiver can be used to calculate the velocity of the particle, given the known spacing of the fringe. Czarske [42] gives an overview of modern LDV systems using powerful solid-state lasers.

LDV is used for medical purposes to measure blood flow in human tissue due to its non-invasive methodology, although it is more commonly known as laser Doppler flowmetry in this application.

### **2.2.3 Multi-hole probes**

Multi-hole pressure probes can be used to measure total and static pressure along with yaw and pitch depending on the number of sensors used. As standard a one-dimensional probe would measure total (and potentially static) pressure when aligned with the local flow, a two-dimensional probe would also be able to measure yaw angle and a fully three-dimensional probe (requiring a 4- or 5-hole probe) would measure both pressures and both pitch and yaw angles. Both one and two-dimensional probes assume zero flow velocity in the other directions.

Pitot-static probes are commonly used to measure both total and static pressure thereby measuring the dynamic pressure and allowing the speed of the flow to be calculated, assuming the probe is facing directly into the flow.

Five-hole probes are a long-used method of measuring the airflow, allowing the measurement of three-dimensional velocity components. They are commonly used in either a conical or hemispherical configuration. The design and construction of these pressure probes has been adapted over the years in order to maximise the efficiency of the design in a particular application. A conical five-hole probe is shown in Figure 2-6.



Figure 2-6 A conical five-hole probe

In the field of turbomachinery, overviews of fast response aerodynamic probes are by Kupferschmied et al [43] and Sieverding et al [44].

Due to the construction method for creating five parallel hypodermic tubes, it is difficult to make this technology smaller than approximately 1 mm. Nearly twenty years ago five-hole probes of not much more than 1 mm in diameter were achievable (Ligrani et al [45]), and yet even recent work using five-hole probes such as Lenherr et al [46] use probe heads with a diameter of 0.9 mm, and this is still much smaller than seen on standard probes. The use of piezoresistive silicon pressure diaphragms in multi-hole probes is addressed by Ainsworth et al [47].

There is a trade-off when using five-hole probes, as when the probe is very small the pressure transducers cannot be very close to the probe head, which has an impact on the frequency response. Where the pressure transducers are incorporated into the probe head, the result is a relatively large assembly. There have been attempts to overcome this problem, notably Babinsky et al [48]. This solution suggests the manufacture of the sensing elements directly on the head of the probe and achieving the required sensitivity by means of a series of fences separating the sensors in the flow. However this method has only been demonstrated at large scales.

The advantage of pressure probes is that they allow the measurement of pressure as well as the velocity vectors. The measurement of stagnation pressure is particularly useful since this allows any pressure losses to be measured.

#### **2.2.4 Hot-wire probes**

Hot-wires operate using the same principle as surface-mounted hot-films, as described in §2.1.4. However, the hot-wire is mounted on a probe to measure the freestream velocity. A single hot-wire mounted normal to the flow can be used to obtain a 1D velocity component, or alternatively arrays of hot-wires can be used to measure 2D or 3D flow. A disadvantage of this type of probe compared with a pressure probe is that only the velocity components are measured and not the pressure as well. The number of velocity components which are measured and the ability to measure directionality depend on the arrangement and number of hot-wires.

Arrays of hot-wire probes can be used to measure velocity vectors such as that presented by Lemonis [49] using a twenty wire probe consisting of five orthogonal four wire probes, or using single-sensor rotatable probes as used by Sherif and Pletcher [50]. However some disadvantages to these techniques are that the probe head size is quite large, they are sensitive to variations in temperature and dust contamination, and can be fragile. Probes such as that used by Samet and Einav [51] or Tsinober [52] have a probe head diameter of 2.5 mm.

A ‘sub-miniature’ four-wire probe as used by van Dijk and Nieuwstadt [53] has a diameter of 1 mm, but due to the small size the cooling characteristics are less ideal.

The construction of a very small hot-wire probe is compromised by the need to have multiple sensing wires, which consequently means that although individual hot-wires can be relatively small, when combined in order to give three-dimensional velocity measurements, the overall size of the probe head is large.

### 2.2.5 Summary

Existing methods of measuring velocity components are divided into invasive and non-invasive methods. The latter, while having the advantage of not disturbing the flow, are usually significantly more expensive to implement than methods using probes.

An overview of the principle advantages and disadvantages of the types of measurement discussed in this section is given in Table 2-2.

Method	Advantages	Disadvantages
Particle image velocimetry	Non-invasive Large area of measurement	Requires optical access Expensive Laser usage
Laser Doppler velocimetry	Non-invasive	Requires optical access Point measurement Laser usage
Multi-hole probes	Simple and cheap measurement Positioning of measurement	Point measurement Invasive
Hot-wire probes	Positioning of measurement	Point measurement Invasive Fragile

Table 2-2 Principal advantages and disadvantages of existing freestream velocity vector measurement methods

The use of probes allows the measurement of velocity components at a single point in space, but disturbs the flow downstream of the probe. Standard probes in current use are normally of the order of several mm across, and the smallest probes are barely below 1 mm in diameter. In order to minimise intrusiveness it is important to reduce the size of the probe as far as possible, which also has the parallel advantage of increasing spatial resolution.

The aim is to produce a sub-millimetre probe head capable of measuring 3D velocity components. The use of MEMS technology will allow the miniaturisation of a probe head beyond what is possible using established conventional techniques. The intention

is to utilise the good points of multi-hole probes such as the relative cheapness and ease of taking measurements, while reducing as far as possible the disadvantage of intrusion into the airflow by minimising the size of the probe head as far as possible.



# **Chapter 3**

## **Experimental Methods**

The MEMS fabrication processes used in the manufacture of the sensors are detailed in this chapter. In addition the testing methods (both mechanical and aerodynamic) are described, as well as the analysis and numerical simulation techniques used to model the sensors.

### **3.1 MEMS fabrication processes**

The MEMS fabrication processes used during this work are outlined here. MEMS structures are fabricated by building up a series of layers of polymer and metal and patterning them by etching back to the layer below. This is done via a photolithographic process using photosensitive polymers to protect layers from the etchant where required.

### 3.1.1 Mask making

All masks for the photolithography process (described in §3.1.2) were made in-house. Masks were drawn using the software CorelDraw and were printed at a scale of 10 times the intended size onto an A3 acetate film, using a Canon i9950 printer.

The design was reduced to the intended size photographically onto a glass plate. The photographic plates used were 2.5" square Slavich plates coated with VRP-M green sensitive emulsion. The plates were positive, i.e. clear regions on the printed image are reproduced as dark on the glass plate, and vice versa. The printouts were consequently drawn with the reversed polarity of the ultimate intended design.

The printed acetate mask was placed on a light box, the glass plate loaded into the camera and the image from the light box was photographed. The camera set-up is shown in Figure 3-1.

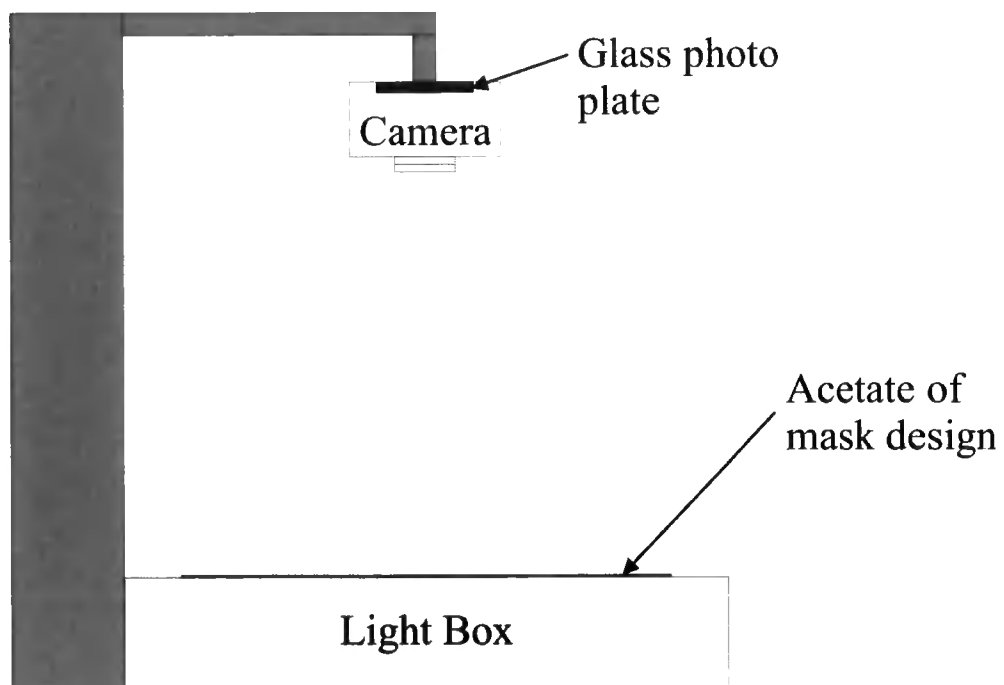


Figure 3-1 Mask making set-up

The exposure dose required varied from between 2 and 4 minutes depending on the size of the features and the photoresist which was exposed through the mask. The glass plates were developed in AGFA G282c developer for between 2 and 3 minutes

depending on the opacity of the mask required, which was again dependent on the type of photoresist used in conjunction with the mask. Although longer development times made for more opaque dark areas on the mask, developing for too long meant that the clear areas started to become less transparent to Ultraviolet (UV) light. Thick resists, which required longer exposure times, started to be affected through the dark areas of the mask if it was not sufficiently opaque to UV light. After developing, the masks were rinsed in deionised (DI) water and then fixed using AGFA G333c fixer for a period of 2 minutes.

Where masks were being used for the exposure of thick negative photoresist, it was not possible to create an emulsion mask with dark areas sufficiently opaque to UV light for long exposures, and thus it was necessary to convert the emulsion mask into metal. The metal masks were formed by a chromium seed layer with a thick gold layer on top. The gold, when evaporated using an electron beam evaporator, was very dense and therefore suitable for this purpose as pinholes in the film are less likely. Because of the small alterations in the mask caused by reproducing it in metal from the emulsion plate, it was necessary to convert whole sets of masks, not just those affected by long exposure times, in order to maintain consistency and avoid distortions.

It was important when designing masks to incorporate alignment marks which were easily found under the microscope of the mask aligner, which had a relatively small field of view. This was critical for ease of alignment as arbitrarily placed alignment marks could be difficult to locate.

### **3.1.2 Patterning**

#### ***Photolithography***

Photolithography involves the patterning of a photoresist via exposure to UV light through a mask. The patterned resist can then be used as a protective layer for etching layers under the resist.

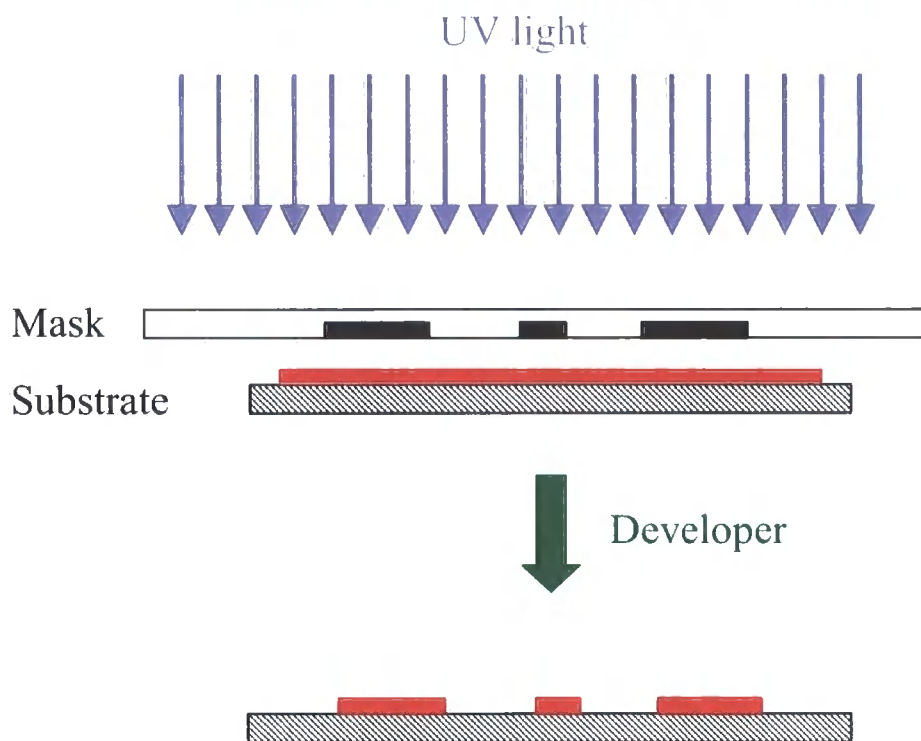


Figure 3-2 The photolithography process with positive photoresist

Two mask aligners were used for the exposure of photoresists. These were an EVG 620 mask aligner and a Karl Suss MJB3 mask aligner. The EVG machine was utilised more frequently due to the superior control available; however, the Karl Suss aligner was used as a back-up when required. The EVG mask aligner has a broadband source operating at 350-450 nm in the near UV range.

### ***Photoresist***

Photoresists are UV sensitive polymers. Both positive and negative photoresists were used for the fabrication of these sensors. For positive photoresists, the UV light breaks down the polymer where it is exposed, increasing the rate at which it is removed in the developer as the shorter chains are more soluble.

Negative photoresists are cross-linked by exposure to UV light (with the addition of a post-baking step), and therefore the regions which are exposed are those that remain after development has taken place. The sidewalls created in negative photoresists are referred to as negative sidewalls, with the remaining structures being broader at the top. This is due to scattering of the UV light as it passes through the photoresist.

The photoresist was deposited on the substrate by a spin coating process. For this a Laurell spin coater, model WS-650S was used. The spin was normally carried out in two steps – a low speed spin initially to spread the resist across the substrate, and then a higher speed process to achieve the desired thickness of the resist layer. The thickness for a given viscosity was dependent on the speed of this second spin step. In order to remove the solvent from the photoresist before it was exposed, the substrate was baked on an Electronic Micro Systems hot-plate (Model 1000-1).

### ***S1813 and AZ4562***

S1813 (manufactured by Microposit) and AZ4562 are both positive photoresists used here as a protective layer when etching metals. They are both made from a phenolic novolak resin and the photoactive compound is diazoquinone ester (DQN). This complex is largely insoluble in developer, but becomes soluble in alkaline aqueous solutions (i.e. a typical developer) through a photochemical reaction of DQN. The main difference between the two resists is in their viscosity. S1813 was the less viscous of the two and was used as the standard resist, having a thickness of approximately 1.3  $\mu\text{m}$  when spun at 3700 rpm and baked. AZ4562 was used where a thicker layer of resist was required, such as where a metal layer over a step in the underlying material was to be etched. The thickness of AZ4562 when spun at 3700 rpm was 6.2  $\mu\text{m}$ . Both of these resists were developed using Rohm and Haas's Microposit 351 Developer.

### ***SU-8***

SU-8 is a negative, epoxy based photoresist, which was originally developed by IBM for use in the semiconductor industry [54]. Because it is chemically resistant and has good mechanical properties, it is suitable for use as a structural layer in a device and can be used for high aspect ratio structures. Layers with thicknesses of up to 250  $\mu\text{m}$  can be achieved with a single spin. The use of polymers as structural materials is of interest due to the rapid fabrication, and also the relatively low costs. It has a variety of potential applications, and is compatible with standard MEMS processing. SU-8 is a glycidyl ether derivative of bisphenol-A novolac, which when exposed to near UV radiation (or e-beam or X-ray radiation) initiates a cross-linking process by the formation of a strong

acid. A post exposure bake step then follows, where acid-initiated, thermally driven cross-linking takes place.

As SU-8 is a negative photoresist, on development a negative sidewall is present (see Figure 3-4 for further discussion of negative sidewalls). However, by careful processing, the overhang of this sidewall can be minimised to give an almost vertical profile [55].

SU-8 is available from Microchem in a range of different viscosities, each allowing a variety of different thicknesses to be achieved depending on the spin speed used. The two resists used for this work were SU-8 10, which gives thicknesses ranging from approximately 10-30  $\mu\text{m}$ , and SU-8 50 which allows thicknesses from 40-100  $\mu\text{m}$ . The resist was developed after exposure and post-baking using Rohm and Haas's Microposit EC Solvent.

### **3.1.3 Thin film deposition**

Three methods of thin film deposition are commonly used in MEMS. These are evaporating, sputtering and electroplating. Electroplating has not been used in the course of this work, and therefore only the other two methods are discussed.

#### ***Evaporation***

Evaporation involves heating a metal until it vaporises and the gas condenses onto the substrate. This is done under a high vacuum to ensure a long mean free path of the gas molecules and to reduce contamination.

The heating of the metal can be achieved by two principle means. The first is to place the metal in a tungsten filament which then has a high current passed through it. This method is resistive evaporation, and is more suitable for the deposition of metals with a low melting point and/or specific heat capacity, as otherwise a very large current is required.

The second method of heating the metal is by using an electron beam. Electrons are generated from a thermionic filament, and the beam is directed through 270° onto the

evaporant using magnets. The metal then melts locally, effectively forming its own crucible which means that contamination is less of a problem than with resistive heating, where the filament is of a different material than the evaporant. The evaporant is placed in a crucible in a water-cooled copper hearth.

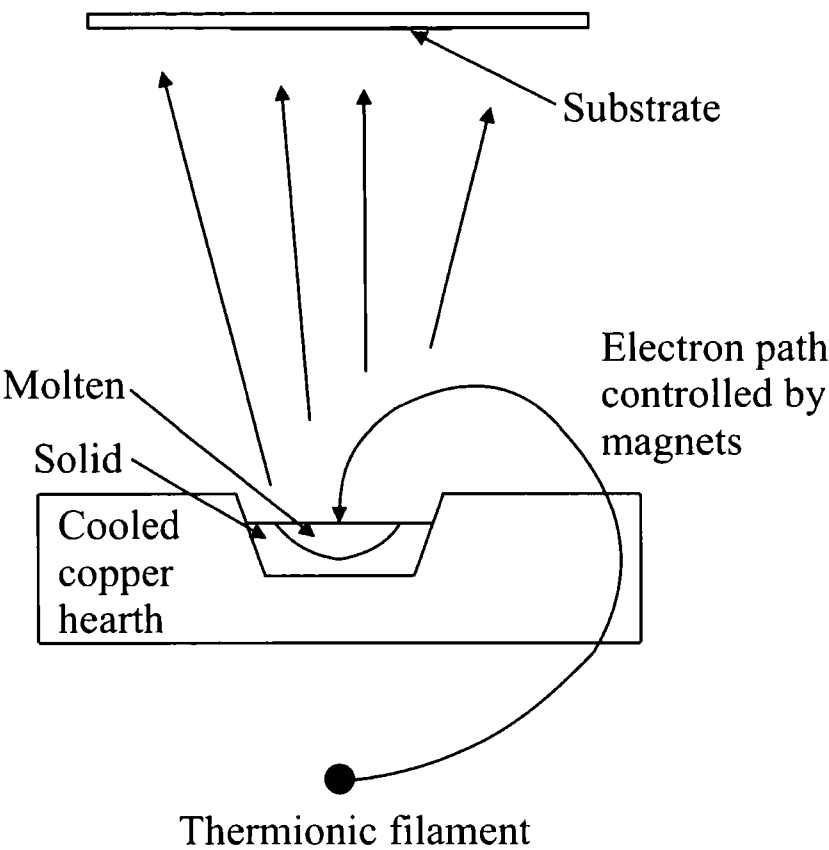


Figure 3-3 An e-beam evaporation set-up

Evaporation by either method is not effective when sidewall coverage is required, except by tilting and rotating the substrate. This is particularly true when a negative photoresist is being evaporated over, due to the negative sidewall.

The effect of evaporating over a negative sidewall is illustrated in Figure 3-4.

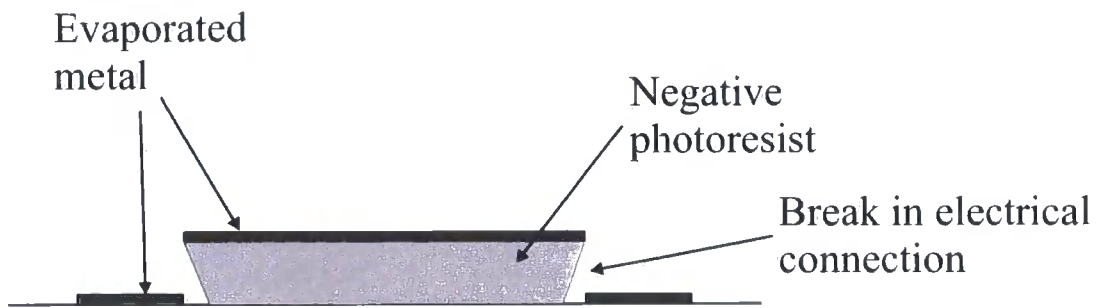


Figure 3-4 Metal evaporation over negative sidewall

The e-beam evaporator used for depositing metals was a Telemark system which uses an 8 kV TT-6 power supply and has a rotatable hearth with six pockets. The type of crucible used in the hearth depended on the metal being evaporated.

### ***Sputtering***

Sputtering takes place when the target material, which is at a high negative potential, is bombarded with positive argon ions from a plasma. Momentum transfer causes neutral atoms to be displaced into the low pressure atmosphere. They are then deposited onto the substrate, which is located at the anode. The rate at which deposition of a specific material takes place is linked directly to the sputter pressure and to the power applied to the plasma.

Unlike deposition by evaporation, the sidewall coverage obtained by sputtering is good. The shorter mean free path of the atoms, due to the higher pressure at which sputtering takes place, leads to multiple collisions between atoms, which then reach the substrate at random angles, giving superior coverage over both positive and slightly negative sidewalls, as shown in Figure 3-5.



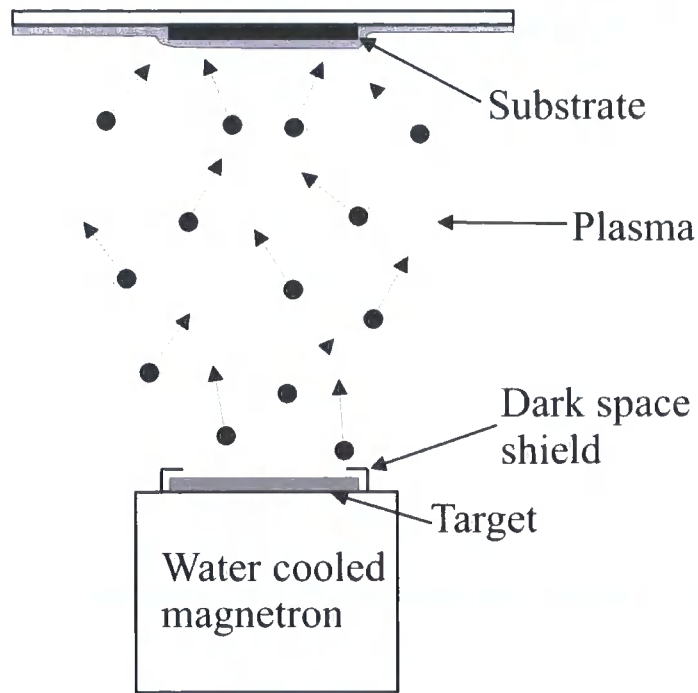


Figure 3-5 The sputtering process

Other advantages of sputtering are that an alloy can be easily sputtered and the composition of the alloy can be accurately controlled. Also, the stress in the film can be controlled by varying the pressure at which sputtering takes place.

The sputterer used to deposit metals was a Moorfield Minilab sputterer. It had two DC magnetrons and an RF magnetron, and one of the former was supplied with high strength magnets in order to allow the deposition of magnetic materials such as nickel. The RF magnetron allowed non-metallic materials such as quartz to be sputtered. In this system the pressure in the chamber was controlled by an automatic gate valve and the gas supply had mass flow controllers to ensure a constant supply.

3.1.4 Wet etching of metals

Etching of metals during the fabrication process was undertaken using wet chemical processes. The etchants used for these metals are shown in Table 3-1.

Metal	Etchant
Gold	4 KI : 1 I <sub>2</sub> : 8 H <sub>2</sub> O
Nichrome	10 (NH <sub>4</sub> ) <sub>2</sub> Ce(NO <sub>3</sub> ) <sub>6</sub> : 1 HNO <sub>3</sub> : 49 H <sub>2</sub> O
Titanium	1 HF : 10 H <sub>2</sub> O
Copper	A) 1 Na <sub>2</sub> S <sub>2</sub> O <sub>8</sub> : 5 H <sub>2</sub> O B) 1 HAc : 1 H <sub>2</sub> O <sub>2</sub> : 10 H <sub>2</sub> O
Aluminum	16 H <sub>3</sub> PO <sub>4</sub> : 2H <sub>2</sub> O : 1 HNO <sub>3</sub> : 1 HAc
Chromium	10 (NH <sub>4</sub> ) <sub>2</sub> Ce(NO <sub>3</sub> ) <sub>6</sub> : 1 HNO <sub>3</sub> : 49 H <sub>2</sub> O

Table 3-1 Wet etching of metals

3.1.5 Sacrificial layer

A variety of sacrificial layers (for releasing the structures from the substrate on which they have been fabricated) have been used or trialled in this work, and the main methods are summarised here.

### ***Positive resist***

AZ4562 was trialled as a release layer for SU-8. However, it was found that, despite an extended hard bake, sufficient solvent was left in the positive resist for it to adversely affect the spinning of the SU-8 layer on top, resulting in the mixing of the two layers.

### ***Omnicoat***

Omnicoat is a spin-on layer manufactured by Microchem which is designed as an adhesion promoter in some instances, but in the case of SU-8 as a release layer. However on wet etching of the Omnicoat layer it was found necessary to place the solution in an ultrasonic bath in order to achieve release and this was found to destroy the more fragile parts of the SU-8 structure.

### ***Polyimide***

Polyimide can be spun onto the substrate and then hard-baked to achieve a polymer layer suitable for processing on. This is often used when a flexible substrate is required, as the polyimide can easily be released from the wafer in water after processing is complete, although this can cause premature delamination problems if care is not taken. In this instance it was found that the polyimide could then be peeled from the back of the released structure, but only when the structure was in excess of approximately 50  $\mu\text{m}$  in thickness, as thinner structures were too fragile.

### ***Prolift***

Prolift is a spin-on polymer designed for the purpose of releasing SU-8 structures and is made by Brewer Science. It can be etched in Tetramethylammonium hydroxide (TMAH) and is a much quicker release method than the others previously discussed, standardly releasing over a period of up to twelve hours depending on the size and residual stress in the structure to be released. However, when the etching of metals was carried out, the patterning and subsequent removal of the positive photoresist layer, used as a shield for the etching, required the substrate to be exposed to both developer and stripper, both of which attacked the Prolift sacrificial layer. This caused delamination of the devices before they were ready to be released. This problem was

particularly apparent in devices where the metal covered a step in the underlying polymer, as a thicker positive photoresist with associated longer development and stripping times was required. The effect of the delamination is shown in Figure 3-6 where it has caused shearing of the metal layer at the base of the sidewall.

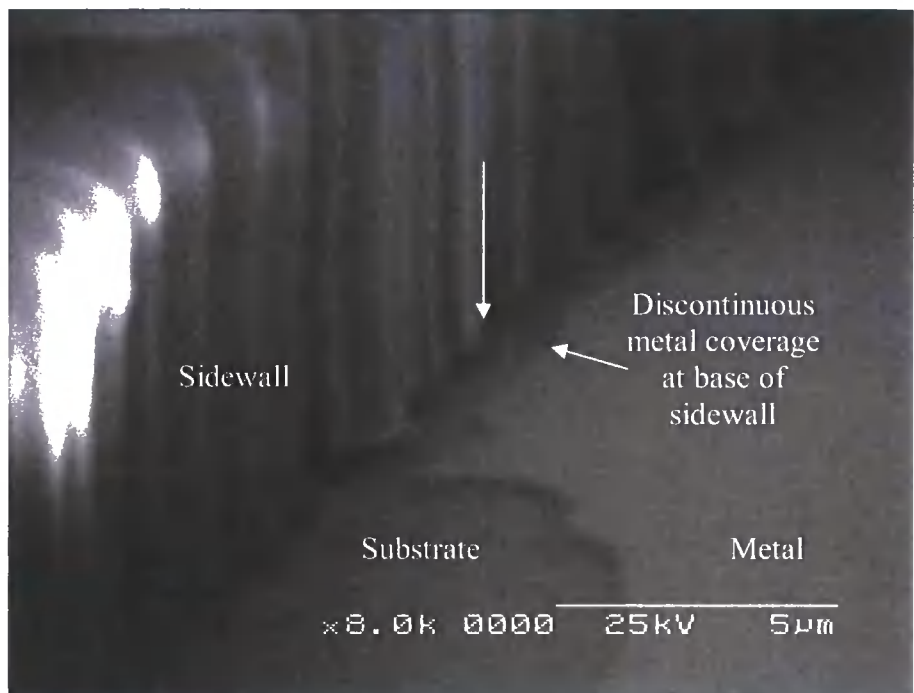


Figure 3-6 Delamination of structure due to attack of release layer which causes shearing of metal layer over step

***Titanium-Copper-Titanium***

Titanium-copper-titanium was deposited on the substrate using the e-beam evaporator. The bottom layer of titanium was used as an adhesion layer for the copper, which was itself the main release layer, and the top layer of titanium had a twofold purpose; that of protecting the copper from the etch used on the nichrome in the devices and also providing a good adhesion layer for the SU-8. To release the structures, the top layer of titanium was removed in HF (the lower layer of titanium being protected beneath the copper layer), and then the copper was etched using one of two etchants. One etchant was sodium persulfate, which undercut the copper fairly rapidly, allowing the structures to be released, but attacked exposed nichrome. The second was acetic acid, which was

more selective, and did not attack the nichrome, but etched at a much slower rate, and was therefore unable to release the devices in an acceptable period of time.

### ***Prolift-Titanium***

Because Prolift etched in both the developer and stripper for the positive photoresist used in etching metals, this posed a processing problem. If the metal was deposited over a step, a significantly thicker layer of the positive photoresist was required, and thus a longer period of development and stripping. This led to the Prolift being exposed to it for significantly longer, and therefore delamination at the edges of the device was seen where the Prolift was undercut, causing the metal at the base of the step to shear, as seen in Figure 3-6. In order to minimise this problem a layer of titanium 100 nm thick was deposited over the Prolift layer. Although this was insufficient to create an impermeable layer, it slowed the attack of the Prolift by the developer sufficiently to allow processing to be completed.

While the top layer of titanium was important for the protection of the Prolift release layer when the metal layer is being etched, it was also useful as an adhesion layer since titanium and SU-8 have good adhesion [56].

To release the structures, first the exposed titanium was etched, and then the Prolift removed, as when processed without the layer of titanium. Once the structures were released, the titanium remaining on the underside was etched.

## **3.2 Force-deflection test rig**

Mechanical and electrical testing of the devices was carried out using a force-deflection test rig. This consisted of a probe mounted on a balance (for measuring the force) which was on alignment stages. These stages allowed the accurate positioning of the device relative to the probe tip in conjunction with the microscope mounted above the alignment stages. The device to be tested was mounted on an arm coming from a nano-positioning stage which had a Linear Variable Displacement Transformer (LVDT) in contact with it to measure the movement of the stage. When electrical measurements were required, connections were made from the device to an ohmmeter. The ohmmeter

and digital voltmeter (DVM) to which the LVDT was connected were all read by the controlling PC using software written in Labview specifically for the control of this test rig. This software also controlled the stage on which the devices were mounted. The test rig is shown in Figure 3-7.

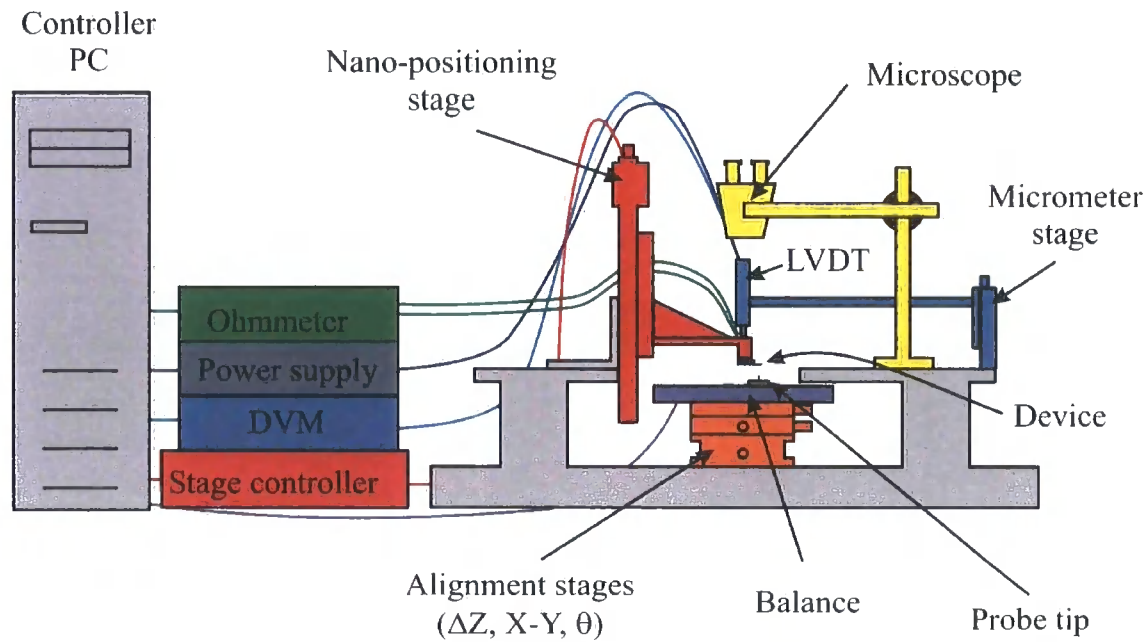


Figure 3-7 The force-deflection test rig

Tests of resistance were carried out independently of force measurement, as the wires leading from the device for the resistance measurements were found to be detrimental to the accuracy of the force measurements by the balance.

In order to carry out force-deflection measurements, the probe tip was brought into contact with the device and then removed by a small margin in order to ensure the deflection was measured from the zero position. The microscope attached to the test rig allowed the accurate alignment of probe tip and device. The stage was then displaced in a series of controlled steps dictated by the software on the controller PC, with the exact distance travelled measured by the LVDT via a voltmeter connected to the controlling PC. Measurements from the balance were also recorded for each step displacement.

Resistance-deflection measurements were carried out by similar means. However, for each step displacement, instead of reading the force measurement from the balance, the resistance was recorded by the PC using the ohmmeter.

### 3.3 Wind tunnel testing

#### 3.3.1 Wind tunnel apparatus

##### *Plint wind tunnel*

The wind tunnel used for testing the wall shear stress sensors (Plint TE44 subsonic wind tunnel) was a ‘blower’ type, closed wall test section, open return wind tunnel with a centrifugal fan upstream of the working section. Downstream of the fan are a diffuser and settling chamber, both of which contain smoothing screens which make the flow more uniform. There is then a contraction (with a ratio of 7.3:1) before the working section, which had a cross-section of 0.46 x 0.46 m and was 1.22 m long. The maximum velocity was 21 m/s and the turbulence intensity of the flow was < 0.5% [57]. The velocity in the wind tunnel was calculated using pressure tapings in the tunnel both before and after the contraction, giving a Reference Pressure Difference (*RPD*) [57]. The calibration to get the dynamic pressure from *RPD* is

$$P_{dyn} = 0.965(RPD) \quad 3-1$$

The pressure tapings were connected to a pressure transducer so that the dynamic pressure could be measured. A Preston tube was connected to a second pressure transducer so that the pressure difference between this and the static pressure from the tunnel could be measured. The pressure transducers used were Sensortech 103LP10D-PCB transducers. The measurable range was  $\pm 1000$  Pa, with an output of 2.5 V per 1000 Pa and an offset of 3.5 V at zero pressure.

A flat plate was suspended from the roof of the working section of the wind tunnel and had a chamfered edge upstream to minimise separation at the leading edge. The sensors were mounted on the underside of this plate for calibration and testing purposes.

This set-up is shown in Figure 3-8.

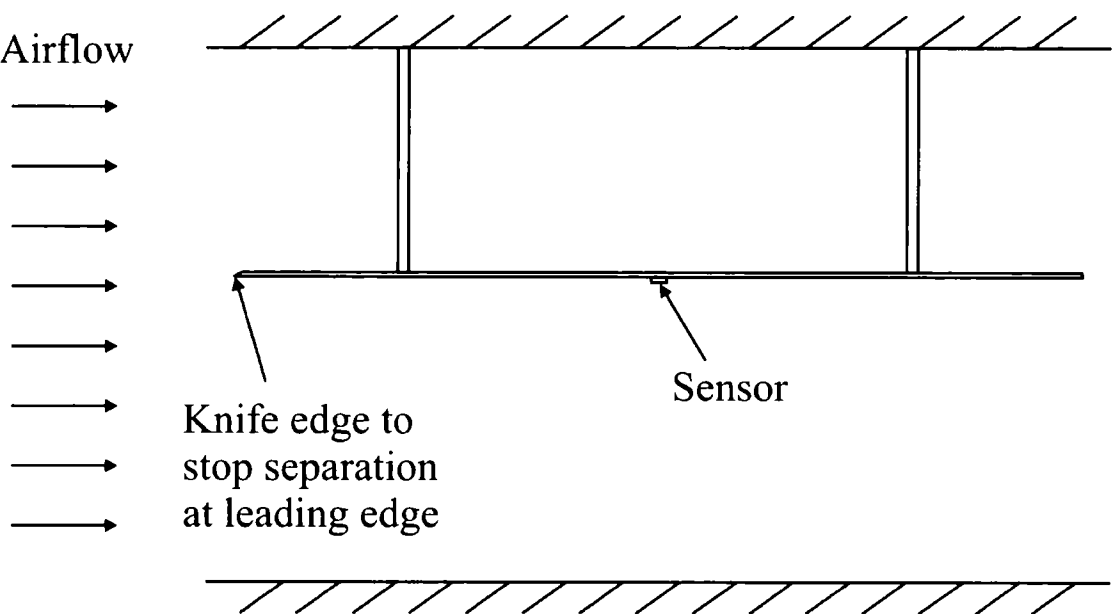


Figure 3-8 Working section of wind tunnel with flat plate

The sensors had thin enamel-coated copper wires attached to the contact pads by silver paint. The copper wires were then attached via screw terminals to coaxial cables which exited the wind tunnel, and were connected to the power supply and data acquisition system (DAQ). Connections to the DAQ were made via BNC connectors, using differential inputs throughout.

A power supply was used to provide a variable input voltage to the Wheatstone bridge in the devices. The output voltage was measured using the DAQ (a NI-DAQPad 6015) which was connected to a PC via USB. The voltage outputs from both pressure transducers were also measured by the DAQ.



A schematic diagram of the set-up of all instrumentation is shown in Figure 3-9.

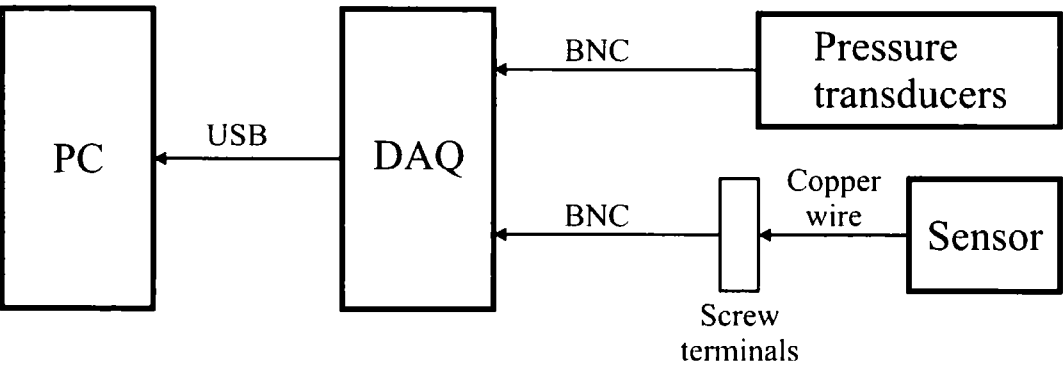


Figure 3-9 Instrumentation set-up for Plint tunnel

The Wheatstone bridge in the device was electrically connected as shown in Figure 3-10.

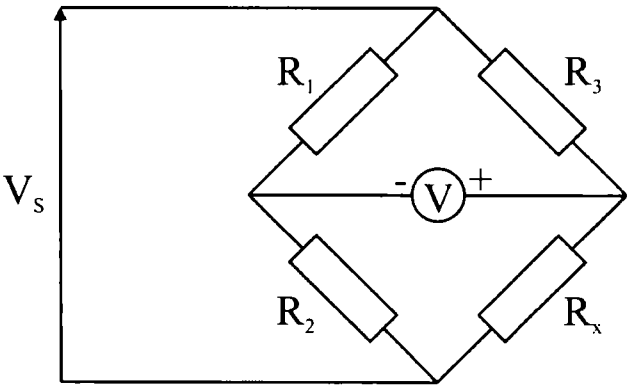


Figure 3-10. Wheatstone bridge connections

With zero load on the sensor the output voltage for a Wheatstone bridge would theoretically be zero. However, slight differences in the resistances of the resistors caused a small offset voltage, typically in the order of a few mV/V.

***Probe calibration test rig***

The probes were tested using the Durham University probe calibration test rig. This test rig consisted of a fan with a honeycomb downstream to straighten the flow, which was then accelerated through a nozzle, exiting it as a jet in which the probe was mounted. The probe mounting was attached to two stepper motors allowing the pitch and yaw of

the probe to be controlled accurately. The probe calibration test rig is shown in Figure 3-11.

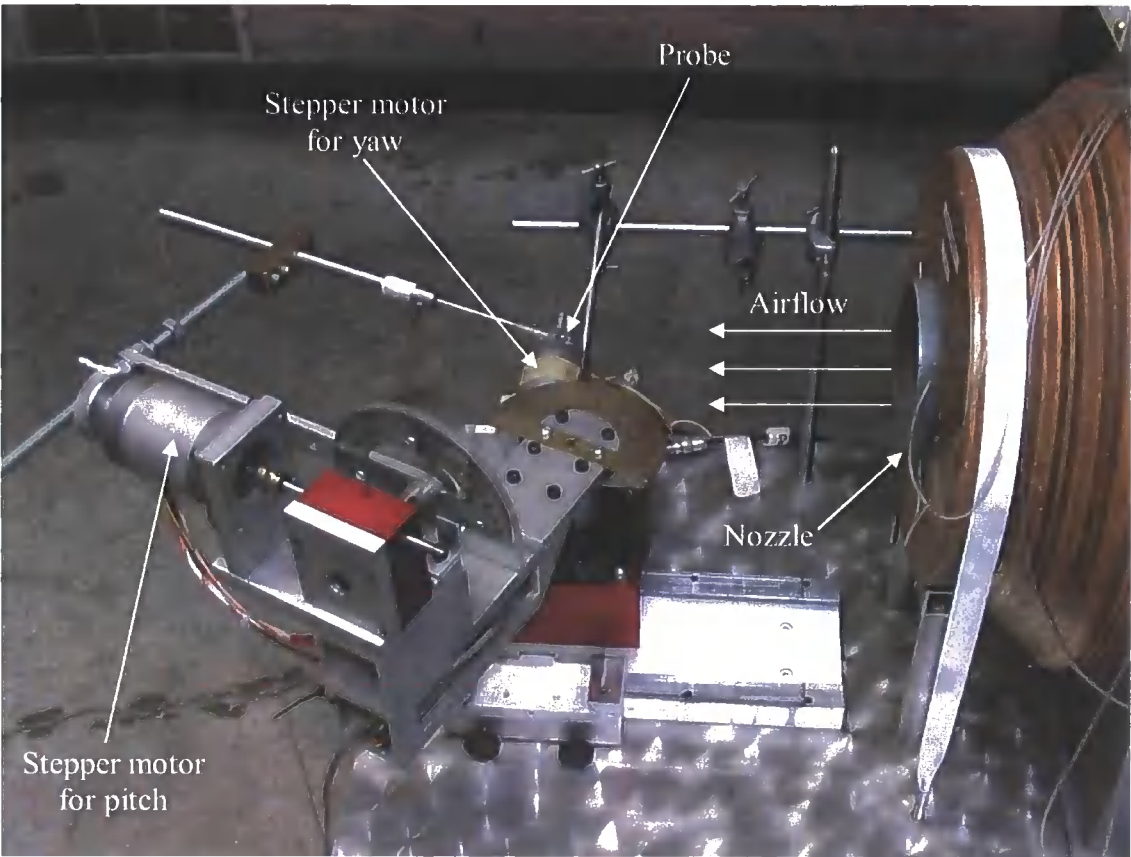


Figure 3-11 Probe calibration test rig

The static pressure before and after the contraction was recorded to give the dynamic pressure since the velocity prior to the nozzle was close to zero. The area contraction ratio of the nozzle was approximately 9:1. A nozzle calibration could be applied to compensate for the fact that the flow was not entirely stationary prior to the contraction.

The instrumentation set-up used was very similar to that used for testing shear stress sensors in the Plint wind tunnel. However the PC was also used to control the traverse by means of a traverse control unit and PK3 stepper motor drive units connected to the stepper motors to control the pitch and yaw angle of the probe.

This altered set-up is shown in Figure 3-12.

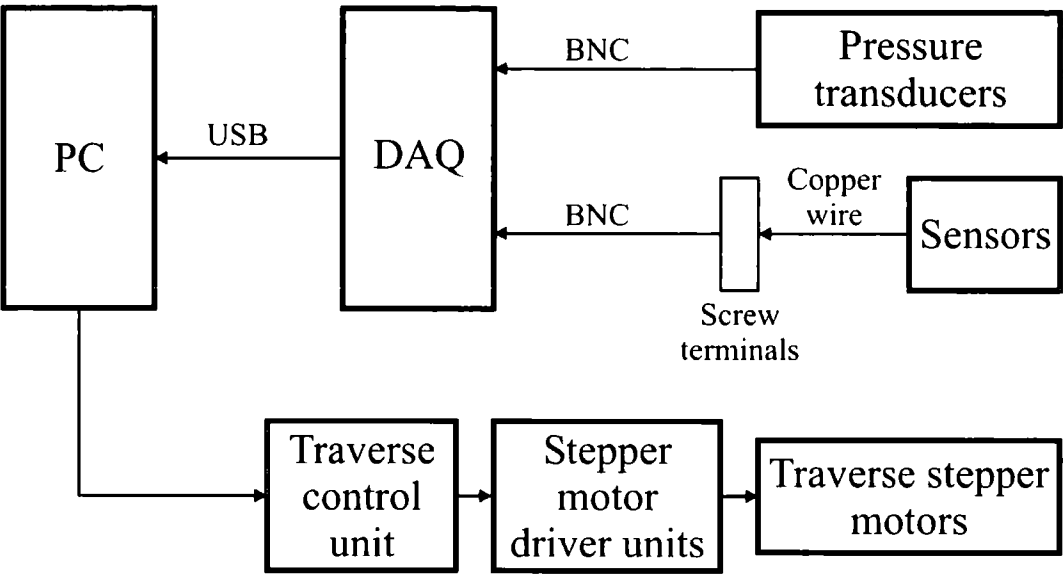


Figure 3-12 Instrumentation set-up for probe calibration rig

### 3.3.2 Data acquisition software

Specialised software for recording data from the experimental set-up was written using Matlab. Since the DAQ is a National Instruments device it was possible to use the Data Acquisition Toolbox of Matlab which contains drivers for most National Instruments devices. The software was written to be as user friendly as possible and also to be adaptable enough for use in a variety of applications.

User inputs are the number of channels to be recorded, along with the appropriate gain for each channel, the frequency at which the channels should be read and the number of readings which should be averaged to give a single data value. The option of logging datums and then subtracting them from any data was offered or alternatively the datums could be logged and then saved with the data allowing the user to utilise them as required. Single data points could be recorded, or alternatively a continuous stream of data could be logged.

Data is saved directly into Excel files when required by the user. This avoids the time-consuming necessity of importing tab-delimited text files into Excel, which are the standard output from most data logging software.

The user interface for the data acquisition software is shown in Figure 3-13.

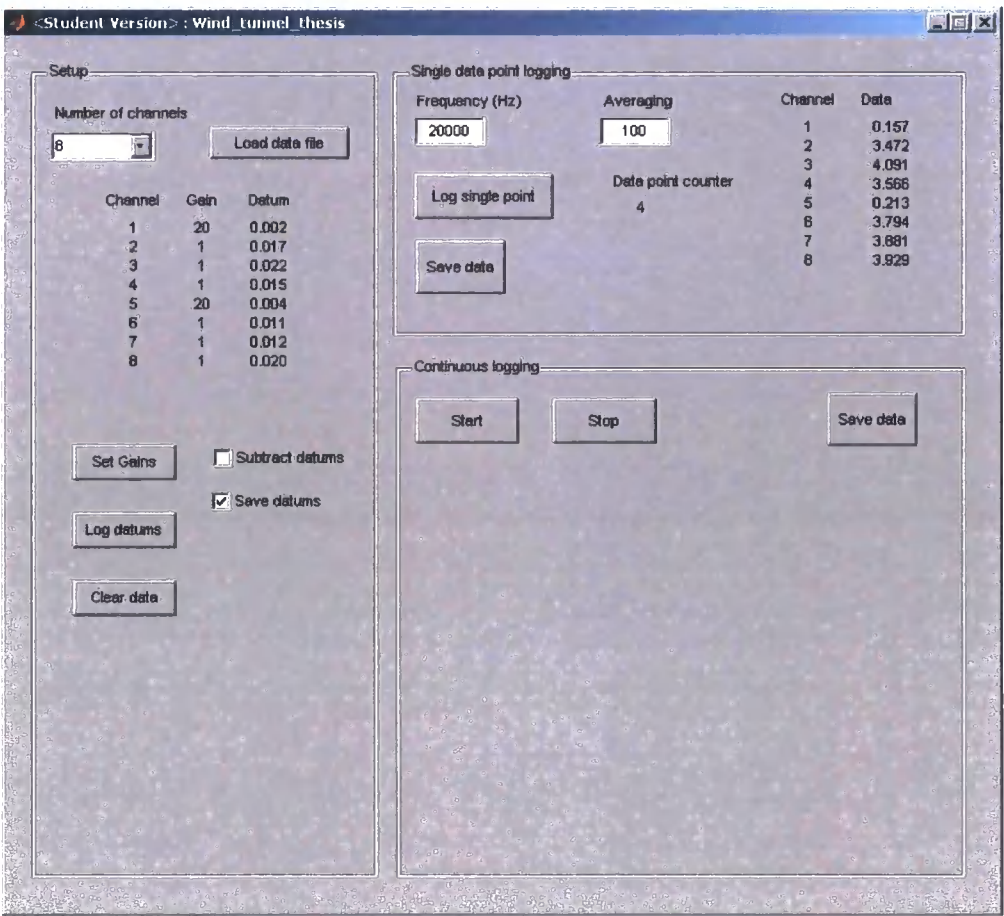


Figure 3-13 User interface of data acquisition software

For testing the probes, the standard ‘Durham Software for Wind Tunnels’ was used because of the additional necessity of controlling the traverse set-up.

3.3.3 Sampling frequency and averaging

For an electrical signal from a device such as a shear stress sensor, noise is often a problem in interpreting the results. A common method of obtaining a more accurate result is to record a certain number of samples and then to take an average of these values. This will remove random noise from the signal, although will not be able to eliminate systematic errors. The number of samples required in order to give a representative value for the data is dependent on the standard deviation, which for this case is representative of the amount of noise on the signal.

Assuming a normal distribution of the data from the sensor, the number of samples required to obtain an average within a certain confidence interval can be calculated. Since

$$k = \frac{c\sigma}{\sqrt{N}} \quad 3-1$$

then  $k$  can be taken to be the maximum allowable error. For a confidence interval of 99%,  $c$  is equal to 2.576 [58],  $\sigma$  is the standard deviation of the data.  $N$  therefore is the number of samples required to give this degree of accuracy to the result.

### **3.4 CFD background and theory**

Computational fluid dynamics (CFD) uses numerical methods to solve complex fluid flows. All CFD modelling was carried out using Fluent.

#### **3.4.1 Fluent**

Fluent is a commercial CFD software package which uses a finite volume method for solving the fluid flow. A range of post-processing tools are available in the software to allow the extraction of relevant data once the solution has been obtained. Turbulence models available in Fluent include the  $k$ - $\varepsilon$  model and the Spalart-Allmaras model. Both structured and unstructured grids can be solved in Fluent, and the pre-processing software Gambit can be used to create compatible meshes for use in Fluent.

#### **3.4.2 Governing equations of fluid flow**

##### ***Navier-Stokes Equations***

Fluid flows are governed by the principles of mass conservation, energy conservation and conservation of momentum. These are expressed mathematically by the Navier-Stokes (momentum) equations, the continuity equation and the energy equation, which describe fluid motion in three dimensions, including viscous effects [59].

The momentum equation, from Newton's Second Law of Motion, is expressed in terms of the pressure and viscous stresses acting upon a particle in a fluid. In component form these are written as

$$\begin{aligned} \frac{\partial(\rho u)}{\partial t} + \frac{\partial(\rho u^2)}{\partial x} + \frac{\partial(\rho uv)}{\partial y} + \frac{\partial(\rho uw)}{\partial z} = \\ \rho X - \frac{\partial p}{\partial x} + \frac{\partial}{\partial x} \left[ \mu \left( 2 \frac{\partial u}{\partial x} - \frac{2}{3} \left( \frac{\partial u}{\partial x} + \frac{\partial v}{\partial y} + \frac{\partial w}{\partial z} \right) \right) \right] \\ + \frac{\partial}{\partial y} \left[ \mu \left( \frac{\partial u}{\partial y} + \frac{\partial v}{\partial x} \right) \right] + \frac{\partial}{\partial z} \left[ \mu \left( \frac{\partial w}{\partial x} + \frac{\partial u}{\partial z} \right) \right] \end{aligned} \quad 3-2$$

$$\begin{aligned} \frac{\partial(\rho v)}{\partial t} + \frac{\partial(\rho uv)}{\partial x} + \frac{\partial(\rho v^2)}{\partial y} + \frac{\partial(\rho vw)}{\partial z} = \\ \rho Y - \frac{\partial p}{\partial y} + \frac{\partial}{\partial y} \left[ \mu \left( 2 \frac{\partial v}{\partial y} - \frac{2}{3} \left( \frac{\partial u}{\partial x} + \frac{\partial v}{\partial y} + \frac{\partial w}{\partial z} \right) \right) \right] \\ + \frac{\partial}{\partial z} \left[ \mu \left( \frac{\partial v}{\partial z} + \frac{\partial w}{\partial y} \right) \right] + \frac{\partial}{\partial x} \left[ \mu \left( \frac{\partial u}{\partial y} + \frac{\partial v}{\partial x} \right) \right] \end{aligned} \quad 3-3$$

$$\begin{aligned} \frac{\partial(\rho w)}{\partial t} + \frac{\partial(\rho uw)}{\partial x} + \frac{\partial(\rho vw)}{\partial y} + \frac{\partial(\rho w^2)}{\partial z} = \\ \rho Z - \frac{\partial p}{\partial z} + \frac{\partial}{\partial z} \left[ \mu \left( 2 \frac{\partial w}{\partial z} - \frac{2}{3} \left( \frac{\partial u}{\partial x} + \frac{\partial v}{\partial y} + \frac{\partial w}{\partial z} \right) \right) \right] \\ + \frac{\partial}{\partial x} \left[ \mu \left( \frac{\partial w}{\partial x} + \frac{\partial u}{\partial z} \right) \right] + \frac{\partial}{\partial y} \left[ \mu \left( \frac{\partial v}{\partial z} + \frac{\partial w}{\partial y} \right) \right] \end{aligned} \quad 3-4$$

where  $\rho$  is the density,  $\mu$  is the viscosity and  $u, v$  and  $w$  are the velocity components in the  $x, y$  and  $z$  directions respectively.  $X, Y$  and  $Z$  represent the components of the body force acting on the fluid.

The continuity equation is based on the principle of conservation of mass and can be expressed as

$$\frac{\partial \rho}{\partial t} + \frac{\partial(\rho u)}{\partial x} + \frac{\partial(\rho v)}{\partial y} + \frac{\partial(\rho w)}{\partial z} = 0 \quad 3-5$$

The energy equation is based on the first law of thermodynamics and can be expressed as

$$\begin{aligned}
 & \frac{\partial(\rho e)}{\partial t} + \frac{\partial(\rho u e)}{\partial x} + \frac{\partial(\rho v e)}{\partial y} + \frac{\partial(\rho w e)}{\partial z} = \\
 & \rho Q + \frac{\partial}{\partial x} \left( k \frac{\partial T}{\partial x} \right) + \frac{\partial}{\partial y} \left( k \frac{\partial T}{\partial y} \right) + \frac{\partial}{\partial z} \left( k \frac{\partial T}{\partial z} \right) \\
 & - p \left( \frac{\partial u}{\partial x} + \frac{\partial v}{\partial y} + \frac{\partial w}{\partial z} \right) - \lambda \left( \frac{\partial u}{\partial x} + \frac{\partial v}{\partial y} + \frac{\partial w}{\partial z} \right)^2 \\
 & + \mu \left\{ 2 \left[ \left( \frac{\partial u}{\partial x} \right)^2 + \left( \frac{\partial v}{\partial y} \right)^2 + \left( \frac{\partial w}{\partial z} \right)^2 \right] + \left( \frac{\partial v}{\partial x} + \frac{\partial u}{\partial y} \right)^2 + \left( \frac{\partial w}{\partial y} + \frac{\partial v}{\partial z} \right)^2 + \left( \frac{\partial u}{\partial z} + \frac{\partial w}{\partial x} \right)^2 \right\}
 \end{aligned} \tag{3-6}$$

where  $e$  is the internal energy,  $\lambda$  is the bulk viscosity,  $Q$  is the heat addition per unit mass,  $T$  is temperature and  $k$  is thermal conductivity.

The Navier-Stokes equations can also be simplified in some cases, such as for an inviscid flow, where the Euler equations are produced, which are the Navier-Stokes equations with zero viscosity.

### ***Reynolds-Averaged Navier-Stokes (RANS) Equations***

A range of methods for dealing with the turbulent nature of flow can be used. The most accurate method is Direct Numerical Simulation (DNS), which captures all scales of turbulent motion even at the smallest levels and therefore does not require the modelling of small-scale turbulence. However this approach is very computationally intensive and as such is impractical for all but the simplest problems at low Reynolds numbers.

In order to circumvent the problems inherent in solving turbulence on all scales, a range of models for approximating the small scale turbulence have been developed. The Reynolds-Averaged Navier-Stokes (RANS) equations are used, where the flow is separated into a mean component and a fluctuating component. This means of averaging the governing equations creates the term known as Reynolds stress to represent the fluctuating component, which is an unknown, and hence turbulence models are used in order to solve the equations.

The mean and fluctuating components of the flow field variables are written as

$$u_i = \bar{u}_i + u'_i \quad 3-7$$

which can then be substituted into the Navier-Stokes equations to give the RANS equations [60].

The momentum equation for the x component becomes

$$\begin{aligned} \frac{\partial}{\partial t}(\bar{\rho u} + \overline{\rho' u'}) + \frac{\partial}{\partial x}(\bar{\rho u u} + \bar{u} \overline{\rho' u'}) + \frac{\partial}{\partial y}(\bar{\rho u v} + \bar{u} \overline{\rho' v'}) + \frac{\partial}{\partial z}(\bar{\rho u w} + \bar{u} \overline{\rho' w'}) = \\ - \frac{\partial \bar{p}}{\partial x} + \frac{\partial}{\partial x} \left( \frac{2}{3} \mu \left( 2 \frac{\partial \bar{u}}{\partial x} - \frac{\partial \bar{v}}{\partial y} - \frac{\partial \bar{w}}{\partial z} \right) - \bar{u} \overline{\rho' u'} - \bar{\rho} \overline{u' u'} - \overline{\rho' u' u'} \right) \\ + \frac{\partial}{\partial y} \left( \mu \left( \frac{\partial \bar{u}}{\partial y} + \frac{\partial \bar{v}}{\partial x} \right) - \bar{v} \overline{\rho' u'} - \bar{\rho} \overline{u' v'} - \overline{\rho' u' v'} \right) \\ + \frac{\partial}{\partial z} \left( \mu \left( \frac{\partial \bar{u}}{\partial z} + \frac{\partial \bar{w}}{\partial x} \right) - \bar{w} \overline{\rho' u'} - \bar{\rho} \overline{u' w'} - \overline{\rho' u' w'} \right) \end{aligned} \quad 3-8$$

The y and z component equations can be derived similarly.

The continuity equation is written as

$$\frac{\partial \bar{\rho}}{\partial t} + \frac{\partial}{\partial x}(\bar{\rho u} + \overline{\rho' u'}) + \frac{\partial}{\partial y}(\bar{\rho v} + \overline{\rho' v'}) + \frac{\partial}{\partial z}(\bar{\rho w} + \overline{\rho' w'}) = 0 \quad 3-9$$

The energy equation becomes (this equation is given in vector format for brevity)

$$\begin{aligned} \frac{\partial}{\partial t}(c_p \bar{\rho T} + c_p \overline{\rho' T'}) + \frac{\partial}{\partial x_j}(\bar{\rho c_p T \bar{u}_j} + c_p \bar{T} \overline{\rho' u'_j}) = \\ \frac{\partial \bar{p}}{\partial t} + \bar{u}_j \frac{\partial \bar{p}}{\partial x_j} + \overline{u'_j \frac{\partial p'}{\partial x_j}} + \frac{\partial}{\partial x_j} \left( k \frac{\partial \bar{T}}{\partial x_j} - \bar{\rho c_p T' u'_j} - c_p \overline{\rho' T' u'_j} - \bar{u}_j c_p \overline{\rho' T'} \right) + \bar{\Phi} \end{aligned} \quad 3-10$$

where

$$\bar{\Phi} = \overline{\tau_{ij} \frac{\partial u_i}{\partial x_j}} = \bar{\tau}_{ij} \frac{\partial \bar{u}_i}{\partial x_j} + \overline{\tau'_{ij} \frac{\partial u'_i}{\partial x_j}} \quad 3-11$$



and

$$\bar{\tau}_{ij} = \mu \left[ \left( \frac{\partial \bar{u}_i}{\partial x_j} + \frac{\partial \bar{u}_j}{\partial x_i} \right) - \frac{2}{3} \delta_{ij} \frac{\partial \bar{u}_k}{\partial x_k} \right] \quad 3-12$$

and  $\delta_{ij}$  is the Kronecker delta function, where  $\delta_{ij} = 1$  if  $i = j$  and  $\delta_{ij} = 0$  if  $i \neq j$ .  $i, j, k = 1, 2, 3$ .

### 3.4.3 Turbulence models

The stress gradients caused by turbulent fluctuations in the flow can be written as

$$(\bar{\tau}_{ij})_{turb} = -\rho \overline{u'_i u'_j} \quad 3-13$$

These are called the Reynolds stresses. Turbulence models aim to approximate these Reynolds stresses.

Commonly used turbulence models in engineering include the  $k$ - $\varepsilon$  model, which is a two-equation model, meaning that two variables are used to represent the turbulent nature of the flow. One of the variables is the turbulent kinetic energy,  $k$ , and the other is the turbulent dissipation,  $\varepsilon$ .

A one equation turbulence model is Spalart-Allmaras, using the turbulent dynamic viscosity to represent the turbulence. This is the turbulence model which has been used in this work.

### 3.4.4 Equation discretization

In order to allow these partial differential equations to be solved by computers, they need to be translated into a form which makes this possible, which is equation discretization. The main methods of solving the Navier-Stokes equations numerically are the finite difference method, the finite volume method and finite element method.

The finite volume method used in Fluent uses a discretization of the integral form of the Navier-Stokes equations. The computational domain is separated into a series of control

volumes and the finite volume method converts volume integrals containing a divergence term to surface integrals using the divergence theorem, and then these terms are evaluated as fluxes at the surface of the finite volume. The advantage of this method is that the flux leaving one volume is identical to that entering the adjacent volume, and therefore conservation is satisfied. This method can be used for both structured and unstructured meshes.

### **3.4.5 Spatial discretization**

For CFD the domain is divided into a series of smaller subdomains. The mesh consists of nodes for which the flow variables are solved.

There are two main types of grids used – structured and unstructured meshes. Structured meshes are usually used in geometries with simpler square or rectangular geometries. However, where complex shapes are present, as is often the case, the formation of a structured grid can be very difficult.

Unstructured meshes use an arrangement of nodes with no particular order, and while they are more convenient for complex geometries they often require a finer mesh to be used to obtain a good degree of accuracy, and thus are computationally more expensive.

It is also possible to create meshes which use a combination of structured and unstructured grids. Different blocks of the domain are meshed using different methods in order to combine the relative simplicity of a structured mesh, where this is possible, and to use the flexibility of an unstructured mesh where this is required.

The grids used for solving flow problems in this work were all structured meshes. The grids consisted of rectangular elements in 2D problems, and tetrahedral elements for 3D problems. This was possible due to the relatively simple rectangular geometry of the devices being modelled.

In all CFD work it is important to check for mesh independence in order to ensure that the mesh is sufficiently fine to achieve acceptable discretization errors. This is carried out by obtaining solutions for meshes of varying resolutions, and using a mesh which

has a constant result but is not so small as to significantly increase the computational time.

### 3.5 Structural analysis

#### 3.5.1 Beam theory

A diagram of a generic beam is shown in Figure 3-14.

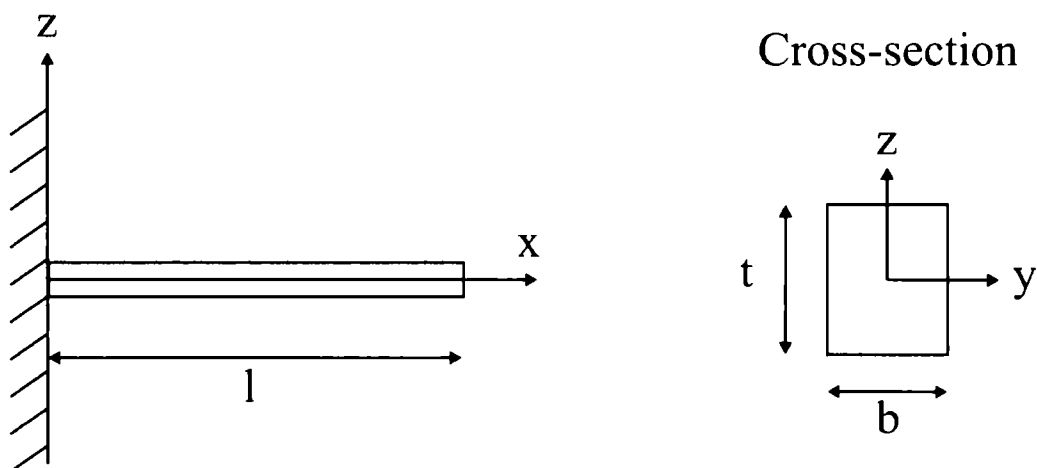


Figure 3-14 Geometry of a beam

The theory of simple bending of beams works under a series of assumptions. These are:

- Beam is long and thin ie.  $l \gg b, t$  (i.e. bending is taking place, not shear)
- Loading is in the z-direction
- There is no torsion or twist
- No stress in y-direction
- Deflections are small (i.e. linear and elastic)

The governing differential equation for deflection of a uniform, static beam is given as

$$EI \frac{d^4 v}{dx^4} = w(x) \quad 3-14$$

where  $EI$  is a constant ( $E$  is Young's modulus and  $I$  is the second moment of area),  $v$  is the deflection of the beam and  $w$  is a distributed load.

The relevant results here [61] are that for a beam with two fixed ends, the deflection at the midpoint is given by

$$v = \frac{wl^4}{384EI} \quad 3-15$$

and for a cantilever with fixed root, the tip deflection is given by

$$v = \frac{wl^4}{8EI} \quad 3-16$$

The relationship between bending stress, moment and geometry is given by

$$\frac{M}{I} = \frac{\sigma}{y} = \frac{E}{R} \quad 3-17$$

where  $M$  is the moment,  $\sigma$  is stress,  $y$  is the distance from the neutral axis and  $R$  is the radius of curvature of the neutral axis.

Superposition theory states that the effect of a combined loading on a structure may be determined by the aggregate of the effects of the separate loads. It assumes that deflections are small, and hence, linear.

For situations where simple beam theory does not apply, such as where the deflection is large (or other of the above assumptions allowing analytical calculation, are incorrect), alternative means of calculating the deflection of the structure are available. However, these equations give a simple way of obtaining a first estimate of deflection and strain, even where the assumptions made are invalid.

### 3.5.2 FEA

Finite element analysis (FEA) is a numerical technique for calculating the behaviour of structures under applied loads. It can be used to calculate deflection, stress, vibration and buckling where deformation is either elastic or plastic. It allows for complicated

structures to be analysed or for cases where assumptions associated with a straightforward analytical calculation are not valid.

FEA involves the subdivision of a structure into a mesh, where elements of the mesh are connected at nodes. The behaviour of an individual element is described by a fairly simple set of equations and these can be built up into a large series of simultaneous equations representing all the elements of the mesh. The elements may be 1D, 2D or 3D and although the structure as a whole may be complex, will individually be simple geometrically.

The matrix stiffness equation can be solved to find the node displacements, and thus the strains and stresses in each element.

For a linear static problem, this equation is

$$F = Kd \quad 3-18$$

where  $F$  is the force vector,  $K$  is the stiffness matrix and  $d$  is the displacement vector.

The loading is applied to the structure in the model, and any constraints on the structure's movement such as fixed points, or where the structure is only able to move in specific directions. Material properties for the structure are also applied, such as the Young's modulus, Poisson's ratio and density of the material.

Because of the number of elements required to obtain a stable result for even a relatively simple geometry, these equations are usually solved using a computer. A finer mesh will give a more accurate result, but at the expense of computational time.

### ***Computer modelling***

Two computer modelling packages have been used for carrying out finite element analysis in this work; these are Coventorware and Strand7. In both packages all meshes used hexahedral brick elements.

Coventorware is a computer package designed for MEMS use, allowing the structure to be built up using the processes as they would be carried out in the fabrication process.

However, it was found that the limitations of this method of building the structure would not allow the device to be modelled in such a way as to replicate the fabrication process.

Since the MEMS design features of Coventorware could not be fully utilised, the standard modelling software Strand7 was also used as it allowed modelling, solving and analysis to be carried out more rapidly. Strand7 allows pre-processing, solving and post-processing to be done in one package. It also allows the use of non-linear static solvers which was necessary for some of the modelling carried out.

By an iterative process it was also possible to use the FEA software to obtain an accurate value for the Young's modulus of a material where the force and deflection are known.

### ***Nonlinearity***

Geometric nonlinearity occurs when the structure deforms in such a way that the loading conditions, or the way the structure reacts to the load, is significantly altered. For example, where a cantilever is deflected such that the deflection is not small when compared with the thickness of the beam, it can be seen that the force applied is no longer acting in the same direction relative to the beam as previously.

Material nonlinearity often occurs when a material is behaving plastically, but can also take place with elastic deformation. In this case the unloading and loading behaviour is the same, but the stress-strain relationship is not linear.

When a problem is nonlinear, the relationship between the force vector and displacement vector is no longer linear. Consequently when a nonlinear static problem is solved in Strand7 the Newton-Raphson method is used [62]. An iterative method is used whereby the load is increased incrementally. The auto-stepping function was used so that the load steps were automatically calculated. For each iteration the current element stiffness matrix is formed based on the deformation and stresses. The elemental nodal force vector is also calculated and consequently the incremental nodal displacement vector. This then allows the incremental strain and stress to be calculated.

Because of the iterative nature of this process it is more computationally intensive and time consuming than undertaking a linear problem.

### **3.6 Summary**

MEMS fabrication processes used for the fabrication sensors and described here include:

- Mask making
- Photolithography
- Metal deposition
- Wet etching
- Sacrificial layers

Mechanical testing of sensors was carried out using a test rig capable of measuring force and deflection and also resistance.

Two wind tunnels were used for testing sensors. A Plint wind tunnel was used for testing the wall shear stress sensors, and a probe calibration test rig for the testing of probes. The instrumentation set-up used in both of these wind tunnels was also described here.

Numerical simulations were carried out to analyse the response of the sensors. The airflow around the sensors was calculated using the CFD package Fluent, and structural analysis of the deflection of the sensors was carried out by FEA using either Coventorware or Strand7.

## **Chapter 4**

# **Fence-style sensor for wall shear stress measurement**

The initial design of shear stress sensor was based on a surface fence structure with an integrated sensing element. The sensor was modelled using CFD and FEA in order to obtain an understanding of the behaviour of the device, and also tested in a wind tunnel.

### **4.1 Theory of operation**

It was decided to use a fence structure for the initial design of shear stress sensor as this is a relatively simple principle for the measurement of shear stress, while allowing a range of shear stresses suitable for models in wind tunnels to be measured with good sensitivity. The range and sensitivity can easily be altered by changing the geometry of the fence itself depending on the application.

The fence deflects under the pressure from the airflow, and a strain gauge can be incorporated into the structure in order to measure the pressure-induced deflection.



In order to maximise the measurable deflection, a slot just above the base of the fence allows the fence to bend along its horizontal axis. This in effect turns the fence into a long beam with fixed ends, as opposed to a short cantilever. There will also be a smaller degree of bending along the vertical axis. The two different modes of bending are described in Figure 4-1.

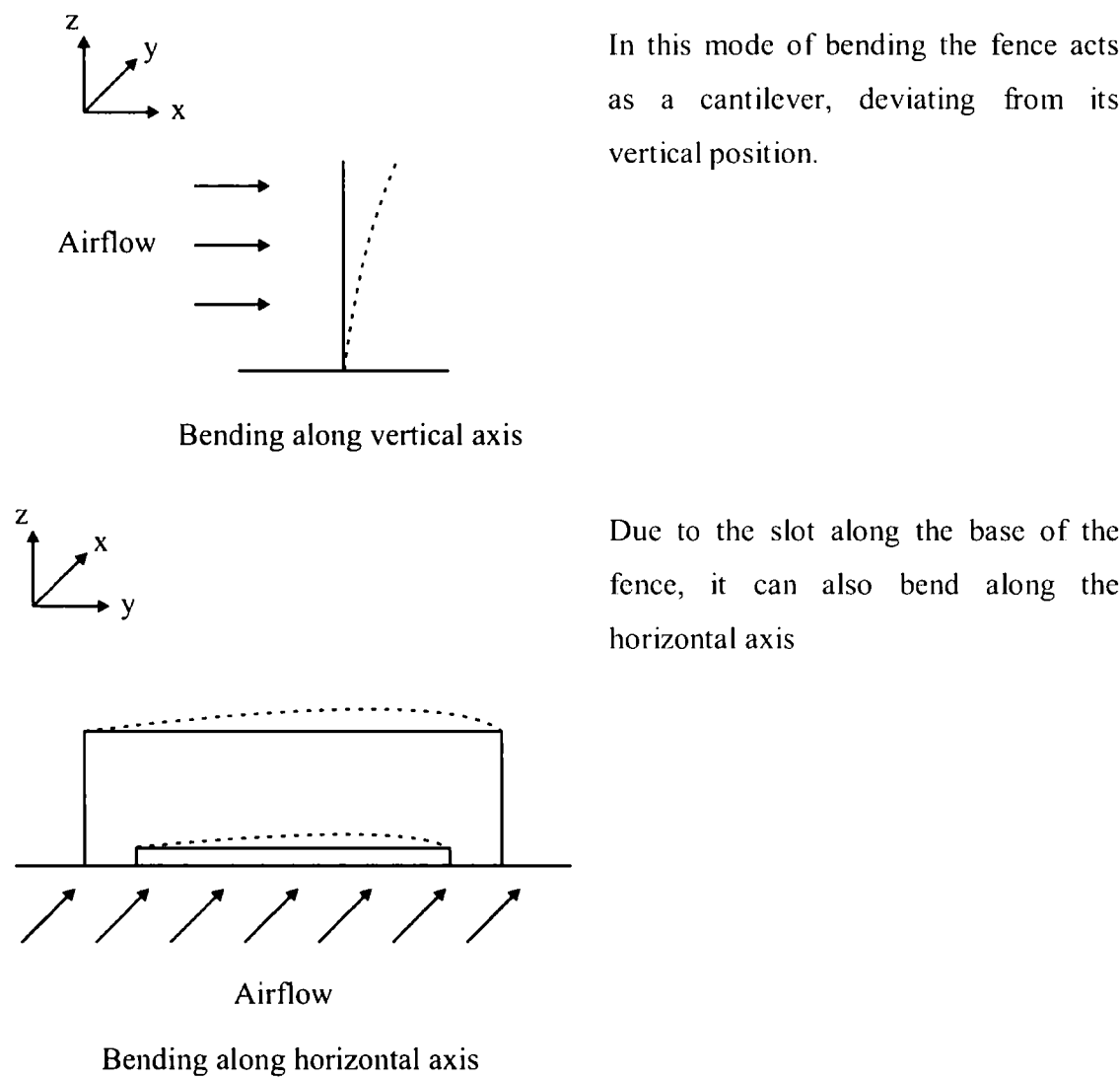


Figure 4-1. Modes of bending in the fence

Although a cantilever will bend more under the same applied load than a beam, in this case the beam can be considerably longer than a cantilever, due to the orientations relative to the airflow, i.e. the y-dimension can be made much larger with less influence on the airflow than a corresponding increase in the z-dimension would cause.

## 4.2 Device Fabrication and Design

### 4.2.1 Design

While p-doped silicon is a good material for constructing a sensor of this type due to the high piezoresistive gauge factor [25], there are alternative MEMS materials that offer other advantages. One of these is the negative photoresist SU-8 which, due to its good mechanical properties, can be used as a structural layer within a device, unlike most other photoresists. This polymer can be used with gold to provide an integrated strain gauge. Although gold has a significantly lower gauge factor than doped silicon, the Young's modulus of SU-8 is also much lower than that of silicon, and therefore the sensitivity of such a device would be comparable to that of one fabricated completely from silicon. Thaysen et al [63] have used this method successfully for the construction of cantilevers. They estimate  $(K/E)_{\text{Si}} = 0.77 \text{ GPa}^{-1}$  and  $(K/E)_{\text{Au/SU-8}} = 0.4 \text{ GPa}^{-1}$ , where  $K$  is the gauge factor and  $E$  is the Young's modulus, although the mechanical properties of SU-8 are very process dependent. It was therefore decided to fabricate the device from the polymer SU-8 with an evaporated gold strain gauge to measure the deflection of the fence.

The sensor consists of the fence, containing a gold meander resistor, and the body of the sensor which contains three identical resistors arranged in a Wheatstone bridge configuration and the four contact pads (see Figure 4-3). The body is mounted within the surface over which the shear stress is being measured, with just the fence itself protruding into the airflow. The fence is 5 mm long, 750  $\mu\text{m}$  high and 20  $\mu\text{m}$  thick. This is on a thicker (120  $\mu\text{m}$ ) body with dimensions of 12 mm x 13 mm.

A diagram of the fence sensor as it would appear embedded into a body is shown in Figure 4-2.

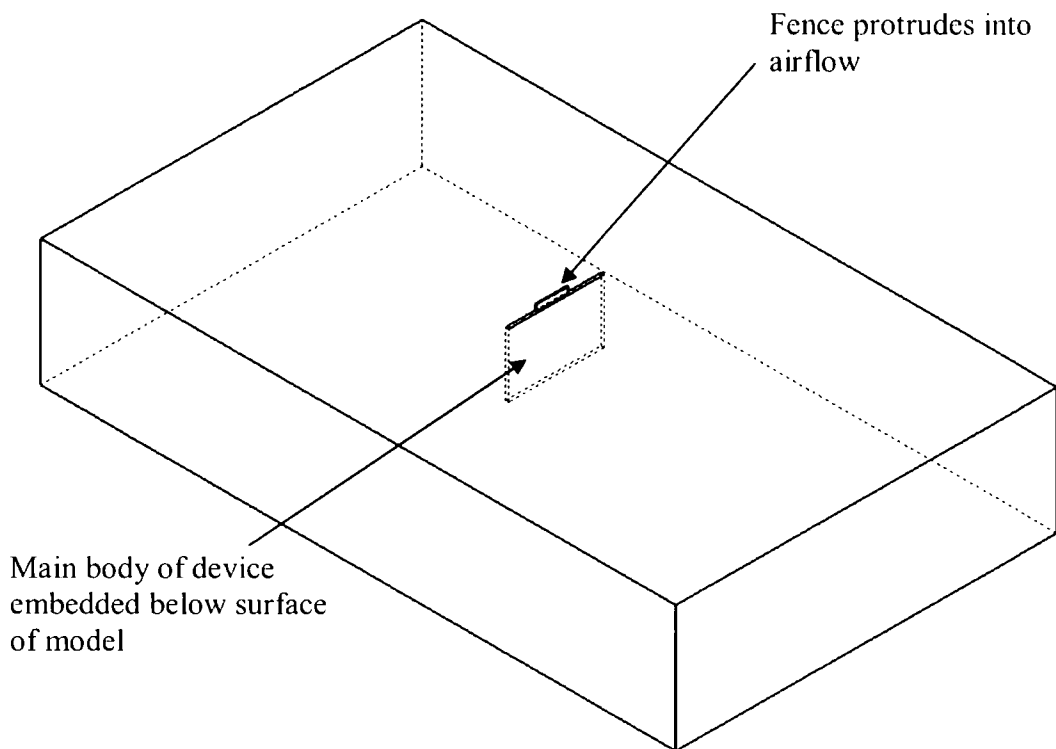


Figure 4-2 Fence sensor embedded in surface

The Wheatstone bridge is designed to reduce changes in the output signal caused by the increase in resistance of the strain gauge as a result of ambient temperature changes. In addition the output signal offset from a Wheatstone bridge is small, which allows a high gain to be applied to the signal. The three resistors of the Wheatstone bridge have exactly the same geometric design as that of the strain gauge in the fence itself. This is because the resistance is altered by the turns in the resistor and therefore variations in the resistance are minimised as far as possible in this way. However, there will be some variations in the deposited film over the area of the substrate, and consequently there will be small variations in the resistance of each element of the Wheatstone bridge.

The strain gauge is designed for measuring the bending along the horizontal axis rather than any bending along the vertical axis which will be small in comparison. The slot

that allows this mode of bending has a height of 100  $\mu\text{m}$  and a length of 4.3 mm. The slot is positioned 50  $\mu\text{m}$  above the base of the fence.

The sensor design is shown in Figure 4-3.

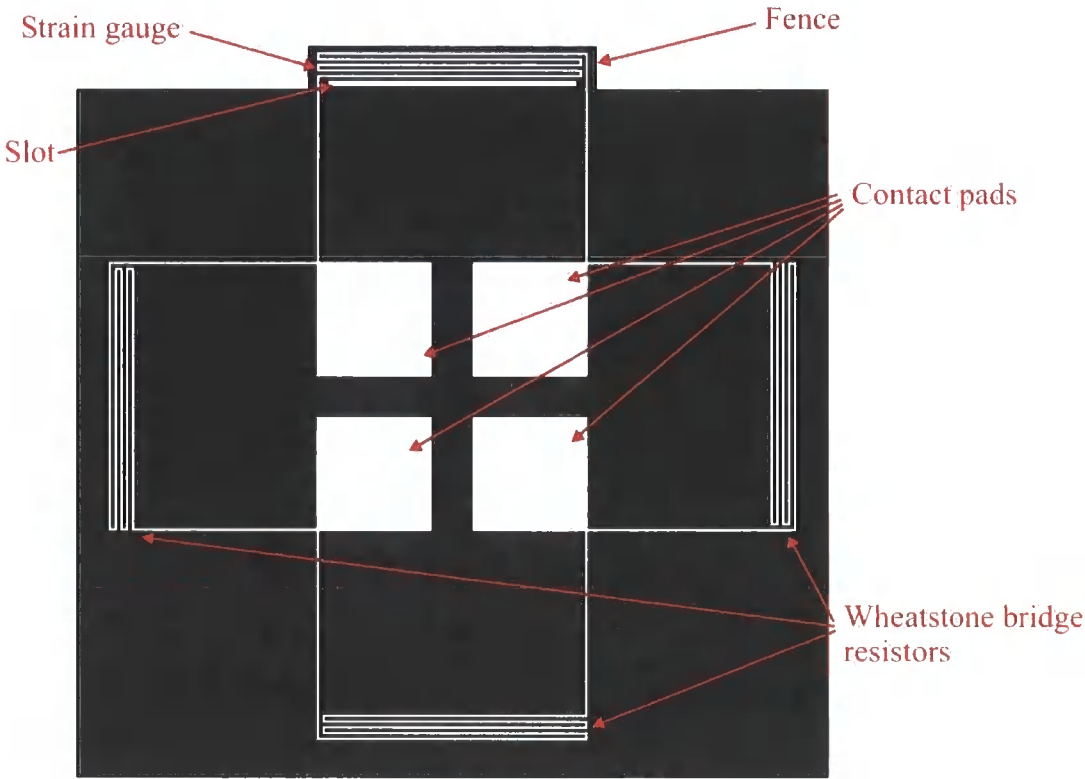


Figure 4-3 Sensor design

#### 4.2.2 Fabrication

The device was fabricated using a four-mask process. It is advantageous to minimise the number of masks used during the fabrication process as far as possible. This is due to the likelihood of defects in the masks themselves as well as the possibility of problems during the photolithography process reducing the yield of devices from a substrate.

The final masks used for fabricating the fence sensors are shown in Figure 4-4. They are shown in the negative format as would be printed onto acetate prior to reproducing the image photographically on a glass plate. The second mask used for defining the metal layer has the opposite polarity of the masks used for SU-8 layers because the resist used

as a protective layer when etching the metal is a positive resist, while SU-8 is a negative resist.

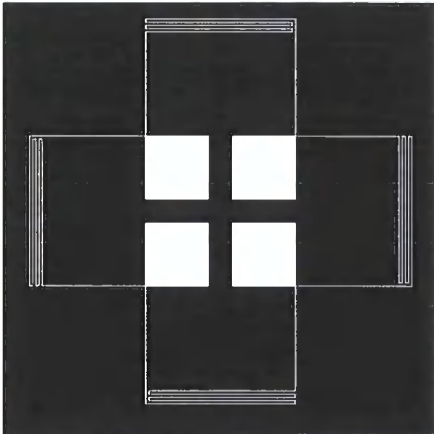
Six devices could be fitted onto each of the in-house masks as the size is limited by reducing an A3 printed page by 10 times.

a)



The first mask is for the initial layer of SU-8 and defines both the body of the device and fence itself.

b)



The second mask defines the metal resistors.

The third mask is identical to the first one for the layer of SU-8, which encapsulates the metal.

c)



The fourth and final mask is used for the thick layer of SU-8 which covers only the body of the device and gives it rigidity and makes the whole sensor easier to handle and mount, without adding stiffness to the sensing element (fence) itself.

Figure 4-4 Masks for fabrication of fence sensors

The two layers of SU-8 on the fence are designed to protect the metal resistors from damage caused by debris in the airflow. Although the thickness of these two layers could be different, it was decided to keep them the same. However, one or both could be reduced in order to decrease the stiffness of the fence and thus increase sensitivity.

The sensor is fabricated on a silicon substrate that is used to handle the devices during fabrication and from which the device is released at the end of the fabrication process. Several different sacrificial layers were used during the initial design of the fabrication process for this device. The most efficient method of releasing the devices was found to be a layer of ProLift. The complete finalised fabrication process flow is shown in Figure 4-5.

a)



A ProLIFT 100 layer is spun onto the silicon wafer at 3000 rpm to act as a final release layer. It is baked for 2 minutes at 95 °C and then 1 min at 245 °C.

b)



A layer of SU-8-10 is then spun on top of this layer at 3000 rpm to achieve a nominal thickness of 10  $\mu\text{m}$  and pre-baked for 2 min at 65 °C and 5 min at 95 °C. This is then exposed at 200  $\text{mJ}/\text{cm}^2$  and post-baked for 2 min at 65 °C and 10 min at 95 °C. The layer of SU-8 is then developed in EC solvent for 2½ min.

c)



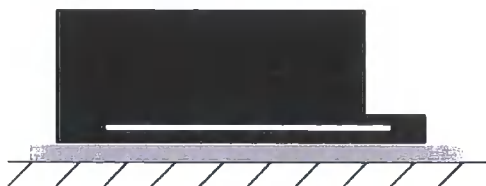
A 30 nm gold layer is then deposited by electron-beam evaporation, and a layer of S1813 spun over the top at 3700 rpm. The resist was then exposed for 3 seconds and developed for approximately 30 seconds. The exposed gold is then etched using gold etch (described in §3.1.4). The remaining resist is then removed by flash exposing the whole of the wafer and developing again.

d)



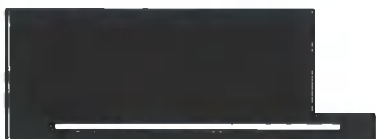
The gold layer is encapsulated in SU-8, as another layer of SU-8-10 is spun on at 3000 rpm and pre-baked for 2 min at 65 °C and 5 min at 95 °C. This is then exposed at 250  $\text{mJ}/\text{cm}^2$  and post-baked for 2 min at 65 °C and 10 min at 95 °C.

e)



A layer of SU-8-50 is spun on at 1000 rpm to give a nominal thickness of 100  $\mu\text{m}$  which is pre-baked for 10 min at 65  $^{\circ}\text{C}$  and 30 min at 95  $^{\circ}\text{C}$ . This is then exposed at 400  $\text{mJ}/\text{cm}^2$  and post-baked for 1 min at 65  $^{\circ}\text{C}$  and 10 min at 95  $^{\circ}\text{C}$ . The second and third layers of SU-8 are then developed together for 20 minutes in EC solvent.

f)



The device is then released by etching the sacrificial layer of Prolift in TMAH.

Figure 4-5. Process of fabrication of SU-8/Au devices

The released device is shown in Figure 4-6. The meander resistor in the fence can clearly be seen, as can the Wheatstone bridge with four contact pads. Access to the contact pads is made by puncturing the thin SU-8 layer covering them. Whilst this is not an ideal solution for making electrical connections to the device, it greatly simplifies the fabrication of the sensor. Nominal resistance of each of the resistors is 300  $\Omega$ .

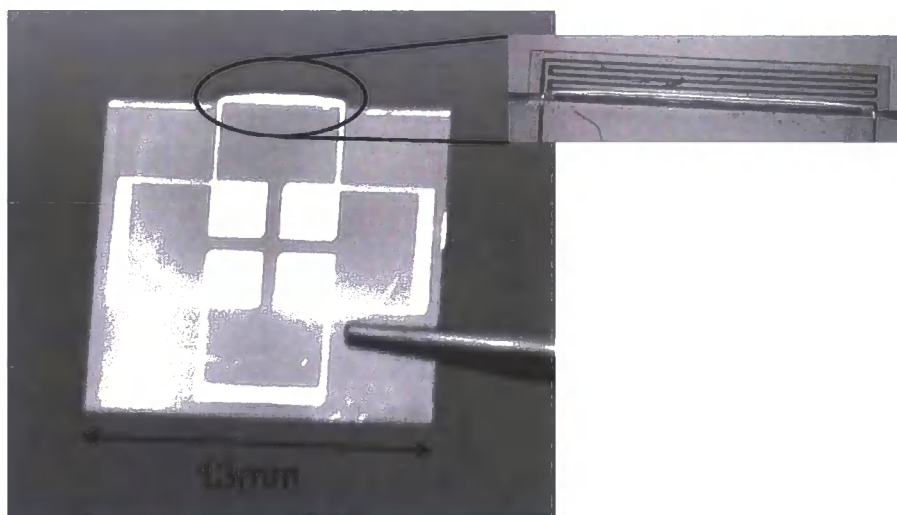


Figure 4-6. Released surface fence sensor



### **4.3 CFD**

Computational Fluid Dynamics (CFD) modelling was undertaken to allow the pressure causing the deflection of the fence to be predicted for a given velocity. The CFD modelling was done in Fluent, with a mesh created in Gambit.

#### **4.3.1 Mesh approach**

The mesh domain was created to mimic the flat plate on which the sensor was mounted for wind tunnel testing. The CFD modelling was carried out in 2D, although it was expected that in reality there would be some leakage around the ends of the fence, which would have some effect on the pressure distribution. A more accurate result might therefore be obtained by carrying out the modelling in 3D, however the computational time would be significantly increased, and therefore a 2D model was used. The influence of the thickness of the fence on the airflow was assumed to be negligible and therefore the fence was modelled as having zero thickness. The base of the CFD domain at inlet was defined as ‘symmetry’ up until 10 fence heights before the base of the fence, where the base was defined as a ‘wall’. The purpose of the ‘symmetry’ section of the base was that this type of boundary was a frictionless wall, and hence there was no impact on the flow passing through this section of the domain. The velocity profile at the inlet of the domain would remain the same until the ‘wall’ section was reached, when the friction of the wall changed the flow, but by minimising this section of the wall to a short distance upstream of the fence this effect was also minimised. The mesh used was structured, with a higher mesh density close to the fence and along the wall.

The mesh used is shown in Figure 4-7.

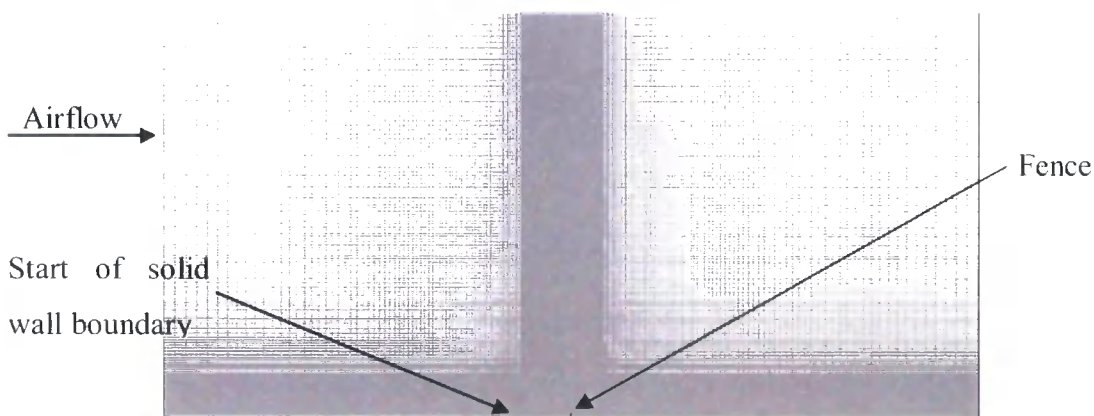


Figure 4-7 CFD Mesh

### 4.3.2 Mesh validation

#### *Boundary layer*

A boundary layer velocity profile was applied at the inlet to the domain, calculated for the appropriate length along a flat plate. The boundary layer at the position of the fence itself was compared with the input boundary layer to observe the influence of the solid base from 10 fence heights before the fence on the airflow. Because of the velocity profile applied, the calculated pressure drop across the fence includes the effects of boundary layer thickness at varying Reynolds numbers as well as the changes in dynamic pressure.

For laminar boundary layers [64] (defined as  $Re < 3 \times 10^5$ ) the boundary layer profile was calculated by first determining the thickness of the boundary layer at the appropriate position along the plate, using

$$\delta = 5.48x Re^{-0.5} \tag{4-1}$$

and then calculating the velocity profile from

$$u = u_{\infty} \left( 2 \left( \frac{z}{\delta} \right) - \left( \frac{z}{\delta} \right)^2 \right) \tag{4-2}$$

This is a good approximation when there is zero pressure gradient along the plate.

For turbulent boundary layers [65], equations 4-1 and 4-2 were revised to

$$\delta = 0.382x \operatorname{Re}^{-0.2} \tag{4-3}$$

And (for the turbulent flow above the laminar sub layer)

$$u = u_{\infty} \left( \frac{z}{\delta} \right)^{1/7} \tag{4-4}$$

where  $\delta$  is the boundary layer thickness,  $x$  is the position along the plate,  $u$  is the velocity in the boundary layer,  $u_{\infty}$  is the freestream velocity and  $z$  is the position in the boundary layer.

The comparison between the theoretical velocity profiles (which are the input into Fluent) and the velocity profiles at the fence position in Fluent are shown in Figure 4-8 and Figure 4-9.

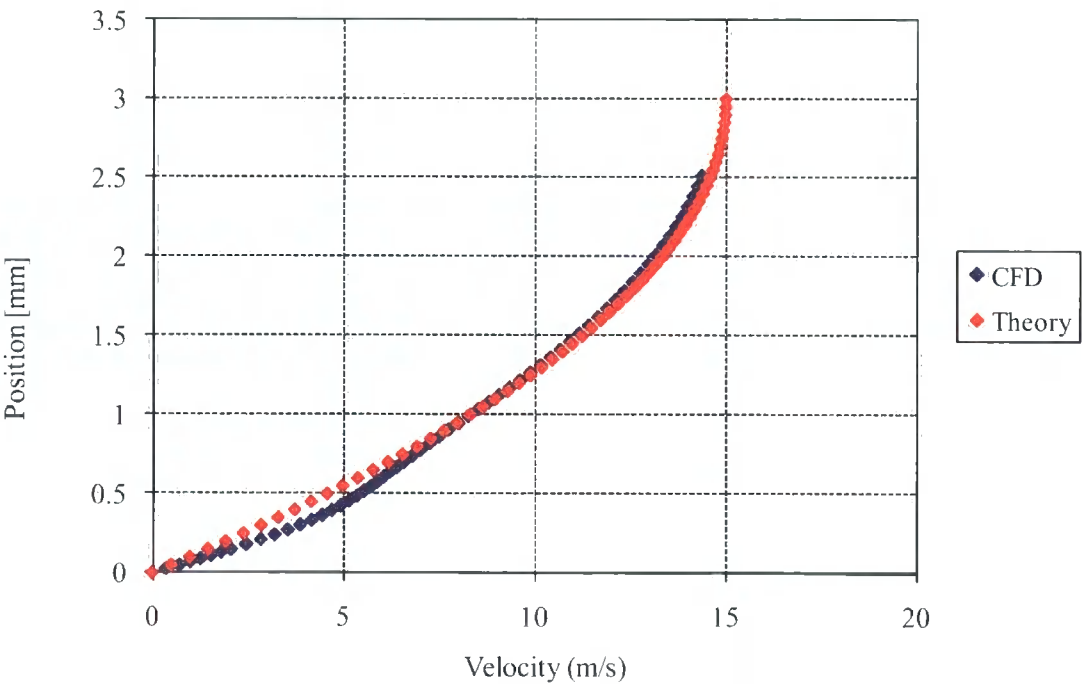


Figure 4-8. Laminar boundary layer profile

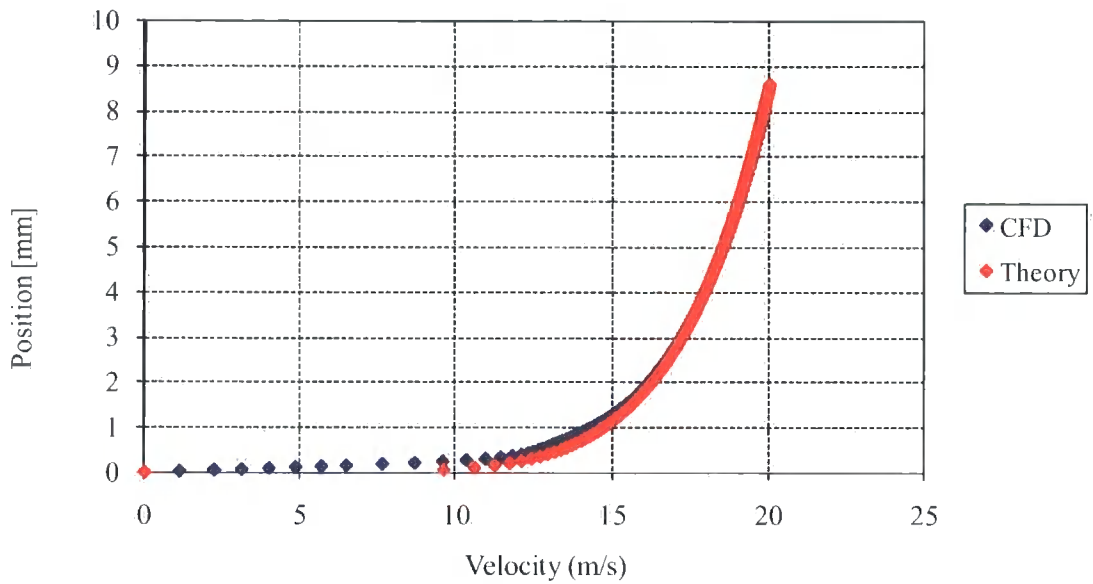


Figure 4-9. Turbulent boundary layer profile

The turbulent flow velocity decreases slightly low down in the boundary layer, as expected, due to the presence of the wall. The shape of the laminar velocity profile appears to have changed which possibly indicates the onset of transition since the test was carried out at a Reynolds number close to that where transition would be expected to occur on a flat plate.

However the differences are small and it can be seen that the boundary layer velocity profile at the fence position remains close to the velocity profile which is used as the boundary condition in Fluent. The presence of a solid boundary for ten fence heights (fence height =  $750\mu\text{m}$ ) in front of the fence does not have a significant effect on the boundary layer before it reaches the fence position.

### ***Grid dependency***

The mesh was checked to find the number of cells which would give a consistent result for the upstream and downstream static pressure. The fence height was divided into cells with the number of cells ranging from 5 to 50. The number of cells along other edges was kept proportional to the number of cells in the fence.

The static pressure drop for the varying number of cells in the fence is shown in Figure 4-10.

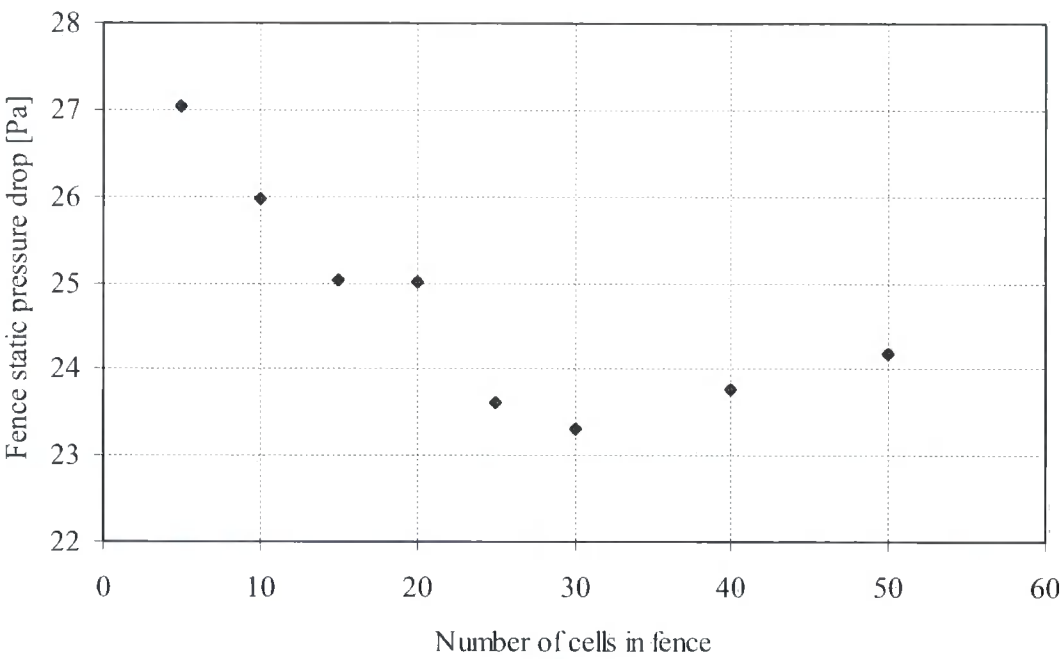


Figure 4-10. Grid dependency

It was decided that the mesh with 25 cells in the fence would be used. Results from finer meshes are within 2.4% of the value for this mesh. Using a finer mesh than this significantly increases the computation time, since the total number of cells increases with the number of cells in the fence height squared. Any errors caused by using an insufficiently fine mesh would be outweighed by those resulting from carrying out the CFD simulation in 2D and using a steady-state calculation to represent an unsteady flow.

**4.3.3 Iteration dependency**

Due to vortex shedding downstream of the fence occurring in some of the situations modelled, the influence of the number of iterations on the static pressure calculated was assessed. The average upstream and downstream static pressures on the surface of the fence were logged for each iteration.

The results of this are shown in Figure 4-11.

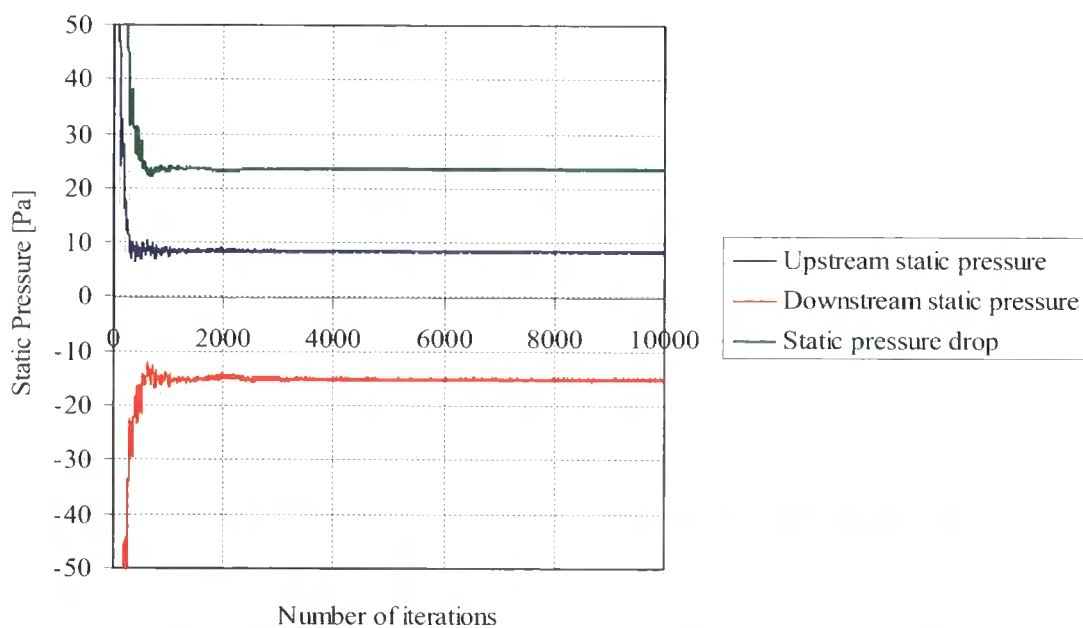


Figure 4-11. Effect of number of iterations on static pressure on fence

From the graph of the residuals (not plotted here), this run would appear to have converged at around 5000 iterations (residuals remain constant from this point), and it can be seen that there have been no significant alterations to the static pressure from approximately 1500 iterations onwards, and therefore it appears that the static pressure calculated will have reached a required degree of accuracy by the time the solution is observed to have converged from the residuals.

Figure 4-12 shows in greater detail the same run between 4500 and 5500 iterations (in the area where the solution would be considered to have converged).

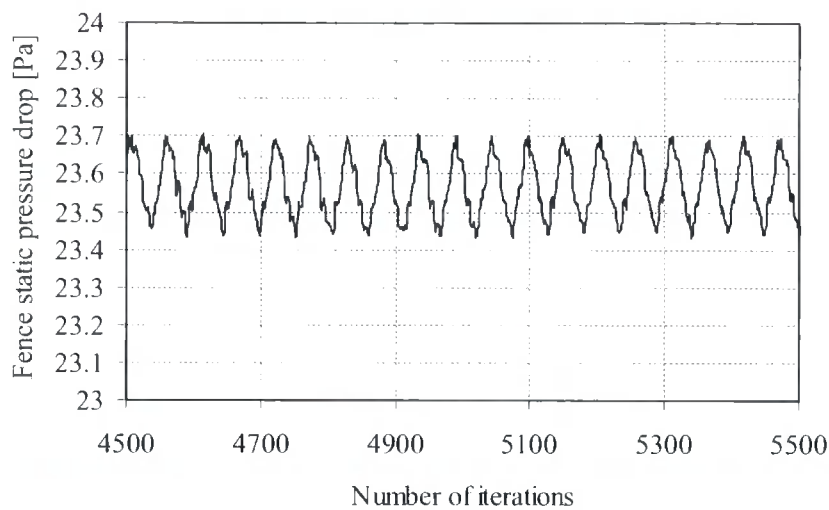


Figure 4-12. Periodic effect of vortex shedding on combined static pressure

It can be seen that there is a periodic variation in the static pressure caused by vortex shedding. However the maximum error expected from this would be just over 0.5%. The upstream and downstream static pressures individually are more influenced by the vortex shedding, but since the variations in pressure upstream and downstream are linked, the variations are to some extent compensated for when the static pressure drop is considered. The magnitude of these variations is also a function of the value of the under-relaxation factors set in Fluent, as when these factors are reduced the effect is to damp out any unsteadiness in the flow. Consequently the error being assessed here is to quantify the effect of which iteration the calculation is halted after, rather than any assessment of uncertainty in the result.

**4.3.4 CFD results**

CFD simulations were carried out for freestream velocities between 5 and 30 m/s at 5 m/s intervals.

The jet of air caused by the slot at the bottom of the fence causes an anti-clockwise recirculation zone immediately behind the fence. The velocities in this recirculation



zone are still low as the fence is within the boundary layer. This vortex is shown in Figure 4-13 for an example inlet velocity of 15 m/s.

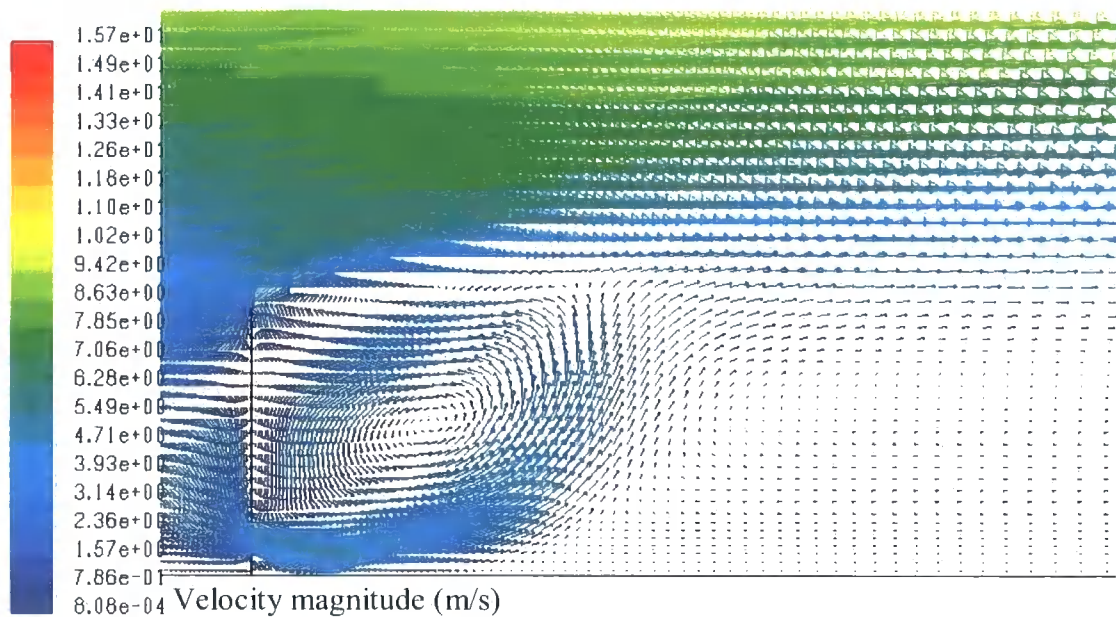


Figure 4-13. Recirculation zone behind fence caused by jetting through slot

This recirculation zone, causing an area of low pressure behind the fence, significantly increases the static pressure drop, which causes the fence to deflect, compared with the stagnation pressure alone, from where the airflow is slowed in front of the fence.

This is then followed by a series of clockwise vortices continuing downstream of the fence to the outlet of the domain, which move downstream with continuing iterations. This implies an unsteady flow caused by vortex shedding from the fence. The vortices can clearly be seen in Figure 4-14 as areas of low static pressure, separated by areas of higher static pressure where the flow reattaches. An inlet velocity of 15 m/s was used here, as in the previous figure.



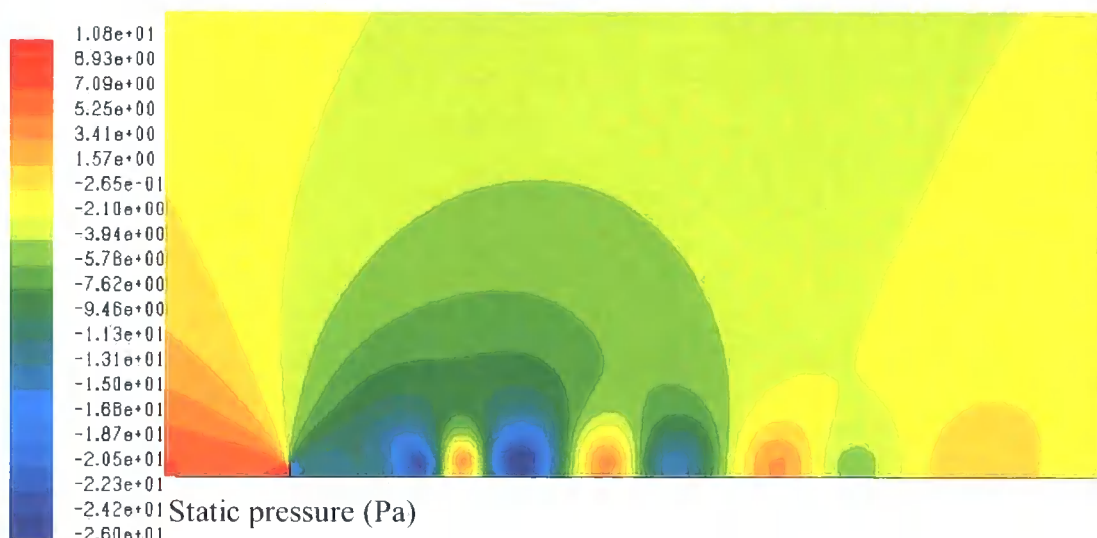


Figure 4-14 Vortex shedding downstream of fence

This vortex shedding is not present in runs at lower inlet velocities of 5 and 10 m/s, but is first visible in the test at 15 m/s. At a freestream velocity of 10 m/s, calculating the Reynolds number using the inlet velocity halfway up the fence height, and the height of the fence as the relevant length, gives  $Re = 84$ . Because the velocity is very low within the boundary layer, and the height of the fence is small, this value of  $Re$  is very small relative to many flows.

Although the sensor design is a fence, because of the slot at the base causing a jet of air underneath, the effect is that of having a flat plate normal to the flow in close proximity to a wall. Work done by Johnson et al [66] shows that at very low Reynolds numbers for flow around an elliptical cylinder, vortex shedding is not seen. Where the aspect ratio of the cylinder is zero (equating to a flat plate normal to the flow) the onset of vortex shedding is found to occur at  $Re > 30$ .

The vortex shedding from the fence with the slot occurs at  $Re > 84$ , and it is probable that this is because the proximity of the plate on which the fence is mounted damps out the vortices at lower Reynolds numbers.

Although carrying out a steady analysis of an unsteady flow introduces inaccuracies in the results, these are relatively small compared with the inaccuracies introduced by modelling the situation as a 2D problem. The use of a steady solver tends to try to damp

out any fluctuations in the flow. However, it can be seen that this has not fully happened in this case. Although iterations do not represent time steps, they have a similar effect on the output pressure drop, as can be seen by the periodicity of the iteration history in Figure 4-12. The exact pressure distribution would then vary depending on the point at which the solution was halted. However, as was previously stated, the variation in the pressure drop across the fence depending on this is  $< 0.5\%$ .

The static pressure drop across the fence is increased significantly when the boundary layer is turbulent, due to the relatively higher velocity very close to the wall for the same freestream velocity. Also, the effect of the recirculation zone behind the fence is also increased, and therefore the ratio of fence static pressure drop to freestream stagnation pressure is considerably higher in a turbulent boundary layer, which for this position of the fence on the plate is predicted with an inlet velocity of greater than 15.25 m/s. The static pressure drop for different velocities is shown in Figure 4-15. The higher pressure drop where the boundary layer is turbulent is clearly visible.

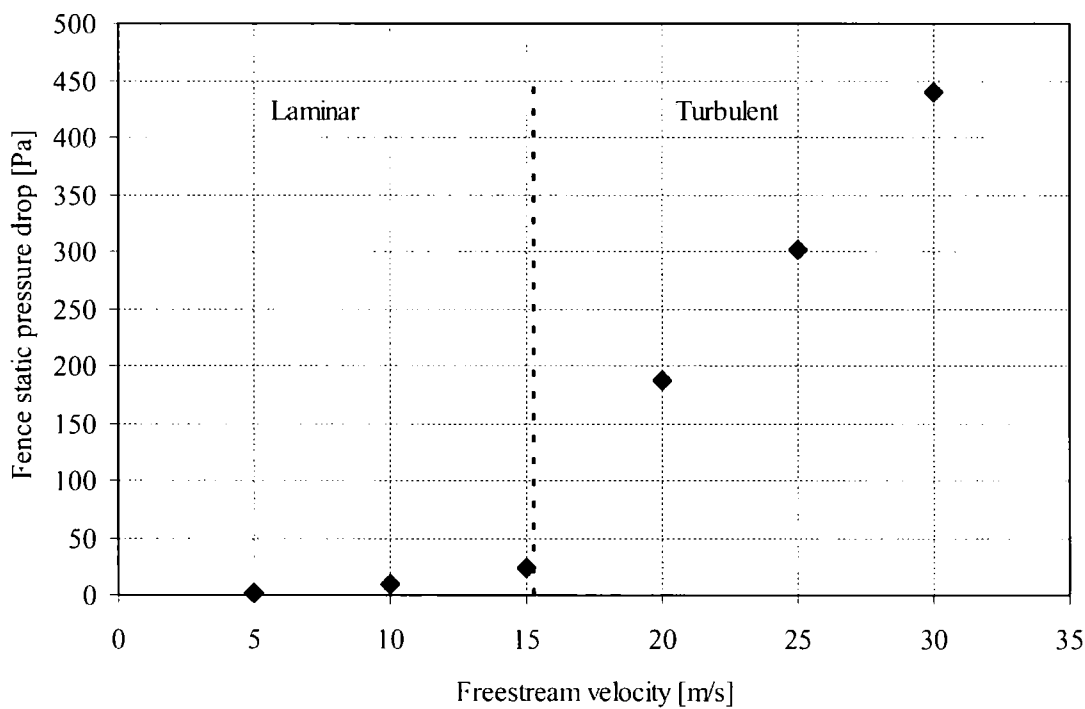


Figure 4-15. Fence static pressure drop from CFD

The effect of the laminar and turbulent boundary layers can be seen more clearly when the non-dimensional pressure coefficient and Reynolds number are plotted. Pressure coefficient  $C_P$  is defined as

$$C_p = \frac{\Delta P}{0.5 \rho u^2} \quad 4-5$$

In this case the velocity used,  $u$ , is the freestream velocity.  $P$  is the pressure and  $\rho$  is the density.

The non-dimensional values are plotted in Figure 4-16.

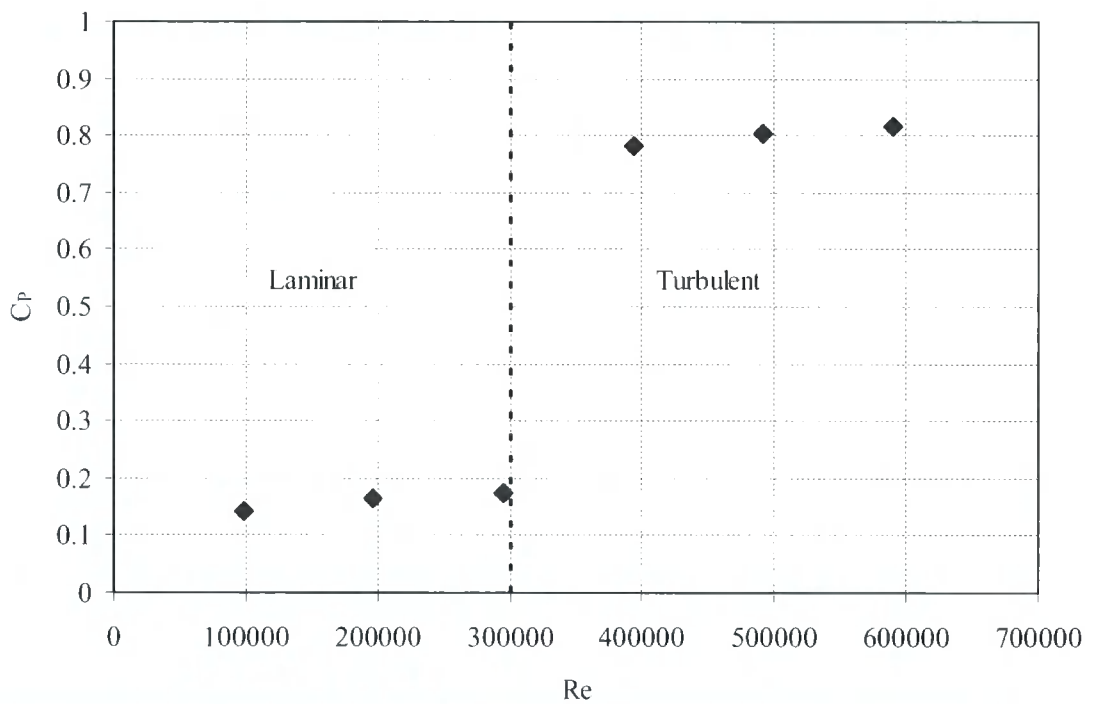


Figure 4-16 Pressure coefficient varying with Reynolds number

The Pressure coefficient increases slightly with increasing  $Re$  since the thickness of the boundary layer decreases. However, it can be seen that when the non-dimensional values are plotted the Pressure coefficient remains virtually the same within the laminar and turbulent regions.

## 4.4 FEM

### 4.4.1 Initial FEM modelling

An FEM model was created in Coventorware™, to model the deflection of the fence and the associated resistance change caused by the pressure change across the fence. The loading applied to the fence was the dynamic pressure caused by the freestream velocity of the airflow. This was used to obtain an initial estimate of the fence deflection. From the deflection of the fence in the model, it was possible to extract the strain and thus the change in resistance given the known gauge factor of gold.

The results from this analysis are shown in Figure 4-17.

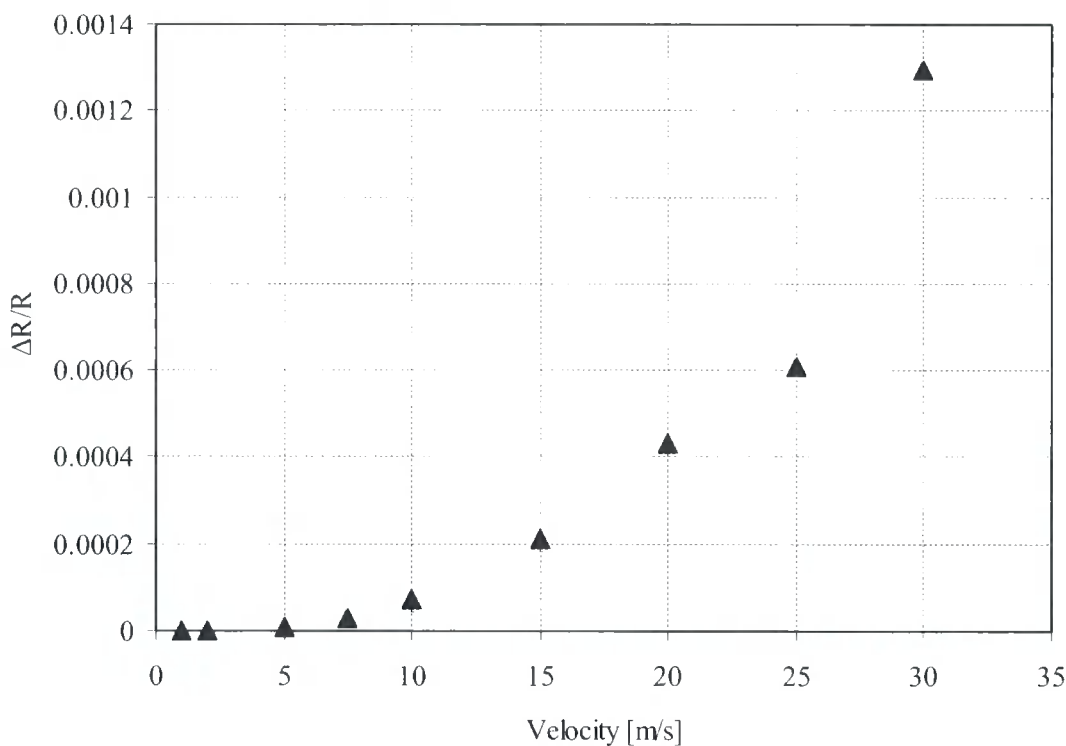


Figure 4-17. Initial FEM results

However, using the freestream dynamic pressure as the input pressure for the model does not take into account the significant reduction in the velocity of the airflow at the position of the fence within the boundary layer. The static pressure across the fence shown in Figure 4-15 is a more realistic input to the model. The static pressure drop across the fence for different velocities was therefore used as the input for the model, in

order to obtain more accurate results for the fence on a flat plate than would be achieved by using the freestream dynamic pressure.

**4.4.2 FEM results**

The modelling software does not allow a spatially varying load to be applied to the side of the fence, and therefore the average pressure calculated in Fluent was used over the whole surface of the fence. A Young’s modulus of 4.4 GPa [67, 68] was used for this modelling. This was done from 5-30 m/s at intervals of 5 m/s, as available from the CFD simulations.

***Fence displacement***

The displacement of the fence for an example freestream velocity of 15 m/s is shown in Figure 4-18. The loading applied was that calculated from the CFD results and would be predicted to be in a laminar flow, and consequently a lower pressure would be seen than in a turbulent flow, causing less of a deflection.

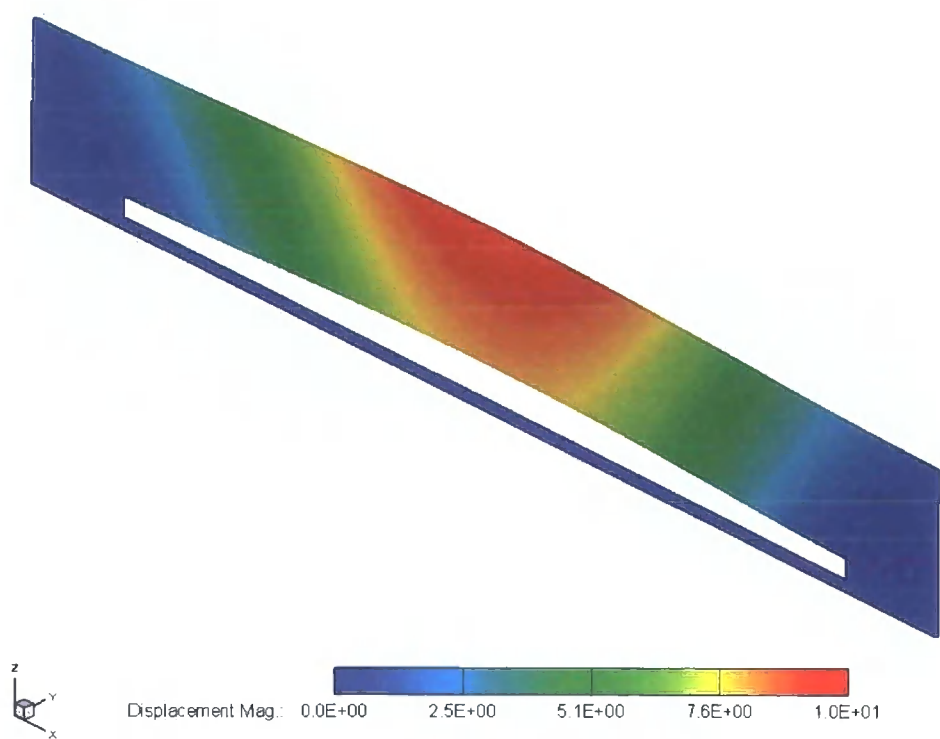


Figure 4-18. FEM results for fence with airflow of 15 m/s (Displacement magnitude in microns)

The deflection of the fence is shown increased by a factor of ten. It can be seen that there are two modes of bending taking place in the structure, as expected. There is greater deflection at the top of the fence than at the base, due to bending taking place along the vertical axis. There is also the main deflection, which is along the horizontal axis, as designed for by placing the slot at the base of the fence. The location and structure of the strain gauge is designed to measure the latter of these two modes of bending – the bending along the horizontal axis. However, it should be noted that if the pressure distribution caused by the position of the fence in the boundary layer (where the pressure is lower at the base of the fence and at a maximum at the top of the fence) were to be applied, this would increase the degree of bending along the vertical axis.

The change in resistance of the strain gauge was calculated from these results by extracting the deflection at points along the lines of the meanders of the strain gauge and calculating the increase in length of each branch of the strain gauge. From this the change in resistance could be calculated given the known gauge factor of gold. The bending along the vertical axis does not have an impact on the resistance of the strain gauge, because in this direction the fence is behaving as a cantilever, and as the strain gauge is along the neutral axis of the cantilever, the strain is zero. The results of this work are shown in Figure 4-19.

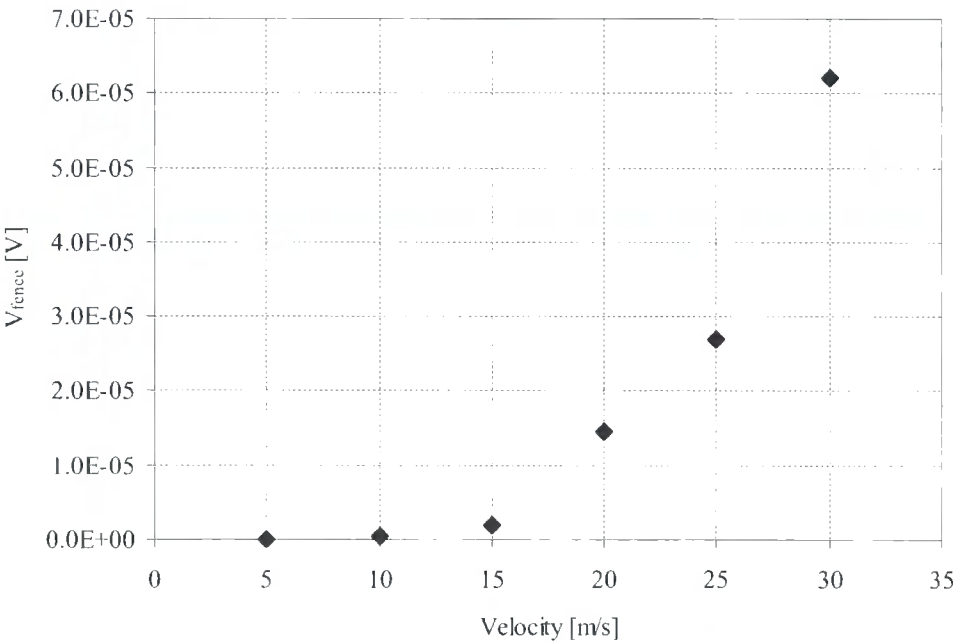


Figure 4-19. Predicted voltage output from Wheatstone bridge

It can be seen that at low velocities the response is expected to be low, while at a velocity of greater than 15.25 m/s the response of the sensor rapidly increases. This is due to the transition of the boundary layer from laminar to turbulent which causes the boundary layer to thin, and the pressure drop across the fence to increase significantly.

***Stress distributions***

The stress distribution for the same case as in Figure 4-18 is shown in Figure 4-20. It can be seen that the highest stresses are at the ends of the slots, especially at the corners, as would have been expected. A way of minimising the stresses would be to round the corners, as this would be simple to do when designing the masks for the fabrication process. This is a big advantage of MEMS fabrication since more complicated designs can be drawn on masks and then easily reproduced by photolithography without affecting the fabrication process in any way. At 30 m/s, the maximum Mises stress is found to be 17 MPa at the corners of the slot.

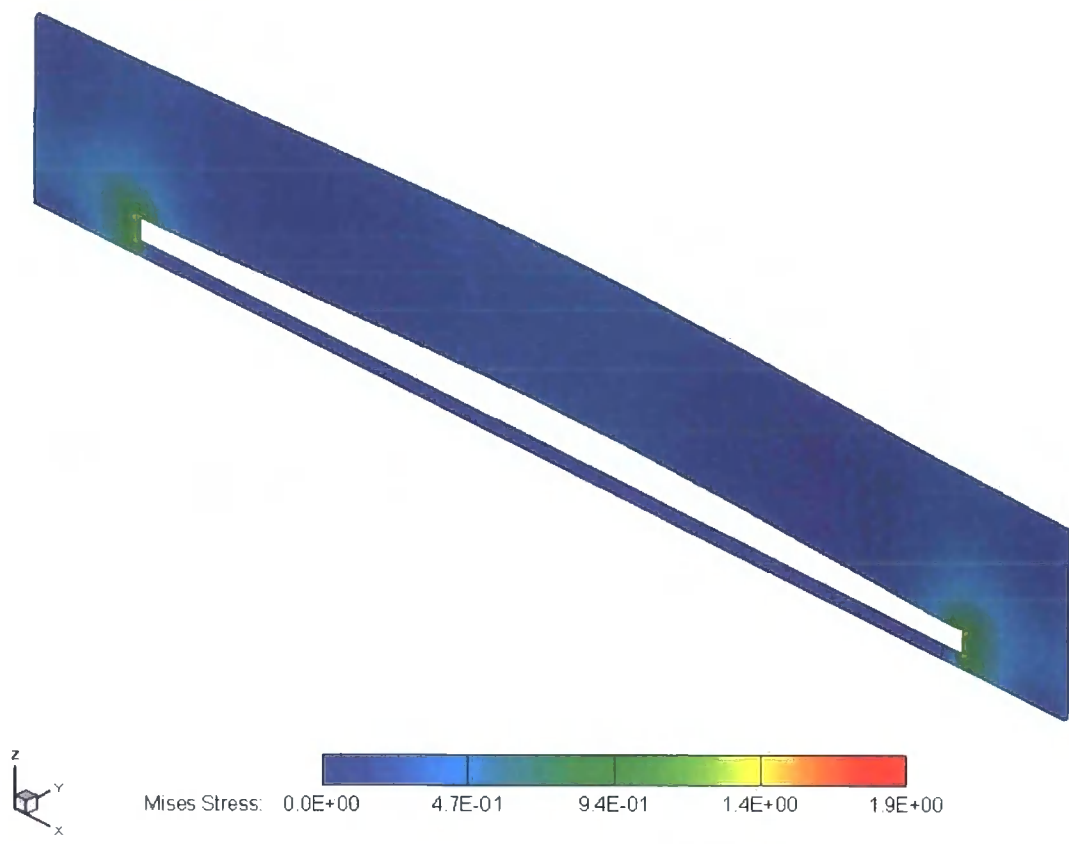


Figure 4-20. Mises stress distribution (Stress in MPa)

The failure of the fence would be difficult to predict as the mechanical properties of SU-8 are very dependent on the fabrication process. However, a failure stress of between 30-50 MPa was found by Chang et al [69] for SU-8 using a range of fabrication processes, which is significantly higher than the maximum stress found in the fence structure. It would therefore be predicted that under standard operating conditions in a wind tunnel, the fence would not come close to the point where it is likely to fail. Also the FEM will overestimate the stress at this point, since in reality a pressure distribution will occur over the surface, with a lower pressure closer to the base, which will reduce the stresses at this point low down in the height of the fence.

## 4.5 Wind tunnel testing

### 4.5.1 Wind tunnel apparatus

The fence sensor was mounted on the rectangular flat plate in the wind tunnel which is described in §3.3.1. The sensor was attached to the upstream side of a narrow slot in the plate which had a thicker piece of metal attached to it at this point with the slot through both pieces, in order to have a greater surface area to fix the sensor to. A Preston tube was mounted at the same distance along the plate (0.295 m from the leading edge), next to the sensor. The set-up is shown in Figure 4-21, where the flow direction is normal to this diagram.

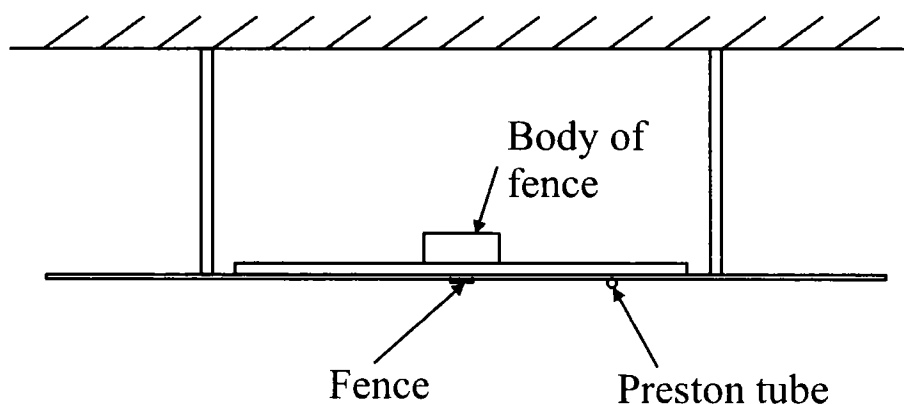


Figure 4-21. Schematic diagram of wind tunnel set-up



The side view of the wind tunnel set-up is shown in Figure 4-22.

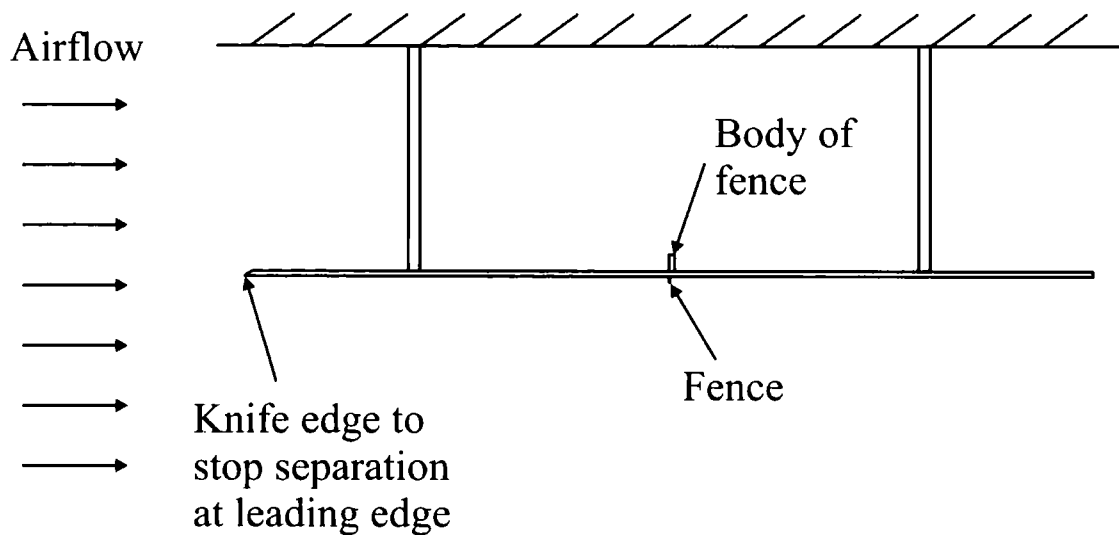


Figure 4-22 Side view of fence mounted in wind tunnel

A pitot-static tube was also mounted in the wind tunnel, upstream of the position of the sensor, but above the plate so that it did not affect the air flowing over the sensor. The pitot-static tube was connected to a pressure transducer so that the dynamic pressure could be measured. The Preston tube was connected to a second pressure transducer so that the pressure difference between this and the static pressure from the pitot-static tube could be measured.

The electrical connections to the Wheatstone bridge in the sensor were made as shown in Figure 3-10. With zero load on the fence the output voltage was expected to be zero, however slight differences in the values of the resistors caused a small offset voltage. When the fence deflected with the airflow, the fence resistance increased and therefore the output voltage also increased due to the imbalance of the bridge.

#### 4.5.2 Noise reduction

Initial tests with this set-up showed a significant amount of noise on the voltage output, and therefore an investigation was undertaken to establish the source of this noise in order to be able to minimise or eliminate it.

Carrying out a Fourier transform of the output signal with the wind tunnel switched off gave the results shown in Figure 4-23.

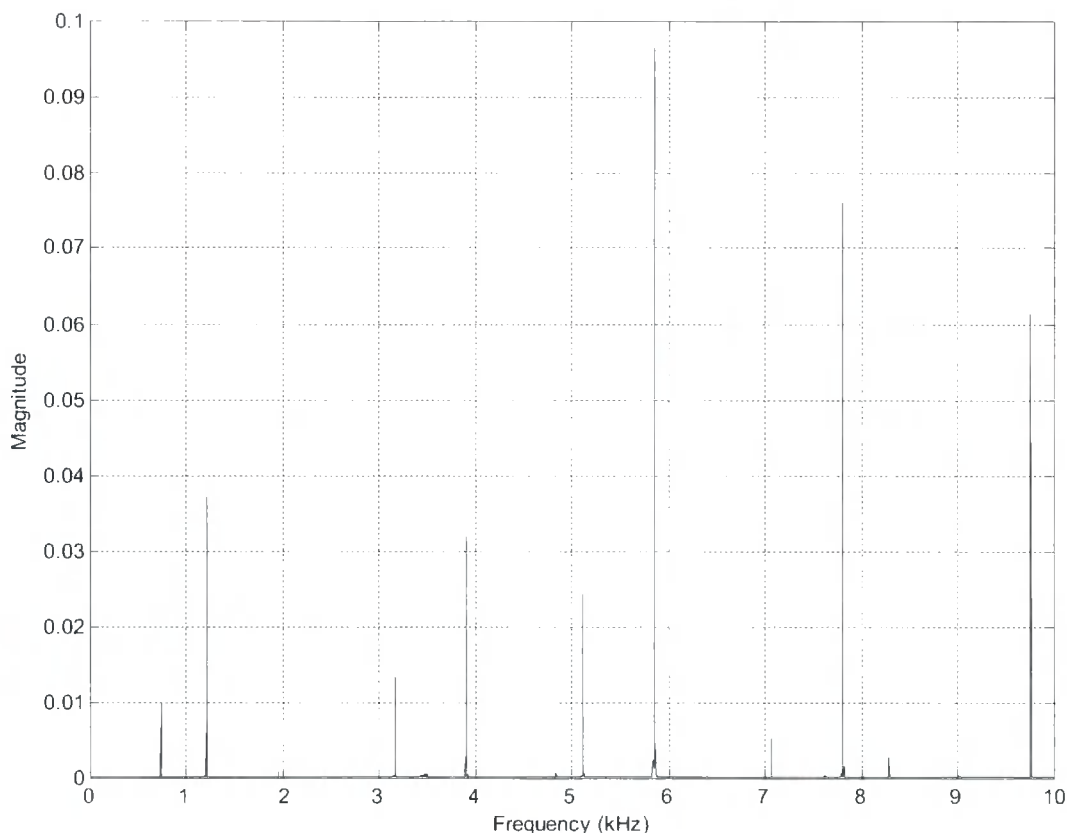


Figure 4-23. Fourier transform of initial results with zero airflow

It can be seen that the significant frequencies of the noise are all in the kHz range. The noise was therefore eliminated by using an analogue filter before the output signal went into the DAQ. The filter used was a second order lowpass filter with a cut-off frequency of 250 Hz.

Using the filter, further data was logged and it was found that the noise had largely been eliminated, except for a ripple at 50 Hz. The possibility that this was caused by the power supply was considered, but the same effect was found when the Wheatstone bridge was powered by a 1.5 V battery. It was therefore considered most likely that this noise was caused within the DAQ itself when logging, or from background 50 Hz electrical noise, and therefore would be very difficult to eradicate. Although the noise was still significant, the effect of switching the wind tunnel on and off was clearly

visible in the data despite the noise, and the noise could be disregarded by using a rolling average on the data.

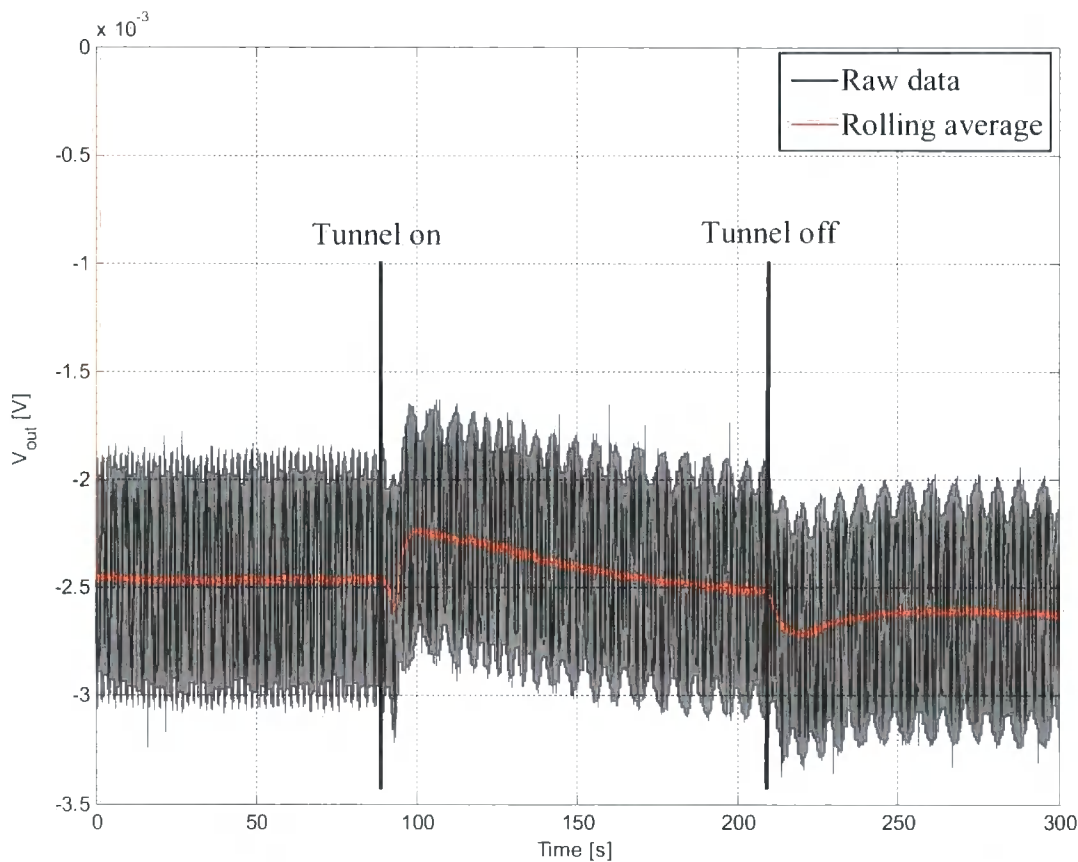


Figure 4-24. Output voltage using filter with wind tunnel on 90-210 seconds

The results from a test using the lowpass filter and turning the wind tunnel on while logging data is shown in Figure 4-24. The offset with the wind tunnel initially switched off can be seen to be approximately -2.5 mV. The response of the fence is clearly seen when the wind tunnel is switched on at 90 seconds and when it is switched off again at 210 seconds. However it is clear that there are other effects than the displacement of the fence causing the output voltage to change. Further testing was therefore carried out in order to establish the cause of the dip in the voltage output immediately after the wind tunnel is switched on, and again after the wind tunnel has been switched off, although it can be seen that this second effect takes place over a longer time period than the first.

4.5.3 Initial wind tunnel results

A series of tests were carried out at different velocities to establish the sensitivity of the device. All testing was carried out with a supply voltage of 1 V applied to the Wheatstone bridge. The behaviour seen in the previous tests was still present and indicated the presence of other significant factors aside from the deflection of the fence, which were causing a variation in the output voltage.

An example of one of these tests is shown in Figure 4-25, which shows the voltage output from the fence (left hand axis) and the voltage output from the pressure transducer connected to the pitot-static tube (right hand axis). It can be seen from the latter that the response of the wind speed in the wind tunnel is very rapid. The voltage output from the fence has a more complex response. The other factors causing the changes in the output voltage are considered most likely to be thermal responses to the airflow.

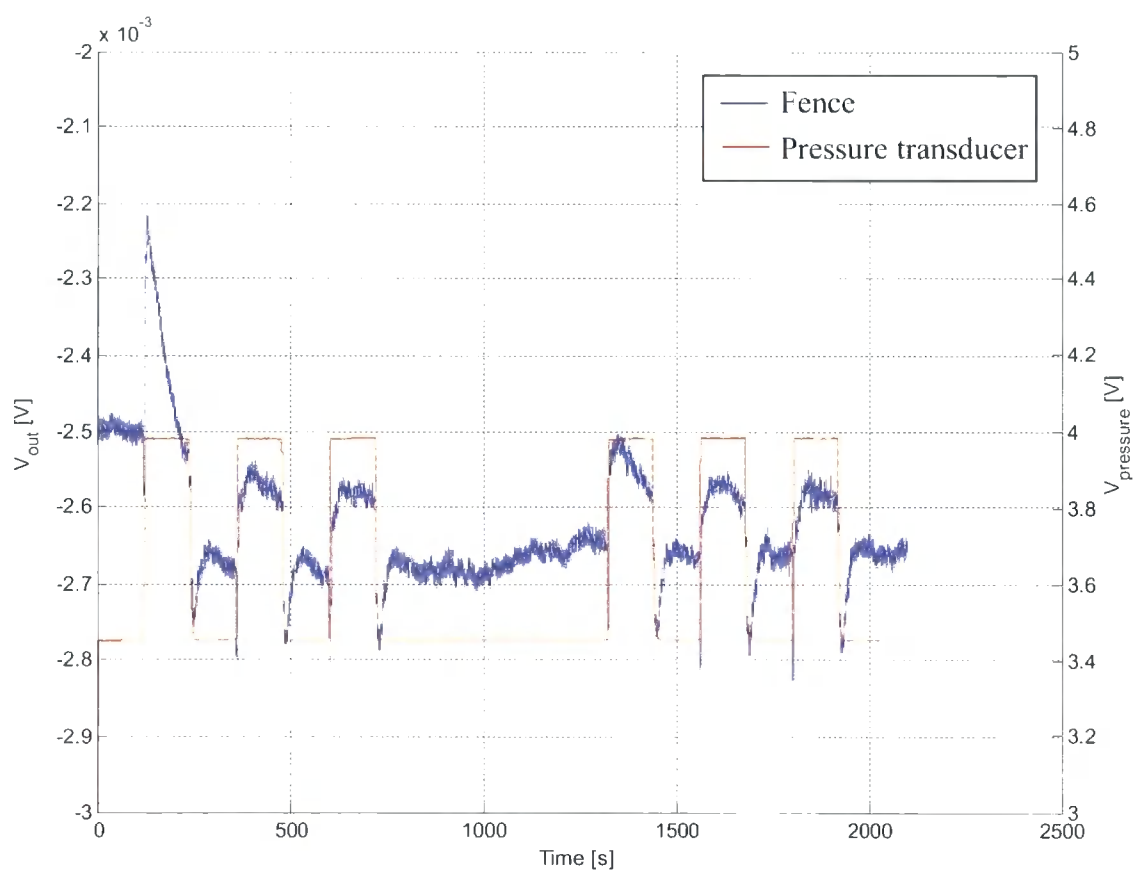


Figure 4-25. Fence voltage output and pressure transducer voltage for wind tunnel test

The current passing through the resistors will cause them to be heated to above ambient temperature and, although the power dissipated is only  $\sim 0.2$  mW, the small surface area of gold in the resistor will cause it to heat up. The work done on the air by the fan as it enters the wind tunnel will cause the air in the wind tunnel to be slightly above that of the ambient temperature. The positioning of the fence on the plate means that both the fence resistor and  $R_2$  (see Figure 3-10) are in the path of the airflow, while  $R_1$  and  $R_3$  are shielded by the plate and are also in contact with the plate.

The effect of the airflow cooling the heated fence resistor will cause a decrease in the fence resistance and therefore a reduction in the voltage output. The same would be true for the heating of  $R_1$ . Because the airflow is slightly above ambient temperature it will have a heating effect on the plate on which the sensor is mounted. This may cause heating of  $R_1$  and  $R_3$  which would have the effect of decreasing the output voltage. Combined with the fact that these resistors are partially obscured by the plate, at the least this would have the effect of decreasing the cooling effect on these resistors or increasing the time taken for the resistors to cool down.

Therefore the voltage response from the fence when the wind tunnel is turned on can be explained as:

- Initial drop caused by rapid cooling of the fence
- Rise caused by the deflection of the fence
- Slow decrease caused by cooling resistor opposite fence and slower cooling of the two other resistors due to their proximity to the plate
- Tunnel off: Rapid drop caused by return to neutral position of fence
- Slower rise due to fence and  $R_2$  heating again

The initial voltage drop caused by the cooling of the fence, which is typically  $\sim 0.15$  mV in this graph, would be caused by cooling of just 0.32 K.

When the wind tunnel is initially started at the beginning of the day, it can be seen that there is a much larger decay of the voltage output while the tunnel is on than in

subsequent tests. This is probably due to the previously mentioned effect of heating the plate on which the sensor is mounted which will have a much longer time constant than thermal changes within the sensor itself. Because the plate returning to ambient temperature will also take a much longer period of time, it has not done so between tests, and therefore this effect is not seen again during the duration of the tests.

The resistor opposite the fence will take slightly longer than the resistor in the fence itself to heat, because the layer of SU-8 surrounding it is thicker and SU-8 is not very thermally conductive.

For ease of identifying the start and end points of the change in voltage caused by the fence deflection, the drop in voltage from the return of the fence to its original position when the wind tunnel is switched off is used to define the fence sensitivity.

**4.5.4 Comparison of theoretical and experimental results**

The experimental results for the fence voltage from the wind tunnel tests, as defined in the previous section, are shown in Figure 4-26 with the results based on the CFD and FEM for comparison.

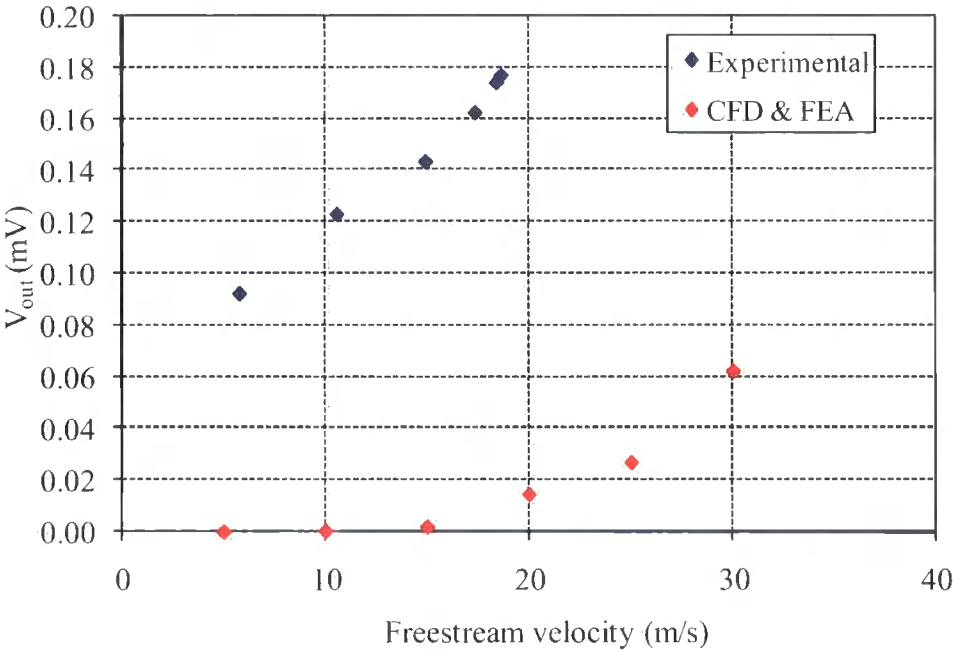


Figure 4-26. Comparison of experimental and numerically simulated results

It can be seen that the experimental results are noticeably higher than the simulated results. This is probably due in part to the Young's modulus used for the FEM modelling. A value of  $E = 4.4$  GPa was used, but the Young's modulus of SU-8 is highly process dependent as the degree of cross-linking varies depending on the UV exposure and the length of the post-bake step. The value of Young's modulus could in fact be considerably lower than the value assumed here.

Another material property which may be causing the difference in the results is the gauge factor of the gold. The bulk value of 2 has been used here, but the thin film gauge factor of gold can be very different to the bulk value [70]. Since the relationship between  $K/E$  and the output from the sensor is linear, it is possible to calculate how varying the gauge factor and Young's modulus between their maximum and minimum values, would affect the fence output. This was carried out for the data at 20 m/s, where with  $K = 2$  and  $E = 4.4$  GPa, the simulated fence output from CFD and FEA was 0.015mV. The experimental value was approximately 0.18 mV. Based on literature [68, 70, 71],  $K/E$  could vary between 0.27 and 47.73 ( $2 < K < 73.5$  and  $1.54 < E < 7.5$ ). The simulated fence output for  $K/E$  varying between these values is plotted in Figure 4-27.

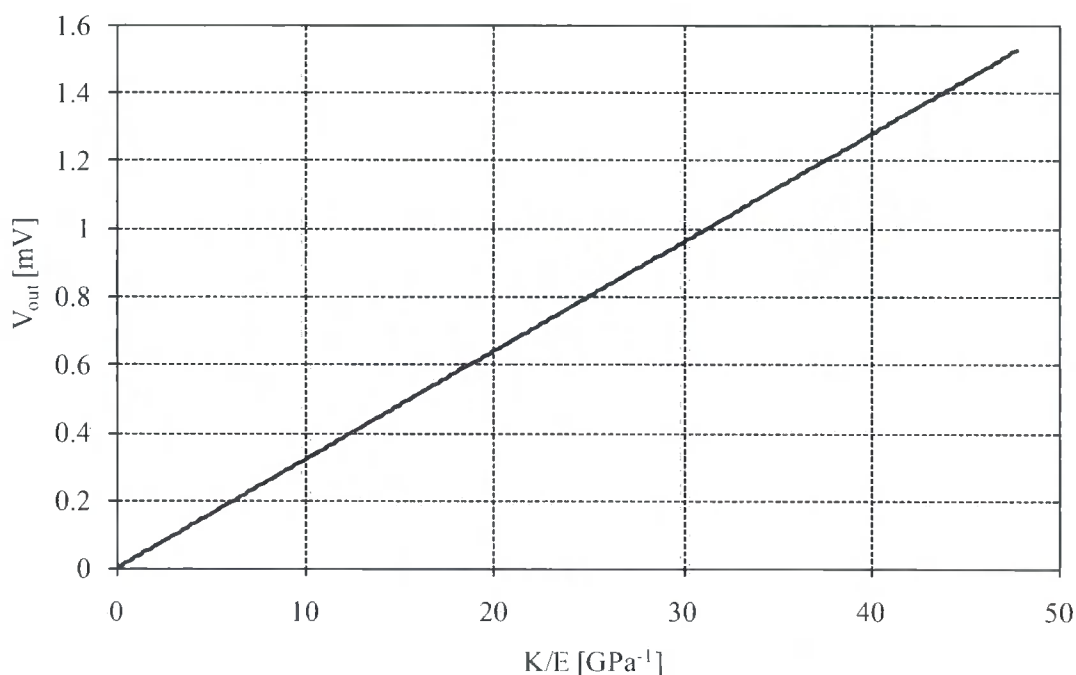


Figure 4-27 Variation of simulated fence output with  $K/E$

It can be seen that the possible values for  $K/E$  give a fence output that includes the experimental value within its range. This value (0.18 mV) occurred at the lower end of the range, with  $K/E = 5.63$ . It is likely that Young's modulus was lower than the initial value used, but that the gauge factor was not significantly higher than the bulk value used in the initial calculations and this is why the response seen was not as high as Figure 4-27 indicated was possible.

Other possible inaccuracies in the theoretical results include the average pressure distribution applied within the FEM model and that the CFD results are 2D and do not take into account the end effects where the airflow goes around the edges of the fence, although the latter would be expected to cause an overestimation of the sensitivity of the fence.

From results from the Preston tube mounted on the flat plate next to the fence sensor, it is possible to obtain the relationship between shear stress and the output voltage from the fence. This data is shown in Figure 4-28.

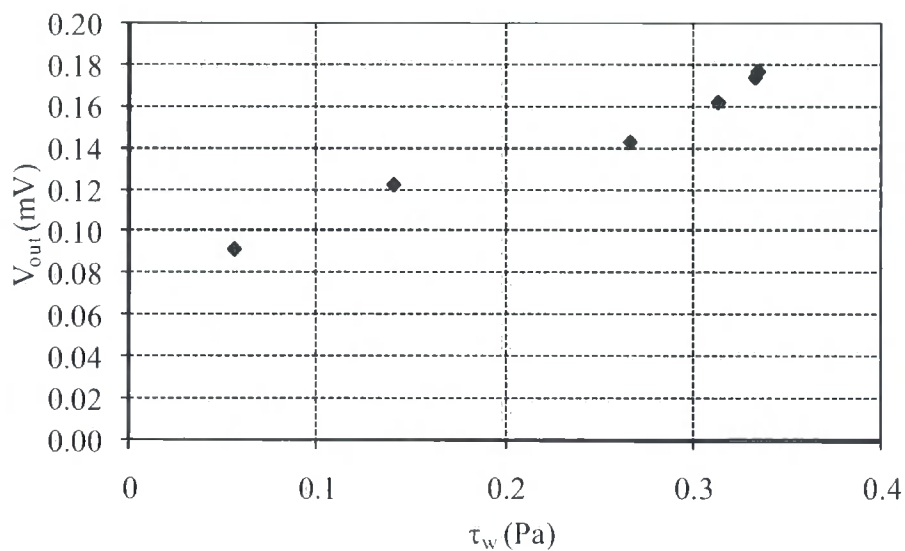


Figure 4-28 Fence voltage output as a function of shear stress

It can be seen that there is a clear relationship between the output from the fence and the wall shear stress. It does not appear that this relationship would correspond to a voltage output of zero when the shear stress is zero, as should be the case. However, the wind



tunnel being used had a minimum speed of slightly over 5 m/s and consequently it was not possible to characterise the behaviour of the fence at very low shear stresses. It would however be expected that the voltage would drop quite rapidly towards zero as the shear stress decreases, and so the behaviour of the fence would not be linear with respect to shear stress.

## **4.6 Summary**

A sensor of a fence design has been successfully fabricated and shown to allow the measurement of the aerodynamic wall shear stress on a flat plate by means of using an integrated strain gauge to measure the pressure-induced deflection.

CFD modelling carried out on this device has allowed the prediction of the pressure distribution over the fence. This modelling was carried out in 2D, and therefore does not take the end effects of the fence into account. It was found that at higher Reynolds numbers, vortex shedding from the fence takes place. This did not however have a large impact on the pressure drop across the fence, as the variation of the results with increasing iterations was found to be small. The slot at the base of the fence caused a jet of air coming underneath the fence, which caused a recirculation zone rotating in the opposite direction than the other vortices shed from the top of the fence.

The average pressure drop across the fence from the CFD was then put into an FE model as boundary conditions. This allowed the deflection of the fence, and subsequently the expected change in voltage of the fence, to be modelled, when airflow was applied.

The sensor was then tested in a wind tunnel in order to validate the numerically modelled results. There was found to be a high level of noise on the voltage output signal from the Wheatstone bridge initially, but this was reduced by means of an analogue filter, and then sampling the data at a high frequency and using a rolling average. Thermal effects were found to have a major impact on the output voltage from the fence in addition to the fence deflection.

It was found that the experimental results showed a significantly greater sensitivity than the modelling had suggested would be the case. The most likely main reasons for this were inaccuracies in the values of Young's modulus and gauge factor used in the modelling, and by varying these values within the bounds of the ranges seen in literature, a value closer to that seen by experimental testing could be obtained. The true values of Young's modulus and gauge factor could be measured experimentally so that more accurate results could be obtained.

Because of the thermal effects present in the output voltage, the post-processing of the wind tunnel data is relatively complex and therefore it is likely that this also leads to some inaccuracy in the experimental results.

A number of areas remain unresolved with the current fence design. Further investigation into the thermal transients could establish the validity of the assumptions made about the reasons for the voltage response from the fence during testing.

The fence design that was tested is limited by the necessity of having the body of the sensor within the model that is being tested. Furthermore, the sensitivity of the device would be severely diminished by reducing the dimensions of the sensor. Reducing the sensor to a smaller size would be very desirable as the sensor is currently relatively large within the boundary layer.

Increasing the sensitivity in order to make the thermal effects less pronounced would be advantageous. Also, finding better ways to minimise the thermal effects would be helpful. Increasing the sensitivity would also be a great advantage to separate the deflection effect from background noise. The thermal effects on resistance of the heating and cooling of the gold resistor in the fence could be reduced by using a metal with a lower thermal coefficient of resistivity, such as nichrome. This is a favoured metal for the fabrication of strain gauges for this reason and also because the gauge factor is relatively high for a metal, being 2.2, compared with the value of 2 for gold. This means that using this metal would also increase the sensitivity of the device.

# **Chapter 5**

## **Cantilever-style sensor for wall shear stress measurement**

A new generation of shear stress sensors was developed to build on the sensor described in the previous chapter. This used an in-plane cantilever with integrated strain gauge to measure the wall shear stress. The sensor was modelled using CFD and FEA and also tested in a wind tunnel. Several different geometries of sensor were tested.

### **5.1 Theory of operation**

The fence design of sensor had a number of limitations associated with it. These included:

- Necessity of mounting the sensor within the wall
- Thermal sensitivity

- Changing geometry for increased sensitivity (by making the fence taller) would increase the impact on the flow

These considerations were therefore addressed when designing a second generation of wall shear stress sensors. The mounting considerations made it necessary to completely redesign the sensor using a different approach to measuring the shear stress so that it could be entirely surface-mounted. This new method of measuring shear stress also needed to minimise the impact on the flow, while increasing the sensitivity of the sensor.

As far as possible it was intended that the fabrication methods for the new sensor would remain as for the production of the fence sensors in order to capitalise on the expertise that had been built up. The sensor was therefore designed to be made from SU-8 as before with a metal strain gauge. However, the metal that was used for this second generation of sensors was nichrome, as not only does this have a higher gauge factor than the gold previously being used, but it also has a much lower thermal coefficient of resistivity which should minimise the thermal sensitivity of the sensor.

It was therefore decided that using a cantilever design as in Figure 5-1 instead of a fence would increase the sensitivity, because a cantilever has a much greater tip deflection for the same applied force than a fence, which is effectively a beam with fixed ends deflecting in the middle (§3.5.1, Equations (3-15) and (3-16)). Using a cantilever would also allow the sensor to be mounted on the surface to be measured, with the cantilever parallel to the surface. This would mean that the sensor also protruded less into the flow, causing less interference.

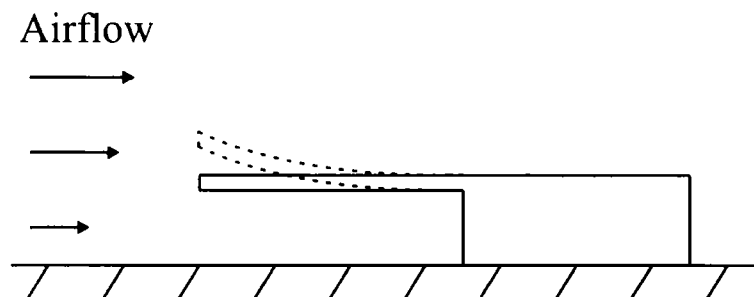


Figure 5-1. In-plane cantilever design of sensor

The airflow under the cantilever would reach close to stagnation pressure as the velocity is slowed to near zero. The reason that the pressure would be likely to be slightly less than stagnation pressure is because the air would leak around the edges of the cantilever due to the narrow width of the structure.

The flow would therefore cause the cantilever to deflect upwards, due to the high pressure under the cantilever, and lower pressure above it. This sensor could be constructed from an SU-8/metal combination with a strain gauge positioned at the root of the cantilever to measure directly the deflection of the cantilever caused by the pressure drop.

The deflection of the cantilever would cause it to occupy a position higher in the boundary layer than when there is no airflow passing over the cantilever. This would cause it to see a greater pressure, which is destabilising, and consequently would cause the cantilever to deflect further. The sensor would reach an equilibrium position where the elastic forces within the cantilever itself would be equal to the forces applied by the airflow.

The advantage of this design of sensor is the capacity to increase the sensitivity without a detrimental effect on the spatial resolution or causing a greater disruption to the airflow. The fence design has a limited sensitivity as it is fixed at both ends. Increasing sensitivity could be achieved by using an artificial haircell configuration [28], which is in effect a cantilever normal to the airflow. However increased sensitivity for this design requires a longer cantilever, which would cause greater disruption to the airflow and come at the expense of spatial resolution. An in-plane cantilever, when lengthened to increase the sensitivity, would cause a minimal increase in the wall-normal dimension. The increase in the axial dimension causes less of a problem, as the velocity gradients in the flow in this stream-wise direction will be lowest. This design of sensor also has the collateral advantage of being easier to mount on a surface without requiring a hole to be made.

## **5.2 Device design and fabrication**

### **5.2.1 Device design**

The sensor was designed to have a similar fabrication process as that which was used to create the fence sensors. A thin layer of SU-8 was used for the cantilever itself with a thick layer of the same material for the body of the sensor (which suspended the cantilever and where the Wheatstone bridge was contained), and a thin film nichrome strain gauge.

It was decided that the probability of debris in the airflow damaging the resistors on the sensor was low, and therefore only one layer of SU-8 was used in the cantilever rather than having a second layer to encapsulate the metal. In this case, if the metal lay in the centre of the two layers, it would be on the neutral axis and therefore there would be no strain. One of the advantages of only using one layer therefore is that the distance of the strain gauge from the neutral axis is maximised, thereby maximising the sensitivity of the sensor. Another advantage is decreasing the number of layers and processes required in order to fabricate the sensors, which decreases the likelihood of defects on the substrate and therefore increases the yield.

Creating a cantilever structure by MEMS fabrication can be a complicated process because of the necessity of having a sacrificial layer under the cantilever that must be removed in order to free the structure when it is fabricated in its final orientation. In order to avoid this problem it was decided to fabricate the cantilevers inverted, so that, once released from the handle wafer, they could be turned over to create the overhanging cantilever structure. The disadvantage of this method is that it makes accessing the contact pads for the Wheatstone bridge more challenging. It was decided that the previous method of having to break a covering layer of SU-8 to gain access to the contact pads was unsatisfactory, and since the cantilever was to be inverted after release the contact pads would have to be fabricated as the bottom layer of the structure during the fabrication process. It was found however that having the nichrome as the bottom layer of the structure was not possible as the adhesion between this metal and SU-8 is not sufficiently good to allow the release of the structures without damage to

the resistors. Consequently the sensors were fabricated such that the thin layer of SU-8 was the initial layer. The contact pads were left as holes in this layer of SU-8 so that when the nichrome layer was deposited over the top, in this area only the nichrome is the bottom layer, but because this is a smaller area, it was still possible to release the structures without damage.

A side view of the cantilever as fabricated is shown in Figure 5-2.

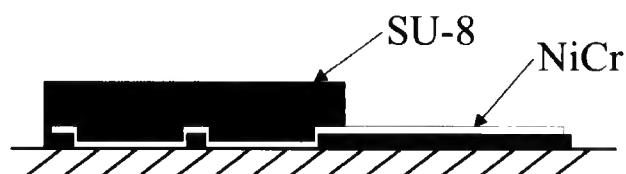


Figure 5-2 Side view of cantilever as fabricated

However, this meant that the nichrome was required to cover a step in the SU-8, which made the deposition and etching of the metal more difficult. The nichrome was sputter deposited, as the alloy could be deposited from a target of the correct composition (80:20 nickel:chromium) without one metal being deposited preferentially, as would be the case with an evaporative method. The other advantage of this method was that because of the relatively short mean free path of the atoms the sidewall coverage was greatly improved over evaporation (Figure 3-4). Altering the pressure at which the deposition was done could change the degree of sidewall coverage if necessary. It was therefore found to be possible to obtain the necessary degree of coverage of the sidewalls in order to achieve electrical contact between the contact pads and the resistors, which are on top of the initial layer of SU-8.

The cantilever was designed with three different lengths and two different widths in order to ascertain the effect of both of these parameters on the sensitivity. The lengths were 2, 3 and 4 mm and the widths were 400 and 600  $\mu\text{m}$ . The thickness of the cantilever was 12  $\mu\text{m}$ . It should be noted that this meant that the longest cantilever had an aspect ratio (length/thickness) of 333, which would be unachievable in the macroscopic world. The strain gauge in the cantilever had a track width of 40  $\mu\text{m}$  and the gap between each loop of the resistor was 20  $\mu\text{m}$ . The track width was increased

compared with those in the fence sensor in order to compensate for any undercutting of the metal when etching, so that the resistors were less likely to be affected by any defects in the masks or photoresist.

A plan view of a 3 mm long, 400  $\mu\text{m}$  wide cantilever sensor is shown in Figure 5-3.

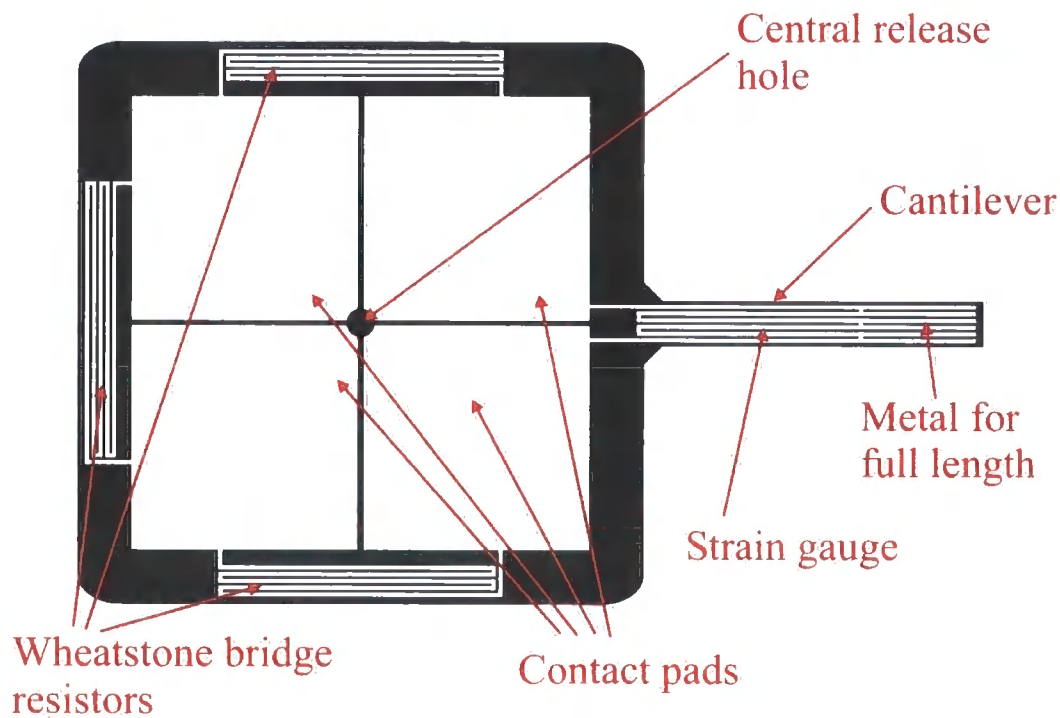


Figure 5-3 Plan view of cantilever sensor

The body of the sensor was 5 mm square. This contained four 2 mm square contact pads and the three remaining resistors of the Wheatstone bridge. Unlike the design of the fence sensor, the design of these three resistors was not identical to that in the cantilever. To make them identical was spatially inefficient and would have required a significantly larger body to the device, which would make it harder to mount and more intrusive to the airflow. Consequently the design of the resistors was changed, however they were redesigned so that not only was the length of resistors the same, but so was the number of right-angled bends, in order to ensure as far as possible that the component values of the resistors in both the body and cantilever were the same. Variations in the metal film that was deposited over the surface of the substrate were



therefore more likely to contribute to variations in the resistance than differences in the design.

The thickness of the thick layer of SU-8 was nominally 100  $\mu\text{m}$ , and this was the layer which was responsible for the suspension of the cantilever above the wall. The thickness of this layer is then equal to the gap between the cantilever and the surface on which it is mounted. A side view of the cantilever once released and inverted is shown in Figure 5-4.

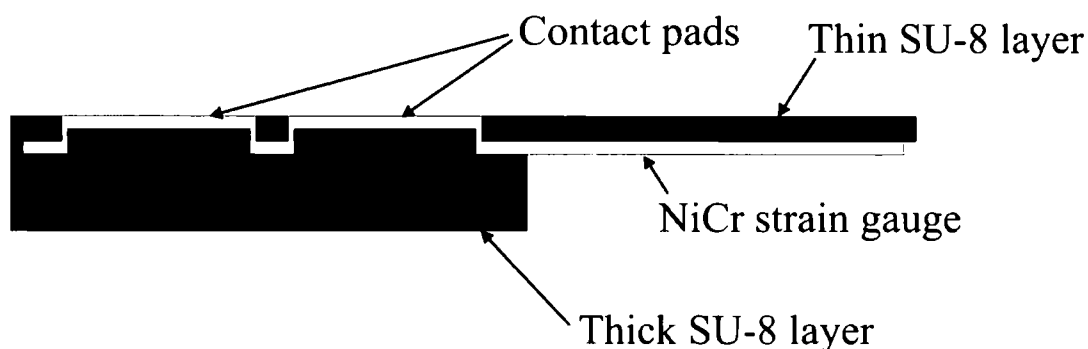


Figure 5-4 Side view of cantilever sensor inverted for use

### 5.2.2 Resistor length

The effect of the resistor length on the cantilever sensitivity and the error (or noise) due to thermal effects was investigated in order to determine whether the meander resistor should be continued for the whole of the cantilever length. As the majority of the stress in the cantilever is near the root, it was thought that the effect of increasing the length of the resistor to the full length of the cantilever would have only a small effect on the response of the Wheatstone bridge, but would have a detrimental effect on the signal-to-noise ratio. The effect of the length of the resistor was therefore analysed along with the effect of other parameters in order to obtain the optimum design of cantilever for maximising the signal and minimising noise.

A diagram of the cantilever sensor is shown in Figure 5-5.

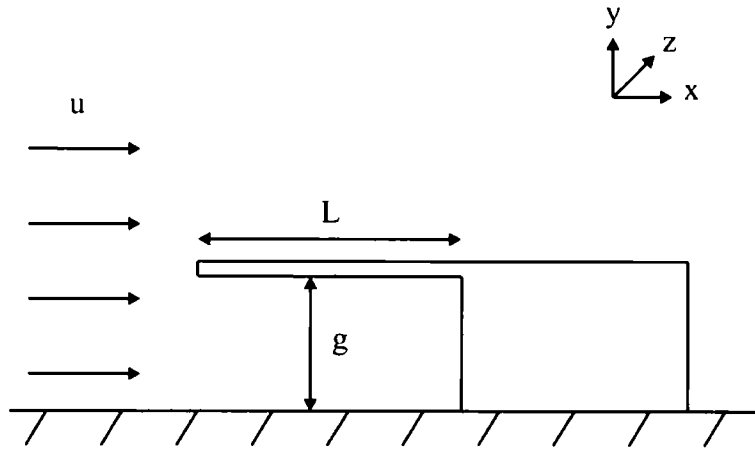


Figure 5-5 Cantilever sensor

The pressure on the underside of the cantilever can be approximated by assuming that the airflow is at stagnation pressure under the cantilever (taking the local static pressure as zero). Thus

$$P = \frac{1}{2} \rho u^2 \quad 5-1$$

where  $P$  is the pressure acting on the cantilever,  $\rho$  is the air density and  $u$  is the velocity of the flow.

If the gap under the cantilever is defined as  $g$ , then the velocity halfway up this gap is given by

$$u = \frac{du}{dy} \frac{g}{2} \quad 5-2$$

where  $du/dy$  is the velocity gradient. This gradient is assumed to be a constant since it is in the near wall region.

Shear stress is given by

$$\tau = \mu \frac{du}{dy} \quad 5-3$$

where  $\tau$  is the wall shear stress and  $\mu$  is the dynamic viscosity of air.

Therefore the local velocity can be defined as a function of the shear stress:

$$u = \frac{\tau g}{2\mu} \quad 5-4$$

which can be substituted into equation (5-1) to give the pressure difference between the top and bottom of the cantilever as

$$P = \frac{1/2 \rho \tau^2 g^2}{4\mu^2} = \frac{\rho \tau^2 g^2}{8\mu^2} \quad 5-5$$

assuming that the pressure on top of the cantilever is equal to static pressure, i.e. a lift coefficient of 1. If the cantilever were inclined relative to the flow, the incidence angle would mean that the pressure on the top surface of the cantilever would be lower than static pressure.

The voltage output from the Wheatstone bridge (shown in Figure 3-10) can be calculated from

$$V = V_s \left( \frac{R_x}{R_x + R_3} - \frac{R_2}{R_1 + R_2} \right) \quad 5-6$$

where  $V$  is the output voltage from the bridge,  $V_s$  is the supply voltage and  $R$  is the resistance of the resistors in the bridge, with  $R_x$  denoting the cantilever strain gauge.

Since in this case  $R_1 = R_2 = R_3 = R$  and  $R_x = R + \Delta R$ , then

$$V_0 + \Delta V = V_s \left( \frac{R + \Delta R}{R + \Delta R + R} - \frac{R}{R + R} \right) \quad 5-7$$

which since  $\Delta R \ll R$  and  $V_0$  (the output voltage when  $\Delta R = 0$ ) is zero when the bridge is balanced can be simplified to give

$$\Delta V = \frac{V_s \Delta R}{2R} \quad 5-8$$

The change in the resistance caused by the thermal heating of the resistor is given by

$$\Delta R_T = \alpha \cdot \Delta T \cdot R \quad 5-9$$

where  $\alpha$  is the thermal coefficient of resistivity and  $\Delta T$  is the temperature rise above ambient temperature.

The power dissipation in the resistor is

$$\frac{\left(\frac{V_s}{2}\right)^2}{R} = x_0 \cdot b \cdot \Delta T \cdot h \quad 5-10$$

where  $x_0$  is the gauge length,  $b$  is the width of the cantilever and  $h$  is the heat transfer coefficient.

This is based on a series of assumptions:

- There is no conduction of heat through the mounting
- All convection takes place from the top surface of the cantilever (much higher velocity above cantilever than below it)
- The SU-8 and NiCr in the resistor region of the cantilever are the same temperature (good conduction across width of cantilever as most of surface covered, and good conduction through thickness of cantilever)
- Convection takes place from the region of the cantilever containing the resistor and not the full length (heat loss through convection preferentially over conduction along length of cantilever)

This rearranges to give

$$V_s = 2\sqrt{\Delta T R x_0 b h} \quad 5-11$$

and since the resistance can be approximated as

$$R = n x_0 \beta \quad 5-12$$

where  $n$  is the number of parallel wires in the strain gauge and  $\beta$  is the resistance/ unit length.

This can then be substituted into equation (5-11) to give

$$V_s = 2x_0 \sqrt{\Delta T n \beta b h} \quad 5-13$$

and hence, substituting into equation (5-8), the change in the voltage output of the sensor caused by the resistive heating is given by

$$\Delta V_T = \frac{V_s \Delta R_T}{2R} = \frac{2x_0 \sqrt{\Delta T n \beta b h} \cdot \alpha \Delta T R}{2R} \quad 5-14$$

which simplifies to

$$\Delta V_T = \alpha x_0 \sqrt{n \beta b h} \Delta T^{3/2} \quad 5-15$$

The change in resistance caused by the deflection of the cantilever can be expressed as

$$\Delta R_p = R \varepsilon K \quad 5-16$$

where  $\varepsilon$  is strain and  $K$  is the gauge factor.

Strain is defined as

$$\varepsilon = \frac{\sigma}{E} \quad 5-17$$

where  $\sigma$  is stress and  $E$  is the Young's modulus.

Stress at the strain gauge is defined as

$$\sigma = \frac{My}{I} \quad 5-18$$

where  $M$  is the moment acting on the cantilever,  $y$  is the distance of the gauge from the neutral axis and  $I$  is the second moment of area.



Thus the strain can be given as

$$\varepsilon = \frac{My}{EI} \quad 5-19$$

The moment on the cantilever can be defined as

$$M(x_1) = bP \int_{x_1}^L x dx \quad 5-20$$

where  $L$  is the cantilever length.

This gives

$$M(x_1) = \frac{bP}{2} (L^2 - x_1^2) \quad 5-21$$

So the change in resistance is given by

$$\Delta R_p = \frac{RK}{x_0} \int_0^{x_0} \varepsilon dx = \frac{RK}{x_0} \int_0^{x_0} \frac{My}{EI} dx \quad 5-22$$

This then gives

$$\Delta R_p = \frac{RKybP}{2EIx_0} \left[ L^2 \int_0^{x_0} dx - \int_0^{x_0} x^2 dx \right] \quad 5-23$$

which becomes

$$\Delta R_p = \frac{RKybP}{2EIx_0} \left( L^2 x_0 - \frac{x_0^3}{3} \right) \quad 5-24$$

and therefore

$$\Delta R_p = \frac{RKybP}{2EI} \left( L^2 - \frac{x_0^2}{3} \right) \quad 5-25$$

This can then be substituted into (5-8) to give

$$\Delta V_p = \frac{V_s R K y b P}{4 E I} \left( L^2 - \frac{x_0^2}{3} \right) \quad 5-26$$

which becomes

$$\Delta V_p = \frac{V_s K y b P}{4 E I} \left( L^2 - \frac{x_0^2}{3} \right) \quad 5-27$$

Substituting for  $P$  from (5-5) gives

$$\Delta V_p = \frac{V_s K y b \rho \tau^2 g^2}{32 E I \mu^2} \left( L^2 - \frac{x_0^2}{3} \right) \quad 5-28$$

And then substituting for  $V_s$  from (5-11)

$$\Delta V_p = \frac{\sqrt{\Delta T R x_0 h} K y b^{\frac{3}{2}} \rho \tau^2 g^2}{16 E I \mu^2} \left( L^2 - \frac{x_0^2}{3} \right) \quad 5-29$$

And substitute for  $R$  from (5-12)

$$\Delta V_p = \frac{\sqrt{\Delta T n \beta h x_0} K y b^{\frac{3}{2}} \rho \tau^2 g^2}{16 E I \mu^2} \left( L^2 - \frac{x_0^2}{3} \right) \quad 5-30$$

So therefore, to obtain the signal to noise ratio

$$\frac{\Delta V_p}{\Delta V_T} = \frac{\sqrt{\Delta T n \beta h x_0} K y b^{\frac{3}{2}} \rho \tau^2 g^2 \left( L^2 - \frac{x_0^2}{3} \right)}{16 E I \mu^2 \alpha x_0 \sqrt{n \beta b h \Delta T}^{\frac{3}{2}}} \quad 5-31$$

Which reduces to

$$\frac{\Delta V_p}{\Delta V_T} = \frac{K y b \rho \tau^2 g^2}{16 E I \mu^2 \alpha \Delta T} \left( L^2 - \frac{x_0^2}{3} \right) \quad 5-32$$

This, in the case that the resistor continues to the end of the cantilever becomes

$$\frac{\Delta V_P}{\Delta V_T} = \frac{Ky b \rho \tau^2 g^2 L^2}{24 E I \mu^2 \alpha \Delta T}$$
5-33

This is the signal to noise ratio, where the noise is caused by thermal heating effects in the resistor. It can be seen therefore from (5-30), that the level of the signal and the signal-to-noise ratio is improved by increasing the gauge factor of the metal used, the distance from the neutral axis and decreasing the Young’s modulus and second moment of area of the cantilever. Increasing the gap between the cantilever and the wall, the length of the cantilever and the width of the cantilever also improves both of these criteria, but at the cost of spatial resolution. Increasing the temperature rise above ambient (ie the voltage input to the bridge) and the length of the strain gauge increases the sensitivity but decreases the signal-to-noise ratio. Increasing the number of loops in the strain gauge, the resistance/unit length and heat transfer coefficient have a beneficial effect on the sensitivity and have no impact on the signal-to-noise ratio. The other variables affecting the signal-to-noise ratio are dictated either by the fluid or the application.

The effects of these variables are shown in Table 5-1.

Variable	Sensitivity	Signal-to-Noise	Spatial resolution
K	↑	↑	-
y	↑	↑	-
E	↓	↓	-
I	↓	↓	-
g	↑	↑	↓
L	↑	↑	↓
w	↑	↑	↓
V <sub>s</sub>	↑	↓	-
x <sub>0</sub>	↑	↓	-
n	↑	-	-
β	↑	-	-
h	↑	-	-

Table 5-1 Effect of altering variables on sensitivity and signal-to-noise ratio



In addition to these calculations, it has been shown experimentally by Engel et al [72] that the sensitivity is increased for a polymer cantilever with a thin film metal strain gauge when it covers a greater proportion of the length of the cantilever, due to the high modulus of the strain gauge relative to that of the polymer beam.

It was consequently decided that the strain gauge should extend for the full length of the cantilever, with as many meanders as could be fitted within the width of the cantilever.

### 5.2.3 Resonant frequency of the cantilever

The resonant frequency of the cantilevers was calculated in order to assess their suitability for measuring a turbulent flow. This is particularly important if time-resolved measurements were to be made. Turbulent eddies within the flow at a frequency close to the resonant frequency could cause the cantilever to vibrate, which would distort steady state results if the response of the cantilever is not linear, as well as affecting time-resolved results. The first resonant frequency was calculated following [73] to be

$$f = \frac{3.52}{2\pi} \sqrt{\frac{EI}{\rho A l^4}} \tag{5-34}$$

The resonant frequency increases as the length of the cantilever decreases. For this application the highest frequency is advantageous as it makes it less likely that this frequency will be excited by the turbulent flow. The first resonant frequency for each length of cantilever, with a width of 400 μm is shown in Table 5-2.

Length of cantilever	Resonant frequency
2 mm	533 Hz
3 mm	237 Hz
4 mm	133 Hz

Table 5-2 Resonant frequencies for varying cantilever lengths

Frequencies of turbulence with flows typically include these frequencies within their range. A very high resonant frequency (>20 kHz), would be the best option for a shear stress sensor in order to minimise the probability that the turbulent eddies in the flow

cause the sensor to vibrate. However despite this the cantilever may not resonate in the presence of these turbulent eddies, but this can only be determined experimentally.

A 3 mm long cantilever was tested in the wind tunnel with no filters on the output from the sensor with data being logged at 5000 Hz. A fast fourier transform was applied to the data to establish whether a peak could be seen at the resonant frequency. The data is shown in Figure 5-6. It can be seen that there is no significant peak at the first resonant frequency of 237 Hz. This implies that the cantilever does not resonate due to structures in the flow. However all measurements and testing done with this sensor have been carried out in a laminar boundary layer, and resonance would be more likely where the flow is turbulent.

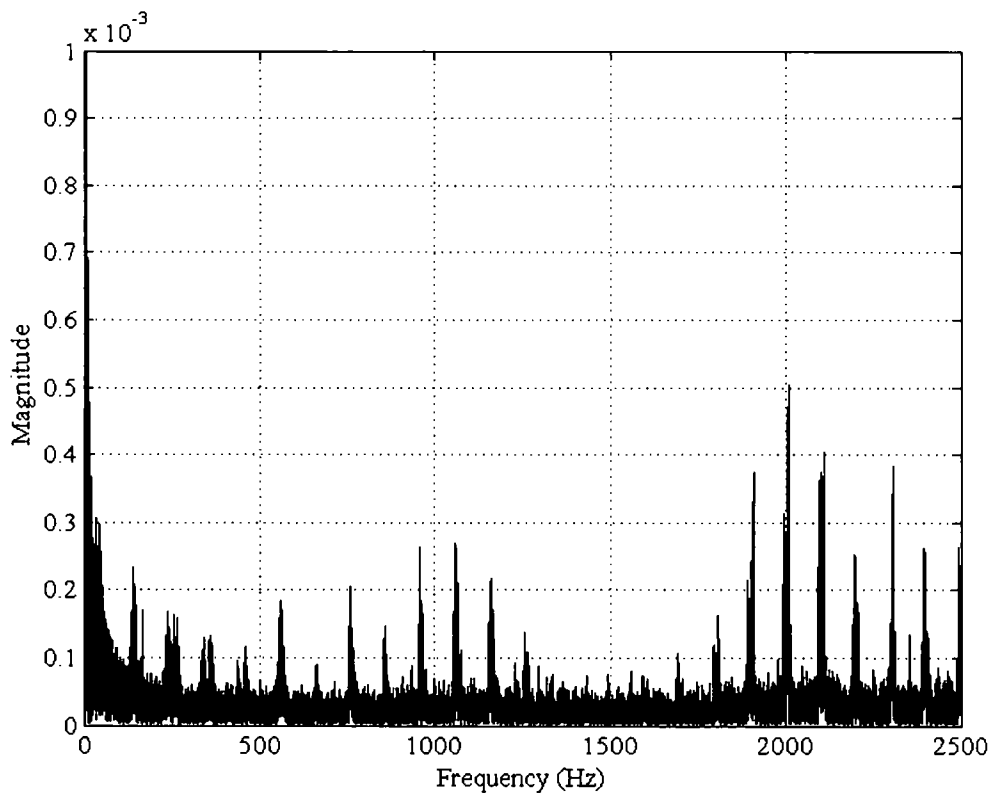


Figure 5-6 Frequencies seen in unfiltered output from 3 mm cantilever

The peaks seen in this graph are of small magnitude and are a result of electrical noise. However flow structures at a frequency to cause resonance might not have been present in this test. More experiments would be required before it would be possible to state that the sensor was not susceptible to resonance. Differentiating between the frequency

response of the sensor, the wind tunnel and other equipment in the system would be complex.

#### 5.2.4 Variation of stress gradient with exposure dose

Due to the processing methods for SU-8, a stress gradient is present through the layer, which causes the cantilever to deflect out-of-plane. This deflection can be either negative or positive depending on the precise processing employed. A number of factors are found to influence the degree of stress gradient, including the exposure dose, post bake time and temperature and hard bake parameters [74].

An example of the type of deflection seen in SU-8 cantilevers is shown in Figure 5-7. The SEM shows a 3 mm long cantilever which is 400  $\mu\text{m}$  wide. The deflection of the cantilever is clearly seen. For the purposes of this work, a positive deflection was defined as upwards, as seen in this case.

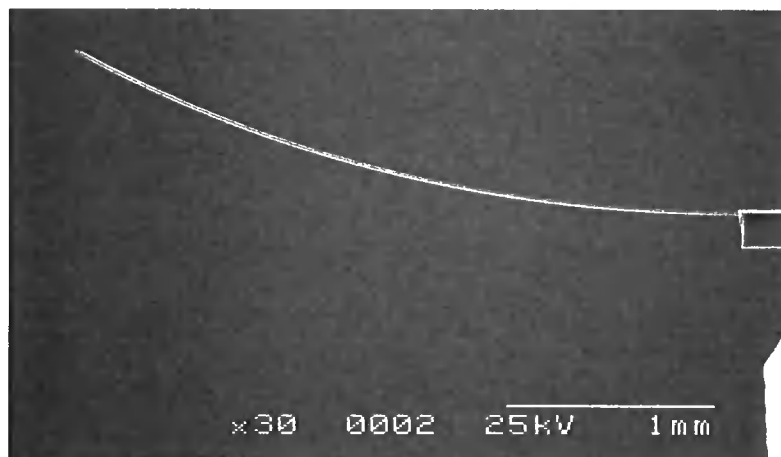


Figure 5-7 Deflection of cantilever caused by internal stress gradient


The stress gradient can be calculated from the tip deflection of the cantilever, using the equation from [75]

$$\frac{\Delta\sigma}{\Delta t} = \frac{E}{1-\nu} \frac{2}{L^2} \delta \quad 5-35$$

where  $\sigma$  is the stress,  $t$  is the thickness of the cantilever,  $E$  is Young's modulus,  $\nu$  is Poisson's ratio,  $L$  is the length of the cantilever and  $\delta$  is tip deflection.

By varying the exposure dose it was found that the stress gradient could be varied from positive to negative while keeping the other variables constant, allowing the degree of curvature to be controlled as required without having to modify other processing parameters. The devices were fabricated and released and the tip deflection then measured. Although the presence of the additional NiCr layer would have an effect on the curvature due to the stress in the metal, the devices were fabricated without the nichrome layer as it allowed a simpler and much quicker fabrication process and the trends found would still be valid when the metal layer was added. This allowed a different release layer to be employed compared with that which was required for the full fabrication process. A Ti-Cu-Ti release layer was utilised. The bottom layer of titanium acts as an adhesion layer for the copper, and the upper layer of titanium is present as an adhesion layer for the SU-8, since the adhesion of SU-8 to copper is less good. To release the structures the top layer of titanium is etched in HF and then the copper is etched in sodium persulfate with the final titanium layer, which is still attached to the devices after release, being etched in HF as before. The method of release should have no impact on the curvature of the cantilevers.

The full fabrication process for the curvature tests is shown in Table 5-3.

<p>a)</p> 	<p>A release layer of Ti-Cu-Ti was evaporated onto the silicon substrate using an e-beam evaporator.</p>
---	--

b)



SU-8-10 was spun on at 3000 rpm for 30 seconds. This layer was then pre-baked at 65 °C on a hotplate for 2 minutes and then at 95 °C for 5 minutes as recommended by the manufacturers. The layer was then exposed at varying exposure doses between 100 and 600 mJ/cm<sup>2</sup>. A post bake step was then applied, baking at 65 °C for 1 minute and 95 °C for 2 minutes. The layer was then developed in EC solvent for 2 minutes. A hard bake of 15 minutes at 160 °C was also carried out. The substrate was then cooled slowly to room temperature.

c)



SU-8-50 was then spun on at 1000 rpm for 30 seconds. This layer was pre-baked at 65 °C on a hotplate for 10 minutes and then at 95 °C for 30 minutes. This layer was exposed at 400 mJ/cm<sup>2</sup>, post-baked at 65 °C for 1 minute and 95 °C for 10 minutes. The layer was developed in EC solvent for 20 minutes.

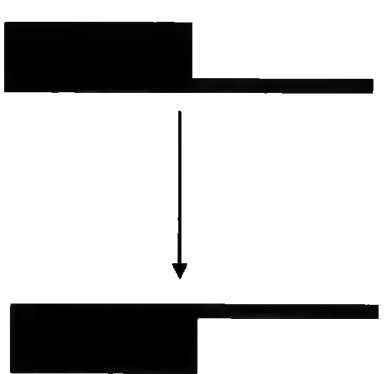
<p>d)</p> 	<p>The device was then released by etching the exposed top layer of titanium in HF. The copper layer was then etched in sodium persulfate to release the devices. The titanium remaining on the structures was then removed in HF, and the structures inverted to form the cantilever structure.</p>
---	--

Table 5-3 Fabrication process for assessing cantilever curvature

Since the devices are inverted for use, the tip deflection was measured in this functional state, with a negative deflection therefore being a deviation away from the substrate.

The tip deflection was measured for a variety of exposure doses (at step (b) in Table 5-3) and the stress gradient calculated, with the results shown in Figure 5-8.

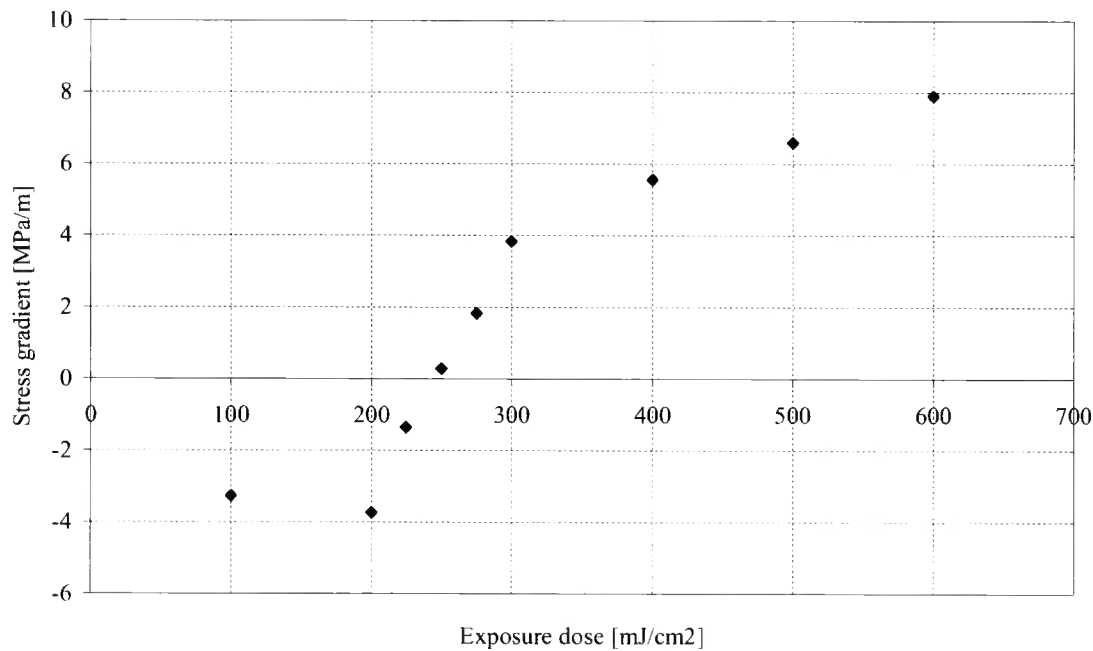


Figure 5-8 Variation of stress gradient in SU-8 with exposure dose

These values are lower, but in the same range, as those found by Bachmann et al [76] of  $13.8 \pm 3.2$  MPa/m, albeit for different processing conditions.

At low exposure doses the effect of the UV exposure is found to dominate. SU-8 shrinks on cross-linking, and therefore where the acid generation is greatest, closest to the UV light, the SU-8 is more fully cross-linked, causing the cantilevers to deflect away from the substrate (a negative deflection).

At high exposure doses, the thermal effects during curing are the dominant effect causing the stress gradient and therefore the deflection is towards the substrate (a positive deflection). These effects are illustrated in Figure 5-9 and Figure 5-10.

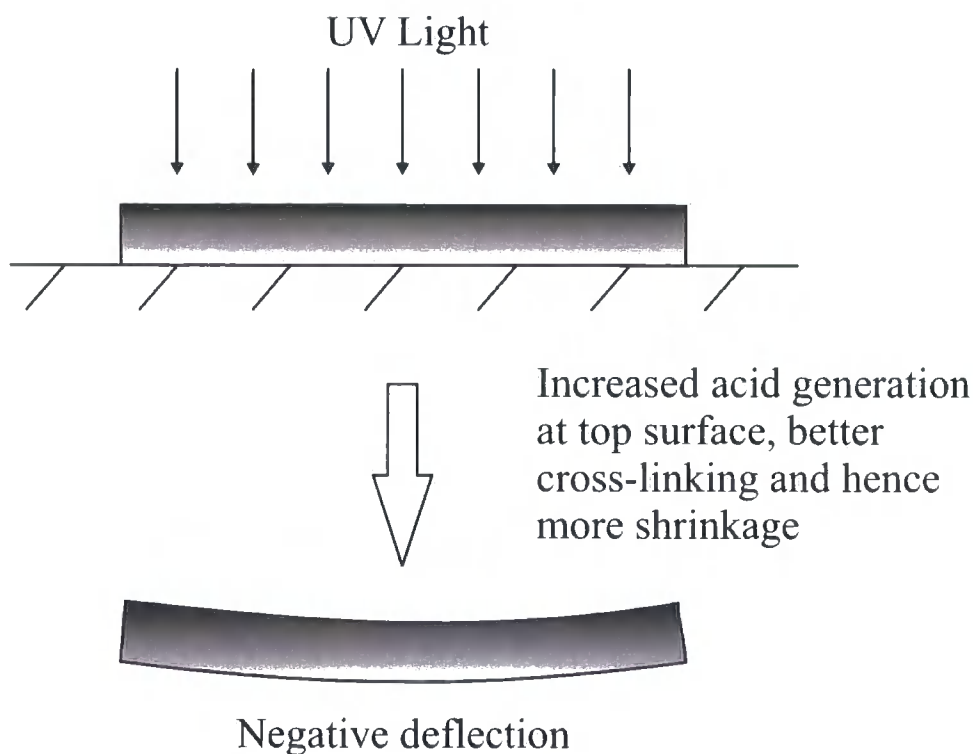


Figure 5-9 Negative stress gradient

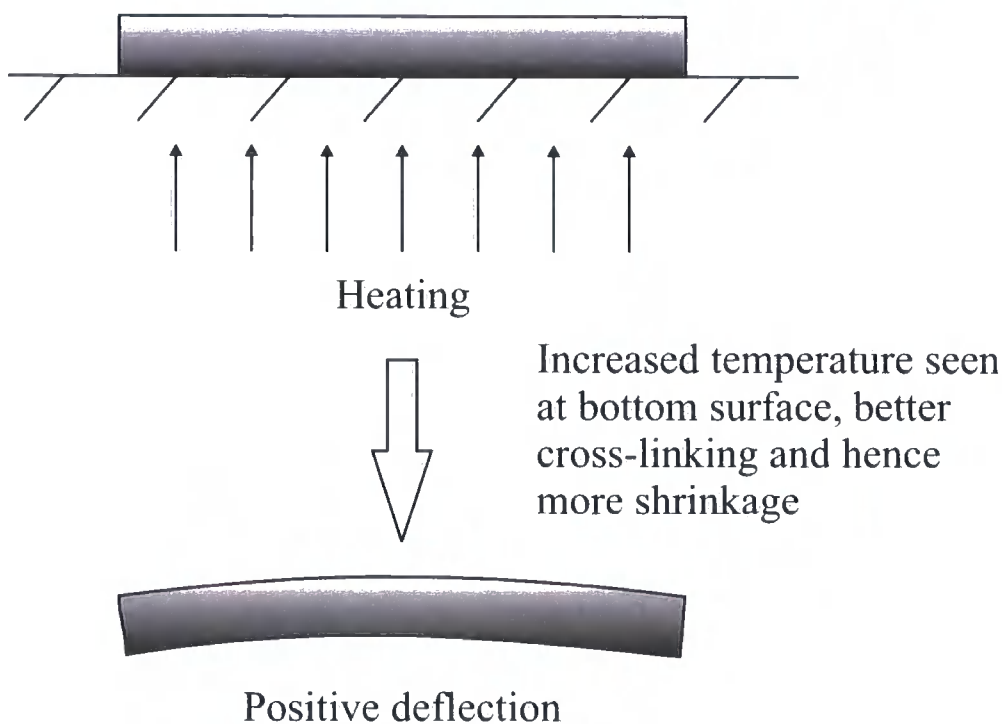


Figure 5-10 Positive stress gradient

The distribution of the deflection across the substrate was investigated in order to establish whether a variation in the cross-linking was present across the surface of the wafer. However the variation in deflection was found to be random across the substrate and not to follow any discernible pattern.

The information obtained here was used to optimise the curvature of the cantilevers in the sensors.

### 5.2.5 Sidewall coverage

Initially the masks were designed such that the contact pads and the holes in the first layer of SU-8 were the same size. However in the case where the two layers were marginally misaligned, on one or more sides of the contact pads the pad itself was electrically connected to the resistor only by a thin bridge up the sidewall, the width of the resistor, which was only 40  $\mu\text{m}$ . This meant that defects in the sidewall coverage could have a significant impact on whether electrical connection was achieved.



An example of these tracks over the sidewall is shown in Figure 5-11.

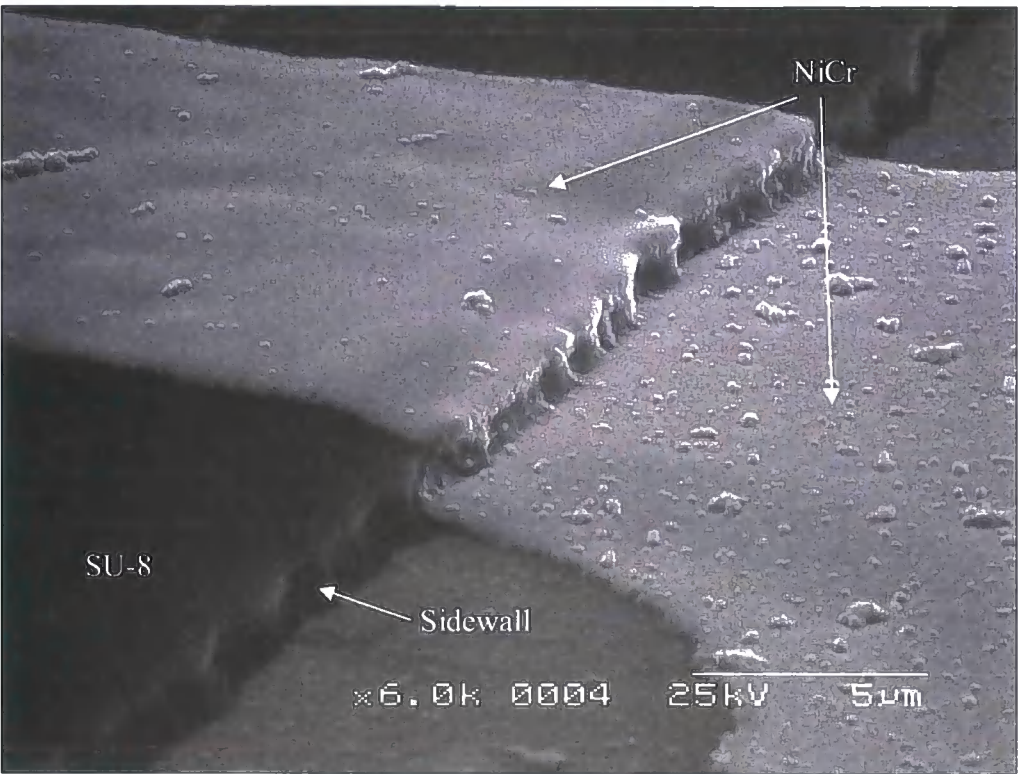


Figure 5-11 Narrow track of NiCr over sidewall of SU-8

In this case the continuity of the nichrome layer over the step in the underlying material can be seen, however this was not always achieved causing failure of the sensors and consequently the masks were redesigned so that the metal contact pad was slightly larger than the gap left in the SU-8 layer.

This change in the contact pad design is illustrated in Figure 5-12.

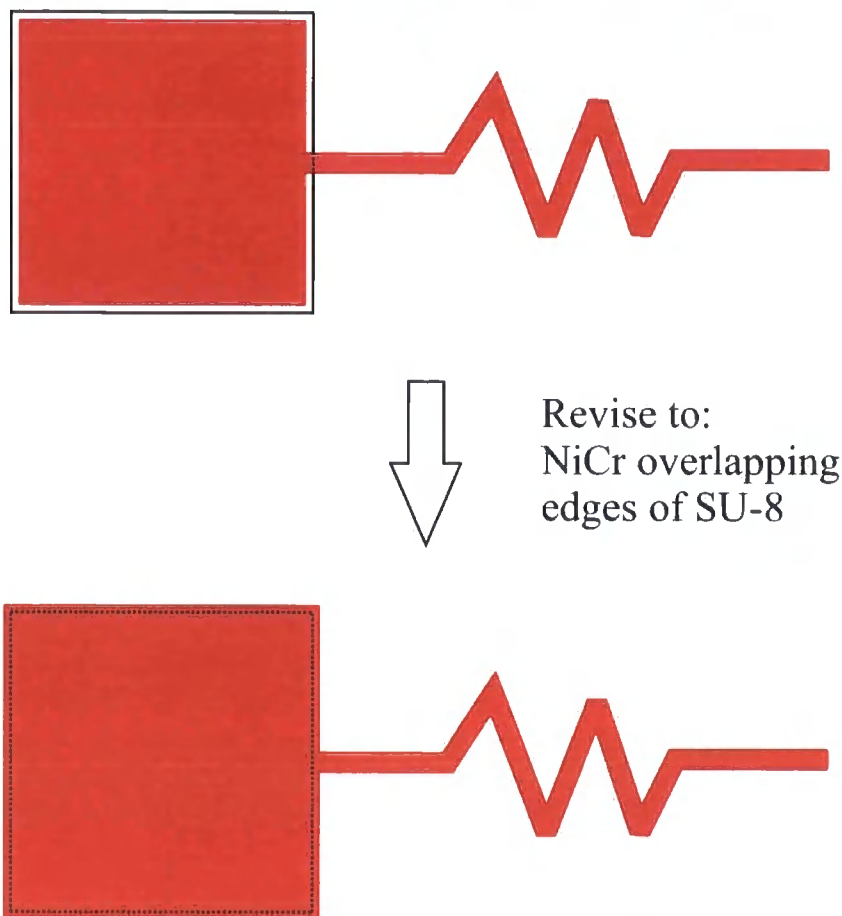


Figure 5-12 Diagram of contact pad design

This meant that the sidewall coverage all the way around the contact pad was maintained after the metal layer had been etched so that the probability of getting electrical connection was much higher. Even if the substrate was not completely flat when mounted in the sputterer so that sidewall coverage was only achieved on some of the walls, connection would still be made to the resistor.

The overlapping design of contact pads are shown in Figure 5-13.



Figure 5-13 Metal contact pads overlapping edges of SU-8

### 5.2.6 Calculation of TCR

For this application a minimum value of thermal coefficient of resistivity (TCR) of nichrome was desirable. This would make the change in resistance of the strain gauge caused by the resistive heating to be as low as possible and therefore the effect of the excitation voltage on the response of the sensor would be minimised.

The electrical properties of thin films of nichrome can be very different from those known for the bulk material [77]. The value of TCR can also be altered by a number of means. This can be achieved by sputtering the alloy in the presence of gases other than argon, such as nitrogen [78], which allows the control of TCR to between  $\pm 100$  ppm depending on the nitrogen content in the deposited film. Annealing the deposited film also has an effect on TCR [79]. Introducing impurities such as aluminium or copper was

also found to decrease the TCR due to the presence of microcrystalline microstructures in the film [80,81]. The proportion of chromium in the alloy was also influential.

The thermal coefficient of resistivity was determined for the specific deposition method, film thickness and composition of nichrome that was being used here. This was done by fabricating the nichrome resistor structure on a layer of SU-8 to act as an electrical insulator between the metal and the silicon substrate on which the processing was being carried out. The substrate was then placed on a hot plate and probes brought into contact with the contact pads of the sensor. These were connected to a multimeter in order to measure the resistance. The hot plate was then gradually heated and the resistance measured in order to obtain the relationship between temperature and resistance.

The results of this test for a 125 nm thick film as used in the sensors are shown in Figure 5-14. When a linear best fit line is drawn through this data, the gradient is found to be 6.0082  $\Omega/\text{K}$ .

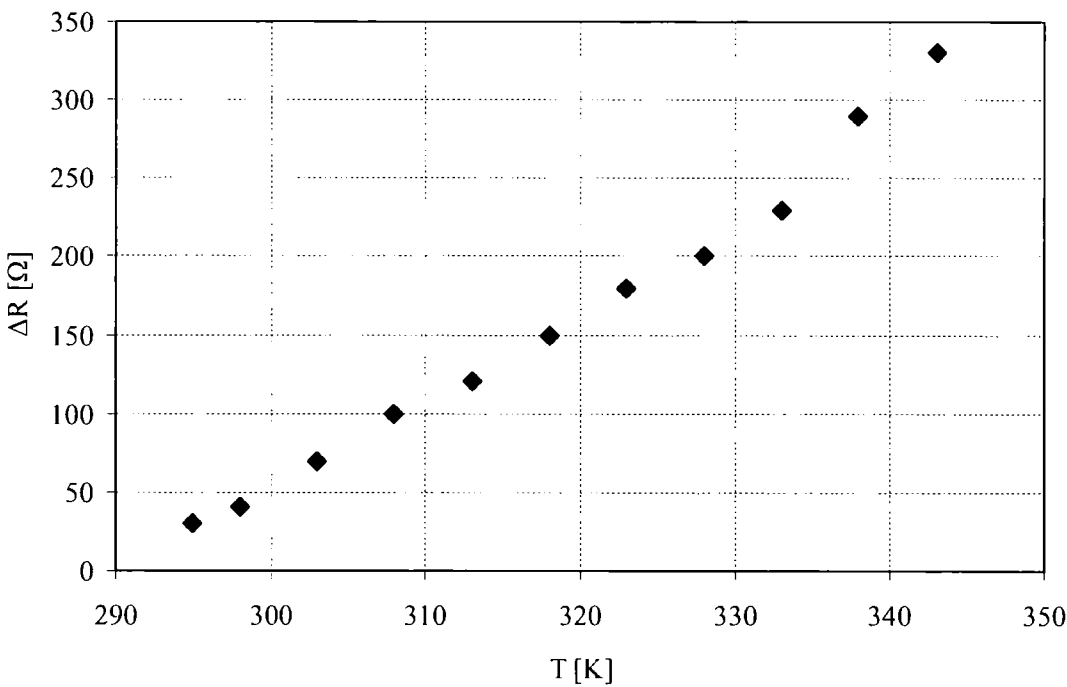


Figure 5-14 Change in resistance of 125 nm thick NiCr film with temperature

The relationship between temperature and resistance is

$$\frac{\Delta R}{R_0} = \alpha \Delta T \quad 3-1$$

where  $\alpha$  is the thermal coefficient of resistivity. The TCR for this film was found to be 139 ppm, which is as would be expected for a thin film of 80:20 nichrome. Because of this relatively low value of TCR it was decided that the time involved in trying to reduce this value further would not be well used unless it was found while using the sensor that the temperature and heating effects were causing problems. This was not found to be the case on experimental testing, and consequently this value of TCR for the nichrome strain gauge was found to be acceptable for this application.

### 5.2.7 Fabrication

In order to make the results from different lengths of cantilevers more comparable, it was decided that the strain gauge should be identical for all the designs of sensor. This meant that the strain gauge was limited in size to the smallest of the cantilever designs, which was 2 mm long and 400  $\mu\text{m}$  wide. However because the metal on the polymer cantilever has its own internal stress, it caused the cantilever to bend differently from the SU-8 alone because of the interaction between the internal stress of the metal, the polymer and also the internal stress gradient of the polymer. (The metal is considered to be sufficiently thin that the internal stress gradient of this material may be ignored.) If, for the longer cantilevers, the metal were only continued for half the length then the cantilever was not found to bend in a smooth curve, but to be influenced by the metal present closer to the root of the cantilever. Towards the tip of the cantilever, the curvature matched that found in an exclusively polymer cantilever, caused by the internal stress gradient of the polymer. Consequently it was decided that the metal should be continued for the full length of the cantilever but that the strain gauge would remain electrically the same i.e. 2mm long. Also the findings of Engel et al [72] are relevant and suggest that the sensitivity of the device will be improved by continuing the metal for the full length of the cantilever.

The width of the strain gauge was also maintained at the narrower width of 400 microns even for the wider cantilevers. It was not found necessary to widen the metal area for the wider cantilevers as there was no bending in the cantilever across its width and therefore the same considerations do not apply as for the length.

Initial designs of masks for the cantilever devices caused cracks around stress concentrating points in the design. These were found at 90° angles at the root of the cantilever and also where the holes were left for the contact pads in the bottom layer. In order to prevent these cracks forming during the fabrication process, the corners were rounded off, or in the case of the root of the cantilever, an angled section was introduced to minimise the concentration of stress here. In addition, to facilitate the release of the structures, a hole was introduced in the centre of the main body, between the contact pads. This allowed the release etchant to undercut from the centre of the device as well as from the edges, decreasing significantly the release time required.

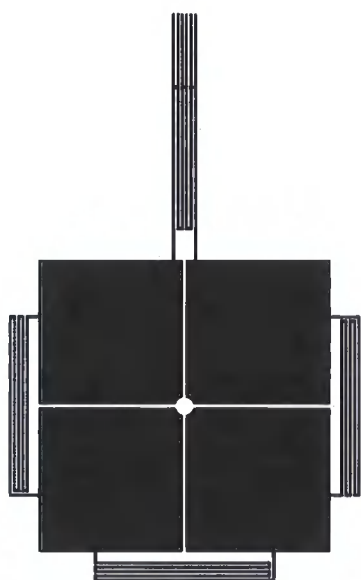
The mask designs used for the fabrication of the cantilever sensors are shown in Figure 5-15. The masks for the 3 mm long, 400  $\mu\text{m}$  wide cantilevers are shown here. On the fabrication masks, all six different geometries were present, and four copies of each design were present on each wafer.

a)



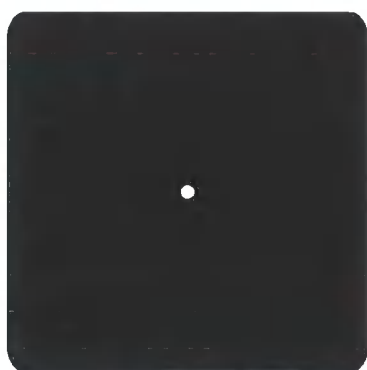
The first mask was for the initial, thin layer of SU-8 and defined both the body of the device and cantilever itself. The curvature of the corners of the device and contact pads can be seen, as well as the angled section at the root of the cantilever, designed to eliminate stress fractures. The hole in the centre of the device was present to reduce release times.

b)



The second mask defined the metal resistors. The contact pads were marginally larger than the holes in the underlying layer of SU-8 in order to allow more reliable side wall coverage. The extension of the metal tracks to the end of the cantilever can be seen, as can how this extension was not electrically connected. The central hole was present in this mask also.

c)





The third mask was used for the thick layer of SU-8 which covers only the body of the device. This provides the support from which the cantilever was suspended. Again the central release hole and the rounded corners can be seen.

Figure 5-15 Masks for fabrication of cantilever sensor (3 mm by 400  $\mu\text{m}$  sensor as example)

The cantilevers were fabricated on a silicon substrate and then released and inverted. The release layer used was a Prolift layer with a sputtered titanium coating. This was because the Ti-Cu-Ti layer used for the fabrication of the cantilevers while analysing the stress gradient was not suitable when the nichrome layer was present, as the sodium persulfate used to remove the copper also attacked the nichrome.



The fabrication process flow is shown in Table 5-4.

<p>a)</p> 	<p>A ProLIFT 100 layer was spun onto the silicon wafer to act as a release layer. A titanium layer was sputtered over the top of the Prolift layer to protect it from prolonged exposure to the positive photoresist developer</p>
<p>b)</p> 	<p>SU-8-10 was spun on at 3000 rpm for 30 seconds. This layer was then pre-baked at 65 °C on a hotplate for 2 minutes and then at 95 °C for 5 minutes as recommended by the manufacturers. The layer was then exposed at 500 mJ/cm<sup>2</sup>. A post bake step was then applied, baking at 65 °C for 1 minute and 95 °C for 2 minutes. The layer was then developed in EC solvent for 2 minutes. A hard bake of 15 minutes at 160 °C was also carried out. The substrate was then cooled slowly to room temperature.</p>






<p>c)</p> 	<p>A 125 nm nichrome layer was then deposited by sputtering, which was then patterned using a standard photolithography process. The NiCr was sputtered in argon at a pressure of 5 mtorr using an RF magnetron at a power of 185 W which gave a rate of 2.5 Å/s. The stage on which the substrate was mounted was cooled to 10 °C and rotated to give an even deposition across the substrate.</p>
<p>d)</p> 	<p>SU-8-50 was then spun on at 1000 rpm for 30 seconds. This layer was pre-baked at 65 °C on a hotplate for 10 minutes and then at 95 °C for 30 minutes. This layer was exposed at 400 mJ/cm<sup>2</sup>, post-baked at 65 °C for 1 minute and 95 °C for 10 minutes. The layer was developed in EC solvent for 20 minutes.</p>
<p>e)</p> 	<p>The top Ti layer was etched in hydrofluoric acid where exposed and then the Prolift layer was removed in TMAH. Once the sensors had been released, the titanium layer still adhering to the underside of the sensor was removed from them individually in HF.</p>

Table 5-4 Fabrication process for cantilever sensors

A long exposure time was used for the cantilever layer of SU-8 to compensate for the compressive stress seen in the NiCr layer.

5.3 Results

5.3.1 Mechanical testing

Mechanical testing of the cantilevers was carried out for two purposes. The first of these was to obtain an accurate value of Young’s modulus for the composite cantilever under these specific processing conditions. The second was to get a relationship between the deflection and the change in resistance of the cantilever strain gauge and thus calculate the gauge factor of the nichrome. Both of these tests were carried out independently of each other on the test rig described in §3.2.

*Measurement of Young’s modulus*

Testing of force and deflection for the calculation of Young’s modulus was carried out without electrical wires connected to the device as these would have interfered with the accuracy of the measurements using the balance. The test was carried out with a 2 mm long, 400  $\mu\text{m}$  wide cantilever. However, because of the very small forces required to give quite a large deflection of the cantilever, the probe tip was actually placed halfway along the cantilever, thereby giving an effective length of 1mm for the purpose of the calculation of the Young’s modulus. The results of this test are shown in Figure 5-16.

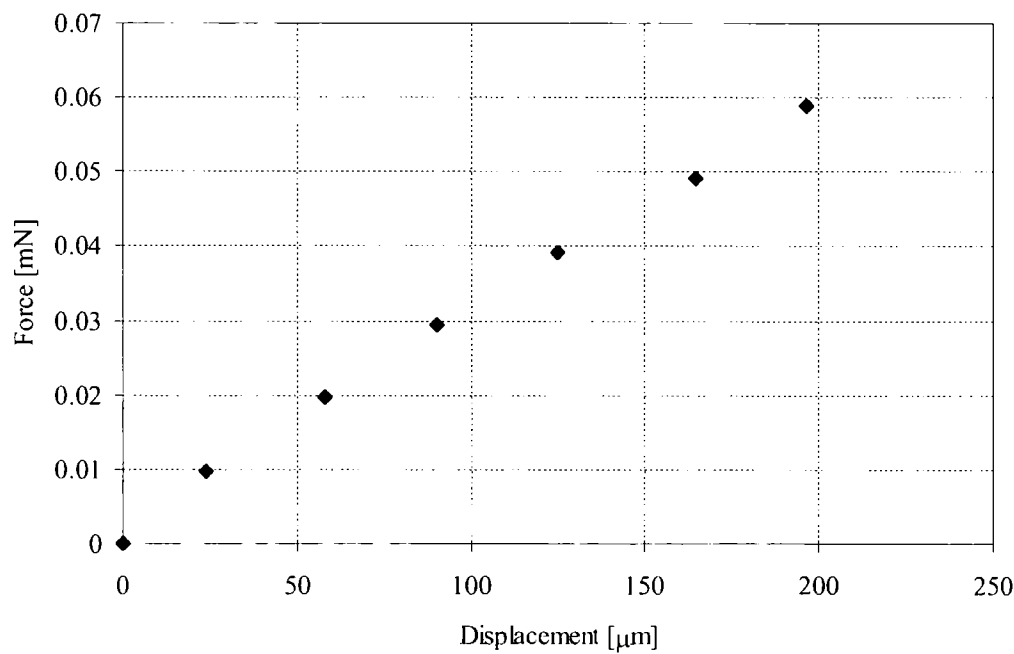


Figure 5-16 Force v. displacement for 2 mm cantilever

The straight line linear best fit of this data is

$$y = 2.92 \times 10^{-4} x \quad 5-36$$

And therefore the gradient of this line is 0.3 N/m. Based on [61], Young's modulus can be calculated as

$$E = \frac{FL^3}{3\delta I} \quad 5-37$$

where  $F$  is the point load applied,  $L$  is the length of the cantilever,  $\delta$  is the tip deflection and  $I$  is the second moment of area of the cantilever. For a cantilever of the dimensions given above and a thickness of 12  $\mu\text{m}$  this means that the Young's modulus can be calculated as 1.69 GPa.

However because the root of the cantilever is widened in order to avoid stress fractures forming during the fabrication process, and also because the body of the device is not fixed at exactly the root of the cantilever, this value slightly overestimates the true value of the Young's modulus of the structure. Consequently FEA was used to achieve a more accurate interpretation of the force-deflection curve. This modelling was carried out using Strand7 with a non-linear solver due to the large deflection. The original calculated value was used as an initial value and then an iterative process was used until the correct value was found. The initial value of Young's modulus was used to run the model and obtain a tip deflection for the applied force. Based on this result the Young's modulus given as a material property was then increased or decreased until the correct tip deflection was seen.

The mesh used for the calculation is shown in Figure 5-17.

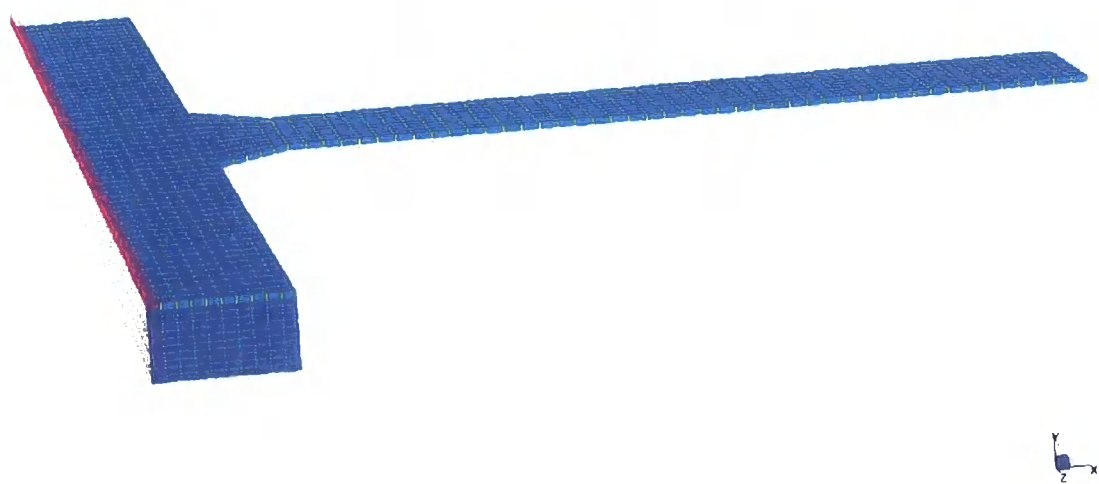


Figure 5-17 Mesh used for FEA modelling of Young's modulus

The load was applied as a point load at the centre of the cantilever width and 1 mm along from the root. This is the most accurate representation of the load applied by the probe tip on the test rig. The deflected model for the final iteration is shown in Figure 5-18 with the real deflection shown.

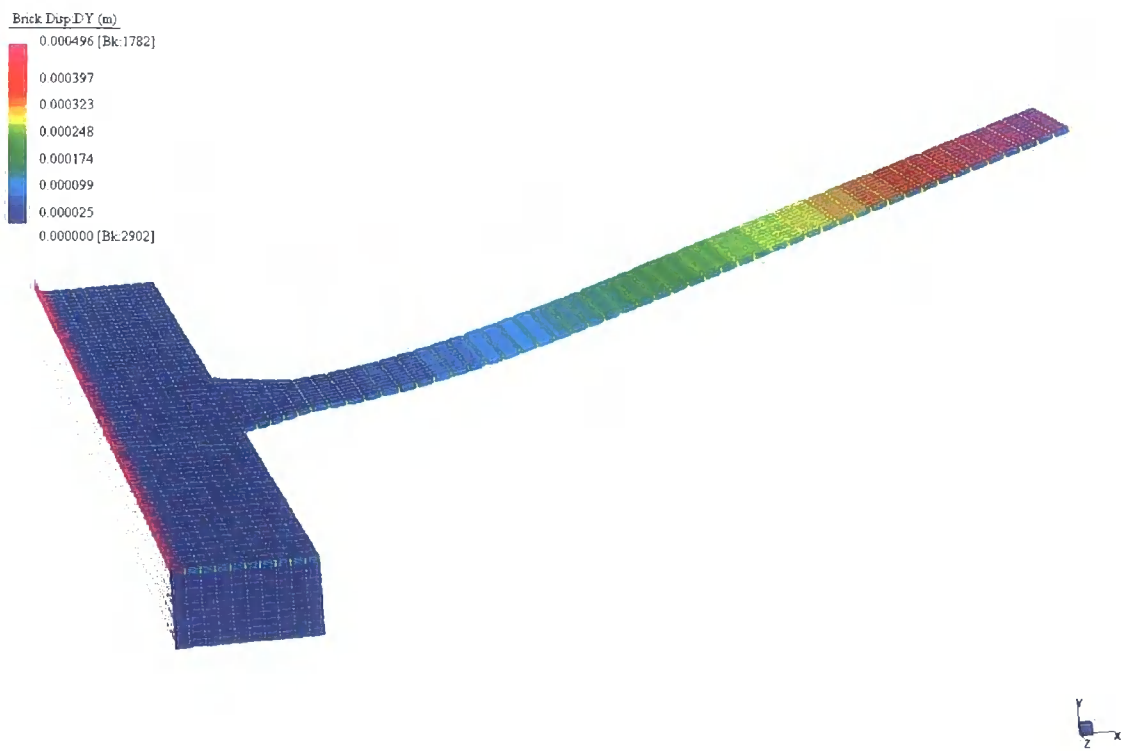


Figure 5-18 Model with load applied for calculation of Young's modulus

This represents a load of 0.059 mN which gives a deflection of 196  $\mu\text{m}$  halfway along the cantilever at a position of 1 mm. This is the deflection seen for the same applied force when carrying out experimental testing. The results from the FE analysis are shown in Figure 5-19.

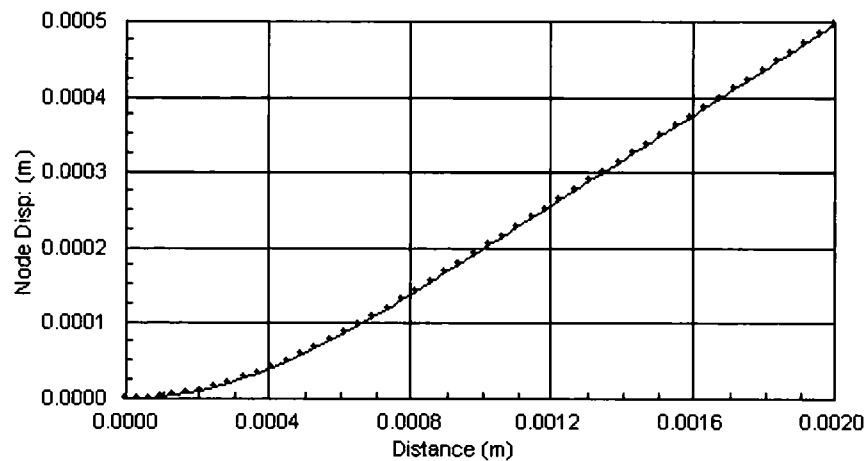


Figure 5-19 Deflection v. distance along cantilever for calculation of Young’s modulus

For this result a Young’s modulus of 1.45 GPa was used for the calculation. This is subsequently the value that has been used in all other calculations where knowledge of Young’s modulus has been required. As expected, this value was slightly lower than that obtained by using simple beam theory to calculate the Young’s Modulus due to the presence of the widened anchor. This value of Young’s modulus is quite low compared with published data for SU-8 (1.54 – 7.5 GPa [69, 71]), but within the same order of magnitude and is the value for the composite SU-8/NiCr cantilever. However, since the bulk Young’s modulus of nichrome is two orders of magnitude greater than that of SU-8, the presence of the thin film on the surface of the cantilever would be expected to increase the modulus of the composite, rather than decrease it, so the actual Young’s modulus for the SU-8 alone may be lower than this calculated value. Conversely the thickness of the NiCr film is two orders of magnitude less than that of the SU-8 cantilever and consequently its effect on the stiffness of the cantilever may be minimal.

**Measurement of Gauge Factor**

Mechanical testing was carried out to find the relationship between deflection and resistance change. For the purposes of this test, electrical connections were made to the

two contact pads closest to the strain gauge. They were not connected as for wind tunnel testing of the device where the Wheatstone bridge was utilised. The result of this connection was that the resistance was in fact being measured in parallel with the other three resistors in series, as shown in Figure 5-20. The reason for this method of connection was that the test rig was set up for the measurement of resistance rather than to supply a voltage and then read a voltage as output as would be the case if the Wheatstone bridge were used.

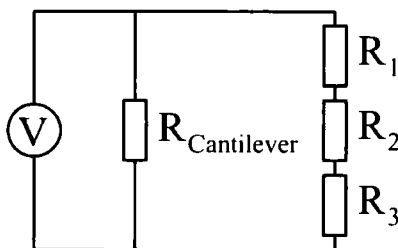


Figure 5-20 Measurement of resistance of strain gauge

This test was undertaken for all three lengths of cantilevers. However, the results from the shortest, 2 mm cantilevers were found to give the most reliable results. The results for one of these 2 mm cantilevers are shown in Figure 5-21. The electrical connections shown in Figure 5-20 were taken into account during the calculation of the cantilever output. The initial resistance of all four resistors was measured, which in all cases was again measured as in Figure 5-20. The actual component value of each resistor could then be calculated and used for the determination of what the cantilever output voltage would be for a supply voltage of 1 V.

These results are shown in Figure 5-21.

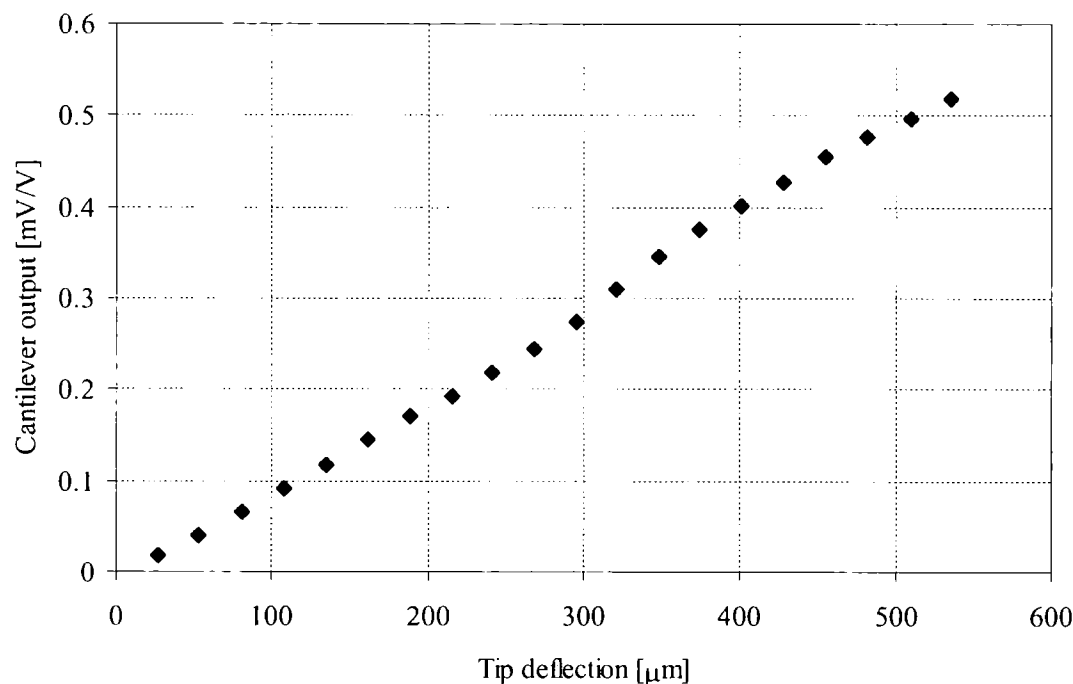


Figure 5-21 Cantilever output as a function of tip deflection

This data shows a deflection of  $9.6 \times 10^{-4} \text{ (mV/V)/}\mu\text{m}$ .

Thus

$$V_{out} = 9.6 \times 10^{-4} V_{in} \delta \tag{5-38}$$

where the output voltage is in mV, the input voltage is in V and  $\delta$ , the tip deflection, is in  $\mu\text{m}$ .

From this result it was possible to calculate the gauge factor of the nichrome. For this case, the FE model was used to calculate the strain along the surface of the cantilever. This strain combined with the measured change in the resistance allowed the gauge factor to be calculated, since

$$K = \frac{\Delta R/R}{\varepsilon} \tag{5-39}$$

Where  $K$  is gauge factor,  $\varepsilon$  is strain and  $R$  is resistance.

For this case, the tip deflection from the FE model could be used to give the expected output in mV/V from equation 5-38. This can then be used to calculate the change in resistance in the strain gauge for a known Wheatstone bridge configuration, since from rearranging equation 5-7

$$\frac{\Delta R}{R} = \frac{2V_{out}}{V_{out} + \frac{V_{in}}{2} - 1} \quad 5-40$$

when all resistors in the Wheatstone bridge have the same resistance.

The strain data from the same case was then used to calculate the gauge factor using equation 5-39. This calculation yielded a gauge factor for the nichrome strain gauge of 1.8. This is lower than the bulk gauge factor of 2-2.5. However, Kazi et al [79], found that for a film of this thickness (125 nm) a gauge factor of approximately 1.3 was seen, with the gauge factor decreasing for film thicknesses between 20 and 150 nm. The films in this study were annealed, however, which could account for the difference in values.

### 5.3.2 FEA results

The cantilever was modelled with a range of pressures applied to the under-surface of the cantilever. The Young's modulus as calculated previously in §5.3.1 was used as the material property required by the model. The tip deflection was obtained from the model for a given pressure difference. The mesh used was the same as that for calculating the Young's modulus and is shown in Figure 5-17. However instead of using a point load at the 1 mm position on the cantilever, a uniformly distributed load was applied over the whole under-surface of the cantilever.



The results of this modelling are shown in Figure 5-22.

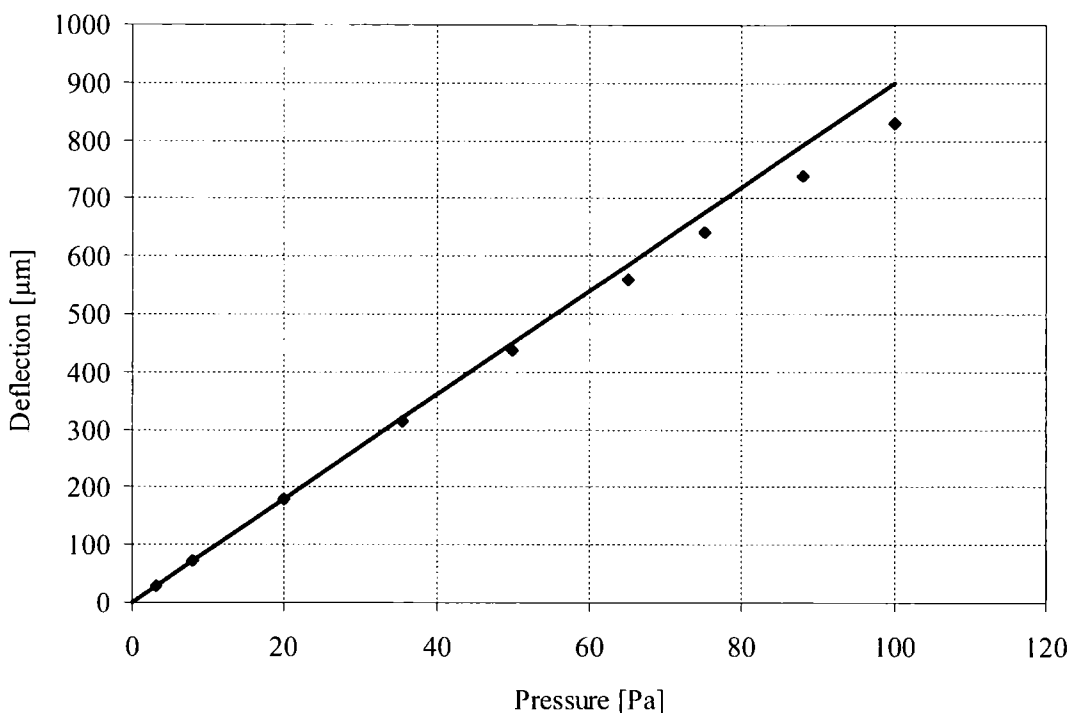


Figure 5-22 Tip deflection for 2 mm cantilever vs pressure difference across cantilever

At low pressures as shown in Figure 5-22, the relationship between pressure and tip deflection is found to be linear. At higher pressures, the relationship deviates from the linear relationship due to the large deflection of the cantilever.

### 5.3.3 CFD results

#### *Thermal heating effects*

The thermal heating effects of the resistor were quantified by a series of tests carried out by CFD. It was found to be impossible to measure the degree of heating of the sensor experimentally. At low supply voltages a FLIR thermal camera was unable to measure the difference between the nichrome strain gauge with power and with the power supply switched off, due to the small temperature difference. It was not possible to measure the absolute temperature of the strain gauge and the surrounding SU-8, as the different emissivities of the two materials meant that the two materials showed up as being at different temperatures even when they were both at room temperature. The size of the

strain gauge made it impossible to measure the temperature using such means as a thermocouple. Consequently CFD was used to estimate the temperature reached by the sensor under operating conditions so that the effect on the resistance change and thus the voltage output from the sensor could be calculated.

This was done by applying a temperature to the exterior surfaces of the sensor in the CFD model and then running simulations at a range of different freestream velocities (0-20 m/s at 5 m/s intervals) and obtaining as an output from the model, the heat flux from the sensor. This could then be compared with the known power output from a resistor (which causes resistive heating) and, by an iterative process, the temperature reached by the sensor could be calculated (for a known supply voltage (and therefore heat flux) and a known freestream velocity). The results of these simulations are shown in Figure 5-23.

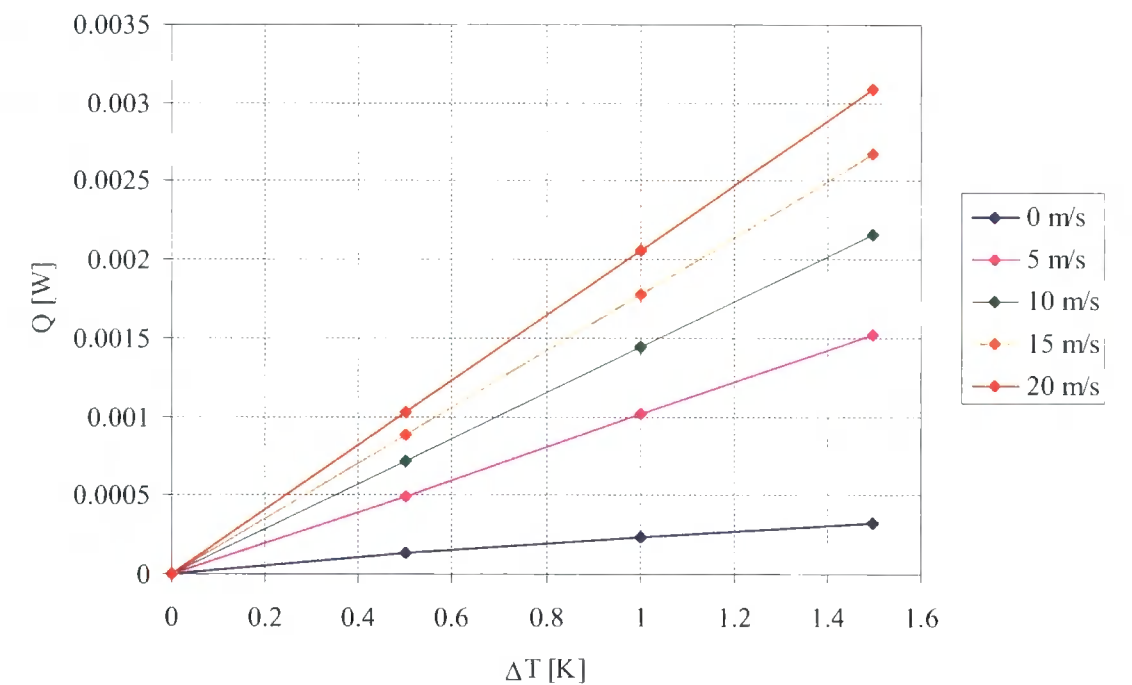


Figure 5-23 Heat flux against temperature for freestream velocities between 0 and 20 m/s

It can be seen that in this range for small values of temperature difference the relationship between  $\Delta T$  and the heat flux is linear. For a supply voltage of 1V for the four resistors of the Wheatstone bridge, each with a nominal resistance of 5 k $\Omega$ , the

power dissipated is 0.8 mW. At 20 m/s this power would cause the resistor to heat by approximately 0.4 K above ambient. This would cause a change in the resistance of 0.06  $\Omega$ , equating to an effect on the sensor output of 0.003 mV/V. This is small compared with the expected response caused by the pressure-induced deflection of the cantilever (0.75 mV/V). At zero velocity the heating effect is greatest as there is no cooling airflow passing over the sensor causing the temperature to be higher.

The ratio of  $Q/\Delta T$  can be plotted against velocity which gives a relationship which could then be used to compensate for the temperature differences at a known velocity. This relationship is shown in Figure 5-24.

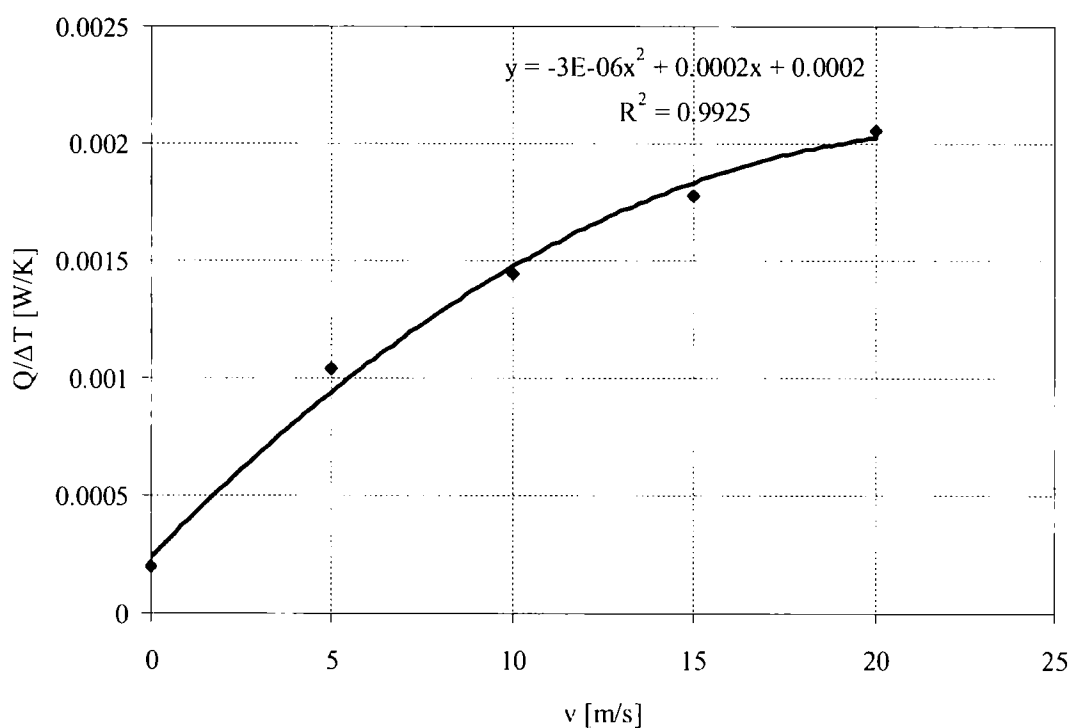


Figure 5-24 Ratio of  $Q/\Delta T$  against velocity derived from CFD

The ratio of convective heat transfer to conductive heat transfer is described by the Nusselt number which is defined as

$$Nu = \frac{hL}{k} \tag{5-41}$$

where  $h$  is the heat transfer coefficient in  $\text{W/m}^2\text{K}$ ,  $L$  is the characteristic length in m and  $k$  is the thermal conductivity of the fluid in  $\text{W/mK}$ .

Since the heat transfer coefficient can be written as

$$h = \frac{Q}{\Delta T.A} \tag{5-42}$$

this can be substituted in to equation 5-41 to give

$$Nu = \frac{QL}{\Delta T.k.A} \tag{5-43}$$

Since for the temperatures being used here the Prandtl number (which is the ratio of momentum diffusivity and thermal diffusivity) is constant for air (usually 0.713 at 20 °C) then we can expect a relationship of the form:

$$Nu = a Re^b \tag{5-44}$$

where *a* and *b* are constants, and Re is the Reynolds number.

Hence, if the Nusselt and Reynolds numbers are calculated for the above data and the logs of these results are plotted, then there should be a linear relationship between the two variables. These results are plotted in Figure 5-25.

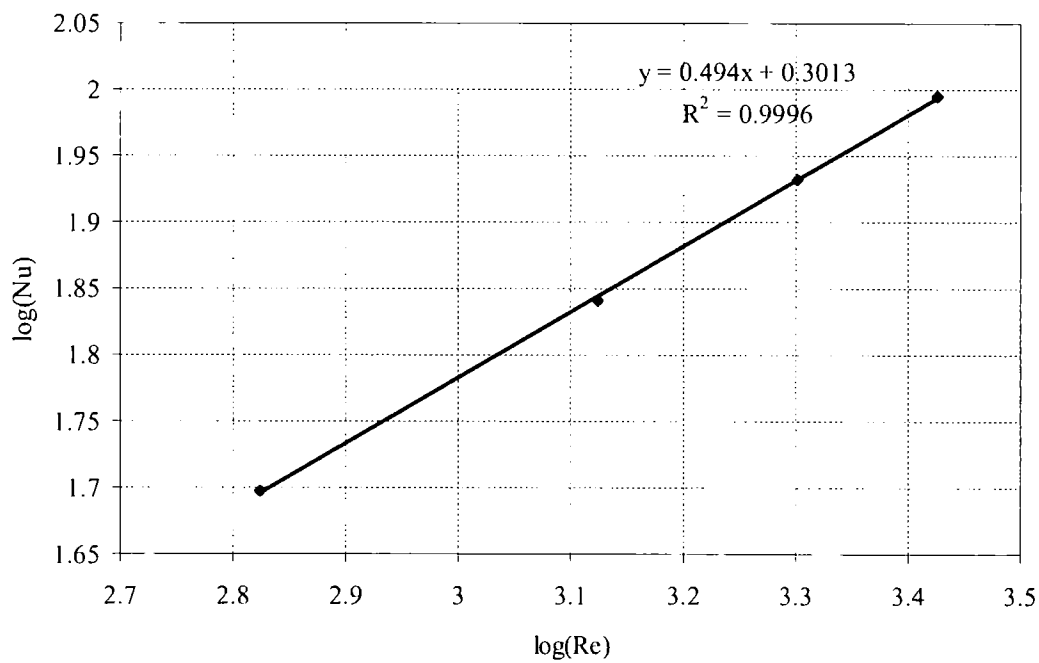


Figure 5-25 log(Nu) v log (Re) for heat loss from cantilever sensor

It can be seen that this gives a linear relationship as expected. The characteristic length that has been used is the length of the cantilever sensor, which is 2 mm. The constants thus calculated as in (5-44) are  $a = 2.00$  and  $b = 0.494$ . For forced convection over a flat plate in a laminar boundary layer, the heat transfer correlation is given by [82] as

$$Nu = 0.664 Re^{0.5} Pr^{0.33} \quad 5-45$$

although in this case as  $Pr$  is a constant this simplifies to the form given in (5-44). It can be seen that the power to which  $Re$  is raised (constant  $b$ ) is very close to what would be expected. This constant remains very similar for differing cases of forced convection over a flat plate, while the constant  $a$  varies depending on the particular configuration and hence has not been compared here.

### ***Effect of incidence angle***

Because the cantilever deflects in the airflow before reaching an equilibrium position the cantilever was modelled at a variety of different incidence angles in order to ascertain the effect that this has on the pressure drop across the cantilever. The cantilever was modelled as a straight structure as this was easier to model in Gambit and was expected to give a representative result. The exact shape of the cantilever was found to vary between different devices and was very difficult to measure accurately. The simulations were carried out at seven different incidence angles ( $0^\circ$ ,  $5^\circ$ ,  $15^\circ$ ,  $30^\circ$ ,  $45^\circ$ ,  $60^\circ$ ,  $75^\circ$ ) and four different velocities (or Reynolds numbers) for each angle (from 5 to 20 m/s at 5 m/s intervals). All simulations were carried out for a 2 mm, 400  $\mu\text{m}$  cantilever. Although the width of the cantilever might be thought unimportant for a 2D model, it is critical for obtaining the correct forces generated on surfaces. A boundary layer profile was used at the inlet to the CFD domain which varied for the specific freestream velocity. Examples of the static pressure contours from these simulations at a velocity of 15 m/s are shown in Figure 5-26 to Figure 5-31 over the next three pages. The colourbar scale has been maintained the same for all plots to allow comparison of the static pressure drop across the cantilever.

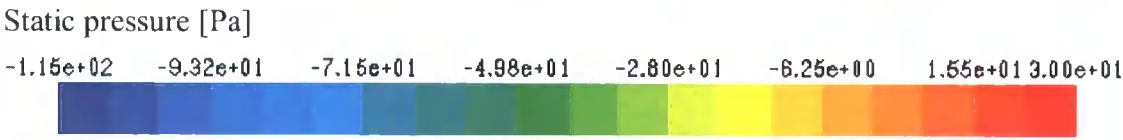
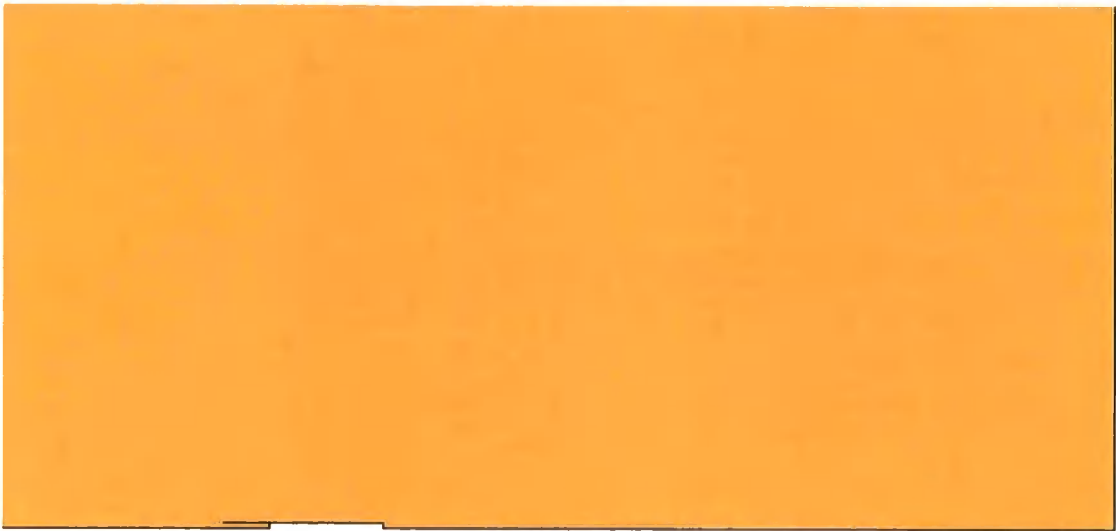


Figure 5-26 Static pressure contours for incidence angle of 0°



Figure 5-27 Static pressure contours for incidence angle of 5°

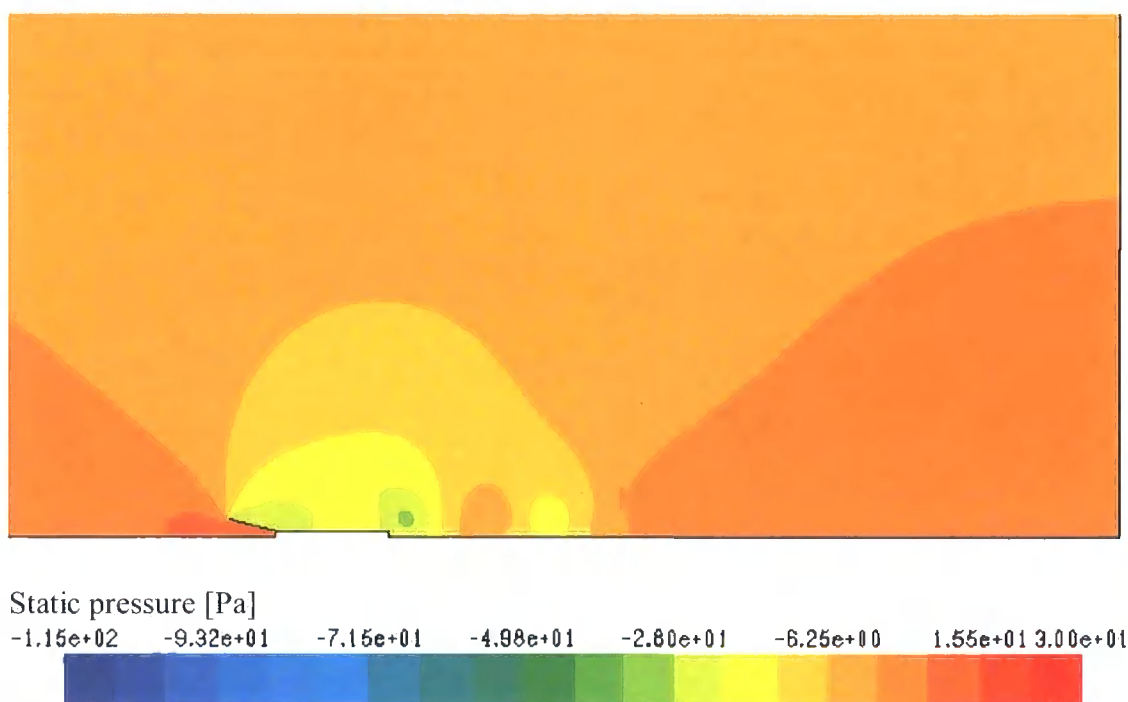


Figure 5-28 Static pressure contours for incidence angle of 15°

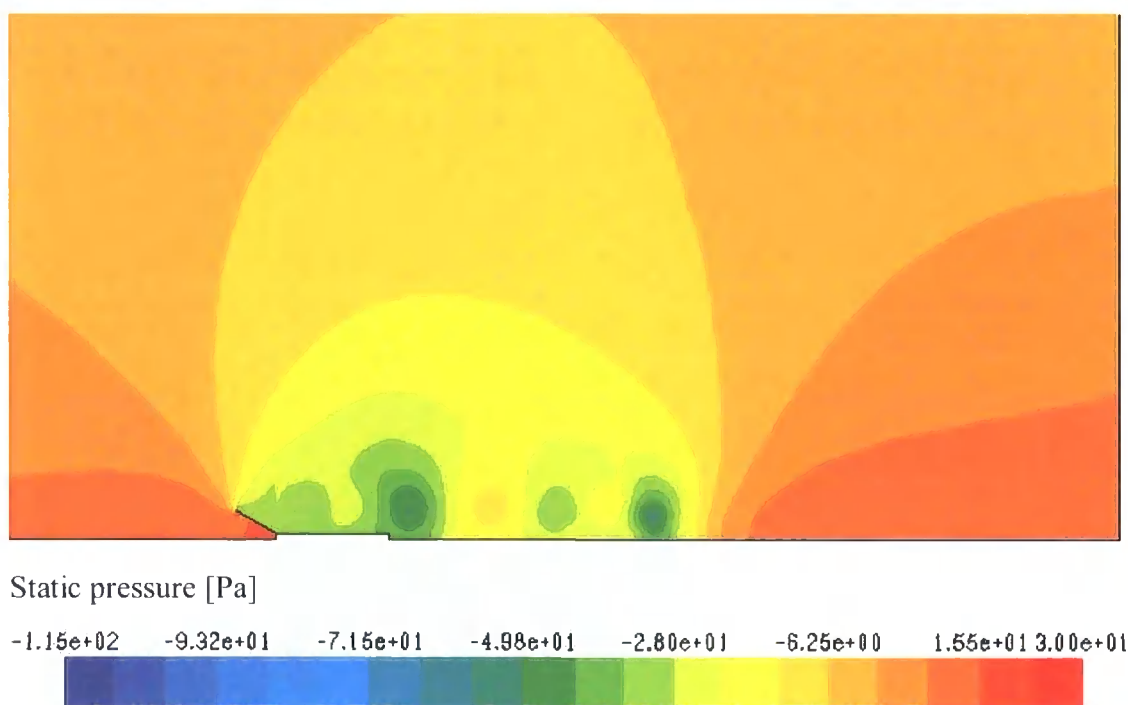


Figure 5-29 Static pressure contours for incidence angle of 30°

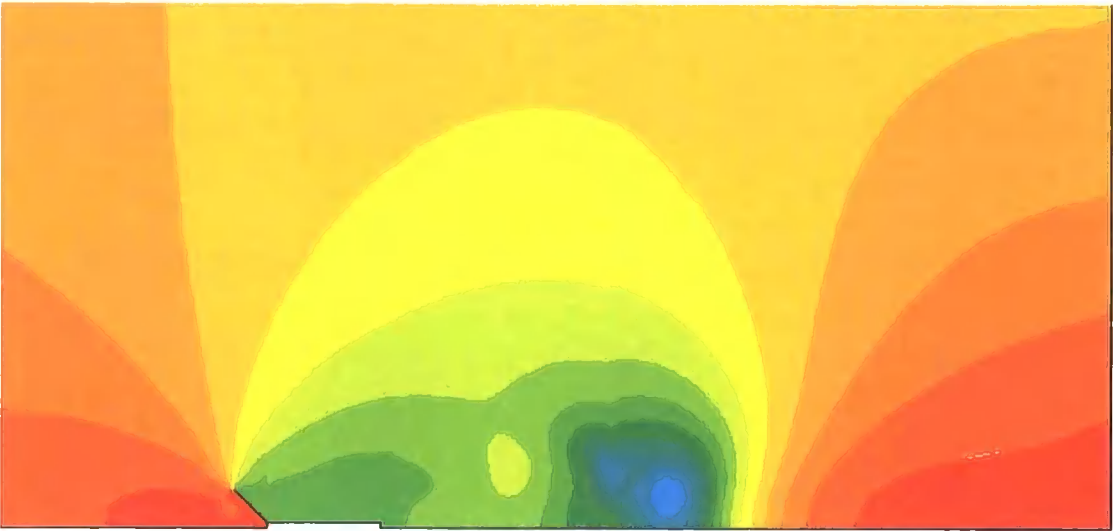


Figure 5-30 Static pressure contours for incidence angle of 45°

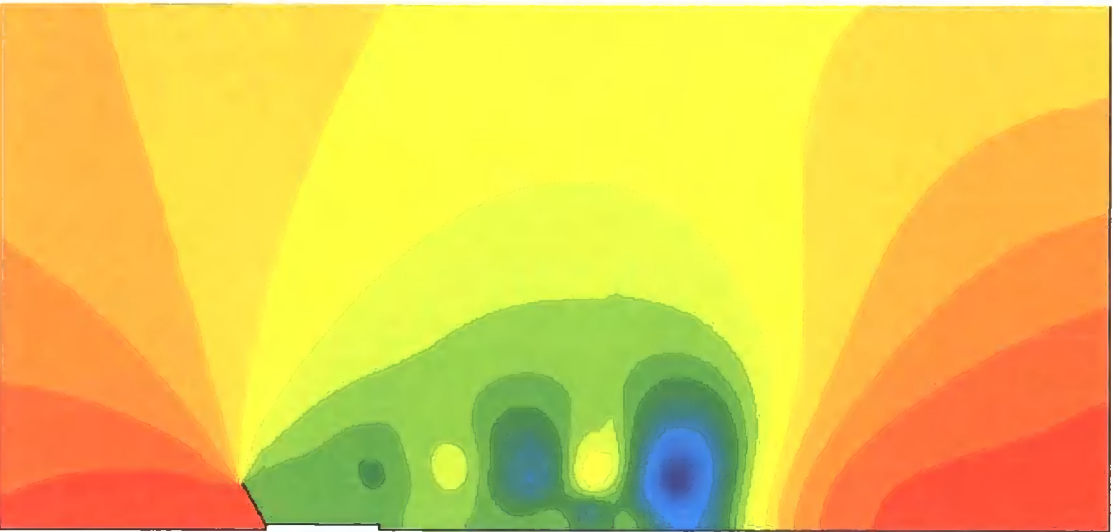


Figure 5-31 Static pressure contours for incidence angle of 60°

It can be clearly seen that, as in the case of the fence, the magnitude of the low pressure in the area above the cantilever is much greater than the magnitude of the high pressure



in the area beneath the cantilever. The high pressure is limited to stagnation pressure  $C_p = 1$ , while low pressure can go down to a value of  $C_p \leq -3$ .

The plots of static pressure indicate that for incidence angles greater than  $5^\circ$  there are vortices shed from the cantilever. This is another incentive for minimising the deflection of the cantilever upwards in the airflow, in order to minimise this behaviour of the fluid flow as far as possible. Since a steady-state calculation has been carried out, the plots here are an attempt to represent a steady flow for these boundary conditions, despite the fact that in reality the flow is transient where vortex shedding takes place and thus a fully converged solution is not reached.

The moment acting on the cantilever for varying incidence angles at different velocities is shown in Figure 5-32.

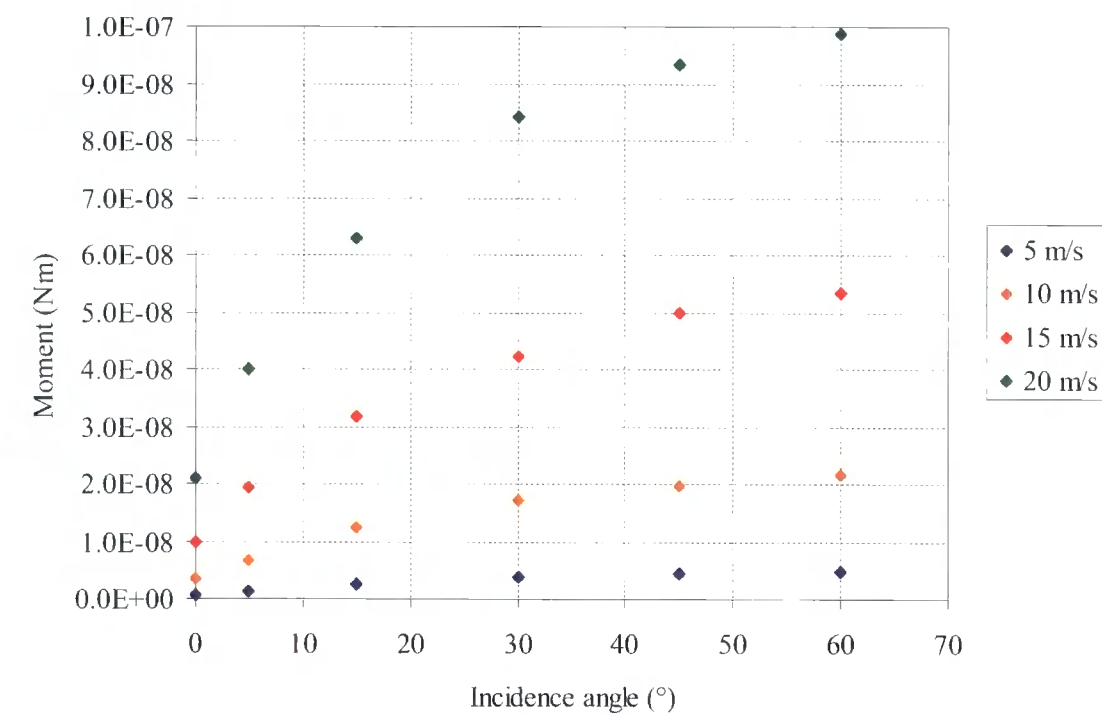


Figure 5-32 Moment on cantilever for varying incidence angle and velocity

It can be seen that the moment acting on the cantilever increased with increasing incidence angle. However, at high incidence angles, as was anticipated, the rate of change of moment decreased as the flow stalls, which decreased the lift on the cantilever. However at these high incidence angles the moment continues to increase as

it becomes dominated by the drag acting on the cantilever. This effect can be seen at all velocities.

The lift generated by the airflow acting on the cantilever is shown in Figure 5-33.

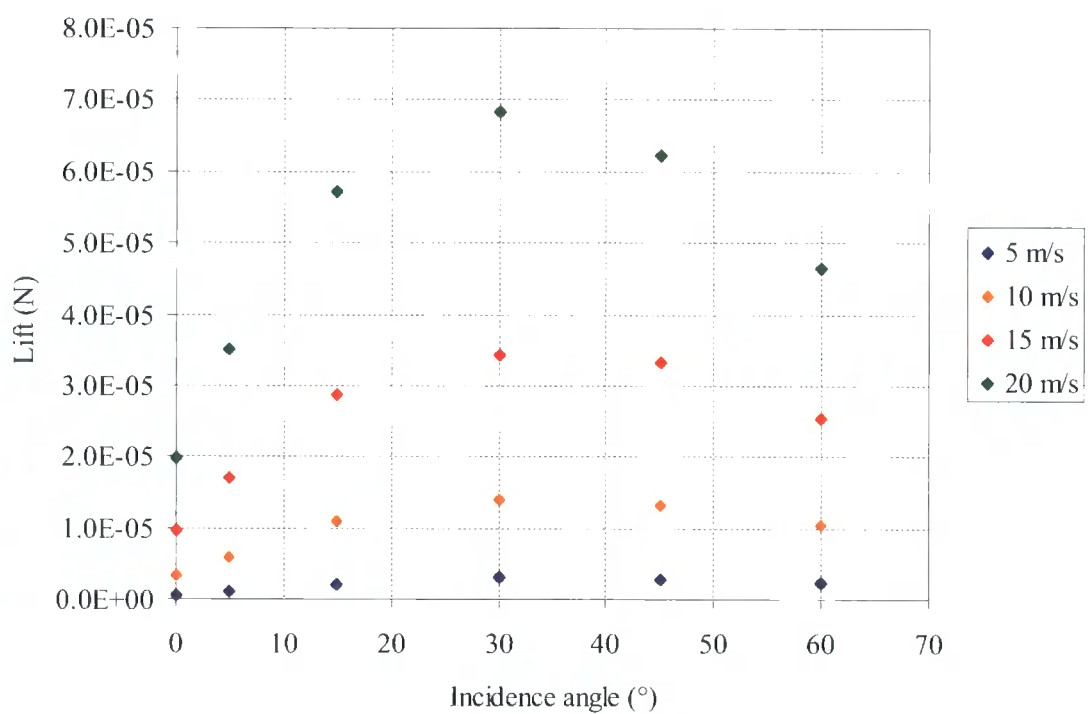


Figure 5-33 Lift on 2 mm cantilever

It can be seen that the cantilever stalls at an incidence angle of between 30° and 45°, where the lift decreases rapidly. The peak lift at 30° at 20 m/s corresponds to a lift coefficient of 1.3, where this was calculated using the local velocity at a position within the boundary layer halfway along the cantilever.

The drag generated by the airflow on the cantilever is shown in Figure 5-34.

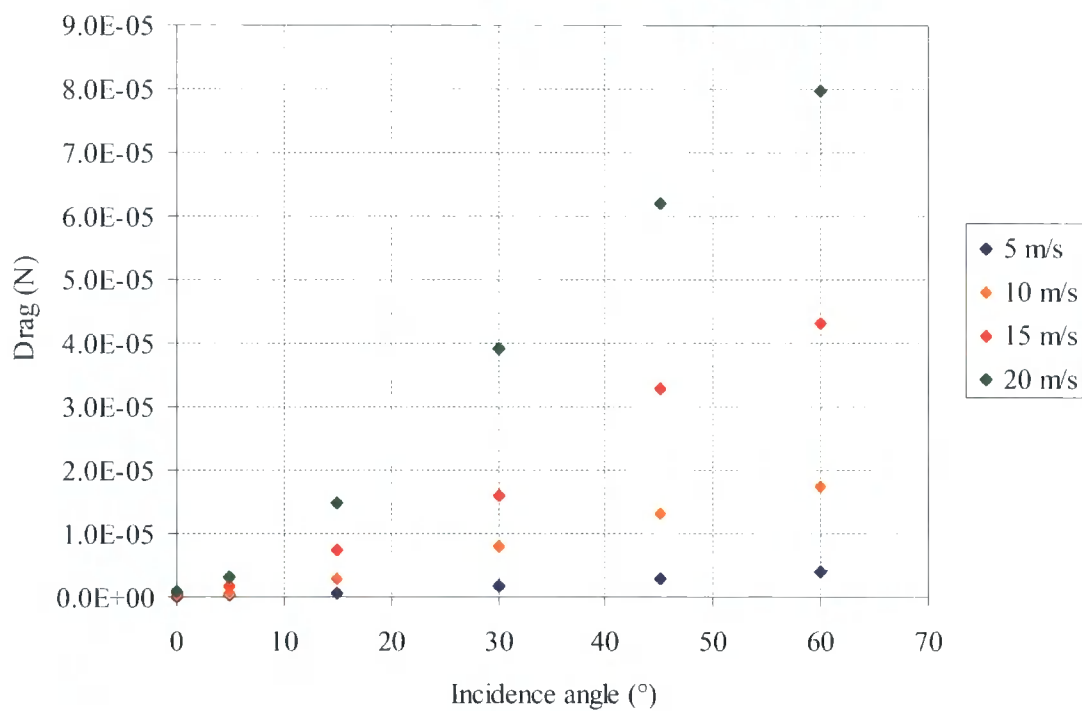


Figure 5-34 Drag on 2 mm cantilever

The drag on the cantilever continues to increase after the airflow has stalled. The drag coefficient at the maximum drag at 60° at 20 m/s is 0.5, again calculated using the local velocity within the boundary layer.

The forces have been plotted here rather than lift and drag coefficients because of the difficulty of obtaining a realistic coefficient for an object within the boundary layer. The velocity (Reynolds number) changes the thickness of the boundary layer and hence the shape of the velocity profile in the region of the cantilever. Changes in incidence angle also alter the position of the cantilever in the boundary layer and therefore the velocity and velocity gradients seen by the cantilever. These variations in velocity make it difficult to define a useful lift coefficient.

The variations in the boundary layer at different velocities and heights are illustrated in Figure 5-35.

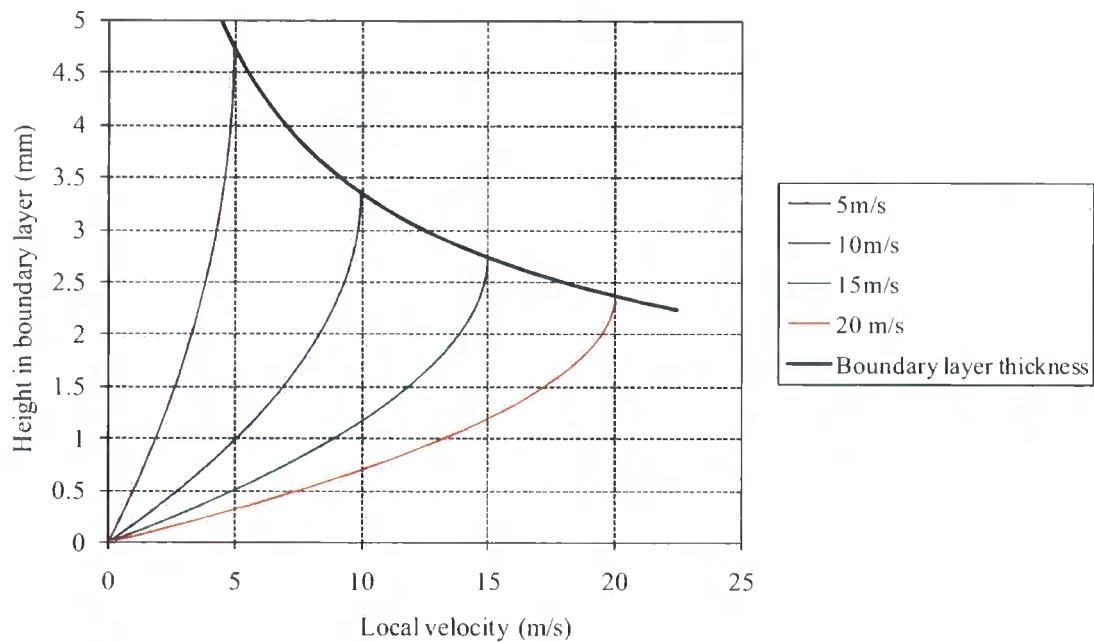


Figure 5-35 Boundary layer profiles and thicknesses for varying speeds

### 5.3.4 Combined CFD and FE results

The results from CFD of the cantilever at varying incidence angles and velocities could be combined with the FE results to predict the pressure difference and deflection of the cantilever for each velocity.

In FE modelling, the deflection for a given pressure difference across the cantilever is calculated as shown in Figure 5-22. The CFD results give a pressure difference (related to moment) for a known incidence angle (and thus deflection) as shown in Figure 5-32. Plotting these two results on the same axes means that the intersection will give the pressure and deflection for a specific velocity. This is a significantly more efficient method than using an iterative approach to the problem. Although it would be possible to use CFD pressure results as an input for the FE model to calculate a new deflection, which could then be reintroduced to the CFD model to give a new pressure for the FE model - this process would then be repeated until a constant result was achieved. However this approach would be computationally expensive as a large number of

iterations would be required to achieve a stable result, and each CFD run at a different deflection would require a new mesh, which is time consuming to produce. The approach used here allows as few as three CFD simulations to be made.

The results for a freestream velocity of 5, 10, 15 and 20 m/s are plotted in Figure 5-36, Figure 5-37, Figure 5-38 and Figure 5-39 respectively.

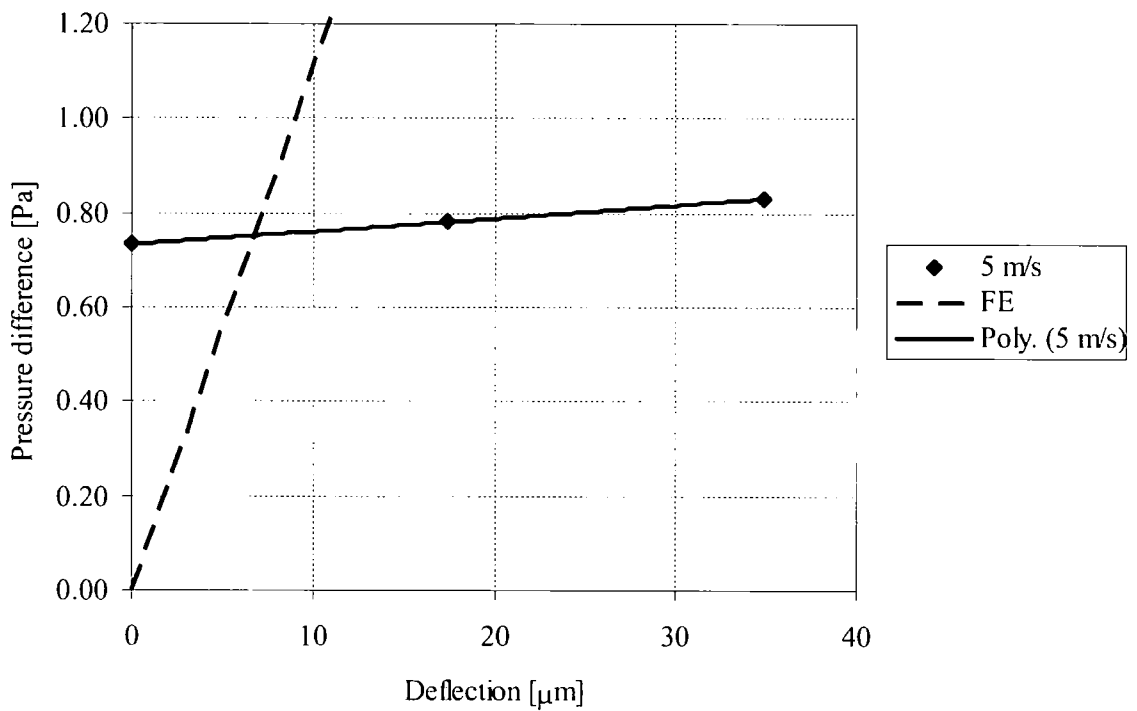


Figure 5-36 CFD and FE results for 5 m/s

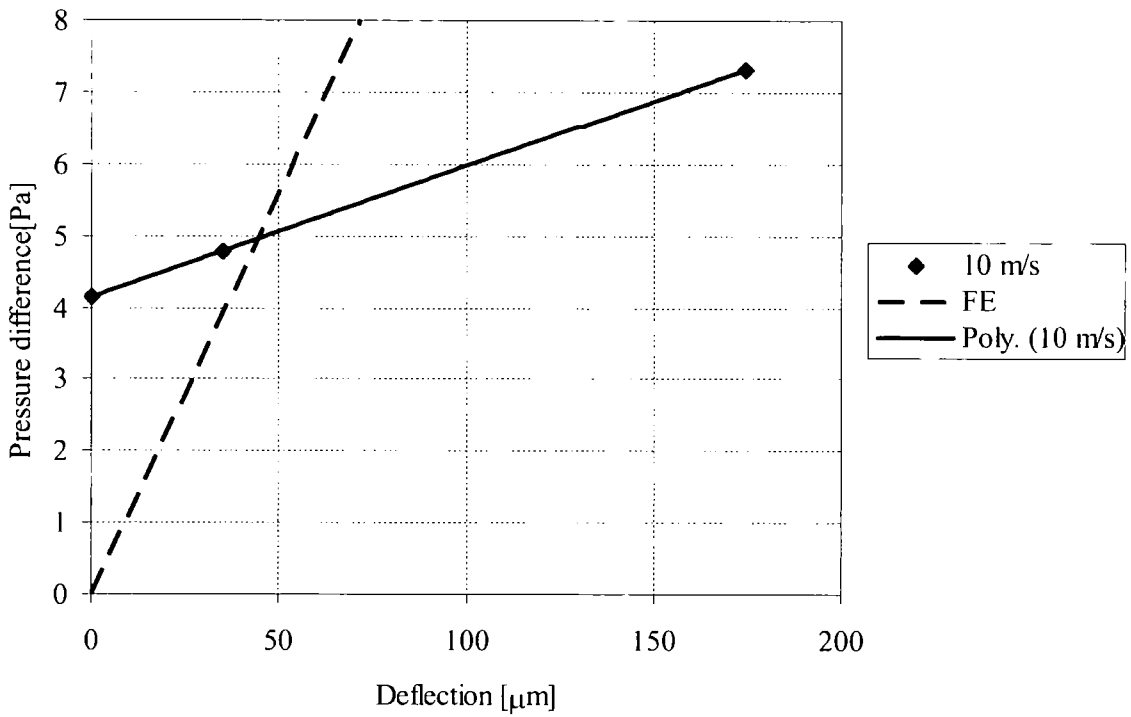


Figure 5-37 CFD and FE results for 10 m/s

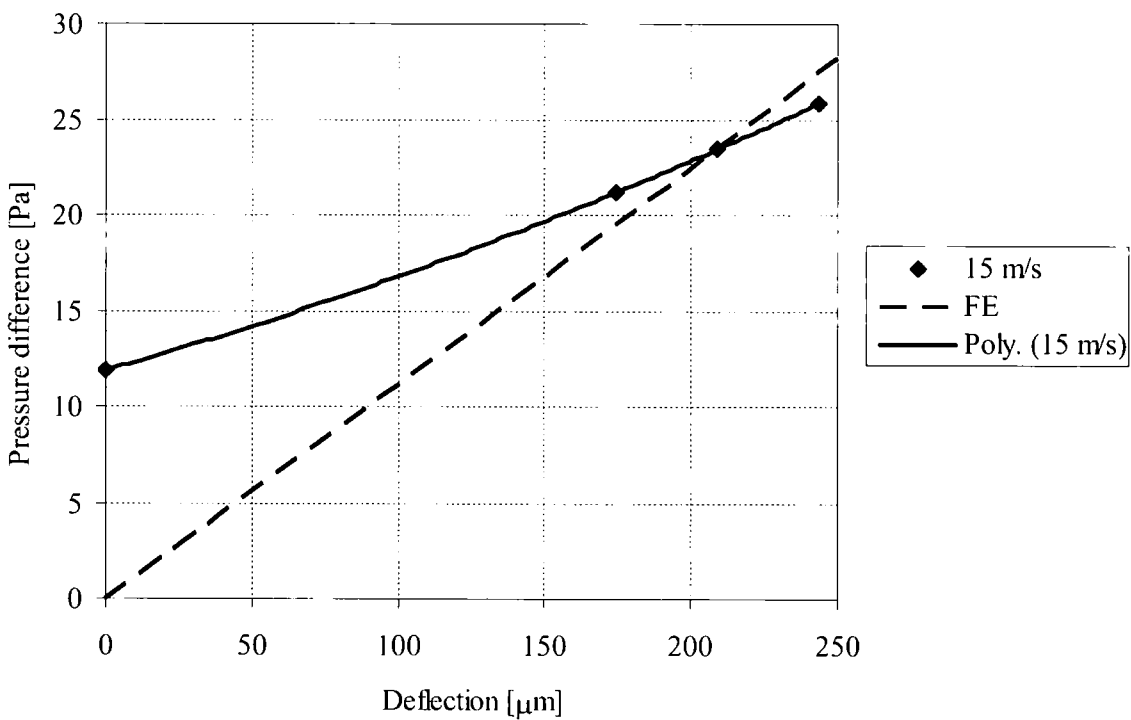


Figure 5-38 CFD and FE results for 15 m/s

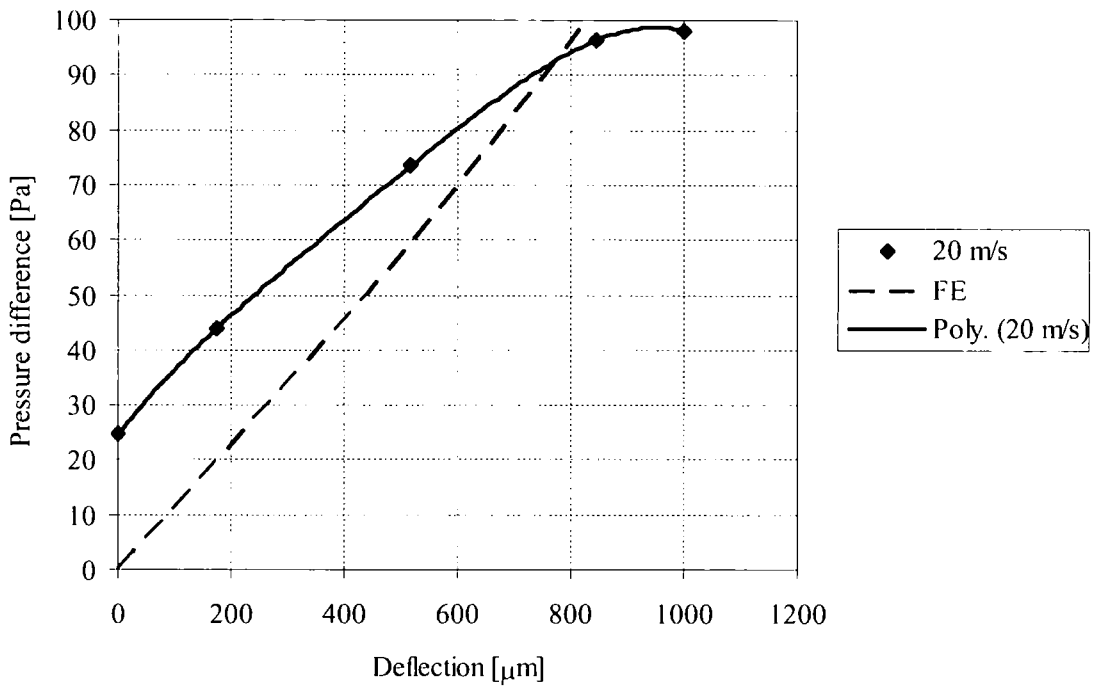


Figure 5-39 CFD and FE results for 20 m/s

The non-linearity of the FE results at high pressures only become important at the highest velocity shown here, of 20 m/s. The deviation from linear can be seen in Figure 5-39. These graphs are combined in Figure 5-40 and Figure 5-41.

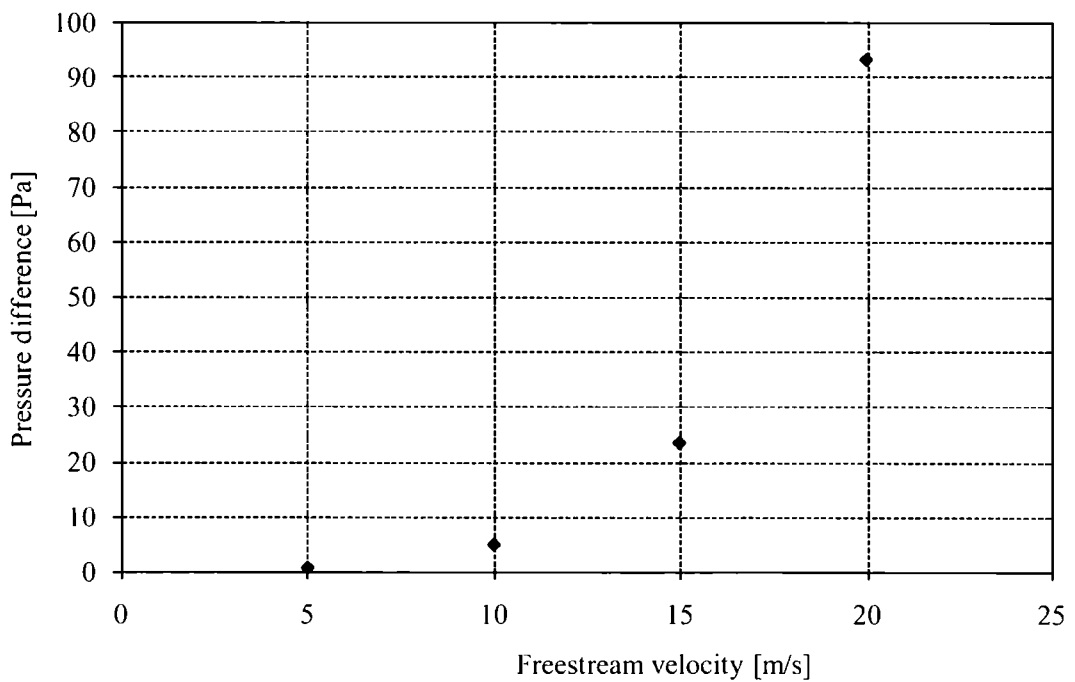


Figure 5-40 Pressure difference v. velocity from CFD and FEA for 2 mm cantilever

As can be seen from Figure 5-40, the pressure difference across the cantilever increases at a more than linear rate, which is to be expected. With a fixed geometry and boundary layer profile, pressures will increase with velocity squared. However the pressure difference would be expected to increase at a rate greater than this due to the decreasing thickness of the boundary layer and the mechanical deflection causing increased loading.

The deflection results are shown in Figure 5-41.

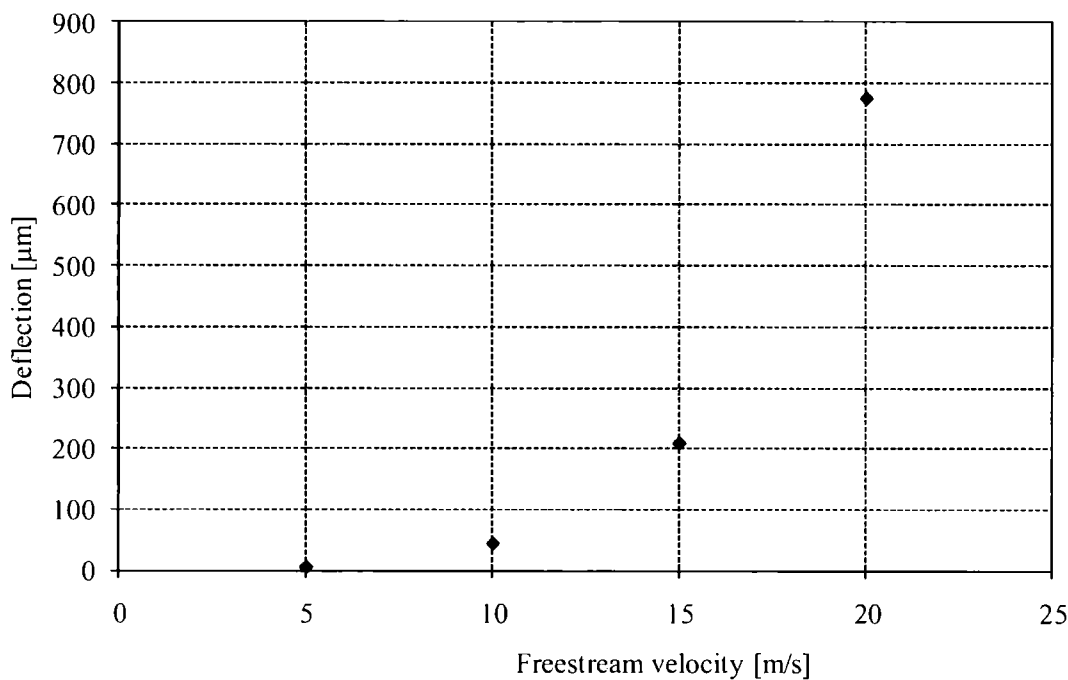


Figure 5-41 Deflection v. velocity from CFD and FEA for 2 mm cantilever

Since deflection and pressure have a linear relationship at lower deflections, the shape of this graph is very similar to that of the graph of pressure.

The results from the mechanical testing of the cantilevers was used to ascertain the change in resistance that could be expected from the strain gauge for a given tip deflection and this was then used to calculate the expected cantilever output for a given tip deflection. This calculation was done using the relationship between tip deflection and sensor output in (5-38).



The results of this analysis are shown in Figure 5-42.

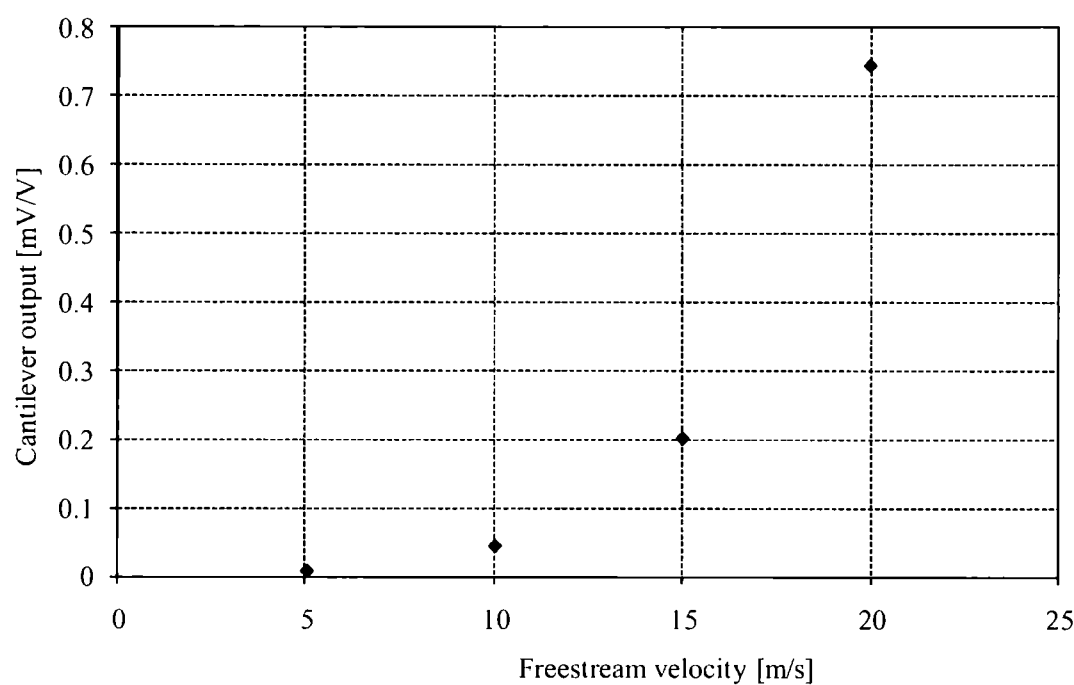


Figure 5-42 Expected output from 2 mm cantilever using CFD and FEA modelling and mechanical testing results

These expected outputs from the sensor are for a 2 mm, 400  $\mu\text{m}$  wide cantilever, and as such would be the lowest expected results. The longer cantilevers would be expected to give a greater sensitivity.

**5.3.5 Wind tunnel results**

*Effect of cantilever dimensions*

Three different lengths of cantilevers and two different widths were tested in the wind tunnel in order to establish how the sensitivity of the device changed with the geometry of the cantilever. The results of the wind tunnel testing are shown separately for different lengths of cantilevers.

A table of the initial tip deflections for all of the cantilevers tested is shown in Table 5-5. Sensors labelled ‘A’ are all from the same substrate, and sensors labelled ‘B’ are all from a different substrate. 1 and 2 denote different sensors from the same substrate.

Length (mm)	Width ( $\mu\text{m}$ )	Sensor	Tip deflection ( $\mu\text{m}$ )
2	400	A1	84
2	400	B1	68
2	600	A1	0
2	600	B1	0
3	400	A1	236
3	400	B1	41
3	400	B2	158
4	400	A1	137
4	400	A2	276
4	400	B1	140

Table 5-5 Initial tip deflections for all cantilever sensors

Results for the 2 mm long cantilevers are shown in Figure 5-43 with both the 400 and 600  $\mu\text{m}$  widths. The results shown include multiple tests for each sensor.

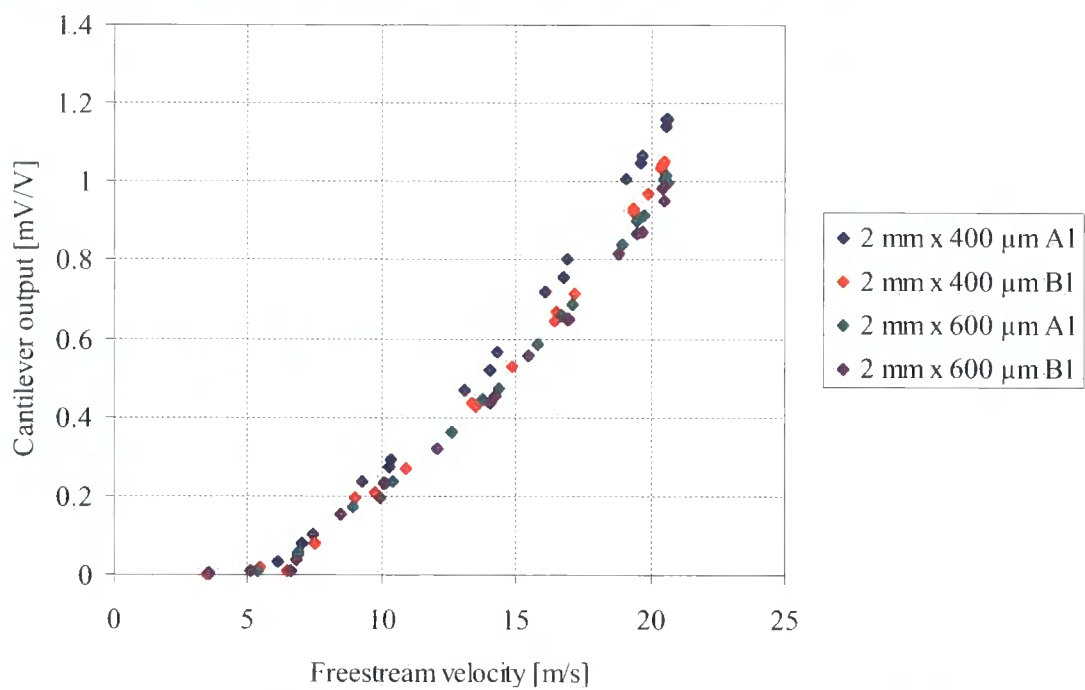


Figure 5-43 Results for 2 mm cantilevers, 400 and 600  $\mu\text{m}$  widths

The results are plotted against freestream velocity as this is accurately measured using the static pressures before and after the contraction in the wind tunnel, and applying the

calibration as described in §3.3.1. Results for shear stress come from the Preston tube on the plate and rely on the gradient of the boundary layer profile being constant in this region, which therefore gives less reliable results.

It can be seen that the repeatability between different sensors is quite good and that the varying widths of the cantilevers has a minimal effect. It is possible that the similarity of the results between the two widths is in fact due to two compensating factors. The wider cantilevers would be expected to have a higher average pressure under them and hence to show a larger response. However the wider cantilevers also had a smaller positive initial tip deflection than their narrower counterparts, which would imply a smaller response and it is possible that these two effects cancel each other out.

The general shape of the response curve is not linear, but a higher order polynomial, which is what would be expected as in Figure 5-42. At low velocities the response is very small and this corresponds with the expected results. As the cantilevers deflect, they see a larger force, as they are higher up in the boundary layer where the velocity is greater. This effect is compounded by the fact that pressure increases with velocity squared and the cantilevers deflection is a function of the pressure drop across the cantilever.

The results for the 4 mm long cantilevers, with a width of 400  $\mu\text{m}$  are shown in Figure 5-44.

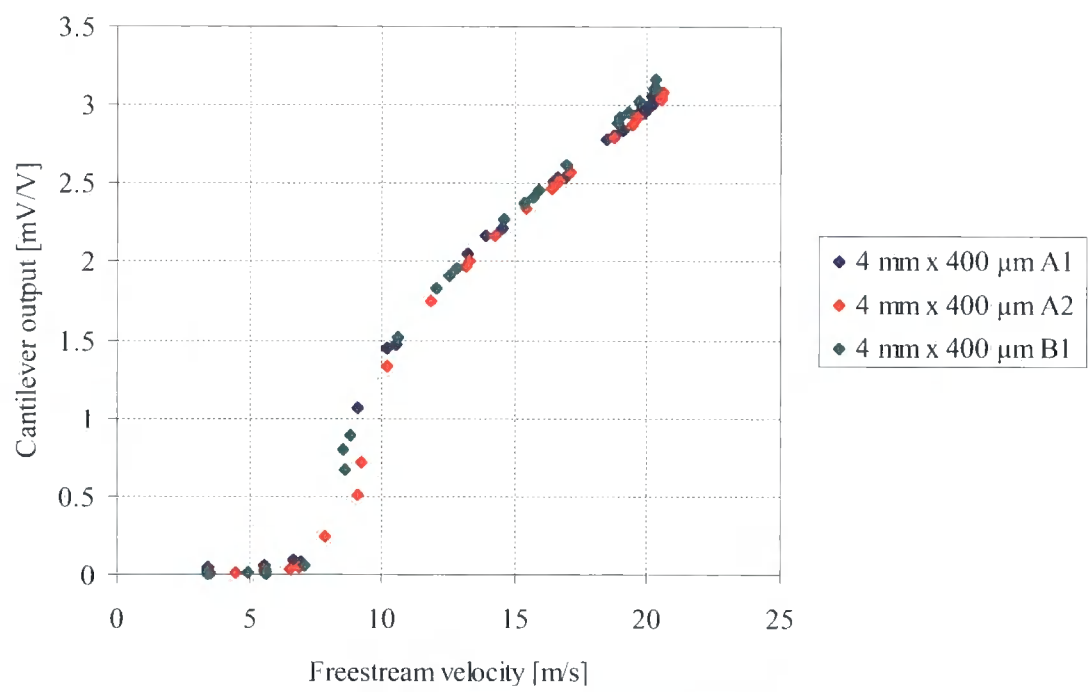


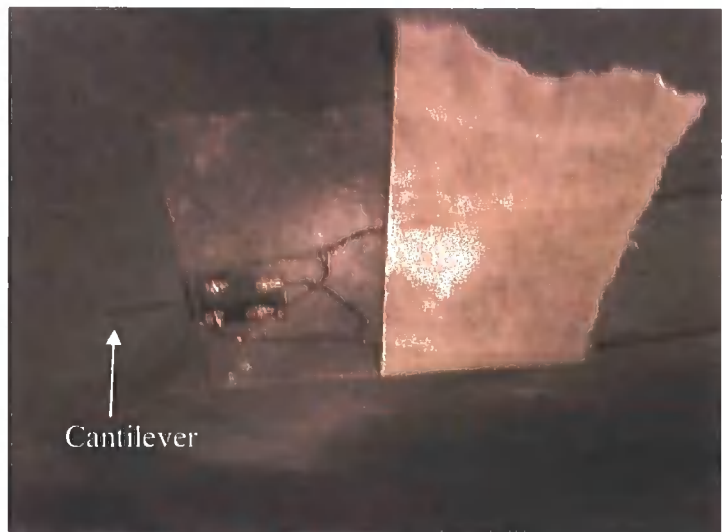
Figure 5-44 Results for 4 mm cantilevers

It can be seen that the sensitivity is significantly increased for this longer cantilever. At 10 m/s the voltage output of the 4 mm long cantilever is approximately six times that for the 2 mm long cantilever.

At low velocities the shape of the calibration curve is similar to that of the shorter cantilevers, but as the velocity increases, the shape deviates from that which might have been expected. This is because these longer cantilevers were observed to curve back over the body of the device in a semi-circular shape and thus, although the strain in the cantilever continues to increase, the rate of change of that strain decreases. As the cantilever deflects it sees a greater pressure and consequently deflects further as this increase in pressure has a non-stabilising effect.

The deflection of the cantilevers is shown in Figure 5-45. The excessive deflection in the airflow can be clearly seen, when compared with the undeflected cantilever. This excessive deflection is the cause of the diminishing rate of change of strain seen in the graph of results. Both the undeflected cantilever in zero airflow and the cantilever in a 20 m/s flow causing the arc deflection are shown.

a)



b)

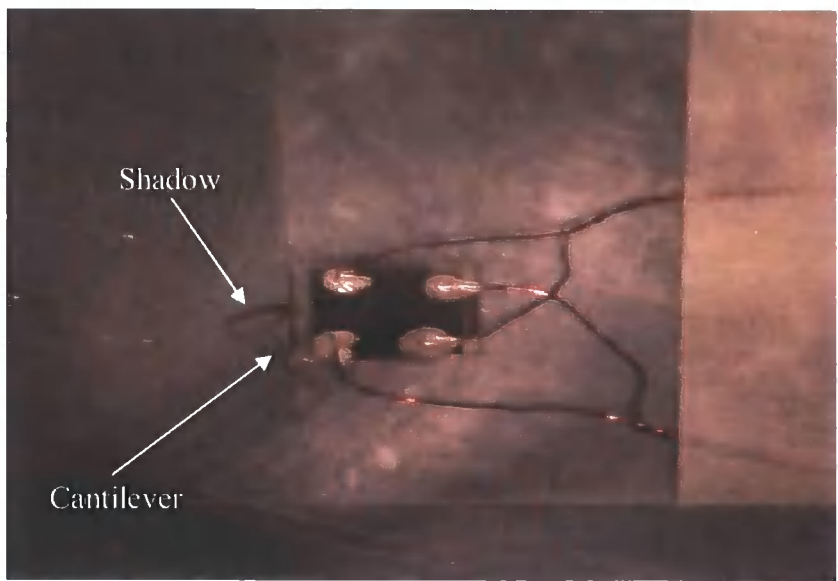


Figure 5-45 (a) Undeflected 4 mm cantilever; (b) Cantilever deflected in airflow

Where the cantilever is deflected in Figure 5-45 (b), the cantilever itself can be seen and also the shadow cast onto the plate on which it is mounted. The sensor is mounted on the underside of the plate.

The results from the 3 mm long cantilevers, with a width of 400  $\mu\text{m}$  are shown in Figure 5-46.

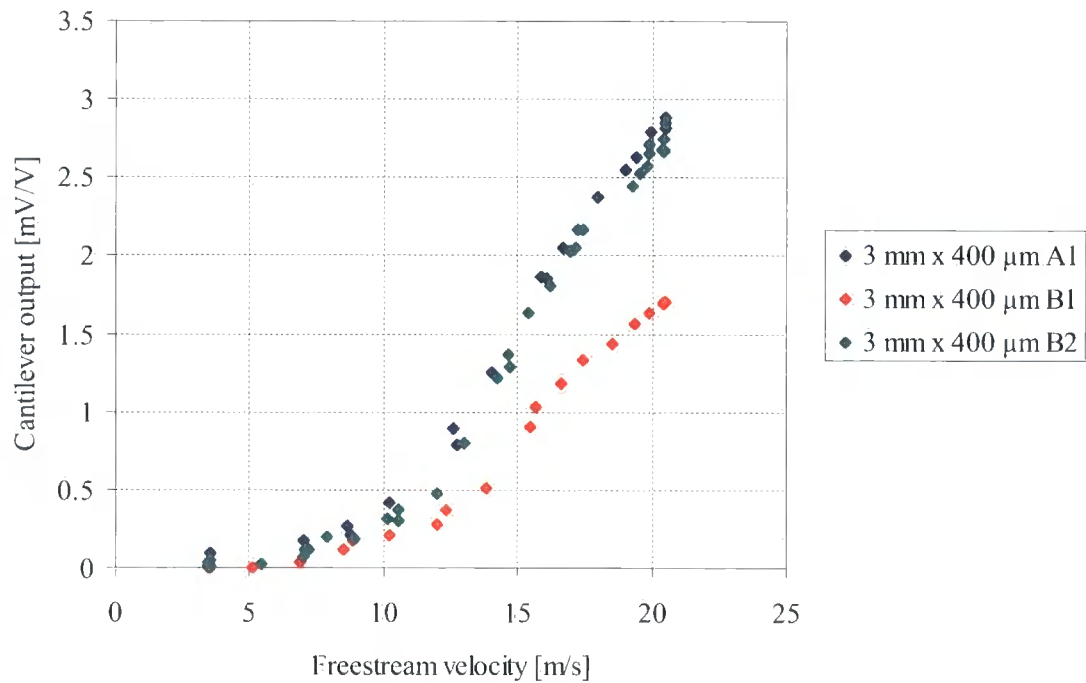


Figure 5-46 Results of 3 mm long, 400  $\mu\text{m}$  wide cantilevers

It can be seen in these results that the initial tip deflection of the cantilever does have an impact on its response. The two devices with similar tip deflections give very similar results. However, the device that has a significantly lower tip deflection (Sensor B1) than the others gives a noticeably smaller response at the same velocity. It appears that where the initial deflection is larger, variations do not have a significant effect, but where the deflection is small a difference is seen. This is why this effect is seen in these 3 mm cantilevers, but not in the longer 4 mm cantilevers, where the anomalous initial tip deflection is larger (Sensor A2) than the typical deflection and not smaller.

It would also appear that the 3 mm long cantilevers are also susceptible to the excessive arc deflection seen in the 4 mm cantilevers but not in the shortest 2 mm long cantilevers. This is what causes the decrease in the rate of change of the voltage output

from the sensor for high velocities. However, as would be expected, the effect is less pronounced in these shorter cantilevers.

*Effect of variation of excitation voltage*

The effect of varying the excitation voltage is shown in Figure 5-47. The sensor used for this test was a 4 mm x 400  $\mu\text{m}$  sensor B as this sensor gave representative results for a sensor of these dimensions.

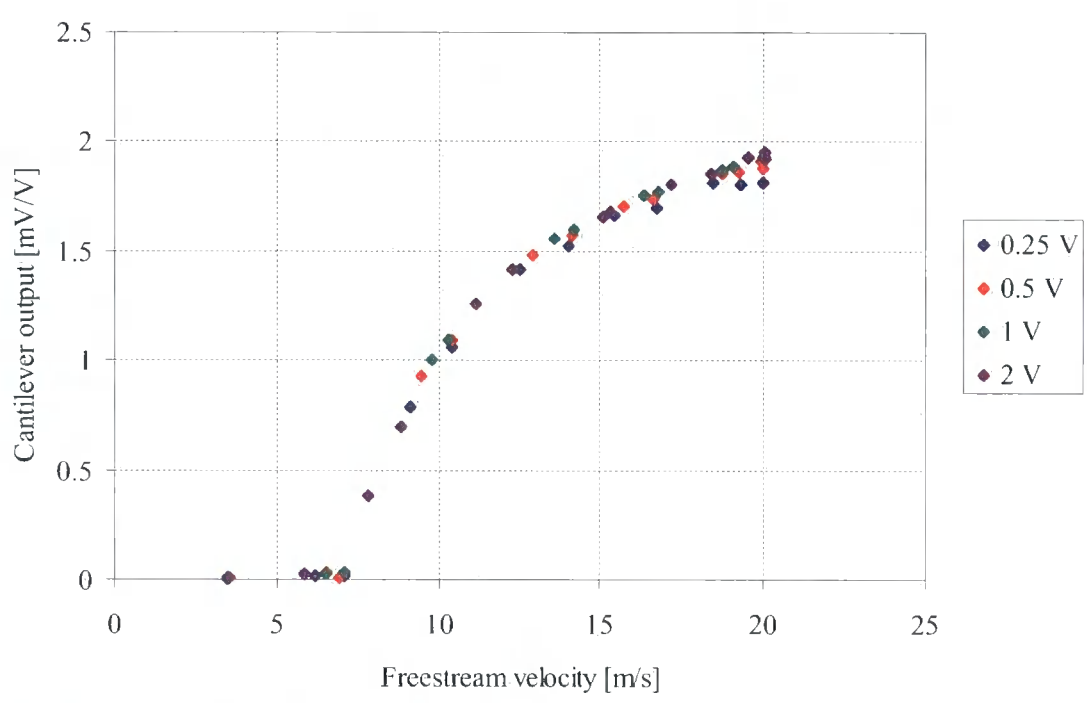


Figure 5-47 Effect of varying excitation voltage

It can be seen that the mV/V sensitivity of the cantilever is independent of the supply voltage. Increasing the supply voltage would be expected to increase the heating of the strain gauge and hence the thermal noise of the sensor.

The thermal effect would be expected to be greatest at low velocities as the cooling effect of the airflow by forced convection has least impact and consequently the resistive heating effect in the strain gauge increases the temperature of the metal by the greatest degree.

However it can be seen that the effect of the resistive heating on the sensor output is negligible, as predicted by the CFD modelling shown in §5.3.2.

*Effect of variation of axial position*

A 4 mm cantilever was placed at two different axial positions, 0.125 m and 0.25 m downstream of the leading edge of the plate, in order to subject the sensor to different boundary layer thicknesses. The sensor used was a 4 mm x 400  $\mu\text{m}$  cantilever A2. The results are shown in Figure 5-48.

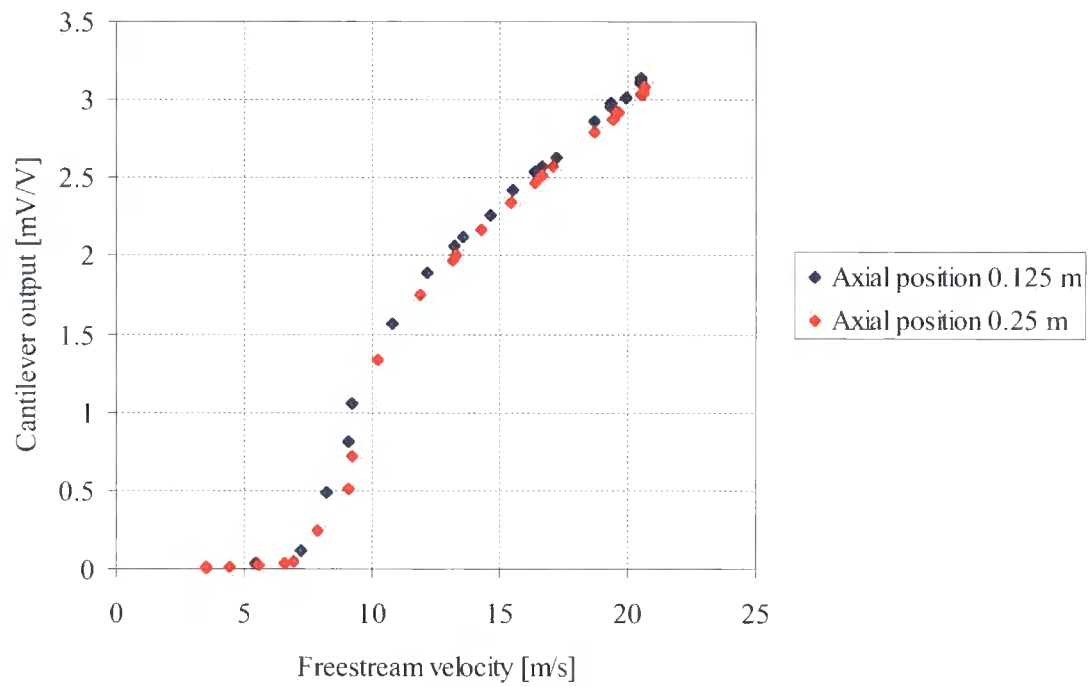


Figure 5-48 Effect of varying axial position, plotted against freestream velocity

These results would give a better indication of the effect of the axial position if they were plotted against shear stress rather than freestream velocity, because although the freestream velocity remains the same regardless of the position of the sensor on the plate, the shear stress changes due to the size of the boundary layer, which at an earlier axial position is smaller than further along the plate. Therefore the shear stress as measured by the Preston tube mounted next to the sensor is what should be compared for the two tests.



These results are shown in Figure 5-49.

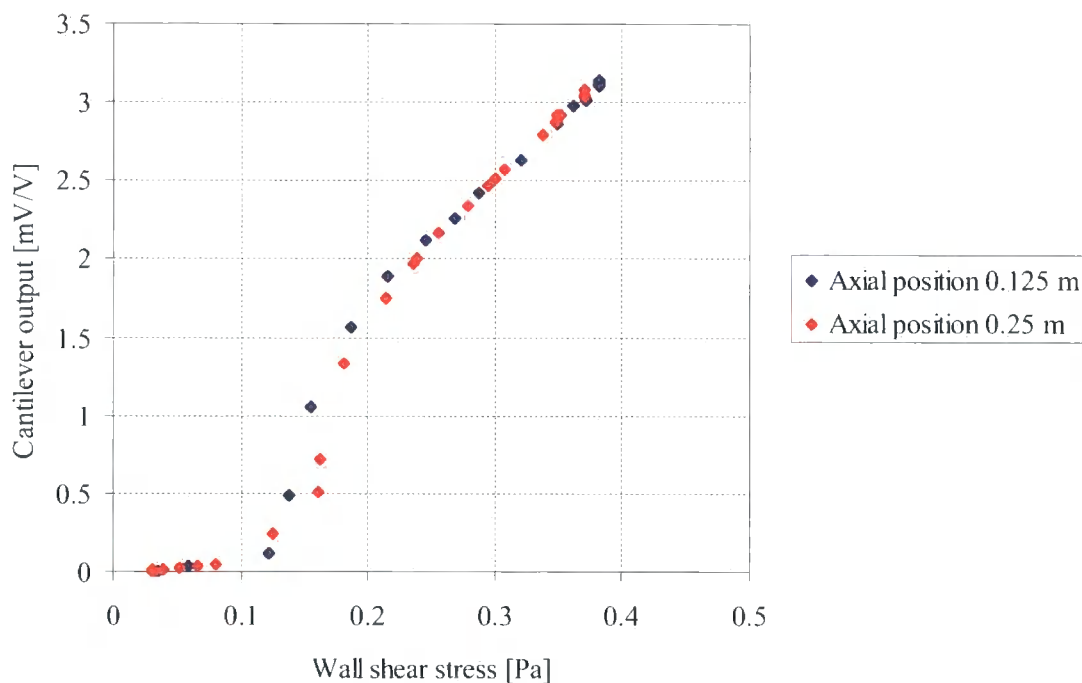


Figure 5-49 Effect of varying axial position, plotted against shear stress

It can be seen that the response in this graph is the same regardless of the position along the plate of the sensor, despite the relative differences in the thickness of the boundary layer at these positions. This means that the sensor is capable of sensing shear stress independently of the shape of the boundary layer.

***Comparison of theoretical and experimental results***

The results for a 2 mm, 400 micron cantilever were compared with the theoretical results obtained from the CFD and FEA modelling; this comparison is shown in Figure 5-50. The reason for comparing data from the 2 mm cantilevers is that they do not curl back over themselves as the longer cantilevers have shown themselves to do, which is something which could not easily be modelled in the FE or CFD modelling and is also an undesirable effect.

The results from the CFD and FEA are taken from the results calculated in §5.3.4.

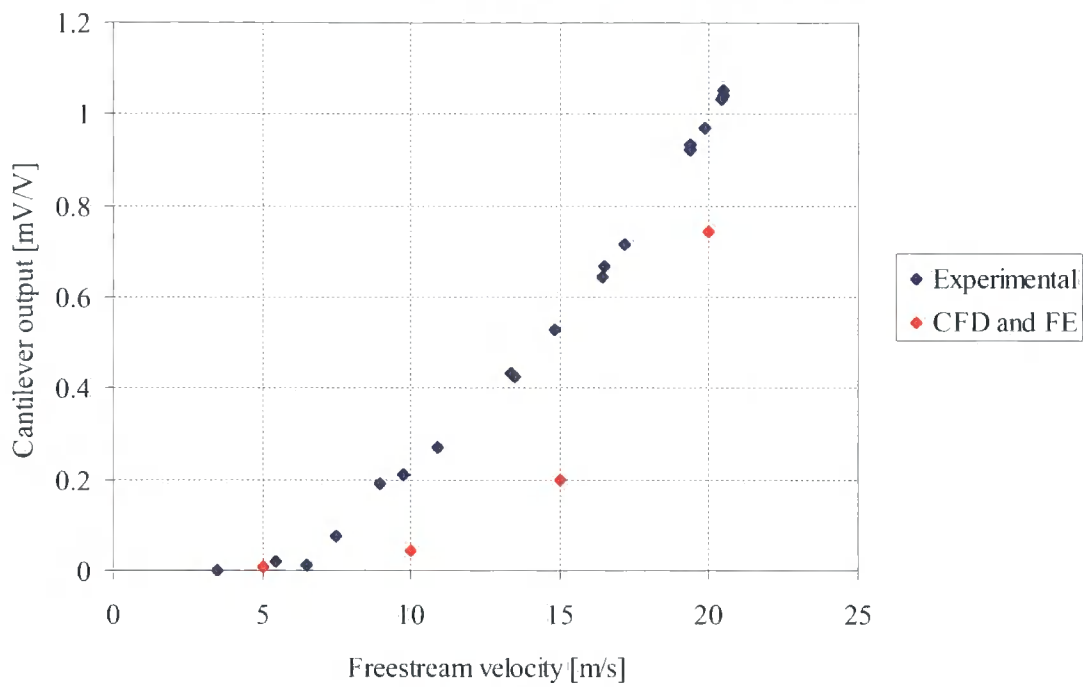


Figure 5-50 Comparison of theoretical and experimental data for 2 mm cantilever

It can be seen that the experimental results do not exactly match those predicted by the theoretical calculations, although the general trend is the same. However there are a number of limitations to the theoretical modelling that has been carried out which would probably account for the differences that are seen here. The CFD modelling has been carried out in 2D and consequently will not be entirely accurate in the prediction of the pressure difference across the cantilever. The most significant effect of the 2D modelling of a 3D situation is that the effect of leakage of the flow around the edges of the cantilever is lost and thus the CFD results would tend to overestimate the pressure difference across the cantilever. In addition the cantilever was modelled as a straight structure, while in reality it was a curved structure. This would also have an impact on the accuracy of the pressure difference that has been calculated.

The FE modelling has been carried out in 3D and consequently should give a reasonably accurate representation of the bending of the cantilever under an applied load. In addition, the Young's modulus of the cantilever that is used for these

calculations should be accurate as it has been measured experimentally for this structure and these processing conditions. However the existing stress and internal stress gradient in the material are not taken into account in the modelling. In addition, the transfer of CFD pressure data into the FE model is not detailed in that a constant pressure over the surface of the cantilever is assumed.

## 5.4 Summary

An in-plane cantilever sensor has been constructed from a composite of SU-8 and nichrome to measure wall shear stress. This sensor has been shown to measure successfully the wall shear stress over a range between 0 and 0.4 Pa. It is a sensor that is not prone to errors caused by changes in ambient temperature as it does not have high thermal sensitivity, due to the low thermal coefficient of resistivity of nichrome. The excitation voltage applied to the sensor does not have an effect on the output from the sensor, due to the lack of thermal heating in the resistor.

The sensor has been fabricated in a number of different geometries so that the influence of altering the length and width of the cantilever could be assessed. As expected it was found that increasing the length of the cantilever had the effect of increasing the sensitivity. However, in the longest 4 mm long cantilevers it was observed that the cantilever deflected back over the body of the sensor in an arc at higher flow speeds. This had a detrimental effect on the designed low impact of the sensor on the airflow. Ideally the sensor would not exhibit this behaviour, and in effect these longer cantilevers were too sensitive for the application for which they were being used.

Varying the width of the cantilever did not have a significant influence on the sensitivity of the cantilever. It would have been expected that the wider of the cantilevers had a greater sensitivity due to leakage of the airflow around the edges of the cantilever being more pronounced for a narrower cantilever, but this was not found to be the case. However where edge effects do not have an effect on the flow, the increased pressure force from the flow would be directly compensated for by the increase in second moment of area, suggesting that the response of the cantilevers would not be affected by the width of the cantilever. This is a very useful effect as the

width of the cantilever can be reduced, with the limiting factor being only fitting the strain gauge within the structure, although the aerodynamic effects of a narrow cantilever may become pronounced at very narrow widths.

The shear stress could be measured by the sensor independently of the shape of the boundary layer when placed at different axial positions. This was ascertained by placing the sensor at a different axial position on the flat plate and comparing its response with that of the Preston tube being used to measure the shear stress along side it.

Altering the excitation voltage of the Wheatstone bridge was not found to have any influence on the response of the sensor. This means that the sensor is not affected by the heat generated in the resistors. This was as predicted by the thermal CFD modelling.

The cantilever was not seen to resonate at its natural frequency, which means that the unsteady structures within the flow did not have an influence on the response of the cantilever, suggesting potential for high frequency measurements. However work done here was carried out in a laminar boundary layer, and the cantilever would be more likely to resonate in a turbulent flow.

One alteration to the current device could improve it in several ways. Making the sensor from a combination of silicon with a doped silicon piezoresistor instead of the current polymer/metal combination would have a number of advantages. One of these would be that while the sensitivity would remain approximately the same due to the high gauge factor of doped silicon [63], but the higher Young's modulus of silicon would mean that the cantilever would deflect far less for the same force. The consequence of this would be that the cantilever would have significantly less impact on the airflow, and would probably remain within the laminar sub-layer of the boundary layer, which would be a great advantage. In addition, the increased Young's modulus would also have the effect of increasing the resonant frequency of the cantilever, which would be an advantage despite resonance not being seen in laminar testing. Although steady state measurements have been carried out in this work, in order to make transient measurements it would be an advantage to have a sensor with a higher resonant frequency as it would be less affected by turbulence within the airflow.

# Chapter 6

## 3D flow vector measurement

In this work the design and manufacturing process of the cantilever shear stress sensor was adapted for use in the measurement of freestream velocity vectors. Four sensors arranged in an orthogonal manner around a square section mounting allowed 3D flow measurements to be taken. The airflow probe was modelled using CFD and FEA and then two different designs of probe were tested in the wind tunnel.

### 6.1 Background

The desirable features of a probe for measuring freestream velocity vectors were described in §1.1. The principle objective in this part of the project was to demonstrate a MEMS probe design able to achieve tip dimensions smaller than the current available minimum of approximately 1 mm diameter. The MEMS probe was designed to give the same information as that available when using a five-hole probe, due to the existing mathematical parameters and experimental infrastructure for calibrating probes of this type. Additionally this type of probe is a commonly used and understood method of taking point measurements of velocity vectors making it a good basis for a new design.

A five-hole probe measures yaw, pitch, and dynamic and stagnation pressures. These are calculated from the yaw and pitch coefficients as well as the dynamic and stagnation pressure coefficients, which are obtained by calibration of a specific probe. There are different methods of defining these coefficients for a 5-hole probe, but those used at Durham University are presented here [83].

The holes are numbered as shown in Figure 6-1. Positive yaw is defined as an increase in pressure on hole 1, and positive pitch as an increase in pressure on hole 3.

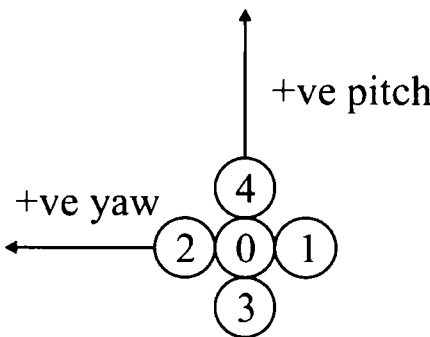


Figure 6-1 Five-hole probe numbering (view onto probe head)

The coefficients for a five-hole probe are calculated as follows:

Yaw coefficient was defined as

$$C_{Yaw} = \frac{P_1 - P_2}{P_0 - P_{av}} \tag{6-1}$$

where  $P_0$ ,  $P_1$  and  $P_2$  are the pressures recorded at holes 0, 1 and 2 respectively, and  $P_{av}$  is defined as

$$P_{av} = \frac{P_1 + P_2 + P_3 + P_4}{4} \tag{6-2}$$

Pitch coefficient was defined as

$$C_{Pitch} = \frac{P_3 - P_4}{P_0 - P_{av}} \tag{6-3}$$

The Dynamic pressure coefficient was defined as

$$C_{D_{yn}} = \frac{P_0 - P_{av}}{P_{D_{yn}}} \quad 6-4$$

where  $P_{dyn}$  is the dynamic pressure

and the stagnation pressure coefficient as

$$C_{P_0} = \frac{P_0 - P_{Tot}}{P_0 - P_{av}} \quad 6-5$$

where  $P_{tot}$  is the total pressure.

The definitions of corresponding coefficients for the MEMS probe were intended to be based on the above definitions for a 5-hole probe.

## 6.2 Theory of operation

The new probe design was intended to use similar methods of calculating the coefficients, and thus required a similar set-up with some devices sensitive to yaw and others sensitive to pitch, where the response of all of the sensors combined could be used to normalise the response of the two pairs. In addition, to allow the measurement of pressure, a hole for measuring the stagnation pressure at the probe tip needed to be incorporated into the design. This would allow the calculation of the stagnation pressure coefficient. The dynamic pressure coefficient could be obtained from the response of all four sensors, as were used to normalise the responses for the yaw and pitch coefficients.

Using multiples of the cantilever shear stress sensors it was possible to measure the velocity vectors. Rather than mounting the sensor on a surface in order to measure the shear stress, the sensors were mounted on a specially designed probe head. Four of them were mounted at 90° to each other. Although theoretically three sensors could be used to obtain the three velocity components, the diameter of the probe tip was not made larger by using four sensors, and therefore it was decided to build some redundancy into

the system. This mimics the structure of a five-hole probe as opposed to that of a four-hole probe if only three of the cantilever sensors were used.

A possible arrangement of the probe sensors is shown in Figure 6-2. The two pairs of sensors to measure yaw and pitch are shown as well as the central hole for pressure measurement. Strain gauges would be incorporated into the cantilever sensors as for measuring wall shear stress, in order to measure the pressure-induced deflection.

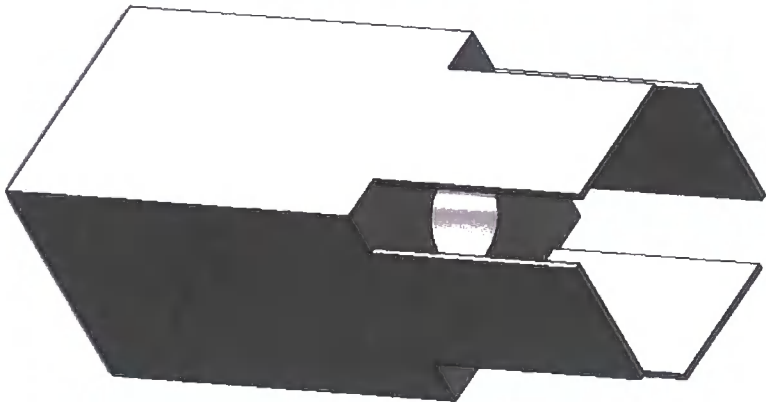


Figure 6-2 Sketch of probe tip and sensors

The four sensors on the probe are numbered as shown in Figure 6-3. Positive yaw is defined as an increase in pressure on the inside surface of sensor 1, and positive pitch as an increase in pressure on the inside surface of sensor 2.

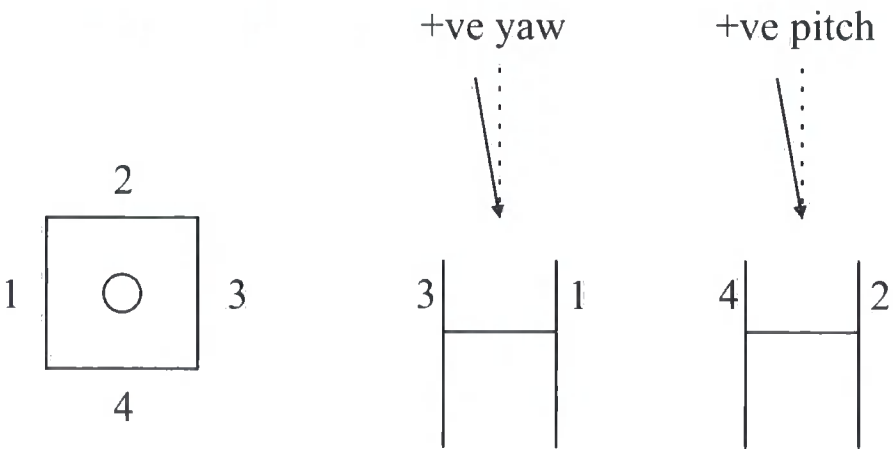


Figure 6-3 Probe sensor numbering



The coefficients obtained from the probe correspond to those which would be used for a five-hole probe. The four coefficients are defined below. They are calculated from the calibration data to produce maps of the four coefficients for varying yaw and pitch. When the probe is being used, the yaw and pitch coefficients can be calculated from the experimental data to give a pitch and yaw for the probe. These values can then be used to obtain the two pressure coefficients from the calibration which will then give the dynamic and stagnation pressures.

The assumption is that the yaw coefficient is dominated by the difference between the two sensors normal to the yaw direction, which are then normalised by using the sum of all four sensors. The pitch coefficient is the same with the other two sensors which are normal to the pitch direction.

Yaw coefficient was defined as

$$C_{Yaw} = \frac{V_1 - V_3}{V_1 + V_2 + V_3 + V_4} \quad 6-6$$

where  $V_1$ ,  $V_2$ ,  $V_3$  and  $V_4$  are the voltage outputs from the sensors in mV/V.

And Pitch coefficient was defined as

$$C_{Pitch} = \frac{V_2 - V_4}{V_1 + V_2 + V_3 + V_4} \quad 6-7$$

The Dynamic coefficient was defined as

$$C_{Dyn} = \frac{V_1 + V_2 + V_3 + V_4}{P_{Dyn}} \quad 6-8$$

where  $P_{dyn}$  is the dynamic pressure.

The stagnation pressure coefficient was defined as

$$C_{P_0} = \frac{P_{Probe} - P_0}{V_1 + V_2 + V_3 + V_4} \tag{6-9}$$

where  $P_{probe}$  is the probe pressure and  $P_0$  is the upstream total pressure.

Although the pitch and yaw coefficients are non-dimensional, the dynamic and stagnation pressure coefficients have units of (mV/V)/Pa and Pa/(mV/V) respectively.

These coefficients would be obtained from calibrating the probe, and would then be used to get the yaw, pitch and dynamic and stagnation pressures when the probe was being used in testing. The process for this is described in Figure 6-4.

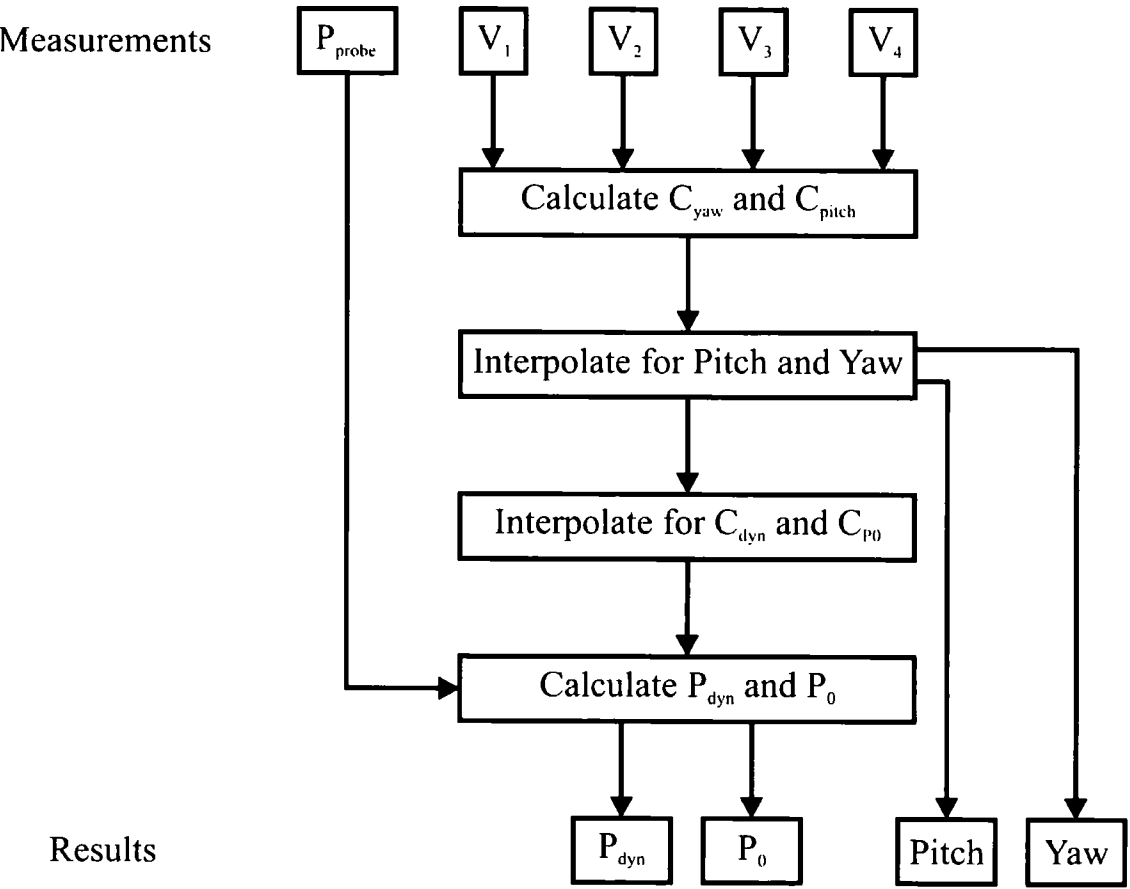


Figure 6-4 Flow chart of the use of coefficients for calculating variables

The main challenge with the construction of this probe was the assembly of the four sensors into a single probe in such a way that the electrical connections required could

be made. In order to attach the wires by silver paint as had been used previously, contact pads on the order of 2 mm across were required. This meant that the probe would have to widen to this size at the position of the contact pads for the Wheatstone bridge. However, the tip diameter could still be minimised, and this was the objective here. The angle at which the probe increased in diameter was minimised as far as possible, but the limits of this are the length of the connections from the strain gauge to the contact pads compared with the length of the actual strain gauge in the cantilever itself.

## **6.3 Design and Fabrication**

### **6.3.1 MEMS Fabrication**

The aim was to use as similar a fabrication process as possible for making the MEMS devices as was used for making the cantilever shear stress sensors. This was largely possible due to the similarity of the sensing structure; however the device could be simplified in some areas, which was found to increase the yield.

It was no longer necessary to incorporate a step to create the cantilever as was required when the sensor was mounted on a surface. Instead the cantilever structure was created by overhanging the sensing element in the way it was mounted on the probe as a whole. This meant that the thick 100  $\mu\text{m}$  layer of SU-8 was unnecessary and could therefore be eliminated, meaning that the number of masks required was reduced from three to two. In MEMS fabrication any reduction in the number of masks is advantageous as the probability of defects occurring increases rapidly with each additional photolithographic step. This is due not only to defects in the masks themselves, but also problems in processing.

In addition, the elimination of this step meant that the contact pads could be fabricated on the same side of the SU-8 layer as the strain gauge meaning that there was no longer a requirement to have good step coverage when depositing the nichrome, as this step could be eradicated. Since the nichrome would therefore no longer be deposited directly onto the sacrificial layer, this also simplified the release method allowing the device to be fabricated directly on Prolift without the overlying layer of titanium required for the fabrication of the shear stress sensors.

The layout of the probe sensor is shown in Figure 6-5.

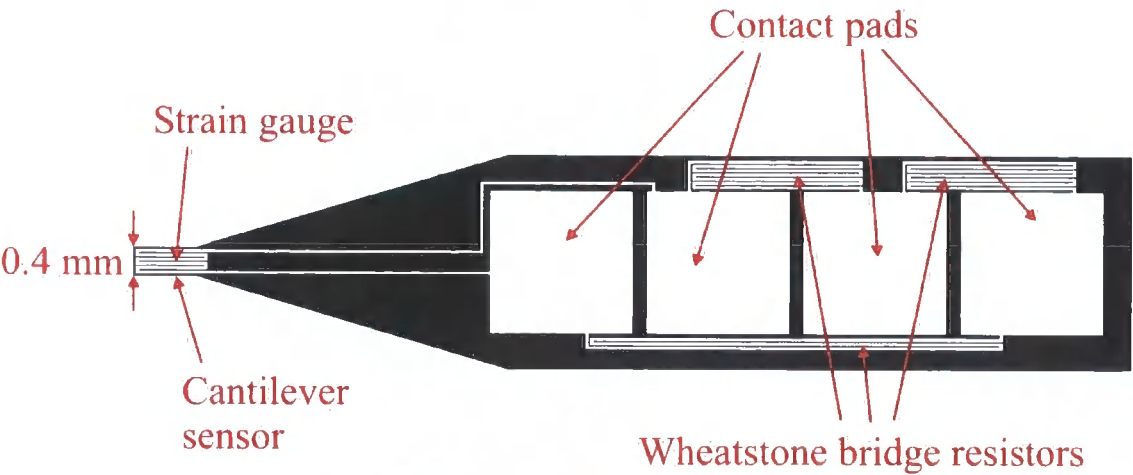


Figure 6-5 The probe sensor

The strain gauge in the cantilever section can be seen as well as the other resistors of the Wheatstone bridge. Because of the need to make the diameter of the probe as small as possible, the layout is constrained to this elongated design. The contact pads are 2 mm square and the width of the section containing the contact pads is 3 mm to allow room for the resistors which make up the Wheatstone bridge. This is one of the four sensors that together make up the probe.

The fabrication flow for the probe sensors is shown in Table 6-1.

a)

A Prolift layer is spun onto the silicon wafer to act as a final release layer.



b)

A 10 μm layer of SU8 is then spun on, and patterned.



c)



A 125 nm nichrome layer is then deposited by sputtering, which is then patterned using a standard photolithography process, and the exposed areas are etched.

d)



The Prolift layer is then etched in TMAH to release the devices.

Table 6-1 Fabrication flow for probe sensors

This fabrication process is significantly simpler than that required to manufacture the cantilever shear stress sensor, which is a significant advantage for increasing the yield of successful sensors from each substrate. However, the devices were found to be quite fragile after release and care was required to avoid tearing them. It was possible to handle them with tweezers, however, and once mounted on the probe head this fragility became less of a problem.

6.3.2 Probe assembly

The probe was assembled from the MEMS devices mounted on to a probe head, produced using a rapid prototyping machine (Objet Eden500V). The smallest resolution nominally achievable using this machine is 0.5 mm, i.e. a 0.5 mm thick wall and a 0.5 mm hole through the material. The problem with achieving very small holes is clearing support material from the hole afterwards. Because of the intention to have a hole through the centre of the probe for measuring total pressure, and to keep the probe tip as small as possible, four different sizes of probe heads were designed, ranging from the largest which had an achievable 0.5 mm wall with 0.5 mm hole, which would thus result in a 1.5 mm total diameter, to the smallest with a total tip diameter of 0.5 mm, with the walls and hole equally spaced, which had an excellent tip diameter, but might

not be achievable using the rapid prototyping machine. A picture of the probe head with a 1 mm tip diameter is shown in Figure 6-6.



Figure 6-6 1 mm tip diameter probe head

The boss seen at the right hand end of the picture is inserted into a stainless steel tube 100 mm long, which has a standard fitting on the other end for use in Durham wind tunnels. Since this tube and the fitting are hollow, this allows the hypodermic tube for measuring the pressure to be passed through it for access to a pressure transducer. Alternatively a compact transducer could be incorporated into the probe head.

It was found that the minimum size which could be successfully produced using the rapid prototyper had a 1 mm total tip diameter, with 0.33 mm walls and a 0.33 mm diameter hole. For structures smaller than this the tip was found to have insufficiently precise edges, which was unacceptable since this forms the root of the cantilever when the MEMS devices are attached.

The MEMS devices were attached to the probe head using UV curable glue. The advantage of this type of glue was that as the probe was being assembled in the clean room, in yellow light, the device could be repositioned as necessary to allow for accurate alignment without the glue starting to set. The glue was then cured using a mask aligner, which allowed rapid curing once the device was in position. The device was exposed to UV light for 1½ minutes which was found to be sufficient to cure the glue. This method was possible because SU-8 is transparent. Under the contact pads the UV light could not penetrate through the nichrome layer, however there was found to be sufficient area around the edges of these pads for adhesion.

The MEMS devices were glued on to the probe head one at a time. This allowed them to be accurately aligned individually without interfering with devices already attached, as once the glue had been cured on one side this device was immovable.

A cross-section through the probe after the sensors have been mounted is shown in Figure 6-7.

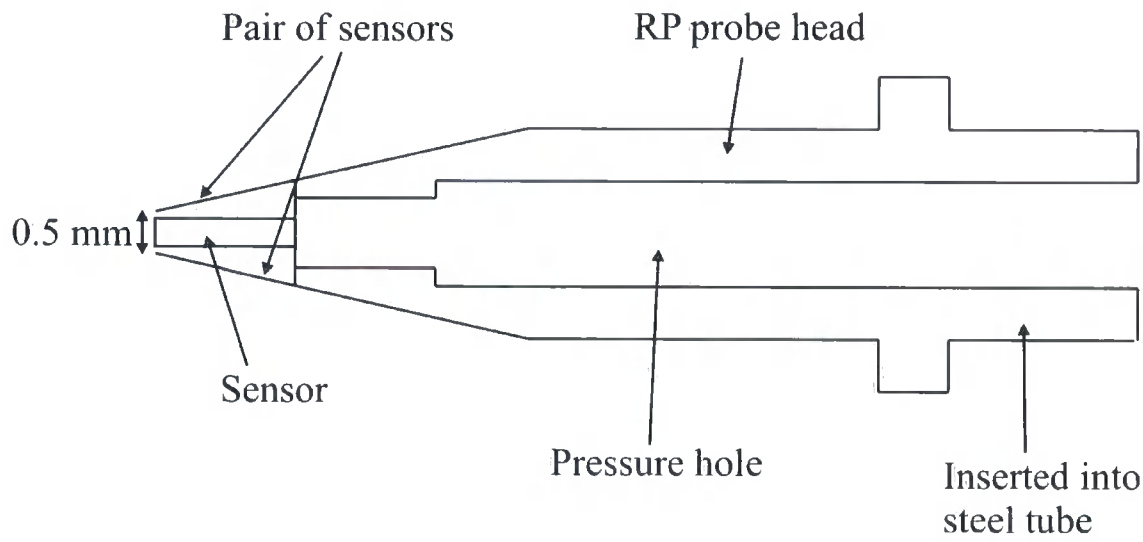


Figure 6-7 Cross-section through probe (not to scale)

A photo of the four devices mounted on the probe head is shown in Figure 6-8. The sensors on two sides of the probe are shown here. Because of the design of the probe mounting, the sensors converge, resulting in a smaller probe tip than would be the case if the sensors were parallel.



Figure 6-8 The four probe sensors mounted on probe head.

Damage can be seen on the contact pads in Figure 6-8. This was caused by measuring the resistance of the strain gauge prior to mounting the sensors on the probe head. This damage was not a problem for connecting the wires to the contact pads.

A close up photograph of the probe tip and the orientation of the cantilevers is shown in Figure 6-9.

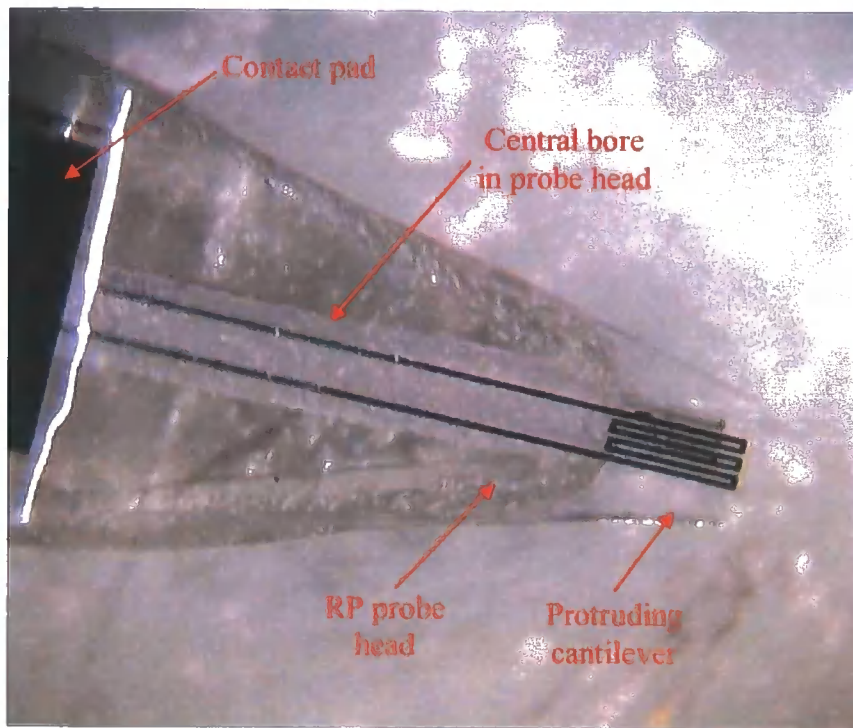


Figure 6-9 Close up of probe tip

The four cantilever sensors can be seen at the tip. The channel running through the translucent probe head material can be seen behind the resistor wires running towards the contact pads on the closest face.

The probe head did not have perfectly precise edges at the tip even with this 1 mm tip diameter and this can be seen in Figure 6-9. This means that the degree of overhang for each of the cantilever sensors could be different which would mean that the response of the probe would not be symmetric.

Once the four devices had been attached, the next step was to attach a hypodermic tube into the end of the probe head for attaching to a pressure transducer. This was done using Araldite, being careful not to block the hole. At the tip of the probe, the diameter of the hole was only 0.33 mm widening to 2 mm once the probe head was wide enough to allow this, and this was where the hypodermic is inserted. The external diameter of the hypodermic tube was 1.24 mm.



The probe head was then mounted into the stainless steel tube before the wires were attached to the contact pads due to the risk of dislodging the wires while handling the probe if this were done the other way round. Whilst ensuring a good electrical contact, silver paint does not allow a large force to be applied to the connection without failing.

Eight twisted pairs of wires were required for connections to the four Wheatstone bridges. These were secured by double-sided tape where the probe head was inserted into the steel tubing in order to minimise the pressure put on the connection.

## **6.4 Results**

### **6.4.1 FEM results**

The probe cantilever was modelled simply as a cantilever with a fixed end, because the geometry was simpler than when the cantilever sensor was being modelled. There was no anchor structure as had previously been used to eliminate stress fractures, as the 90° angle which caused them was not present in the probe sensor. The same Young's modulus was used as for the cantilever shear stress sensor.

The sensor was still modelled using the non-linear solver, although as the cantilever was shorter the deflections were smaller. At lower pressures it was found that the strain in the cantilever varied linearly with the pressure applied to the surface of the cantilever. The strain measured was on the top surface of the cantilever with the force applied to the underside of the cantilever, and consequently the strain was negative.

From the results of strain in the cantilever, it was possible to calculate, for a given gauge factor of nichrome ( $K = 1.8$  as calculated in §5.3.1) and a known Wheatstone bridge arrangement, the expected output from the sensor.

The strain in the cantilever caused by the applied load is shown in Figure 6-10 and the expected output from the sensor is shown in Figure 6-11.

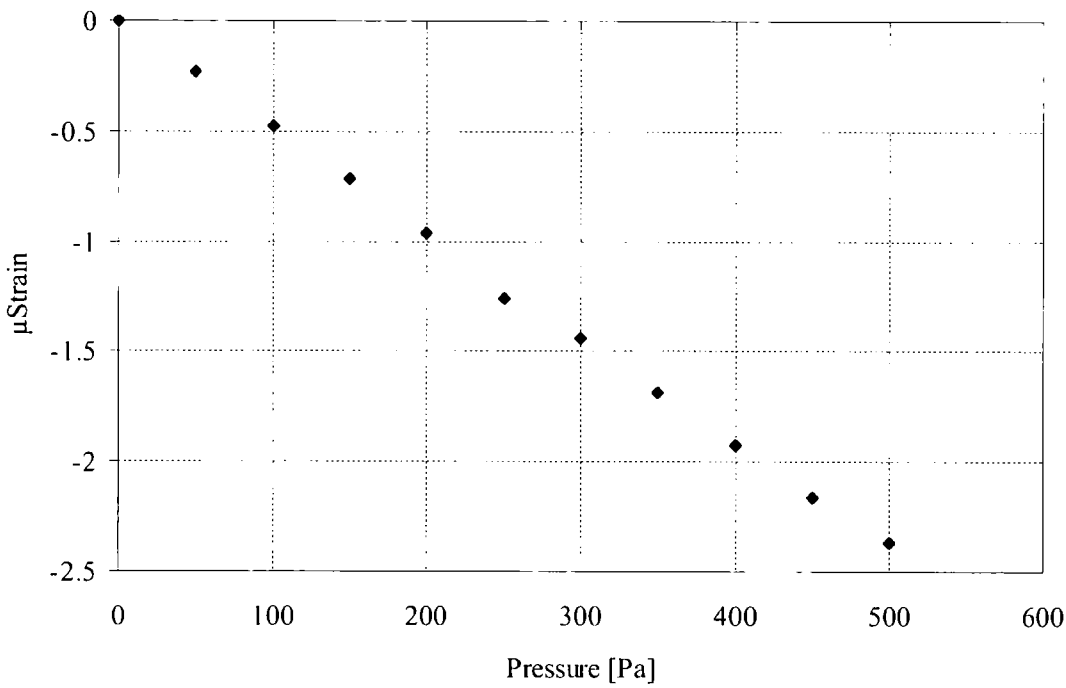


Figure 6-10 Microstrain against pressure difference for probe sensor

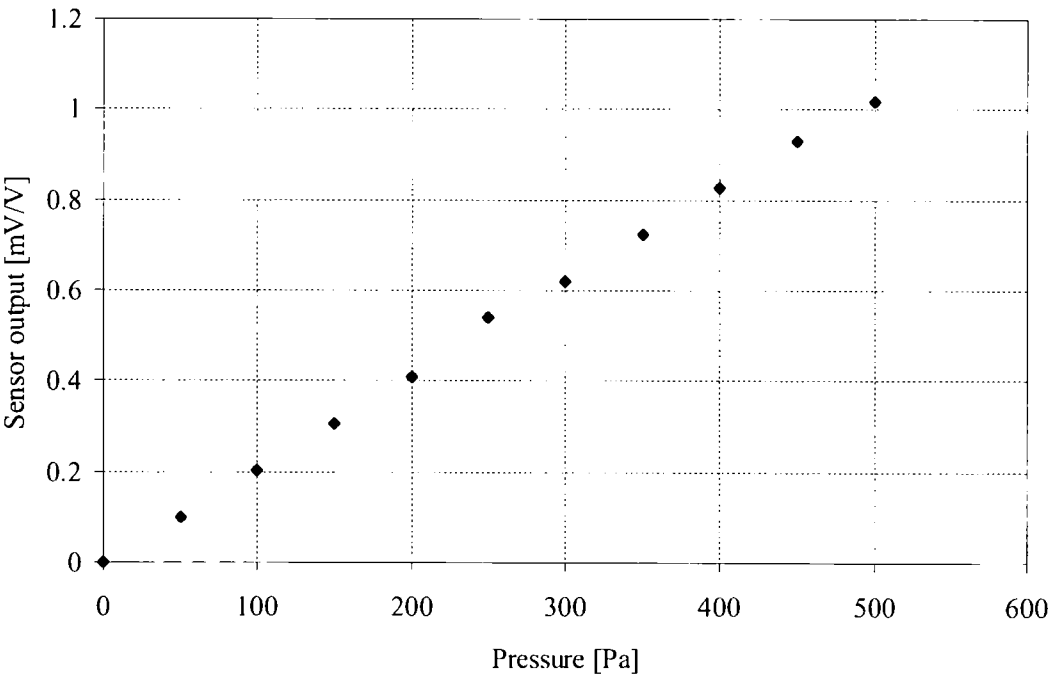


Figure 6-11 Sensor output for applied uniformly distributed load

As a result of the linear relationship between pressure and sensor output in the relevant range, it was found possible to convert from calculated pressure on the sensor surface to expected sensor output by the following equation.

$$\Delta V_{sensor} = 2.06 \times 10^{-3} \Delta P \tag{3-1}$$

where  $\Delta V_{sensor}$  is in mV and  $\Delta P$  is in Pa.

The tip deflection was also linear with pressure. The results for deflection are shown in Figure 6-12. It can be seen that due to the shorter length of the cantilever, the deflections are much smaller than those seen in the cantilever shear stress sensor.

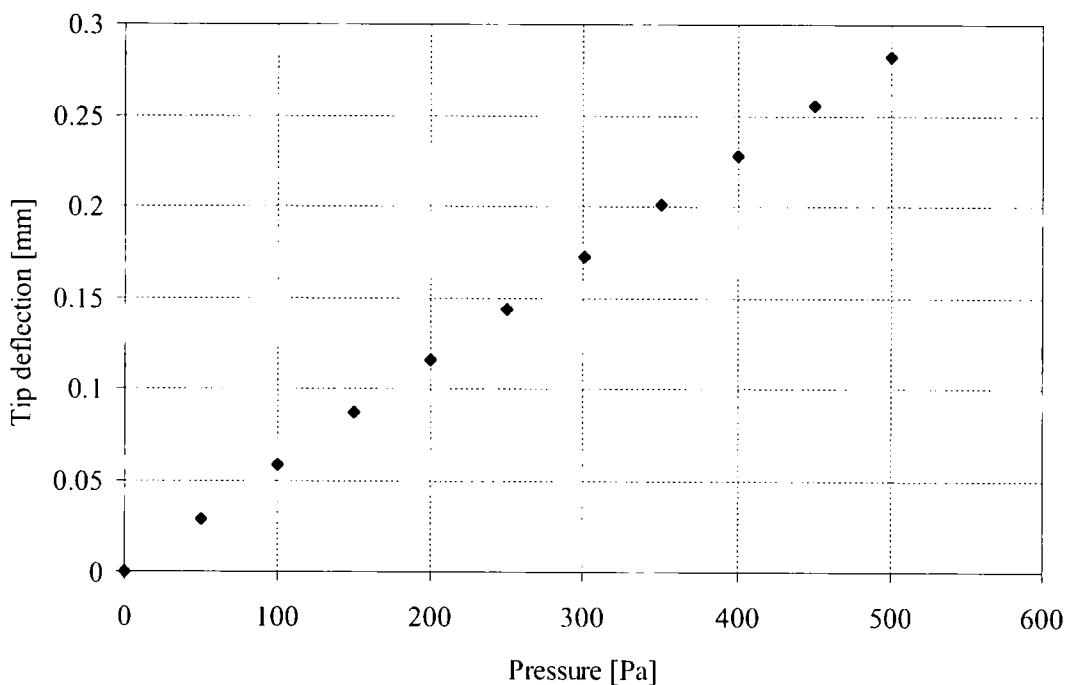


Figure 6-12 Tip deflection against pressure for probe sensor

6.4.2 CFD Results

The probe was modelled using CFD in order to obtain an estimate of the pressure drop across the sensors which make up the probe. This then allowed the response of the sensors to be calculated.

The probe was modelled in 3D because the interaction between all four sensors was expected to have a significant effect on the pressure drop calculated across them. If there were no gap at the corners of the sensors then the importance of this would be less pronounced, but with their presence allowing the flow to be diverted around the sensor it is important to model the flow in 3D.

The CFD domain was constructed to be large compared with the size of the probe head, in order to ensure that the boundaries of the domain did not have an effect on the flows calculated in the vicinity of the probe tip. Because the inlet flow was to be modelled at a variety of different yaw angles, it was necessary to have two sides of the rectangular domain as inlets, and two sides as outlets. The top and bottom faces of the domain were defined as ‘symmetry’. The inlet flow velocity was defined in component form in order to allow a variety of different yaw angles to be modelled.

The outline of the domain used for modelling the probe is shown in Figure 6-13.

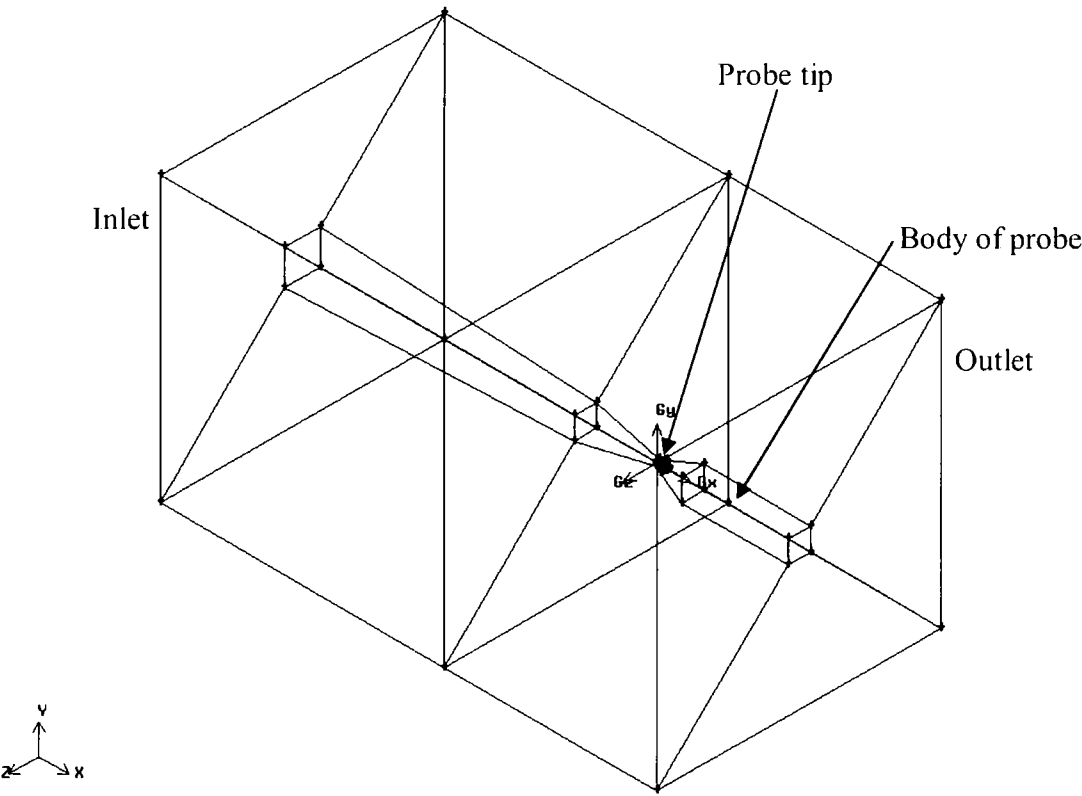


Figure 6-13 Structure of probe CFD domain

The domain was constructed in order to allow a mesh with very small cells in the region of interest around the probe tip, but to give a smooth graduation to relatively large cells at the edges of the domain. This minimised the total number of cells, making the mesh quicker to solve.

The origin (0,0,0) is situated at the tip of the probe - at the end of the probe cantilevers, which is the smallest part of the probe.

The mesh that was created was checked to ensure that the results were not mesh dependent. Increasing the number of nodes in the mesh edges by 20% was found to have no significant effect on the results of the static pressures on the surfaces of the sensors, but caused a large increase in the computational time required to solve the mesh.

The pressure tapping was represented by a recess 1 mm deep was set into the face of the tip of the probe in order to accurately model the pressure that would be seen by the pressure transducer connected to the probe. However, although in reality this hole was circular, in CFD it has been modelled as having a square cross-section in order to facilitate meshing the model with a structured grid. This would not be expected to have any significant effect on the pressure calculated.

The mesh remained the same with different inlet velocities and incidence angles being applied. Runs were done at 10 m/s and 20 m/s for incidence angles of 0 to 50° at 10° intervals. These velocities represented Reynolds numbers in the region of 1000, using the tip diameter of the probe as the representative length, and thus a laminar model was used. The pressure difference across all four sensors was calculated as well as the pressure measurement from the probe.

The pressure drop across the sensors for varying yaw angles is shown in Figure 6-14.

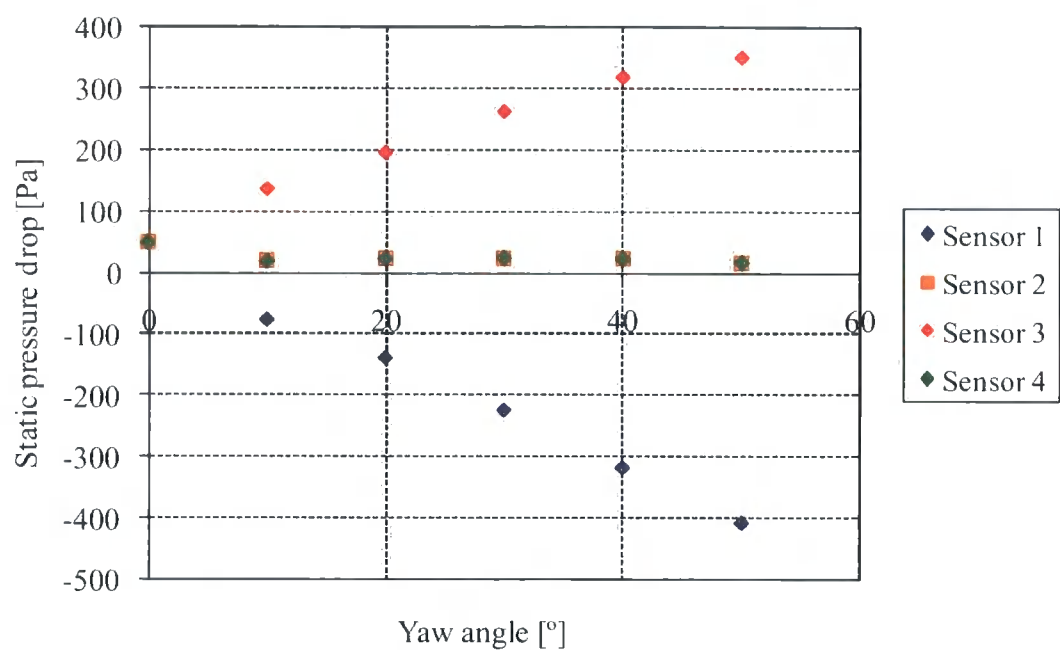


Figure 6-14 Static pressure drop across all four sensors at 20 m/s for varying incidence angles

The two sensors parallel to the flow direction (2 and 4) were found to have the same response due to the symmetrical nature of the probe. This response was not found to alter significantly as the yaw angle increased. This was as expected since these two sensors would be expected to be sensitive to pitch, not yaw. At zero incidence, all four of the sensors deflected outwards, but once the incidence angle was increased, the sensor closest to the flow was found to deflect inwards. At very high incidence angles, above 50 °, this sensor partially occluded the flow onto the sensor on the opposite side causing the pressure difference across this sensor to decrease.

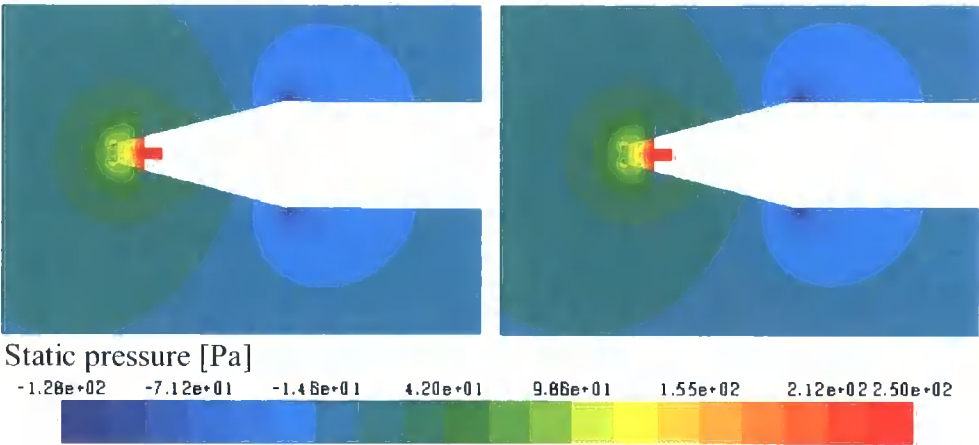
Maps of the static pressure around the probe tip for cross-sections through the centre of the domain in the horizontal and vertical planes for different incidence angles are shown in Table 6-2, spread over the next two pages. The flow incidence is varied in the horizontal plane, corresponding to yaw angle.

Incidence  
angle [°]

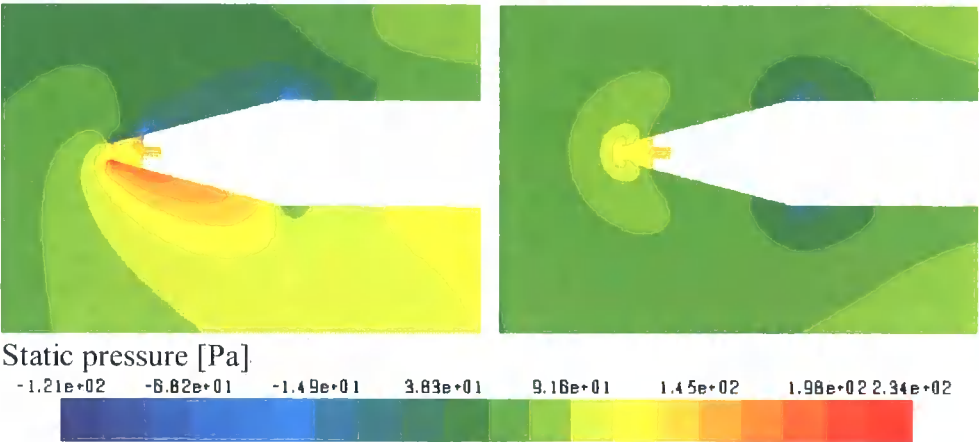
Horizontal plane

Vertical plane

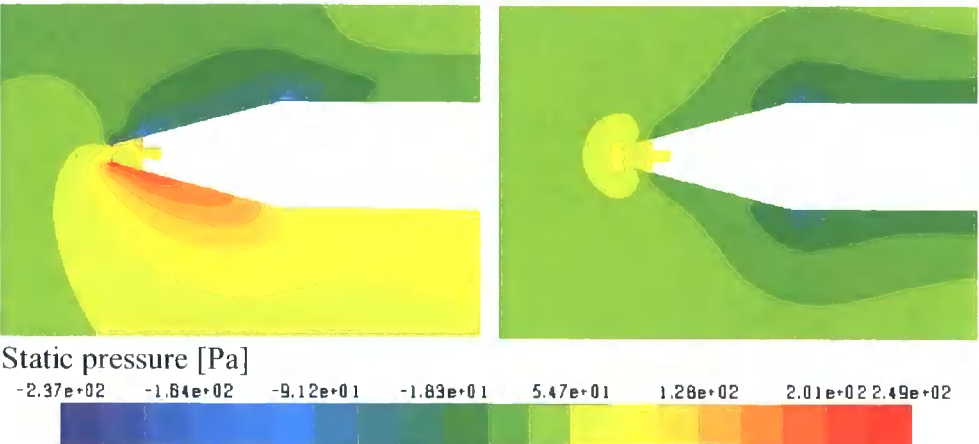
0



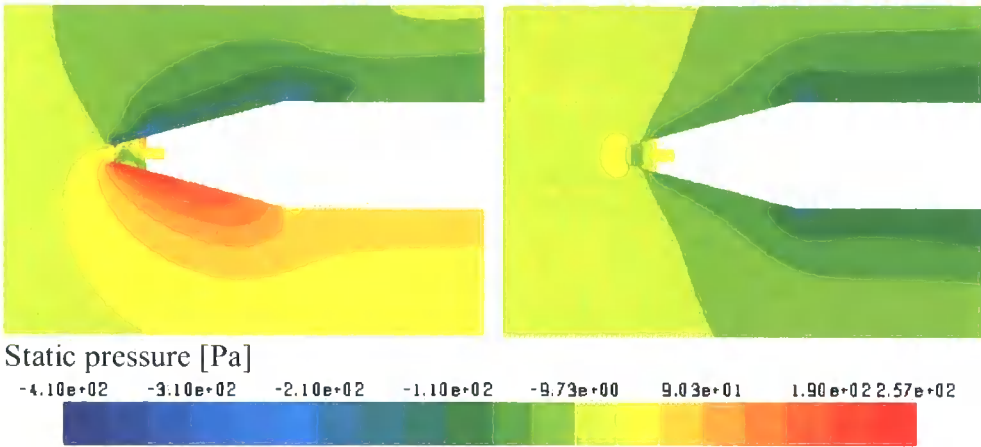
10



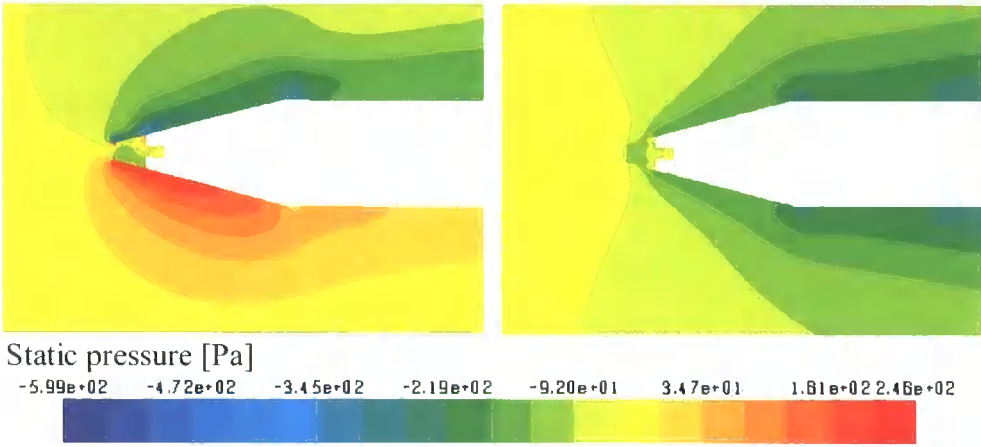
20



30



40



50

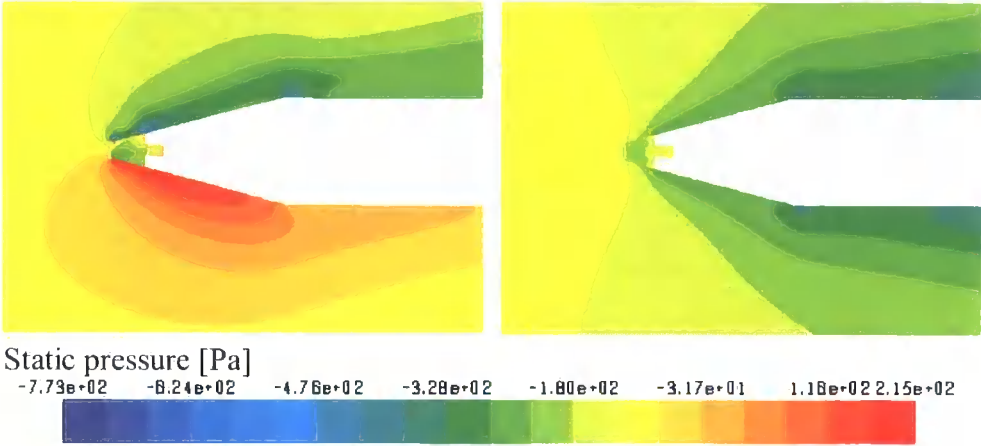


Table 6-2 Static pressures for varying incidence angles

It can be seen that the flow in the vertical plane remains fairly constant as the angle of the flow remains the same in this plane. However in the horizontal plane, as the incidence angle increases, the pressure on the sensor at the outside of the probe tip increases and on the far side from the flow inlet, the pressure drop behind the sensor is



more pronounced. The pressure measured at the pressure tapping, which in the CFD model is represented as a recess between the sensors, can be seen to decrease as the incidence angle increases, and to be negative at higher incidence angles.

From the FE results and mechanical testing, it was possible to convert the static pressure drop into the expected sensor output from each of the four sensors. These results are shown in Figure 6-15.

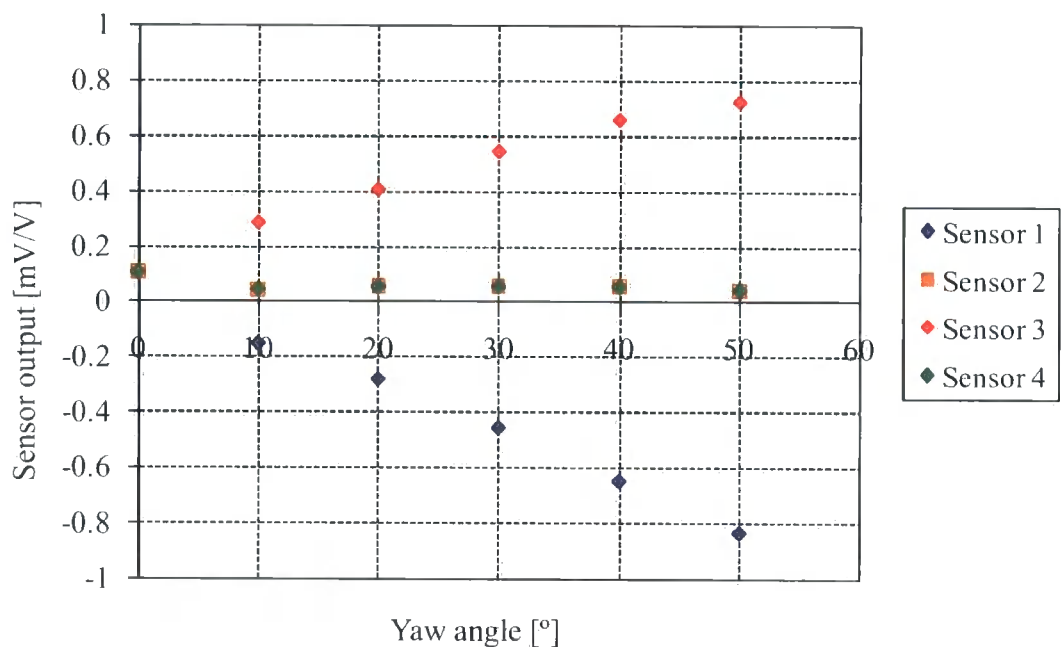


Figure 6-15 Sensor output for each sensor at varying incidence angles from modelling

The results from the CFD modelling were used to assess the calculations of yaw coefficient, pitch coefficient, dynamic coefficient and the stagnation pressure coefficient.

These are the coefficients as they would be calculated from wind tunnel calibration data (defined in §6.2). For these to be calculated from the theoretical results the pressure drop across the cantilever was converted into the expected voltage output from the sensor in mV/V. However since this relationship was found to be linear, this was actually unnecessary for calculating the pitch and yaw coefficients, but would have an effect on the pressure coefficients.

Since only yaw was modelled in the CFD simulations, the pitch coefficient was not calculated. The yaw coefficient is shown in Figure 6-16.

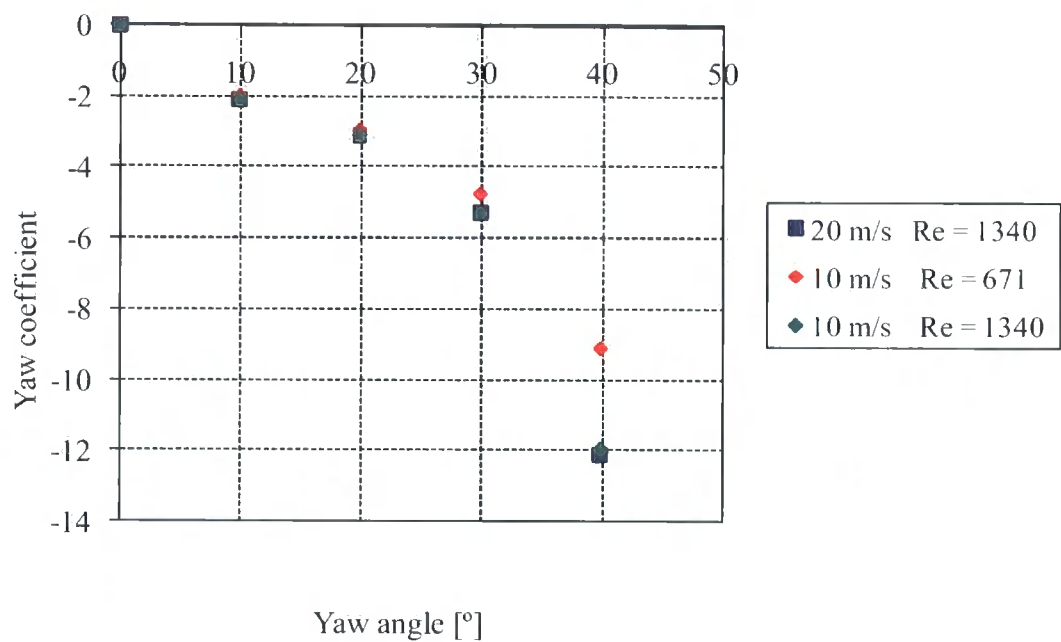


Figure 6-16 Yaw coefficients at varying incidence angles at 10 and 20 m/s

It can be seen that at increased incidence angles the calculated yaw coefficient is not independent of velocity as would be expected. However this discrepancy can be attributed to sensitivity to Reynolds number. This was confirmed by redoing the runs at 10 m/s, but halving the viscosity in order to artificially maintain the Reynolds number at the same value as the runs at 20 m/s. Altering the viscosity in order to achieve the same Reynolds number results in the same yaw coefficient at the two different velocities. At very high yaw angles, the negative pressure on the sensor closest to and normal to the flow dominates the positive pressures on the other sensors with the result that the sum of the pressure on the sensors (which is used to non-dimensionalise the pitch and yaw coefficients) becomes very small and eventually negative. This has the effect of driving the coefficients very large before they suddenly become negative. It is at this point that the probe can be considered to be out of range.

The pressure measured by the centre pressure tapping in the probe was also obtained from the CFD simulations. These results are shown in Figure 6-17.

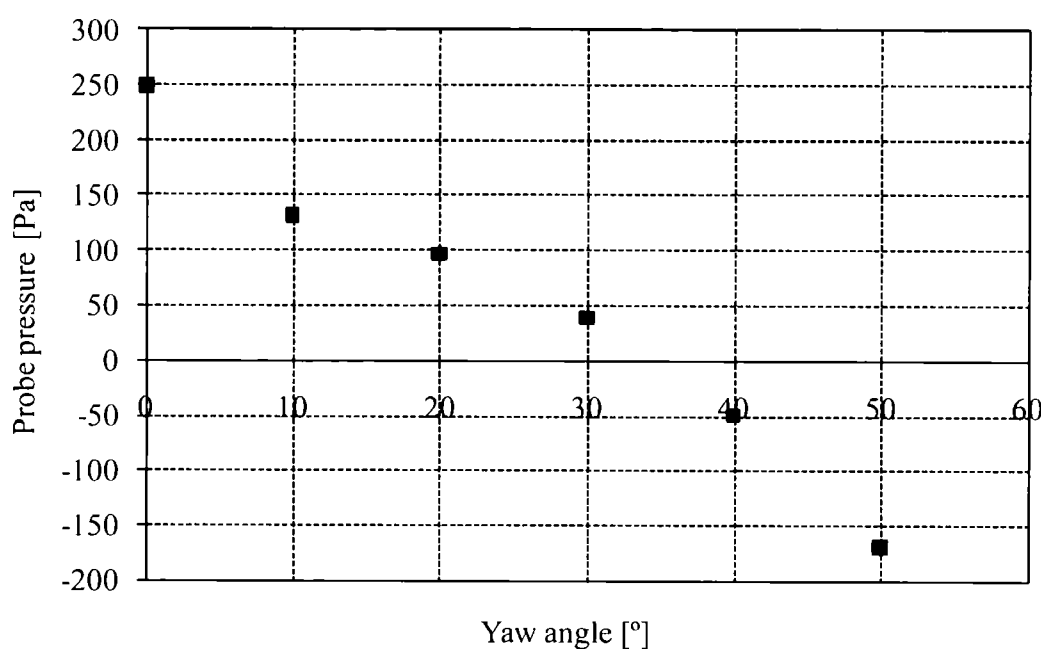


Figure 6-17 Centre hole pressure at varying incidence angles at 20 m/s

As expected, at zero incidence the value of this pressure is approximately the dynamic pressure. However as the incidence increases the pressure measured decreases until, at angles above 30°, the pressure becomes negative, i.e. is below freestream static pressure. This effect is altered by the presence of the sensors interrupting the flow before it reaches the pressure hole.

In order to establish the effect of the sensors on the pressure seen by the probe, the simulations were re-run with the sensors removed.

The results from this are shown in Figure 6-18 along with the original results with the sensors present. It can be seen that the probe pressure is much higher when the sensors are not present as they do not obstruct the airflow into the pressure tapping hole.

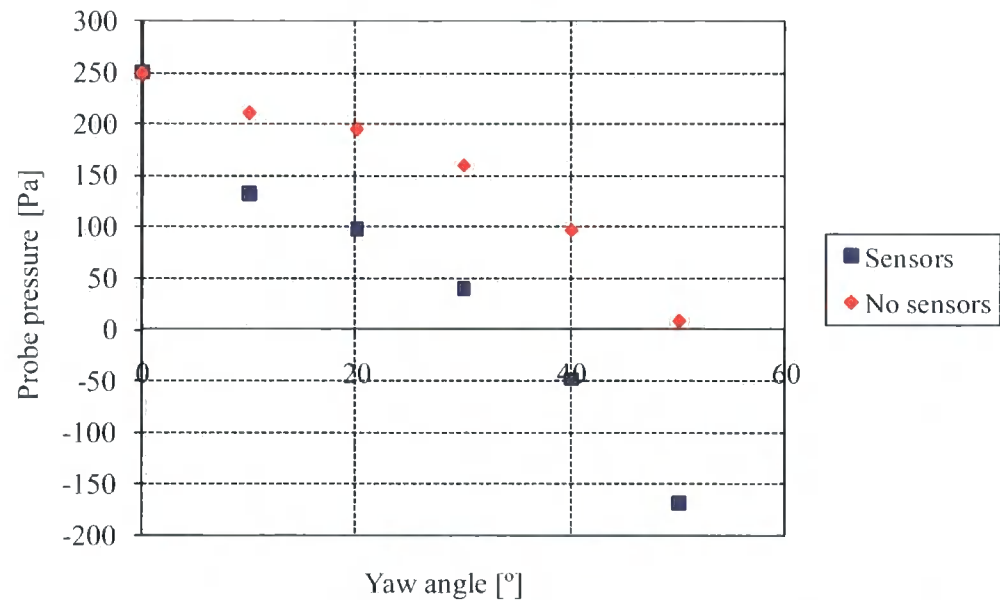


Figure 6-18 Probe pressure at varying incidence angles at 20 m/s with sensors and in absence of sensors

The stagnation pressure coefficient calculated from this pressure is shown in Figure 6-19.

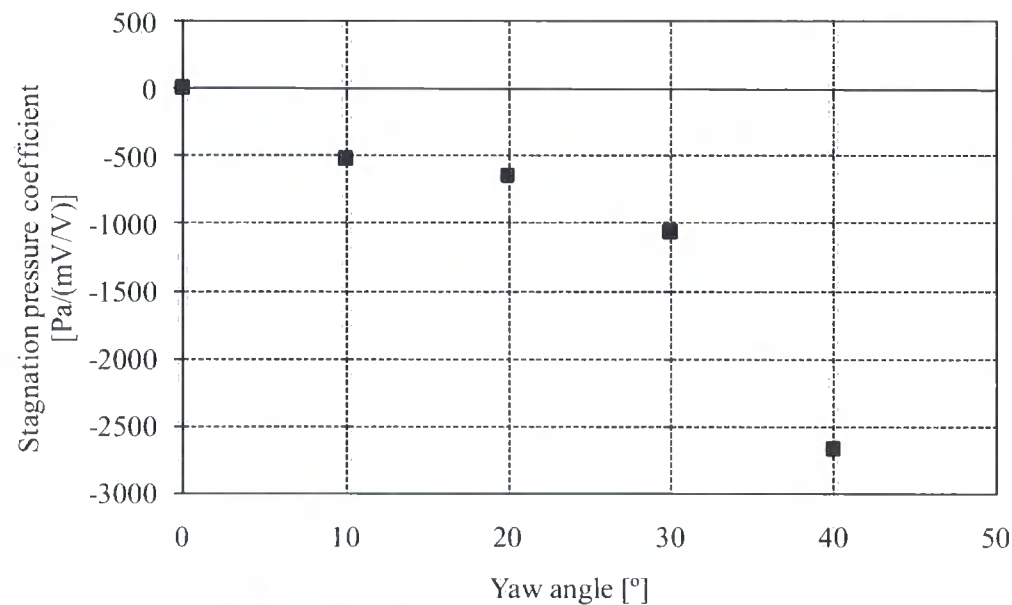


Figure 6-19 Stagnation pressure coefficient for varying incidence angle

As was expected, the stagnation pressure coefficient decreased with increasing incidence angle. The coefficient would always be negative as the probe pressure is referenced to total pressure.

The dynamic pressure coefficient was also calculated and is shown in Figure 6-20.

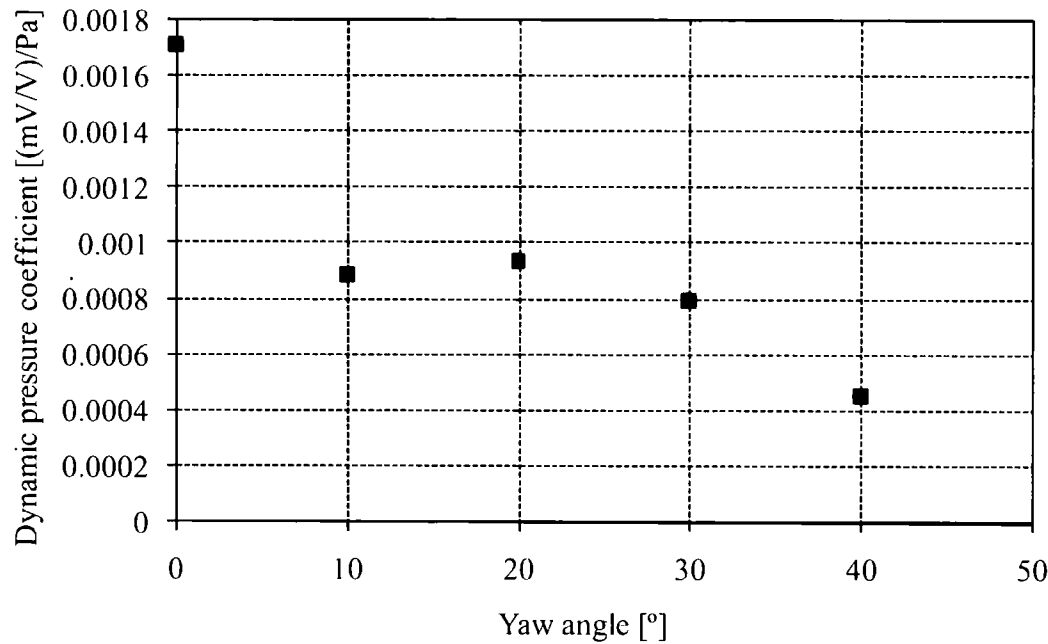


Figure 6-20 Dynamic pressure coefficient for varying incidence angle

The dynamic pressure coefficient decreases slightly at increasing yaw angles, as would be seen when using a 5-hole probe.

### 6.4.3 Wind tunnel results

The probe was mounted in the probe calibration test rig for airflow testing. The probe and test rig are shown in Figure 6-21.

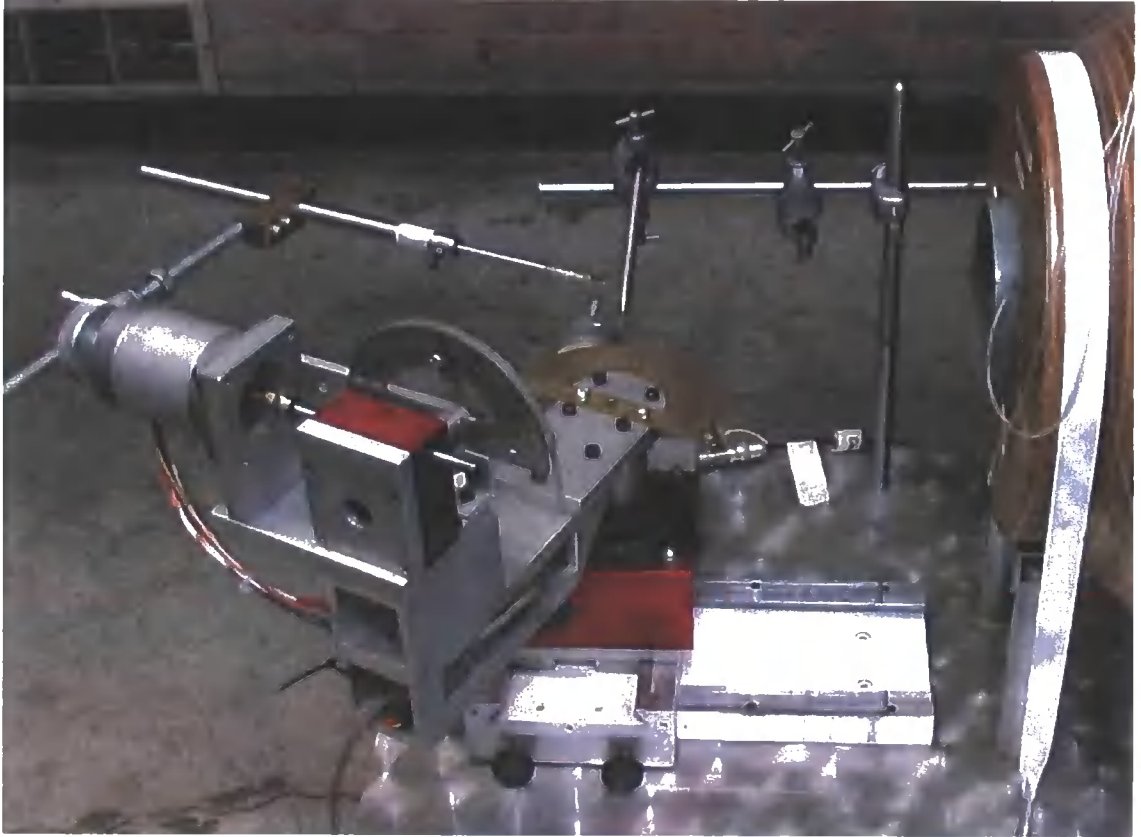


Figure 6-21 Probe mounted in probe calibration test rig

The probe is mounted in the test rig and the four Wheatstone bridges are connected up to the voltage supply and the DAQ. The same voltage supply was used for all four bridges with them connected in parallel, since the current demand in each bridge is very low. The probe pressure is connected to a pressure transducer, referenced to the upstream total pressure and a second pressure transducer measures the static pressure, also referenced to the upstream total pressure. Both these pressure transducers are also connected to the DAQ. Also measured by the DAQ was the input voltage to check whether this supply voltage varied with time. Further details on the probe calibration test rig were given in §3.3.1.

The probe is shown in close up in Figure 6-22.

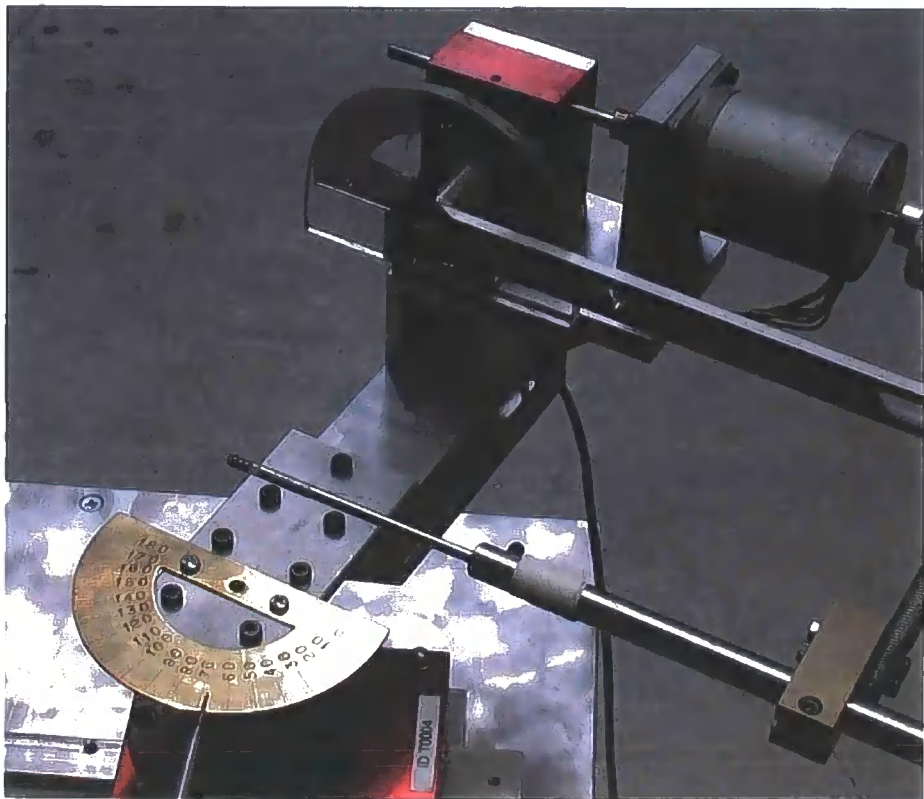


Figure 6-22 Probe and mountings for accurate angular displacement

The wind tunnel was set to a constant velocity for a series of tests to be completed. A range of different angles to the flow were applied, with measurements of the voltage output from the Wheatstone bridge taken at each position. The stepper motors allowed the angle at which the probe was positioned to be set accurately.

The raw data from these tests were analysed to give results in  $\text{mV/V}$ , which are normalised for the input voltage. These results would then be used for the calculation of the coefficients used to define the behaviour of the probe. Maps of the coefficients could then be plotted for a range of pitch and yaw angles, which would then be used as calibration maps for the probe. The coefficients calculated could then be compared with those expected from the theoretical data.

Due to the difficulties in reliably assembling a probe with all four sensors electrically connected, a probe with a single sensor which was fully functional was used for

measurements. The other three sensors were all mounted on the probe head, which was important for the aerodynamic response, but were not electrically connected.

The results for two sensors, Sensor 1 and Sensor 2 (for definitions see Figure 6-3) to the flow are shown in Figure 6-23 for varying yaw angles.

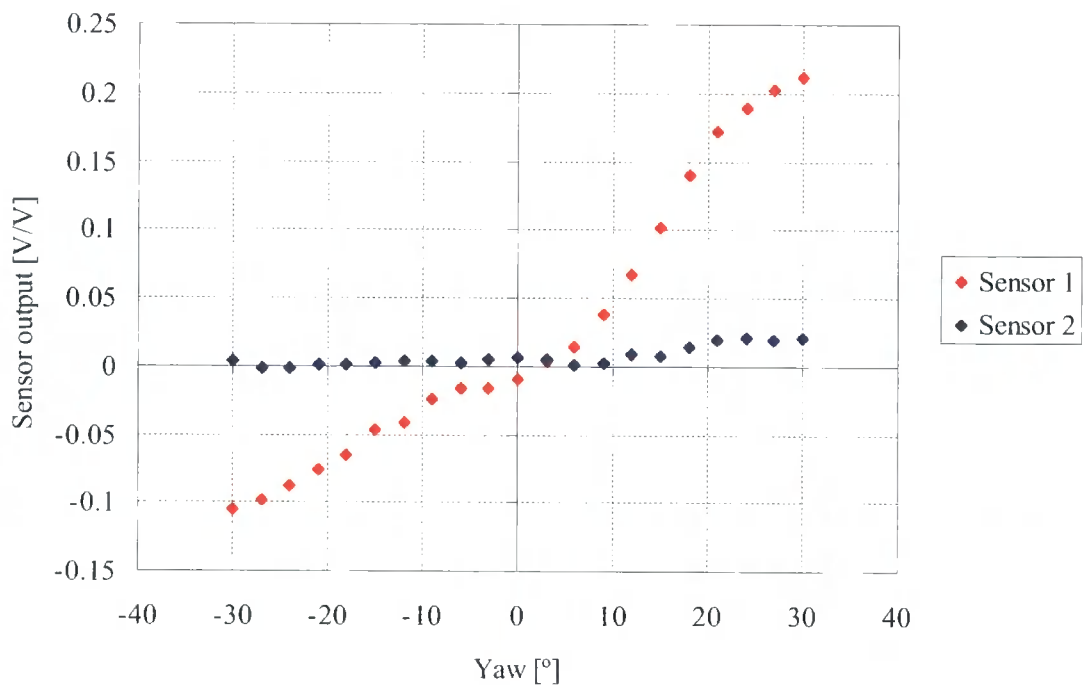


Figure 6-23 Response of sensors parallel and perpendicular to flow at varying yaw angles

It can be seen that the response of the sensor parallel to the flow shows it was very little influenced by the variation in yaw angle. In contrast the sensor perpendicular to the flow showed a clear response to the changes in the yaw angle. This is as would be expected, with one pair of sensors on the probe sensitive to changes in the yaw angle, and the other pair sensitive to changes in the pitch angle, between them allowing the accurate measurement of both pitch and yaw.

The response of the yaw sensor is not the same for positive and negative yaw angles. This is because, although at a negative yaw angle the sensor is deflecting inwards, and is directly in the path of the flow, at positive yaw angles the sensor is partially hidden



by its opposite sensor which is now deflected inwards and affects the flow onto the sensor downstream, which is now deflected outwards, giving a positive signal response.

Although the trends in these plots look suitable, when calculating the non-dimensional coefficients the variations in the original data were found to be magnified by the calculations producing maps of coefficients with unacceptable levels of variation. This problem is illustrated here. Plots from all four sensors at a pitch angle of  $-12^\circ$  for varying yaw angles are shown in Figure 6-24.

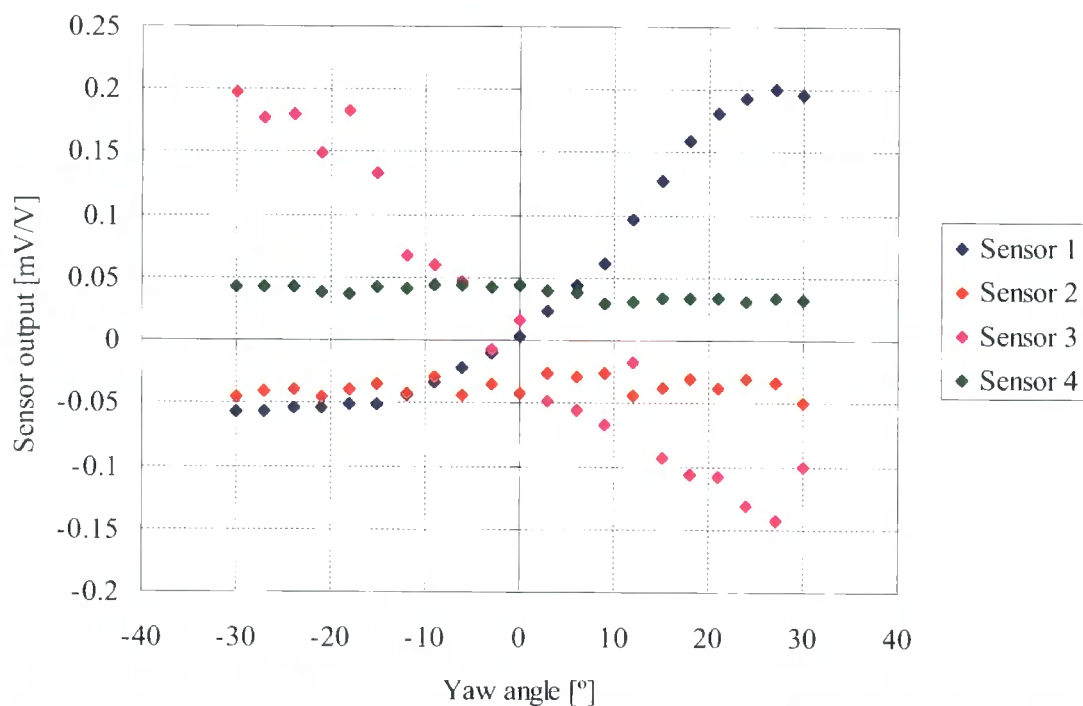


Figure 6-24 Plots of all four sensors at pitch angle  $-12^\circ$

Although there is more variation than might be expected for Sensor 3, it is not great enough to be expected to be a problem.

Plots of  $V_1 - V_3$  and  $V_2 - V_4$  are then shown in Figure 6-25 and Figure 6-26.

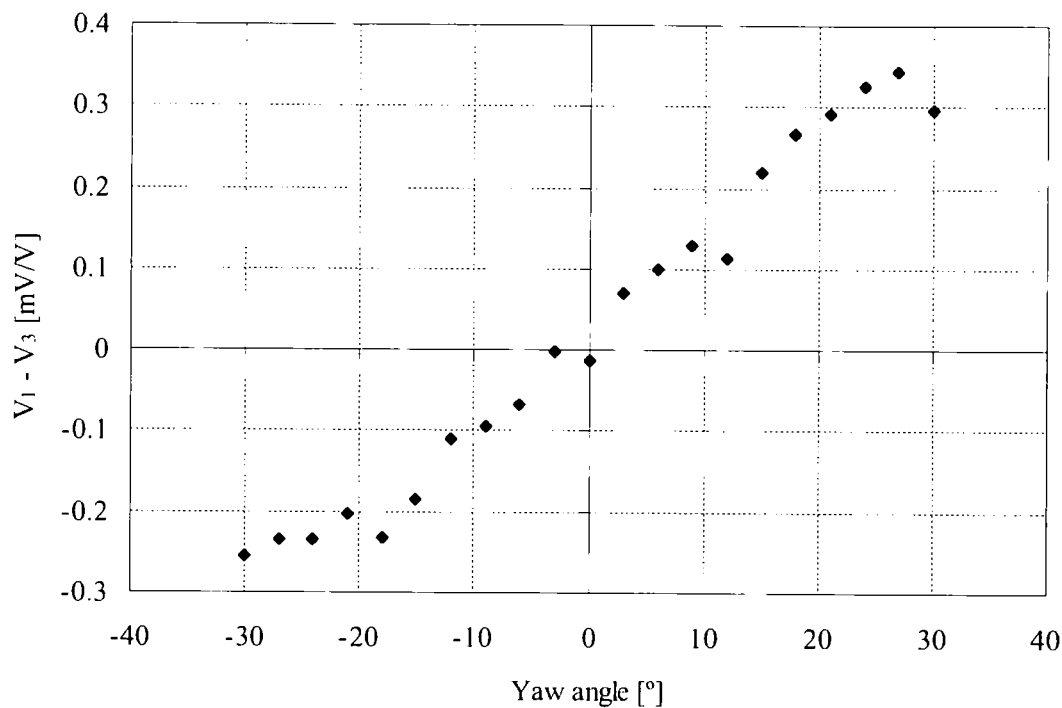


Figure 6-25  $V_1 - V_3$  for pitch angle  $-12^\circ$

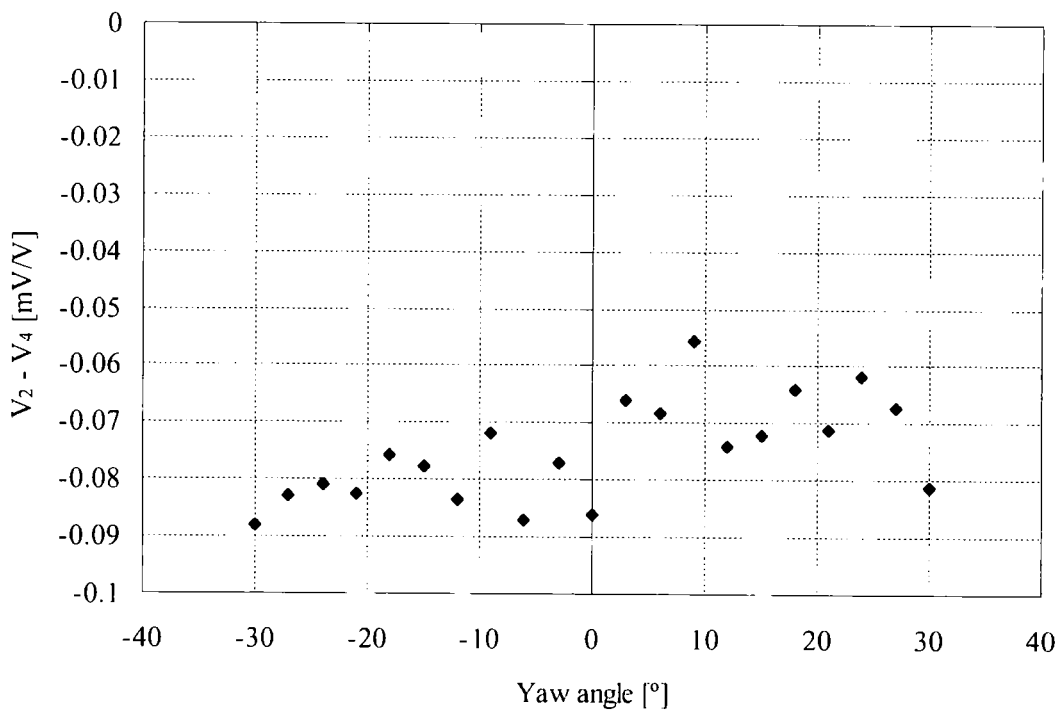


Figure 6-26  $V_2 - V_4$  for pitch angle  $-12^\circ$

There are no obvious problems with this data, and it can be seen that sensors 1 and 3 are sensitive to yaw and sensors 2 and 4 are sensitive to pitch.

$V_{total}$  is plotted in Figure 6-27.

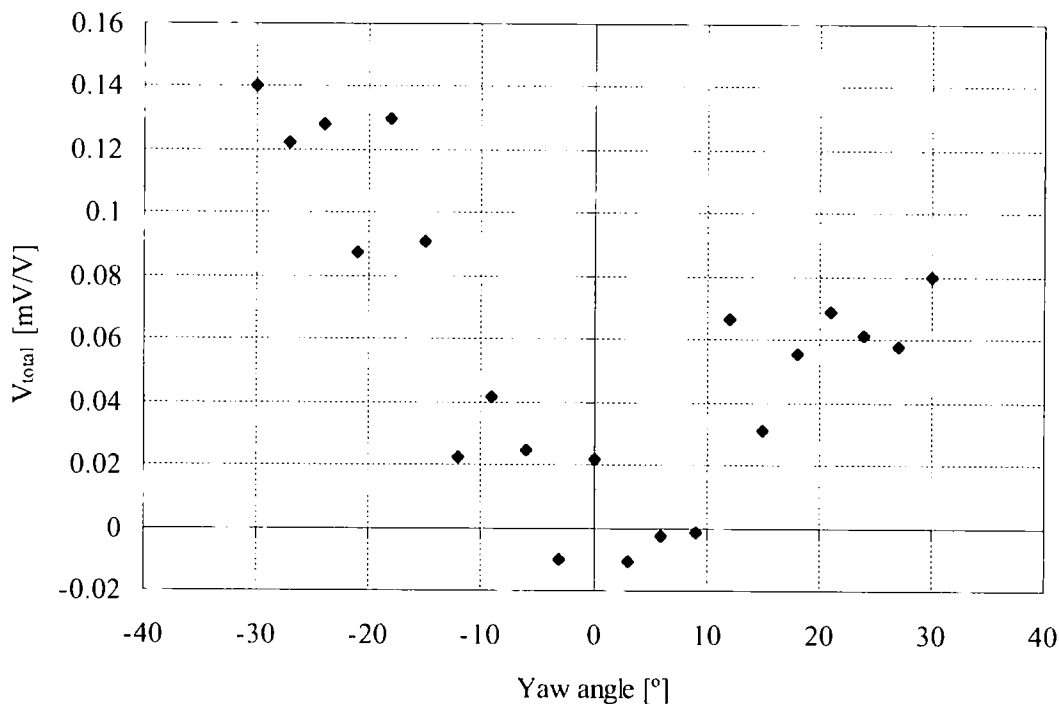


Figure 6-27  $V_{total}$  for pitch angle  $-12^\circ$

This data shows no obvious major issues, although some variation, but note how close the values at yaw angles of 6 ° and 9 ° are to zero.

Then plotting pitch and yaw coefficients in Figure 6-28 and Figure 6-29, it can be seen the huge effect these very small values of  $V_{total}$  have on the coefficients calculated. The variation of yaw coefficient which should be seen with changing yaw angle is lost because of variations in the total voltage when this is near zero.

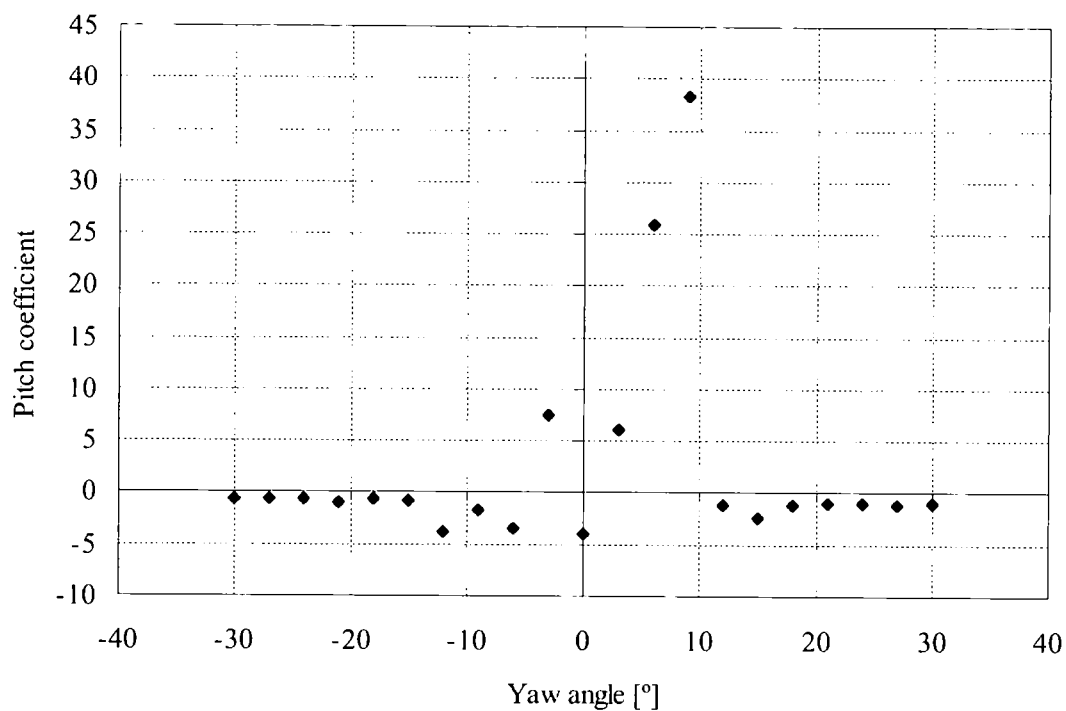


Figure 6-28 Pitch coefficient at pitch angle of  $-12^\circ$

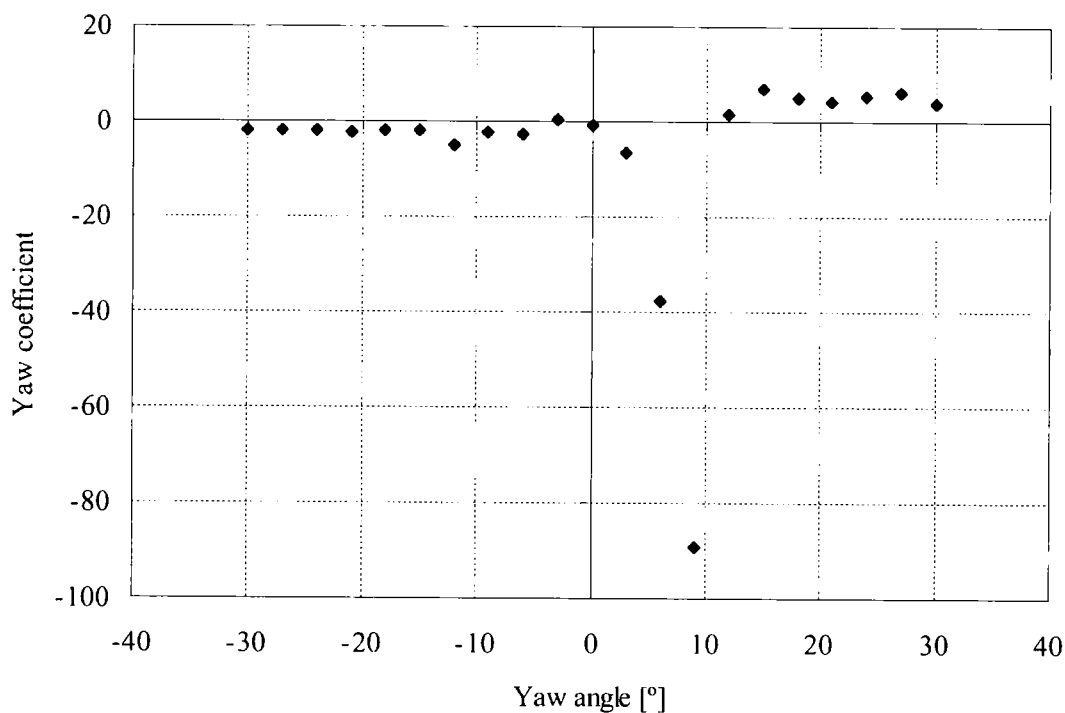


Figure 6-29 Yaw coefficient at pitch angle of  $-12^\circ$

This problem could be partially alleviated by increasing the sensitivity of the sensors, so that there is always more deflection of the cantilever sensors. Additionally, although the

probe is effective at measuring pitch and yaw, it does not have a good response to changes in the velocity of the flow. The response of a probe sensor at varying velocities with zero incidence is shown in Figure 6-30.

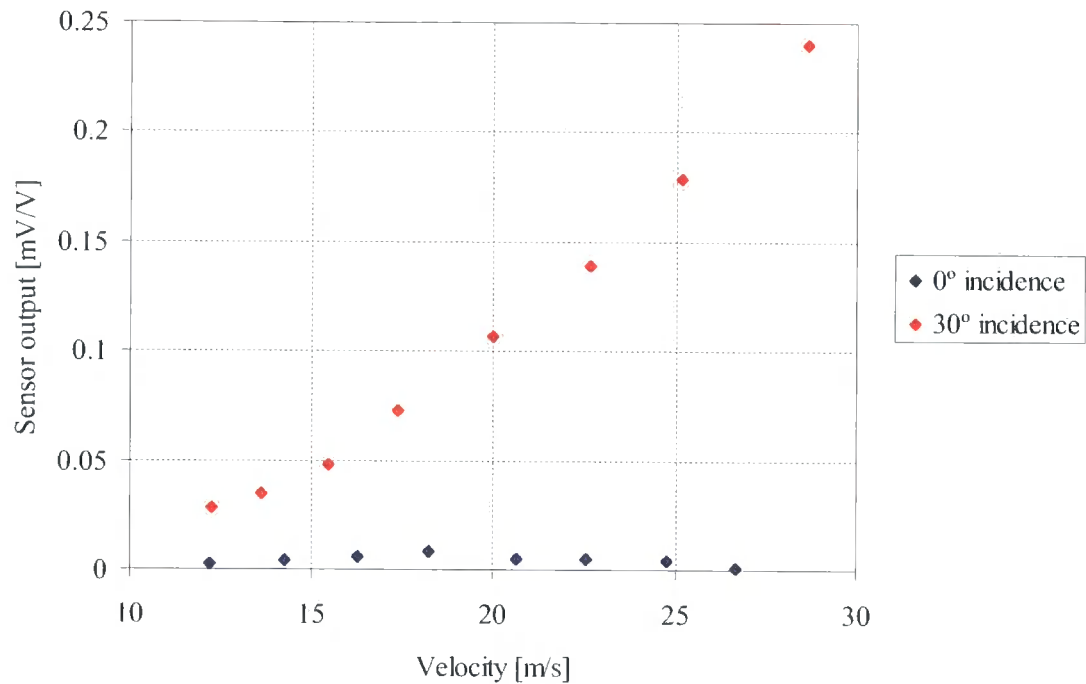


Figure 6-30 Response of probe sensor to changes in velocity at two different incidence angles

It can be seen that the probe shows very little response to the changes in velocity at zero incidence, relative to the sensitivity to the incidence angle, and indeed that there is no correlation between the increase in velocity and the voltage output.

However, when the same measurements are repeated with an incidence angle of 30°, the effects of the changes in velocity are clearly visible. Consequently the sensor appears to be able to measure changes in dynamic pressure but only at a significant incidence angle. The lack of sensitivity at zero incidence is probably due to the cancelling out of the forces caused by the stagnation pressure at the centre of the probe i.e. on the inside of the sensor, and the force from the pressure on the outside of the sensor caused by the sensor being angled in towards the tip.

The overall response of the probe sensors is much lower than that predicted by the CFD and FE modelling (Figure 6-15). The most likely reason for this is the presence of the glue securing the sensors to the probe head. This glue can extend along the free under-surface of the cantilever due to the assembly process. The glue would then increase the stiffness of the cantilever sensor.

## **6.5 Revised probe design**

### **6.5.1 Design**

Due to these problems with the original design of probe, it was decided to alter the design to try and improve the aspects which were causing problems. Although the probe had been found to be relatively sensitive to pitch and yaw, the sensitivity to changes in dynamic pressure at low incidence angles was a problem and also the sensitivity overall would benefit by being increased.

In order to address these issues two changes were made to the design of the probe. The problem of measuring velocity was tackled by changing the design of the probe head on which the sensors were mounted. Instead of using the simpler angled design which aimed to keep the probe tip diameter to a minimum, the pairs of sensors were mounted parallel to each other instead of converging. The probe head, after narrowing down then had sides parallel to each other for a length in order to allow this. This was expected to increase the outward bend of the cantilevers when at zero incidence. However in order to achieve this design by rapid prototyping, the minimum achievable wall thickness was 0.5 mm with a 0.5 mm hole running through it. This meant that the tip diameter of the probe would be increased to 1.5 mm from 0.5 mm. Increasing the diameter of the probe tip was considered worthwhile in order to establish the viability of the new design, and it would be possible to reduce the probe size again once the principle had been verified by the use of an alternative rapid prototyping system (possibly stereolithography), capable of manufacturing objects with thinner walls and also achieving narrower holes.

The revised probe head is shown in Figure 6-31.

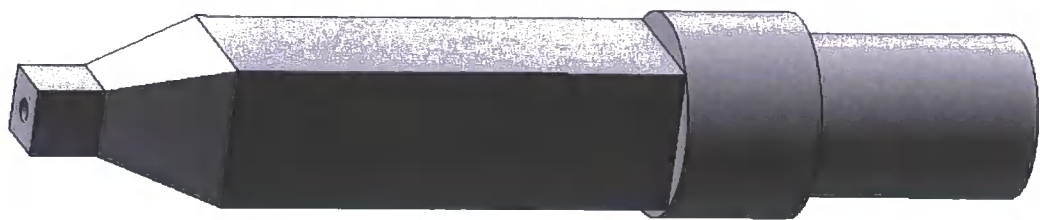


Figure 6-31 Revised probe head

To increase the sensitivity of the sensors overall, the length of the sensing cantilever was increased from 1 mm to 1.5 mm. The new sensor design is shown in Figure 6-32. The design is very similar to the previous one, with the exception of the longer cantilever, and an extended narrow section behind the strain gauge to allow the sensor to be mounted on the new probe head design. In addition, the angle at which the sensor narrowed from the contact pad region to the cantilever and also the length between these two points was altered for the same reason. The fabrication process was identical to that of the initial design, with the different masks being used.

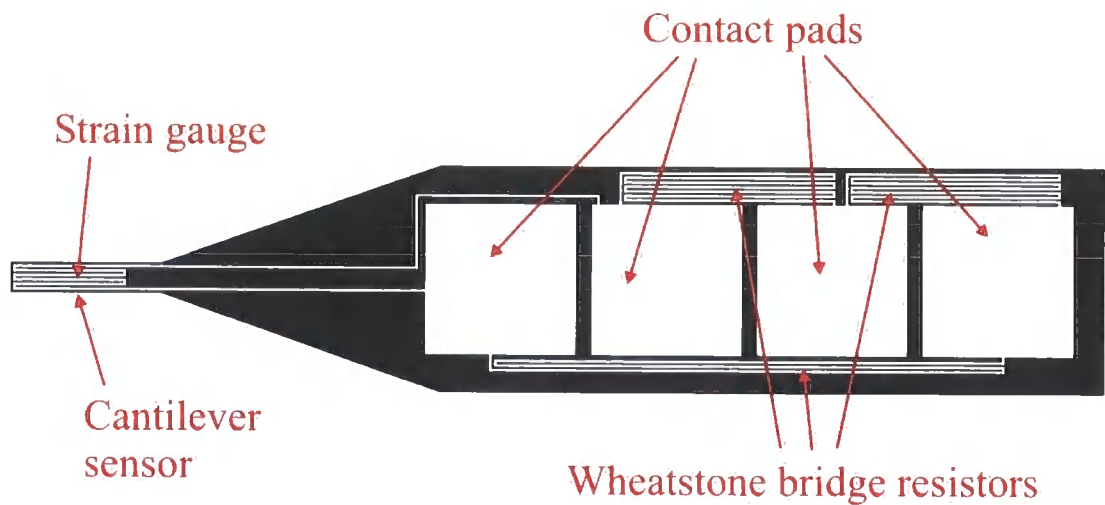


Figure 6-32 Diagram of revised probe sensor

The construction of the probe was carried out using the same method as previously.

A close-up of the tip of the new probe is shown in Figure 6-33. The parallel nature of the cantilevers compared with the previous design where the cantilevers converged towards the tip can clearly be seen in this picture.



Figure 6-33 Close-up of tip of revised probe design

6.5.2 Wind tunnel results

The response of the sensor when parallel and perpendicular to the flow at varying yaw angles at 20 m/s is shown in Figure 6-34.

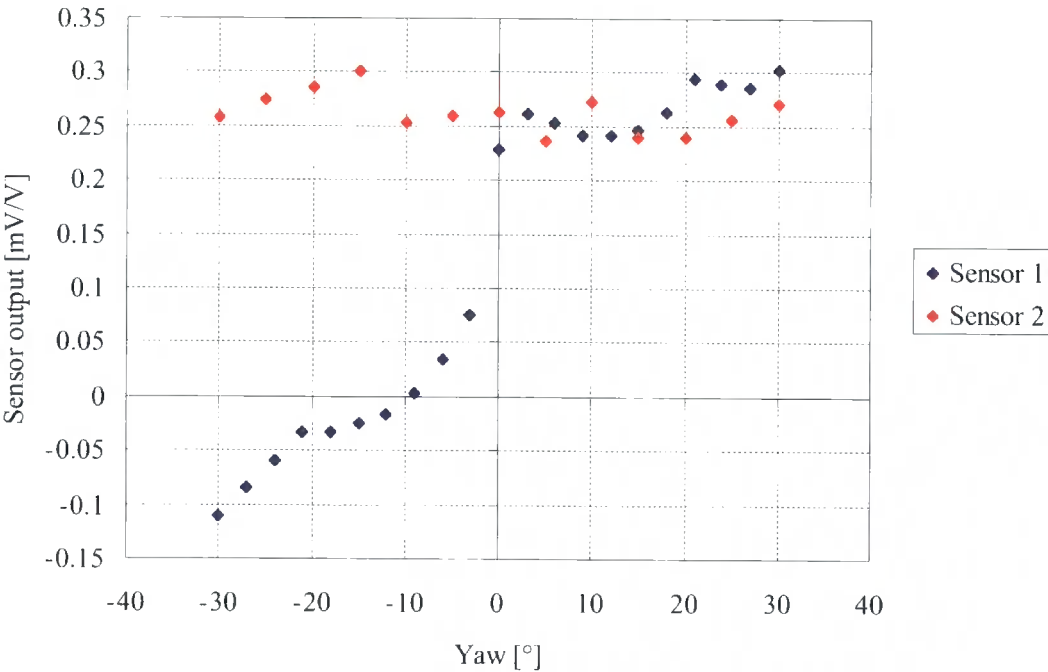


Figure 6-34 Response of revised sensors parallel and perpendicular to flow at varying yaw angles



The response of the sensor when perpendicular to the flow is very similar to that of the previous design of probe, but gives a greater magnitude of response as intended by increasing the length of the cantilever. However, the response of the sensor when parallel to the flow is much greater than with the previous design. This indicates that the probe is more sensitive to flows at low incidence angles, which was one of the issues being addressed by the new design of probe. Sensor 2, which should be sensitive to pitch, is seen to be independent of yaw angle, indicating good decoupling of pitch and yaw sensitivities.

As seen with the previous design, the response of the sensor was not the same for negative and positive yaw angles. This is because at positive yaw angles, the flow onto this sensor is occluded by the upstream sensor of the pair.

The response of the probe to changes in velocity was tested as with the previous design. The results of this testing are shown in Figure 6-35.

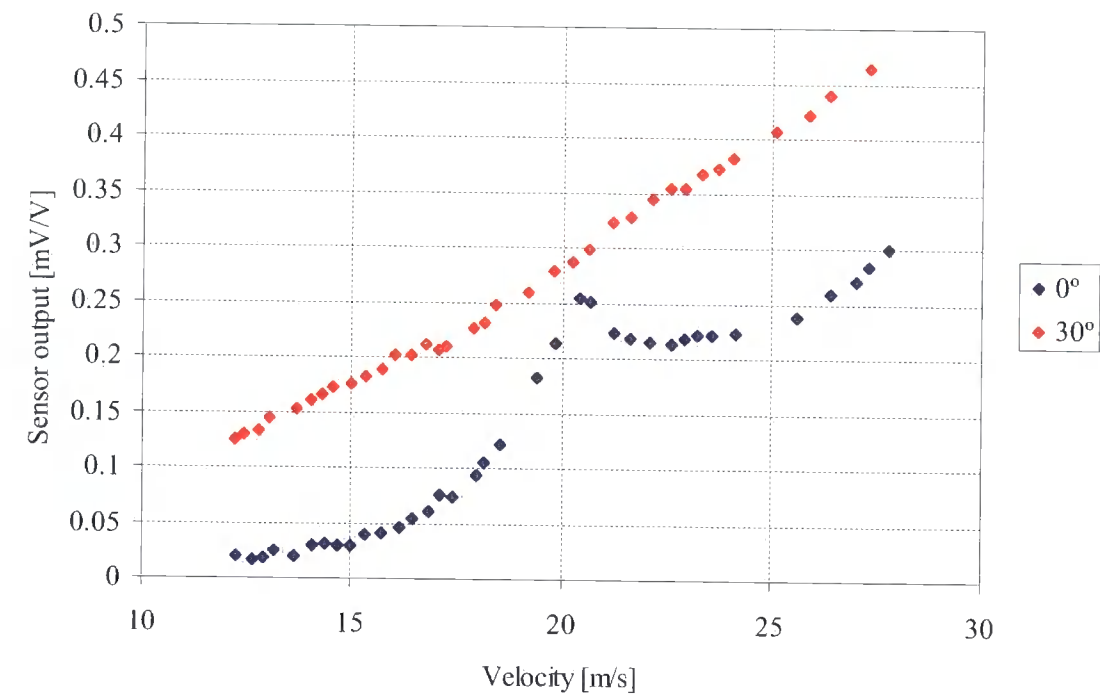
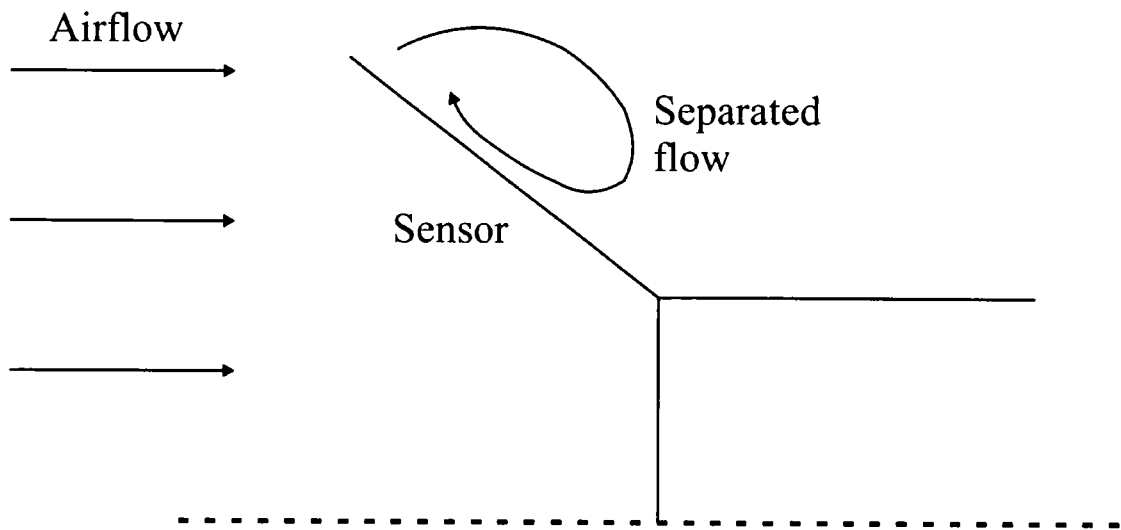


Figure 6-35 Response of revised probe sensor to changes in velocity at two different incidence angles

It can be seen that the response of the sensor at zero incidence now has a response to variation in the velocity compared with the previous design of probe which had no response. This objective had therefore been achieved by altering the angle of the sensors from converging to parallel. The response of the sensor when it is at an incidence angle of  $30^\circ$  is seen to have a greater offset than that at  $0^\circ$ .

The decrease in the sensor output just above 20 m/s is most likely to be caused by the flow over the cantilever stalling. The stalling of the flow over the cantilever is shown in Figure 6-36.



Sensor deflects to angle where flow behind cantilever separates, causing stall and loss of lift and subsequent decrease in deflection

Figure 6-36 Stalling of flow over cantilever sensor

To verify this, the response of the sensor at other incidence angles was also measured.

The results of these experiments are shown in Figure 6-37.

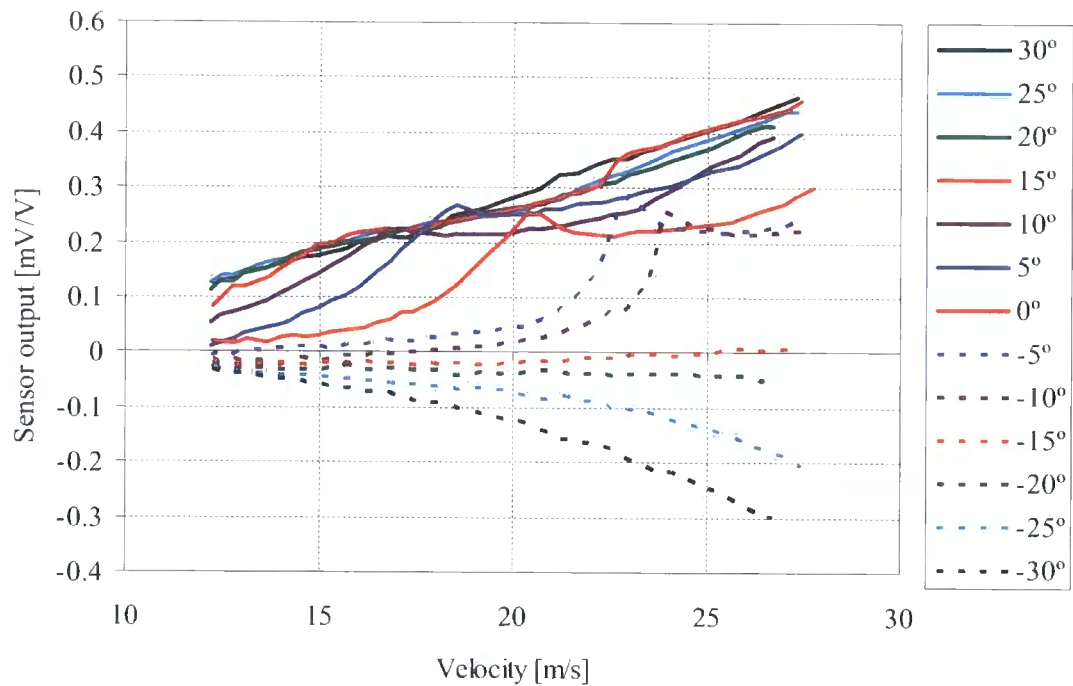


Figure 6-37 Response of revised probe sensor to changes in velocity at varying incidence angles

It can be seen that as incidence angle increases the peak of the response moves to the left. This is as would be expected, since if the initial incidence angle is greater, then a lower velocity would be required to cause the cantilever to deflect to a position where the flow stalls. At very high incidence angles the flow has stalled at a lower velocity than the range shown here, hence why the effect was not seen for an incidence angle of 30° in the previous figure.

At negative incidence angles the stall shifts to the right i.e. a higher velocity because the initial incidence is less. At greater negative incidence angles, the flow onto the outside of the cantilever sensor causes a greater pressure than the pressure between the sensors, and thus the cantilever bends inwards. In the range of velocities shown here, a high enough incidence angle is not reached to cause stall when the cantilevers are deflected inwards.

The stall of the sensors would not have been seen in the modelling as the deflection of the sensors was not introduced into the CFD work.

The standard deviation of the data was considered for zero incidence. This is shown in Figure 6-38.

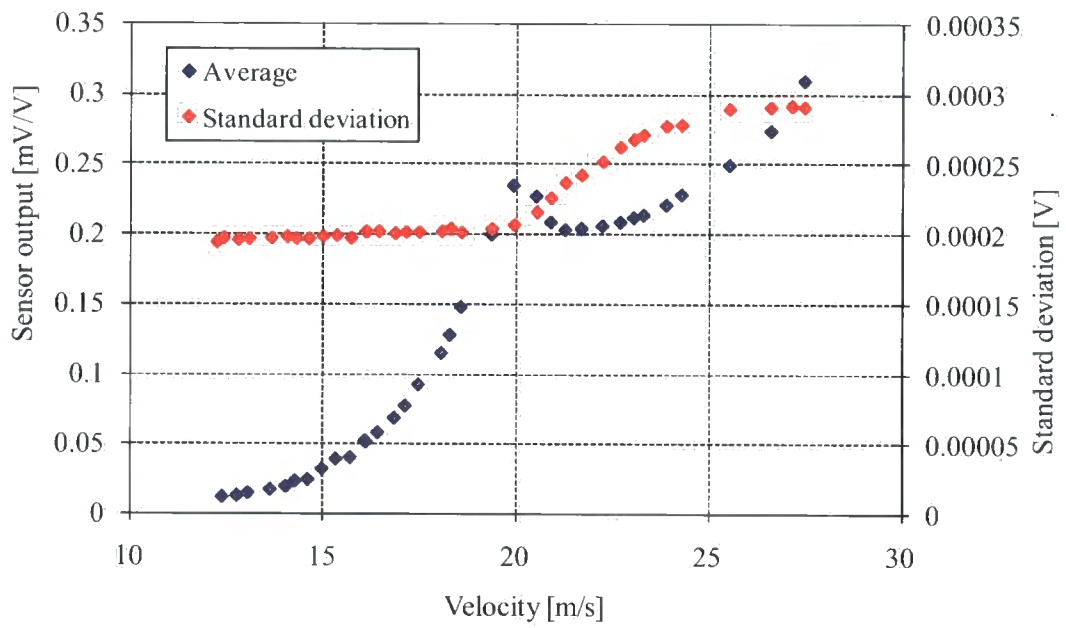


Figure 6-38 Standard deviation of data at stall

The increase in the standard deviation after the flow has stalled backs up the theory that this is what is taking place to cause the decrease in the sensor output.

An increased velocity would cause an increased curvature of the cantilever; this would increase the effective incidence angle, causing the flow to stall. The ‘lift’ on the cantilever would then be decreased causing the curvature of the cantilever and thus effective incidence angle to decrease again, possibly causing the reattachment of the flow. This cycle would repeat so that although the peak response of the cantilever would be increased, the mean value would decrease. This increase in the amplitude of the signal is reflected in the increasing standard deviation. Where the velocity is high enough that the flow does not reattach there would still be increased fluctuations in the position of the cantilever due to the likelihood of vortex shedding taking place.

Because of the disruption at around 20 m/s caused by stalling at incidence angles close to zero, the response of the sensor to yaw (perpendicular and parallel to the flow) was repeated at 27 m/s. The results are shown in Figure 6-39.

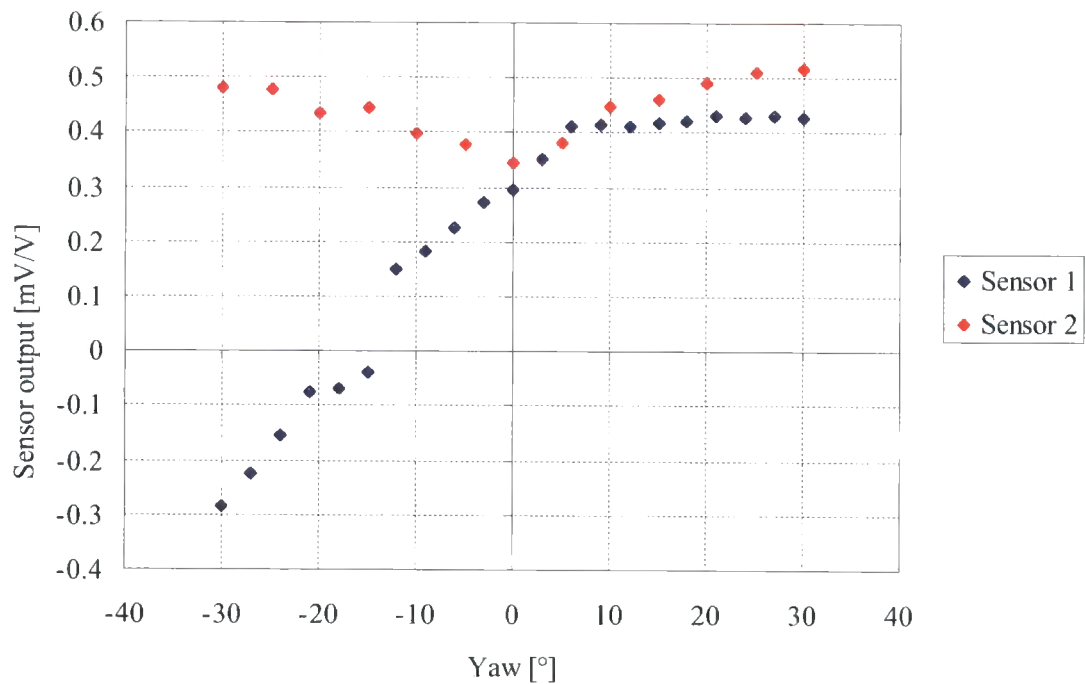


Figure 6-39 Response of revised sensors parallel and perpendicular to flow at varying yaw angles (Velocity = 27 m/s)

At this velocity, the dips in sensor output at positive yaw angles are not seen, as the range of angles seen here are not close to stall at this velocity. The variation seen where the sensor is parallel to the flow is much more defined, with a clear increase in the response of the pitch sensors at high yaw angles, compared with the response at zero incidence.

The apparently constant response of the sensor at positive incidence angles above 5° is probably due to the upstream sensor partially occluding the flow onto the downstream sensor. This should not be a problem for the calculation of the yaw coefficient since at corresponding negative yaw angles there is still a significant gradient at these values, and thus the difference between the upstream and downstream sensors will still vary with yaw angle.

Using these results to calculate the coefficients gives the following results:

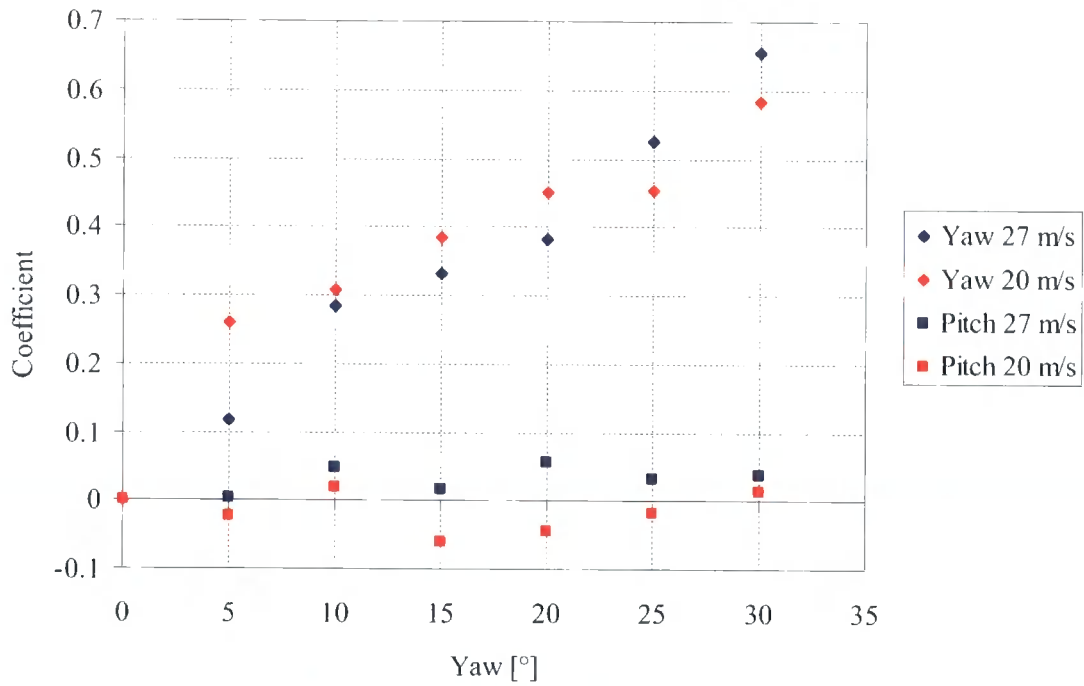


Figure 6-40 Yaw coefficient for revised probe design

The yaw coefficient increases for increasing yaw angles as would be expected. The coefficient for 20 m/s where the flow is close to the stall point shows a different response to that at a higher velocity where the flow is more similar regardless of yaw angle. Ideally the yaw coefficient would be the same, independent of the velocity. However a degree of Reynolds sensitivity means that the yaw coefficient of probes is often found to vary with velocity. The stall of the flow over the cantilevers, in this case, does however exacerbate the problem.

The pitch coefficient is close to zero for varying yaw angles.

The stagnation pressure coefficient is plotted in Figure 6-41.

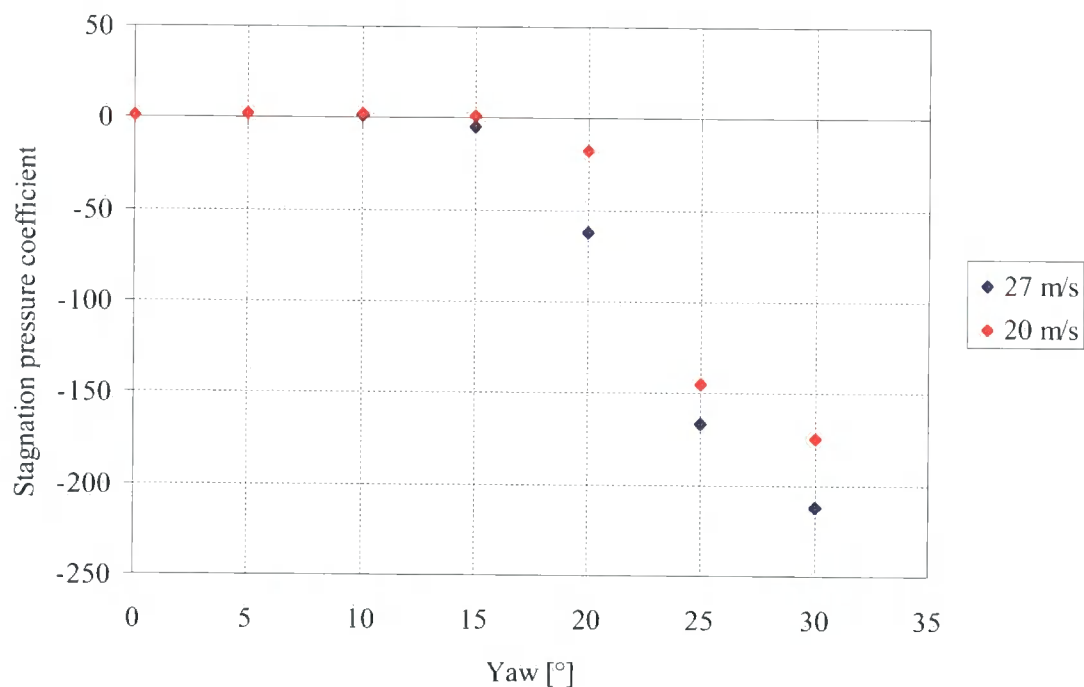


Figure 6-41 Stagnation pressure coefficient for revised probe design

The stagnation pressure coefficient decreases with increasing yaw angle as would be predicted. The coefficient is always negative as the probe pressure is referenced to total pressure and therefore must always be less than zero. The difference between the coefficients at different speeds when at higher yaw angles is due to Reynolds sensitivity.

The angle for which the probe pressure stays close to total pressure indicates that the probe is still seeing stagnation pressure at angles up to approximately 15°. Sheppard [84] states that a hemispherical pitot-static tube would have an error of less than 2.5% for angles of up to 30°. However, the presence of the sensors and the blunt nature of the tip would reduce this angle.

The dynamic pressure coefficient is plotted in Figure 6-42.

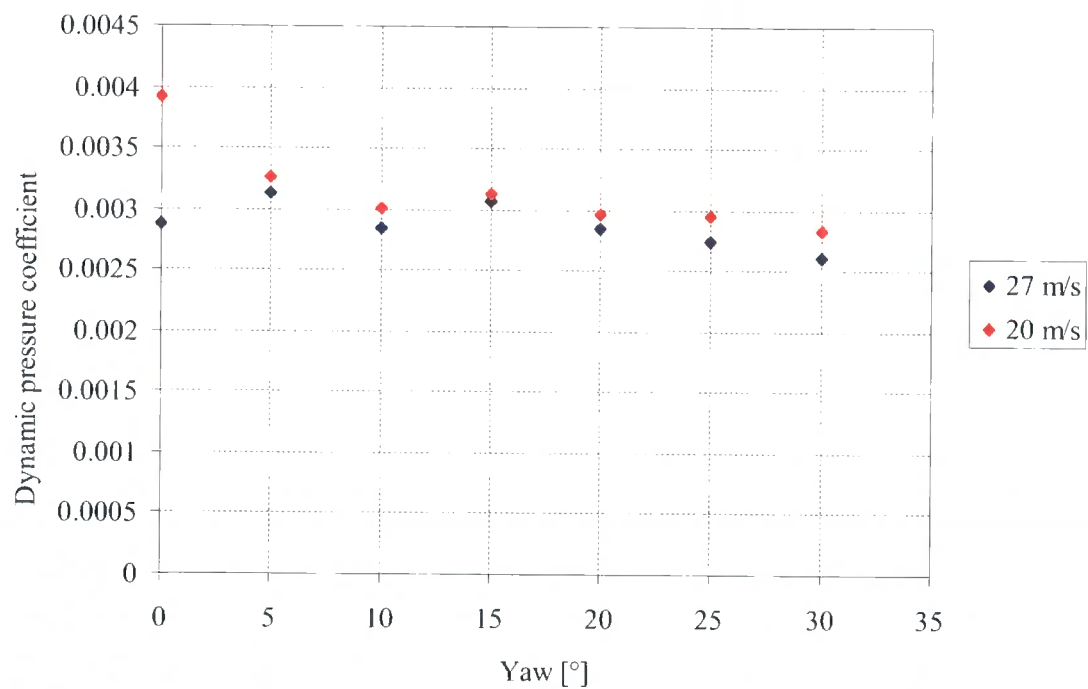


Figure 6-42 Dynamic pressure coefficient for revised probe design

The dynamic pressure coefficient remains quite similar regardless of Reynolds number and deviates little with yaw angle, decreasing slightly as the yaw angle increases. The major difference for the two velocities at zero yaw is due to the stalling of the cantilever that occurs at this angle at approximately 20 m/s. This does however cause a significant problem with the use of this coefficient for calculating the dynamic pressure from the sensor outputs.

If the total voltage output from all four sensors is plotted against dynamic pressure (Figure 6-43) it can be seen that in the region between 240 and 420 Pa, as many as three different dynamic pressures can be associated with the same voltage output. Because at zero incidence all four sensors are affected by stall at the same velocity, it is impossible to identify which of the dynamic pressures is the correct one for a particular data set.

At increased incidence angles, although one of the sensors may be close to stall the opposing sensor will not be in this region and therefore looking at both sensors



individually could be used to identify the true dynamic pressure. However at very small incidence angles this does not provide a solution.

Unless a solution to this problem was found, probes would be out of range for a specific range of velocities at small yaw angles. Changing the length of the sensors would alter the region to be considered out of range.

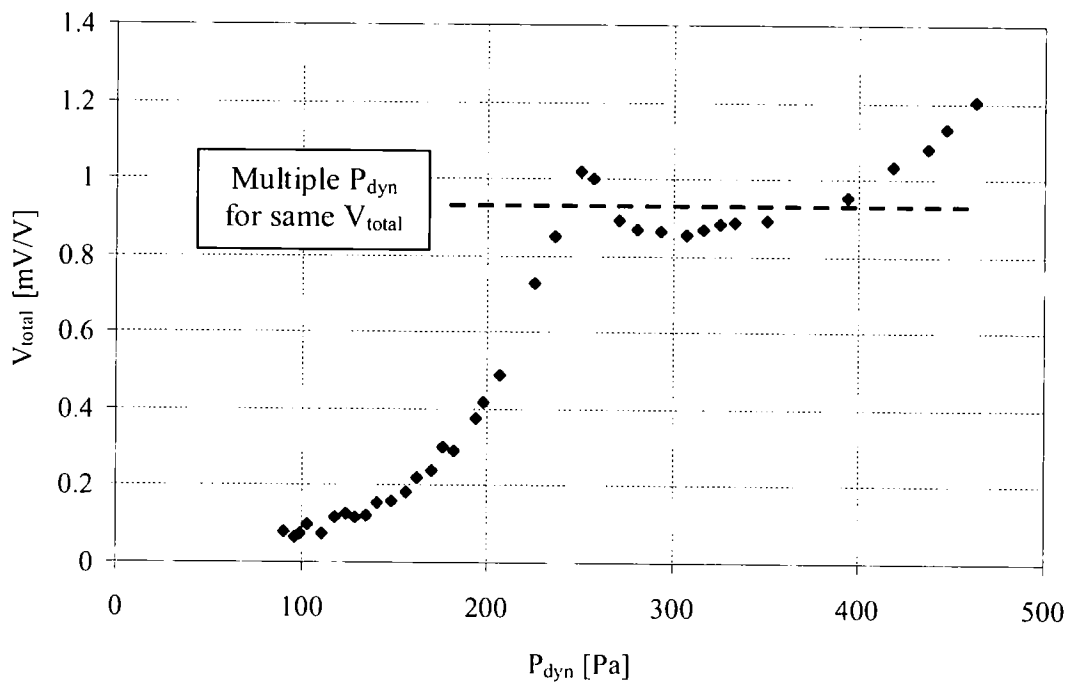


Figure 6-43 Dynamic pressure v. Total voltage output

Examples of the contour maps which would be generated when calibrating the probe are shown in Figure 6-44 to Figure 6-47. These results are taken from the data obtained from one sensor and generating the results from all four sensors, assuming that they have the same response. This data is for tests carried out at 27 m/s.

In reality it is unlikely that the coefficients would be as symmetrical as those shown here, since different sensors would be likely to have slightly varying responses. It would therefore be necessary to calibrate individual probes separately.

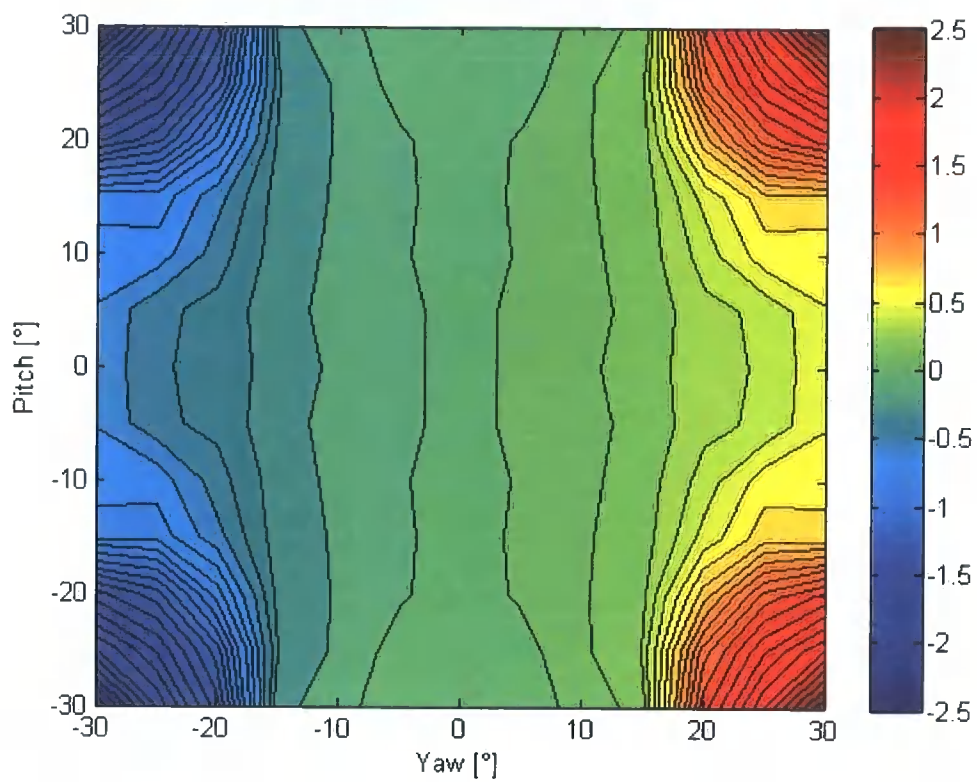


Figure 6-44 Map of yaw coefficient

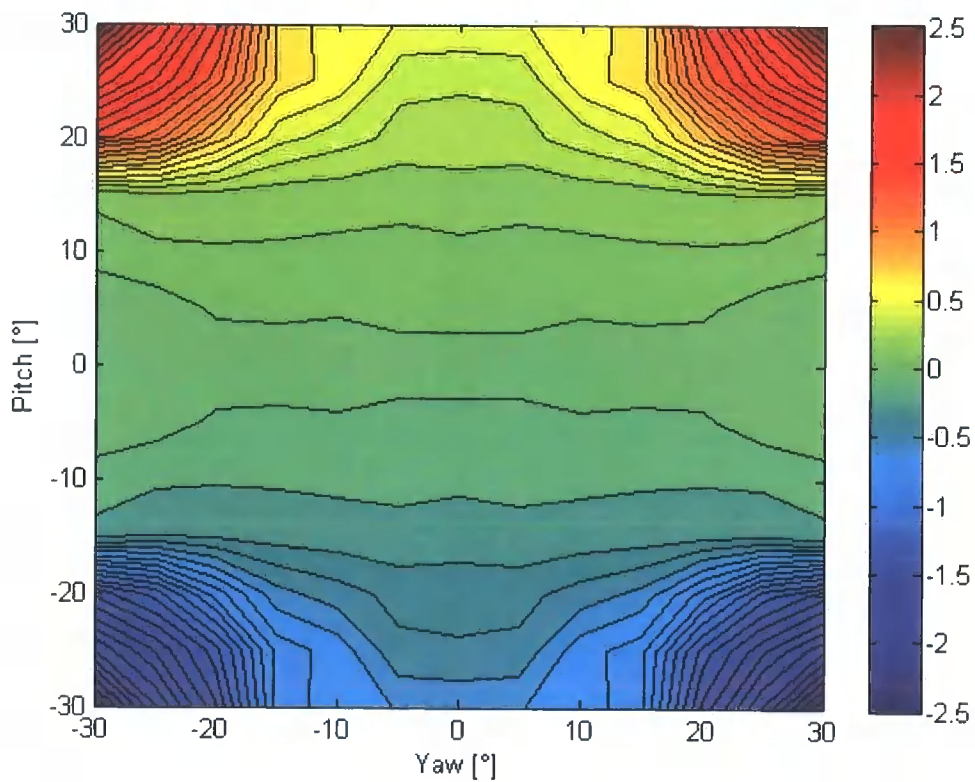


Figure 6-45 Map of pitch coefficient

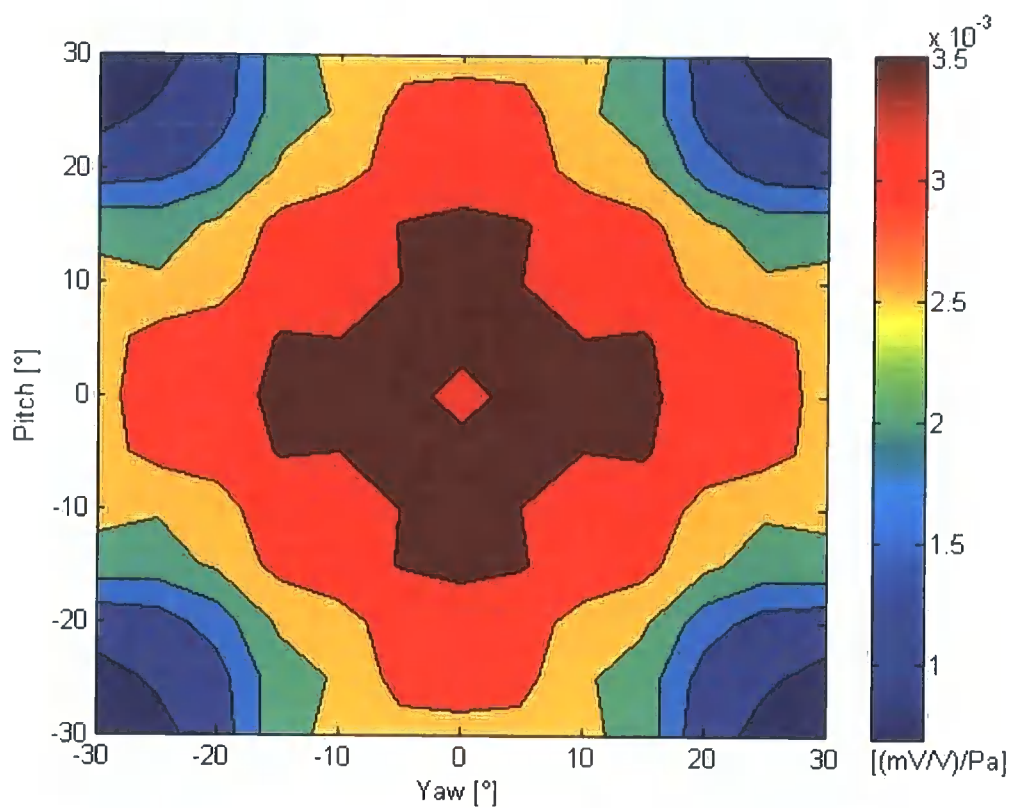


Figure 6-46 Map of dynamic pressure coefficient

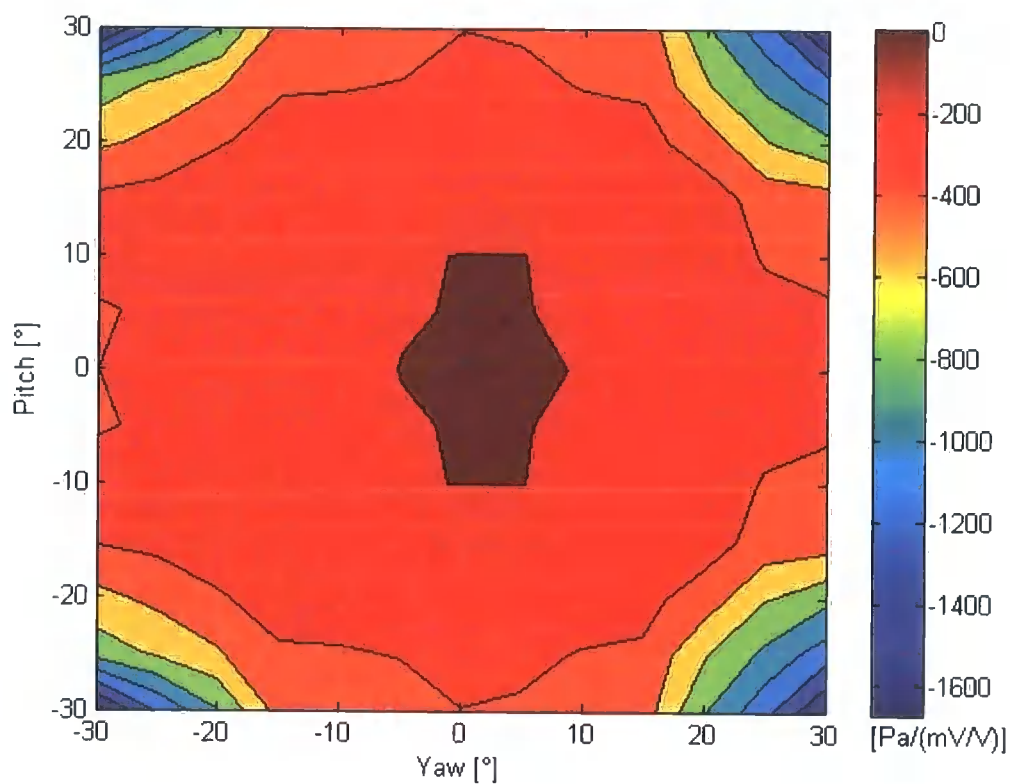


Figure 6-47 Map of stagnation pressure coefficient

These plots show that the probe gives suitable results in the regions between pure yaw and pure pitch, which were looked at in more detail previously. The good decoupling of pitch and yaw sensitivity is clear, and additionally it can be seen that the stagnation pressure coefficient is relatively independent of yaw and pitch, except at extreme angles.

## **6.6 Summary**

A probe constructed from four cantilever sensors with a central pressure tapping was used to measure pitch and yaw and also to give dynamic and stagnation pressure. This design represented an entirely new method of constructing an airflow probe, utilising MEMS technology to allow sensing elements smaller than could be achieved with standard fabrication processes. This would lead to the construction of a probe with a smaller tip diameter than is possible with conventional designs.

The probe design was modelled using CFD and FEA modelling which predicted that the probe would be effective for measuring pitch and yaw coefficients at incidence angles of up to  $\pm 40^\circ$ .

Initial wind tunnel testing of the original probe design showed that the sensors were not as sensitive as had been predicted by the modelling. In addition to this the probe had very little sensitivity to changes in velocity at zero incidence.

To improve these difficulties, the probe was redesigned. The cantilever sensor's positions were altered to be more parallel to the flow at zero incidence, which ensured that the sensors bent outwards at zero incidence. When the sensors were orientated inwards, for them to bend outwards required the pressure at the tip of the probe (close to stagnation pressure) to be greater than the pressure on the outer surface of the cantilever.

The new design of probe proved to have a much improved response to changes in dynamic pressure at zero incidence. The response was very similar to that seen for a sensor perpendicular to the flow when at incidence, but with a smaller magnitude of the response, as would be expected. However for certain velocities at zero incidence, due to

the deflection of the sensor, the flow around the cantilever was seen to stall, causing an irregularity in the response at a velocity of around 20 m/s. This stall point was also observed at small positive and negative incidence angles, although the velocity at which they occurred varied, due to the yaw angle causing a different effective incidence of the flow onto the cantilever.

The stalling of the airflow meant that the probe would be ineffective at measuring airflows at close to zero incidence angle to the flow, for a range of velocities around the point where the flow stalled.

The overall sensitivity was also improved with the new design, due to increasing the length of the cantilever by 50%. The sensitivity was still not as good as that which was predicted by modelling however, and this decrease in the sensitivity was attributed to the glue used to attach the sensors to the probe mounting extending along the under-surface of the cantilever and making it stiffer than would be expected from the SU-8 polymer alone.

The method of using cantilever sensors to measure the velocity components when constructed into a probe has been shown to be possible, allowing the creation of a probe with a tip smaller than that which has been possible with previous methods. However there are a number of improvements which could be made on the existing design. An increase in the sensitivity of the sensors would improve the signal-to-noise ratio and thus make the sensors more reliable. Improving the sensitivity would also allow the cantilevers to be shortened, reducing the problem of stalling as this would then occur at higher velocities. It would also be advantageous to increase the sensitivity sufficiently that a stiffer material could be used in order to limit the deflection of the cantilevers back into the airflow, as in the case of the shear stress sensor. However, the use of silicon with a doped silicon piezoresistor would not be as applicable here, as the current fabrication process requires some flexibility of the sensor for it to be mounted on the probe head.

In addition the failure rate when assembling the probe is high and this should be addressed. A number of problems can occur including shorting of the resistors when

attaching the wire, which could be solved by adding an additional layer of SU-8 over the resistors which would not cover the contact pads. However this additional layer of processing would be likely to increase the failure rate when fabricating the sensors. The resistors are also prone to being damaged while being glued onto the mounting and this aforementioned solution would also address this problem.

The assembly process is complex and prone to faults and an alternative assembly method which would produce a more reliable result would be a significant improvement. However because of the 3D nature of the probe, constructing the entire probe by MEMS fabrication processes is not possible and therefore some degree of assembly would always be required.

Once these fabrication problems were overcome it would be possible for a probe to be constructed that would be fully functional and, in addition, an alternative rapid prototyper (possible SLA (Stereolithography Apparatus)) would allow a probe tip to be created which was as small as 0.5 mm or less, which would be a significant improvement on existing probes for measuring flow vectors.

# Chapter 7

## Conclusions

The aim of this thesis was to apply MEMS technology to the fabrication of airflow sensors in order to improve the current available instrumentation. This required an innovative approach to airflow measurement in order to fully utilise the potential of the available techniques.

### 7.1 Fence-style shear stress sensor

Two different designs of shear stress sensors have been designed, fabricated and tested. The first design was an adaptation of a surface fence design, which incorporated a strain gauge into the fence structure in order to measure directly the pressure-induced deflection of the fence. This structure was fabricated from the photo-definable polymer SU-8 with a gold strain gauge incorporated within the fence to measure the deflection of the fence caused by the airflow. This strain gauge was connected to a Wheatstone bridge, which was within the body of the sensor to which the fence was attached.

CFD and FE modelling was carried out on the fence sensor to gain an understanding of the response of the sensor to the airflow. Vortex shedding was found to take place at higher Reynolds numbers.

The fence design of sensor was found, on wind tunnel testing, to be capable of measuring wall shear stress. A response from the sensor of 0.18 mV was measured at a shear stress of 0.35 Pa for an input voltage to the Wheatstone bridge of 1 V. However, there were thermal effects caused by the resistive heating of the gold resistor and the cooling that took place in the airflow. In addition to this the mounting of the fence sensor required it to be embedded within the surface of the model that was being tested. Also the fence protruded too high into the boundary layer, which would disturb the airflow as it passed over the sensor.

## **7.2 Cantilever-style shear stress sensor**

In order to address these issues, this initial sensor design was then built upon to create an innovative new design of sensor, using an in-plane cantilever to measure the shear stress by means of a built-in strain gauge to determine the pressure-induced deflection of the cantilever.

The use of a cantilever allows greater sensitivity than the use of a fence, which is effectively a beam with two fixed ends and the advantage of this in-plane cantilever design over one mounted normal to the wall surface is that increasing the sensitivity by increasing the length does not increase the frontal area of the cantilever seen by the airflow. The velocity gradients in the axial direction are smallest and therefore the spatial resolution of the sensor is least affected by the increase of the length of the sensor in this direction. The width of the cantilever has no influence on the sensitivity of the sensor and, although increasing the height of the cantilever above the wall would increase the sensitivity, the sensor would then be higher in the boundary layer and thus have a greater impact on the airflow passing over the sensor.

The pressure under the cantilever would be close to stagnation pressure, and a much lower pressure would be seen above the cantilever. This would cause the cantilever to deflect upwards and this deflection would be measured by a strain gauge incorporated



into the cantilever. The cantilever was fabricated from SU-8 as with the fence sensor, but the strain gauge was fabricated from nichrome, which has a higher gauge factor than gold, and also has a much lower thermal coefficient of resistivity which reduces the thermal sensitivity of the sensor.

Modelling of the cantilever by CFD allowed a greater understanding of the airflow passing over the sensor to be obtained. It was found that vortex shedding took place at higher Reynolds numbers where the incidence angle of the cantilever was greater. The airflow over the cantilever was found to stall as the incidence angle increased, but although the lift consequently decreased, the drag continued to increase and therefore the moment acting on the cantilever continued to increase after the flow stalled, albeit at a slower rate. CFD modelling also predicted that the resistive heating of the strain gauge would be minimal and have a negligible effect on the results from the cantilever. FE modelling was also carried out to predict the voltage output response from the sensor, which was found to be an order of magnitude greater than that of the fence sensor.

Mechanical testing was also carried out on the cantilever sensor in order to obtain an accurate Young's modulus and gauge factor for the sensor, which were 1.45 GPa and 1.8 respectively.

Wind tunnel testing showed that the modelling of the sensor was quite accurate. The shortest cantilever tested (2 mm long) was found to have a response of approximately 1 mV/V at 0.35 Pa. Longer cantilevers (3 and 4 mm long) were seen to bend back over themselves at higher velocities. This would have a big impact on the airflow passing over the sensor, and thus is an undesirable response indicating that the sensor is overly sensitive for this application. Varying the width of the cantilever was not found to have any effect on the response of the sensor.

There were found to be no thermal effects using this sensor as seen when using the fence sensor. In addition the excitation voltage was found to have no effect on the response of the sensor. Varying the axial position of the sensor showed that the sensor can measure the shear stress where the boundary layer velocity profile varies.

The cantilever sensor was shown to effectively measure the wall shear stress for steady state measurements in the laminar boundary layer. The device had a sensitivity an order of magnitude better than that seen for the fence sensor.

The stated specification for the shear stress sensor designed in this work has largely been achieved. A sensor capable of measuring low shear stresses has been demonstrated. Although stresses up to 10 Pa have not been measured, the design of the sensor is such that altering the geometry would allow stresses up to this magnitude to be measured. The sensor is independent of ambient temperature as required and the design of the sensor allows it to be surface-mounted on any existing model. The requirement for high frequency measurements did not come within the scope of this work.

### **7.3 Probe for freestream flow vector measurement**

The cantilever shear stress sensor was adapted into a probe for measuring freestream velocity components and would also allow the measurement of stagnation and dynamic pressures.

Four sensors were incorporated into one probe head in order to allow three-dimensional measurement. These sensors were mounted in two pairs normal to each other. One pair of sensors was largely sensitive to yaw, and the other pair was sensitive to pitch. The probe head on which the sensors were mounted had a hole running through it allowing the pressure at the centre of the probe to be measured for the calculation of the stagnation pressure. The movement of all four sensors together could measure the dynamic pressure.

Modelling of the probe was carried out using CFD in 3D. This predicted pressure differences across the cantilever sensors which, when combined with finite element modelling predictions gave expected output values similar to those seen in the cantilever wall shear stress sensor. This was because, despite the shorter length of the cantilever, the velocity seen by the cantilever was significantly greater as the sensor was not in the boundary layer where the velocities were much lower.

Wind tunnel testing of the probe showed significantly lower sensitivity than predicted, which was attributed at least in part to the fabrication method causing glue to reduce the deflection of the cantilever. However in addition to this the probe was found to have a negligible response to varying velocities at zero incidence angles.

To address this issue the probe was redesigned, and the new design was found to partially deal with this problem. The sensor was sensitive to changes in velocity at zero incidence. However, the flow over the sensor stalled at a velocity of just over 20 m/s at zero incidence, meaning that a probe of this design would be out of range for very small incidence angles in the region around this velocity. The sensitivity of the device was also improved with this new design. A single sensor at  $+30^\circ$  incidence at 20 m/s gives a response of 0.3 mV/V, with a response of -0.1 mV/V at  $-30^\circ$  incidence at 20 m/s.

Four sensors in this arrangement have been shown to allow the measurement of pitch and yaw, as well as the stagnation and dynamic pressures.

The objectives for this work have been partially achieved. A probe with the capability of measuring 3D flow vectors in the velocity range specified has been demonstrated. The stated yaw and pitch range is within the capability of the probe. However it was not found possible to minimise the probe tip beyond what was already possible with a conventional five-hole probe. However there is the potential to reduce the tip diameter with further work. The development of the probe for high frequency measurements was not completed within the scope of this work.

## **7.4 Further work**

### **7.4.1 Wall shear stress sensors**

Since the cantilever design of wall shear stress sensor supersedes the fence design, the focus here on future work will be directed toward the cantilever design.

The current materials used for the construction of the sensors allow a good sensitivity by means of a low Young's modulus that compensates for the fact that the gauge factor of a metal strain gauge is relatively low. However this means that the deflection of the

sensor is relatively large, which has a detrimental effect on the airflow. A method of overcoming this problem would be to achieve the sensitivity by means of a high gauge factor, with a relatively higher Young's modulus. This could be accomplished by fabricating the sensor from silicon with a doped silicon strain gauge.

A collateral advantage of this alteration would be to increase the resonant frequency of the cantilever, which would be an advantage in the measurement of turbulent, unsteady flows.

The current set-up for shear stress measurement is only suitable for steady state measurements as the signal-to-noise ratio is sufficiently low as to require a filter to be used to reduce the noise level. The use of a lock-in amplifier might allow this problem to be addressed in such a way that the frequency response of the sensor would be unaffected, allowing time-varying measurements to be taken. However lock-in amplifiers are normally used for ac voltage measurements.

#### **7.4.2 Probe for freestream flow vector measurement**

The assembly of the probe offers several opportunities for improvement. If, as postulated, the decrease in sensitivity compared with that which was predicted was due to the glue applied during the assembly process, then modifying this fabrication process should improve the sensitivity of the sensors. Also, the difficulty of attaching wires to such small contact pads could also be improved. There is the possibility of wire bonding for making the connections to the sensors, which would allow the size of the probe to be kept small close to the probe tip; however the difficulty of attaching wires, of dimensions large enough to handle, to the fine wires used for wire bonding would remain. Once this assembly problem had been addressed, a probe with four fully functional sensors could be created, which could then be tested in a real application.

The deflection of the cantilever sensor should be minimised as was the case with the wall shear stress sensor, in order to keep the probe tip size as small as possible during operation. However the use of silicon as suggested for that application would not be suitable here since the assembly process relies on the flexibility of the SU-8 to allow the sensors to be mounted on the probe.

## References

- 1 Fernholz HH, Janke G, Schober M, Wagner PM and Warnack D New developments and applications of skin-friction measuring techniques *Meas. Sci. Technol.* **7** 1396-1409 (1996)
- 2 Sheplak M, Cattafesta L and Nishida T MEMS shear stress sensors: promise and progress 24<sup>th</sup> *AIAA Aerodynamic Measurement Technology and Ground Testing Conference* (2004)
- 3 Naughton JW and Sheplak M Modern developments in shear-stress measurement *Progress in Aerospace Sciences* **38** 515-570 (2002)
- 4 Squire LC The motion of a thin oil sheet under the boundary layer on a body *J. Fluid Mech.* **11** 161-179 (1961)
- 5 Tanner LH and Blows LG A study of the motion of oil films on surfaces in air flow, with application to the measurement of skin friction *J Phys E* **9(3)** 194-202 (1976)
- 6 Murphy JD and Westphal RV The laser interferometer skin-friction meter: a numerical and experimental study *J Phys E* **19** 744-51 (1986)
- 7 Pradeep AM and Sullerey RK Application of shear stress sensitive liquid crystals in flow visualisation and skin friction estimation *Optical Diagnostics in Engineering* **7** 1-9 (2004)
- 8 Buttsworth DR, Elston SJ and Jones TV Directional sensitivity of skin friction measurements using nematic liquid crystal *Meas. Sci. Technol.* **9** 1856-1865 (1998)
- 9 Fujisawa N, Aoyama A and Kosaka S Measurement of shear-stress distribution over a surface by liquid-crystal coating *Meas. Sci. Technol.* **14** 1655-1661 (2003)
- 10 Padmanabhan A, Goldberg HD, Breuer KS and Schmidt MA A silicon micro-machined floating-element shear-stress sensor with optical position sensing by photodiodes *Proc. of Transducers* (Stockholm, Sweden) p 436-439 (1995)
- 11 Horowitz S, Chen T, Chandrasekaran V, Tedjojuwono K, Nishida T, Cattafesta L and Sheplak M A micromachined geometric moiré interferometric floating-element

- shear stress sensor AIAA Paper 2004-1042 42<sup>nd</sup> Aerospace Sciences Meeting and Exhibit (Reno, NV) (2004)
- 12 Zhe J, Farmer KR and Modi V A MEMS device for measurement of skin friction with capacitive sensing *Proc. of IEEE MEMS 2001* (Berkeley, CA) p 4-7 (2001)
- 13 Desai AV and Haque MA Design and fabrication of a direction sensitive MEMS shear stress sensor with high spatial and temporal resolution *J. Micromech. Microeng* **14** 1718-1725 (2004)
- 14 Alvin Barlian A, Park S-J, Mukundan V and Pruitt BL Design and characterization of microfabricated piezoresistive floating element-based shear stress sensors *Sensors and Actuators A* **134** 77-87 (2006)
- 15 Bruun HH Hot wire anemometry: Principles and signal analysis Oxford University Press 237-253 (1995)
- 16 Sheplak M, Chandrasekaran V, Cain A, Nishida T and Cattafesta LN Characterization of a silicon-micromachined thermal shear-stress sensor *AIAA Journal* **40** 6 (2002)
- 17 Huang JB, Jiang FK, Tai YC and Ho CM A micro-electro-mechanical-system-based thermal shear-stress sensor with self-frequency compensation *Meas. Sci. Technol.* **10** 687-696 (1999)
- 18 Elvery DG and Bremhorst K Directional sensitivity of wall mounted hot-film gauges *Meas. Sci. Technol.* **7** 1410-1417 (1996)
- 19 Dengel P and Fernholz HH An experimental investigation of an incompressible turbulent boundary layer in the vicinity of separation *J. Fluid Mech.* **212** 615-636 (1990)
- 20 Chen J, Zou J and Liu C A surface micromachined, out-of-plane anemometer *Proc. of IEEE MEMS 2002* (Las Vegas, NV) p 332-335 (2002)
- 21 Liu C, Huang J-B, Zhu Z, Jiang F, Tung S, Tai Y-C and Ho C-M A micromachined flow shear-stress sensor based on thermal transfer principles *J. of Microelectromech. Sys.* **8** 90-99 (1999)

- 22 Tung S, Rokadia H and Li WJ A micro shear stress sensor based on laterally aligned carbon nanotubes *Sensors and Actuators A* **133** 431-438 (2007)
- 23 Fourgette D, Modarress D, Taugwalder F, Wilson D, Koochesfahani M and Gharib M Miniature and MOEMS flow sensors *AIAA Paper 2001-2982* (2001)
- 24 Vagt JD and Fernholz H Use of surface fences to measure wall shear stress in three-dimensional boundary layers *Aeronautical Quarterly* **24** 87-91 (1973)
- 25 Papen T, Steffes H, Ngo HD and Obermeier E A micro surface fence probe for the application in flow reversal areas *Sensors and Actuators A* **97-98** 264-270 (2002)
- 26 Papen T, Buder U, Ngo HD and Obermeier E A second generation MEMS surface fence sensor for high resolution wall shear stress measurement *Sensors and Actuators A* **113** 151-155 (2004)
- 27 Schober M, Obermeier E, Pirskawetz S and Fernholz HH A MEMS skin-friction sensor for time resolved measurements in separated flows *Exp. in Fluids* **36** 593-99 (2004)
- 28 Chen J, Engel J and Liu C Development of polymer-based artificial haircell using surface micromachining and 3D assembly *Transducers 2003* (Boston) (2003)
- 29 Brücker C, Spatz J and Schröder W Wall shear stress imaging using micro-structured surfaces with flexible micro-pillars *Exp. in Fluids* **39** 464-474 2005
- 30 Große S and Schröder W Mean wall-shear stress measurements using the micro-pillar shear-stress sensor MPS<sup>3</sup> *Meas. Sci. Technol.* **19** 015403 (2008)
- 31 Patel VC Calibration of the Preston tube and limitations on its use in pressure gradients *J. Fluid. Mech.* **23** 185-208 (1965)
- 32 Adrain RJ Twenty years of particle image velocimetry *Exp. in Fluids* **39** 159-169 (2005)
- 33 Adrian RJ Scattering particle characteristics and their effect on pulsed laser measurements of fluid flow: speckle velocimetry vs particle image velocimetry *Appl. Opt.* **23** 1690-1691 (1984)

- 34 Pickering CJD and Halliwell NA Laser speckle photography and particle image velocimetry: photographic film noise *Appl. Opt.* **23** 2961-2969
- 35 Maas HG, Gruen A and Papantoniou D Particle tracking velocimetry in three-dimensional flows Part 1. Photogrammetric determination of particle coordinates *Exp. in Fluids* **15** 133-146
- 36 Pereira F and Gharib M Defocusing digital particle image velocimetry and the three-dimensional characterization of two-phase flows *Meas. Sci. Technol.* **13** 683-694 (2002)
- 37 Barnhart DH, Adrian RJ and Papen GC Phase-conjugate holographic system for high-resolution particle-image velocimetry *Appl. Opt.* **33** 7159-7170 (1994)
- 38 Royer H Holography and particle image velocimetry *Meas. Sci. Technol.* **8** 1562-1572 (1997)
- 39 Santiago JG, Wereley ST, Meinhart CD, Beebe DJ and Adrian RJ A particle image velocimetry system for microfluidics *Exp. in Fluids* **25** 316-316 (1998)
- 40 Penner SS and Jerskey T Use of lasers for local measurement of velocity components, species densities and temperatures *Annu. Rev. Fluid Mech.* **5** 9-30 (1973)
- 41 Wang CP and Schnyder D Laser Doppler Velocimetry: Experimental Study *Appl. Opt.* **13** 98-103 (1974)
- 42 Czarske JW Laser Doppler velocimetry using powerful solid-state light sources *Meas. Sci. Technol.* **17** R71-R91 (2006)
- 43 Kupferschmied P, Koppel P, Gizzi W, Roduner C and Gyarmathy G Time-resolved flow measurements with fast-response aerodynamic probes in turbomachines *Meas. Sci. Technol.* **11** 1036-1054 (2000)
- 44 Sieverding CH, Arts T, Denos R and Brouckaert J-F Measurement techniques for unsteady flows in turbomachines *Exp. in Fluids* **28** 285-321 (2000)
- 45 Ligrani PM, Singer BA and Baun LR Miniature five-hole pressure probe for measurement of three mean velocity components in low-speed flows *J. Phys. E: Sci. Instrum.* **22** 868-876 (1989)



- 46 Lenherr C, Kalfas AI, and Abhari RS A flow adaptive aerodynamic probe concept for turbomachinery *Meas. Sci. Technol.* **18** 2599-2608 (2007)
- 47 Ainsworth RW, Miller RJ, Moss RW and Thorpe SJ Unsteady pressure measurement *Meas. Sci. Technol.* **11** 1055-1076 (2000)
- 48 Babinsky H, Kuschel U, Hodson HP, Moore DF and Wellard ME The aerodynamic design and use of multi-sensor pressure probes for MEMS applications *15<sup>th</sup> Bi-annual Symposium on Measuring Techniques in Turbomachinery* (Florence, Italy) (2000)
- 49 Lemonis G Three-dimensional measurement of velocity, velocity gradients and related properties in turbulent flows *Aerospace Science and Technology* **7** 453-461 (1997)
- 50 Sherif SA and Pletcher RH A normal sensor hot-wire/film probe method for the analysis of three-dimensional flows *Flow Meas. Instrum.* **5** 150-154 (1994)
- 51 Samet M and Einav S A hot-wire technique for simultaneous measurement of instantaneous velocities in 3D flows *J. Phys. E: Sci. Instrum* **20** 683-690 (1987)
- 52 Tsinober A, Kit E and Dracos T Experimental investigation of the field of velocity gradients in turbulent flows *J. Fluid Mech.* **242** 169-192 (1992)
- 53 Van Dijk A and Nieuwstadt FTM The calibration of (multi-) hot-wire probes 2. Velocity-calibration *Exp. in Fluids* **36** 550-564 (2004)
- 54 Shaw JM, Gelorme JD, LaBianca NC, Conley WE, Holmes SJ Negative photoresists for optical lithography *IBM J. Res. Develop.* **41**(1/2) (1997)
- 55 Chuang Y-J, Tseng F-G, Lin W-K Reduction of diffraction effect of UV exposure on SU-8 negative thick photoresist by air gap elimination *Microsyst. Technol.* **8** 308-313 (2002)
- 56 Dai W, Lian K, Wang W A quantitative study on the adhesion property of cured SU-8 on various metallic surfaces *Microsyst. Technol.* **11** 526-534 (2005)
- 57 Plint and Partners Plint Wind tunnel TE44 Manual
- 58 Kreyszig E Advanced Engineering Mathematics 8<sup>th</sup> ed. John Wiley & Sons Inc. p.1110 (1999)

- 59 Massey B Mechanics of Fluids 7<sup>th</sup> ed. Stanley Thornes (Publishers) Ltd 369-375 (1998)
- 60 Tannehill JC, Anderson DA and Pletcher RH Computational Fluid Mechanics and Heat Transfer 2<sup>nd</sup> ed. Taylor and Francis (1997)
- 61 Benham PP, Crawford RJ and Armstrong CG Mechanics of Engineering Materials 2<sup>nd</sup> ed. Longman p.206 (1996)
- 62 Strand7 Finite Element Analysis System Documentation
- 63 Thaysen J, Yalcinkaya AD, Vettiger P and Menon A Polymer-based stress sensor with integrated readout *J. Phys. D: Appl. Phys.* **25** 2698-2703 (2002)
- 64 Massey B Mechanics of Fluids 7<sup>th</sup> ed. Stanley Thornes (Publishers) Ltd 326 (1998)
- 65 Fox RW, McDonald AT, Pritchard PJ Introduction to Fluid Mechanics 6<sup>th</sup> ed. John Wiley and Sons 427 (2004)
- 66 Johnson SA, Thompson MC, Hourigan K Flow past elliptical cylinders at low Reynolds numbers 14<sup>th</sup> *Australasian Fluid Mechanics Conference* (2001)
- 67 Dellmann L, Roth S, Beuret C, Racine G, Lorenz H, Despont M, Renaud P, Vettiger P and de Rooij N Fabrication process of high aspect ratio elastic and SU-8 structures for piezoelectric motor application *Sensors and Actuators A* **70** 42-47 (1998)
- 68 Lorenz H, Despont M, Fahrni N, LaBianca N, Renaud P and Vettiger P SU-8: a low-cost negative resist for MEMS *J. Micromech. Microeng.* **7** 121-124 (1997)
- 69 Chang S, Warren J and Chiang F Mechanical testing of EPON SU-8 with SIEM *Proc. Of Microscale Systems: Mechanics and Measurement Symposium* Orlando, FL 46-49 (2000)
- 70 Wen Y-H, Yang GY, Bailey VJ, Lin G, Tang WC and Keyak JH Mechanically robust micro-fabricated strain gauges for use on bones *Proc. of 3<sup>rd</sup> Annual IEEE EMBS Conf. on Microtechnologies in Medicine and Biology* Oahu, Hawaii (2005)
- 71 Khoo HS, Liu K and Tseng F Mechanical strength and interfacial failure analysis of cantilevered SU-8 microposts *J. Micromech. Microeng.* **13** 822-831 (2003)

- 72 Engel J, Chen J and Liu C Strain sensitivity enhancement of thin metal film strain gauges on polymer microscale structures *Appl. Phys. Lett.* **89** 221907 (2006)
- 73 Thomson WT Theory of Vibration with Applications 4<sup>th</sup> ed. Chapman and Hall (1993)
- 74 Sameoto D, Tsang S-H, Foulds IG, Lee S-W, Parameswaran M Control of the out-of-plane curvature in SU-8 compliant microstructures by exposure dose and baking times *J. Micromech. Microeng.* **17** 1093-1098 (2007)
- 75 Ericson F, Greek S, Söderkvist J and Schweitz J High sensitivity surface micromachined structures for internal stress and stress gradient evaluation *J. Micromech. Microeng.* **7** 30-36 (1997)
- 76 Bachmann D, Schöberle B, Kühns S, Leiner Y and Hierold C Fabrication and characterization of folded SU-8 suspensions for MEMS applications *Sensors and Actuators A* **130-131** 379-386 (2006)
- 77 Rolke J Nichrome thin film technology and its application *Electrocomponent Science and Technology* **9** 51-57 (1981)
- 78 Sato Y, Watanabe M and Sato S Electrical properties of Ni-Cr-N thin films deposited by multitarget reactive sputtering *Jpn J. Appl. Phys.* **40** 5091-5094 (2001)
- 79 Kazi I, Wild P, Moore T and Sayer M The electromechanical behaviour of nichrome (80/20 wt.%) film *Thin Solid Films* **433** 337-343 (2003)
- 80 Lee B-J, Lee D-C Electrical properties of sputtered Ni-Cr-Al-Cu thin film resistors with Ni and Cr contents *Journal of the Korean Physical Society* **40** 339-343 (2002)
- 81 Lee B-J, Lee B-H and Lee D-C Quaternary alloy films for thin film resistors *Jpn J. Appl. Phys.* **42** 1405-1409 (2003)
- 82 Pohlhausen E Der Wärmeaustausch zwischen festen Körpern und Flüssigkeiten mit kleiner Reibung und kleiner Wärmeleitung. *Z. Angew. Math. Mech.* **1**, 115-121 (1921)
- 83 Durham Software for Wind-Tunnels, User manual
- 84 Sheppard PA Anemometry: A critical and historical survey *Proc. Phys. Soc.* **53** 361-390 (1941)

